COMPLETE-COOLING-LOOP BASED TRANSFORMER THERMAL STUDIES THROUGH CFD SIMULATIONS AND EXPERIMENTATION

A thesis submitted to The University of Manchester for the degree of

PhD

in the Faculty of Science and Engineering

2022

SICHENG ZHAO

Department of Electrical and Electronic Engineering

School of Engineering

Contents

List of Figure

List of Table

Nomenclature

T	Temperature (K)
T_{hs}	Hot-spot temperature (K)
T_{top}	Top liquid temperature (K)
$T_{top-rate}$	Top liquid temperature at the rated loading level (K)
$T_{top-mid}$	Top liquid temperature measured at the middle of top buffer zone in experimental setup (K)
$T_{top-outlet}$	Top liquid temperature measured at the outlet of winding in experimental setup (K)
T_{bot}	Bottom liquid temperature (K)
$T_{bot-mid}$	Bottom liquid temperature measured at the middle of bottom buffer zone in experimental setup (K)
$T_{bot-inlet}$	Bottom liquid temperature measured at the inlet of winding in experimental setup (K)
T_{avo}	Average liquid temperature ($(T_{top} + T_{bot})/2$) (K)
T_{avw}	Average winding temperature (K)
T_{amb}	Ambient temperature (K)
T_w	Radiator surface temperature (K)
ΔT_{oil}	Liquid temperature rise ($T_{top} - T_{bot}$) (K)
ΔT_{top}	Top liquid temperature rise over ambient ($T_{top} - T_{amb}$) (K)
ΔT_{bot}	Bottom liquid temperature rise over ambient ($T_{bot} - T_{amb}$) (K)
ΔT_{avw}	Average winding temperature rise over ambient ($T_{avw} - T_{amb}$) (K)
ΔT_{hs}	Hot-spot temperature rise over ambient ($T_{hs} - T_{amb}$) (K)
V	Transformer thermal ageing rate
R	Ratio of the load loss at the rated load to the no-load loss
H	Hot-spot factor
K	Loading level
g_r	Temperature gradient between the insulating liquid and the winding ($T_{avw} - T_{avo}$) (K)

x	Liquid exponent
y	Winding exponent
h	Transformer thermal head (m)
C	Geometry related constant of frictional pressure loss
L'	Equivalent length of liquid complete-cooling-loop (m)
H'	Equivalent diameter of liquid complete-cooling-loop (m)
C_g	Geometric characteristics of liquid complete-cooling-loop
P	Total power loss/ injection/ dissipation (W)
q_{con}''	Heat flux by convection effect ($W/(m^2)$)
q_{radi}''	Heat flux by radiation effect ($W/(m^2)$)
$Q_{oil-top}$	Total liquid flow rate at radiator top (m^3/s)
v_{oil}	Liquid velocity at the winding inlet (m/s)
ρ	Density (kg/m^3)
ρ_{top}	Liquid density at radiator top (kg/m^3)
ρ_{bot}	Liquid density at winding inlet (kg/m^3)
c_p	Specific heat capacity ($J/(kg \cdot K)$)
k	Thermal conductivity ($W/(K \cdot m)$)
p	Pressure (P_a)
p_{amb}	Ambient pressure (P_a)
τ	Viscous shear stress tensor (P_a)
$\vec{g}$	Gravity vector (m^2/s)
β	Thermal expansion coefficient ($1/K$)
$\vec{u}$	Fluid velocity (m/s)
u	Velocity x-component (m/s)
v	Velocity y-component (m/s)
w	Velocity z-component (m/s)
h_{air}	Air heat transfer coefficient ($W/(m^2 \cdot K)$)
ε	Emissivity

σ	Stefan–Boltzmann constant
A	Radiator surface area (m^2)
A_{out}	Radiator outwards facing surface area (m^2)
A_{bot}	Winding inlet surface area at winding bottom (m^2)
L	Radiator panel length (m)
W	Radiator panel width (m)
s	Radiator pitch distance (m)
S	Geometric distance of inwards facing radiator surface (m)
L_h	Entrance length of pipe flow (m)
D	Characteristic length of the isothermal pipe (m)
R_e	The Reynolds number
R_{aL}	The Rayleigh number (geometric characteristic using L)
R_{as}	The Rayleigh number (geometric characteristic using S)
P_r	The Prandtl number
N_u	The Nusselt number

Abstract

Achieving carbon net-zero ambitions requires electrification of heat and transport. It is expected to see wider integration of low carbon technologies into the electrical power networks. Both existing and new transformers will inevitably experience higher and more dynamic loads in the future. Therefore, it is important to optimise transformer thermal design during the manufacturing process and to improve thermal loading management during operation. Past transformer thermal studies have focused on individual components, i.e., either windings or radiators and under oil forced cooling mode. This thesis aims to develop a complete-cooling-loop (CCL) based Computational Fluid Dynamics (CFD) model of liquid natural cooled transformers, which includes both the winding and the radiator. The CCL CFD model is used to investigate liquid temperatures and velocities under a wide range of conditions. In addition, both the developed CFD modelling methodology and its simulation results are verified by corresponding experiments.

First, a CCL based experimental setup including both a winding section and a 4-panel 1-meter-high radiator was established. The setup successfully achieves the spontaneous liquid flow and has the abilities to vary the total power loss injection and the thermal head.

Next the radiator modelling strategy was investigated. A full radiator CFD model including the air domain was built as the reference. Experimental verifications showed that the differences of the bottom liquid temperature, the radiator surface temperature and the total heat dissipation between the simulation and measurement results are less than 0.9 K, 3.3 K and 4.3%, respectively. Through parametric sweep simulations by the full radiator CFD model, a reduced radiator CFD model which uses an air heat transfer coefficient (h_{air}) equation to replace the air domain simulation, was developed. The reduced model, by adopting a dimensionless form, was experimentally verified and proven to be valid for different insulating liquids and under different ambient temperatures.

A CCL CFD model was finally developed by incorporating the reduced radiator model, which makes the computational demand manageable. Experimental verifications showed that the differences of the liquid temperatures and the liquid velocities between the simulation and measurement results are less than 2.2 K and 12.3%, respectively. The developed CCL CFD model was then used to investigate the liquid thermal behaviours, under a wide range of conditions, including 14 thermal loading levels, 3 thermal heads, 5 ambient temperatures and 3 insulating liquids.

The simulation results showed that the liquid velocity is proportional to the square root of the product of the total power loss and the thermal head, which is due to the pressure equilibrium in the liquid flow. The conclusion is also confirmed by the experimental data. When the ambient temperature increases, the top liquid temperature rise over the ambient temperature decreases, while the bottom liquid temperature rise over the ambient temperature increases.

In terms of thermal performances of different insulating liquids under natural cooling mode, the Gas-to-Liquid behaves similarly to the mineral oil. However, the liquid velocities of the synthetic ester liquid are lower than those of the mineral oil under different loading conditions investigated in this thesis. Similar studies based on analytical methods published in the literature are proven to be inaccurate, which shows the necessity to conduct the CCL CFD modelling for the natural cooling mode.

The significance of this work is to further advance the development of a cost-effective way of modelling the complete cooling loop of a liquid-immersed power transformer.

Declaration

I declare that no portion of the work referred to in the thesis has been submitted in support of an application for another degree or qualification of this or any other university or other institute of learning.

Copyright Statement

(I). The author of this thesis (including any appendices and/or schedules to this thesis) owns certain copyright or related rights in it (the "Copyright") and s/he has given The University of Manchester certain rights to use such Copyright, including for administrative purposes.

(II). Copies of this thesis, either in full or in extracts and whether in hard or electronic copy, may be made only in accordance with the Copyright, Designs and Patents Act 1988 (as amended) and regulations issued under it or, where appropriate, in accordance with licensing agreements which the University has from time to time. This page must form part of any such copies made.

(III). The ownership of certain Copyright, patents, designs, trademarks and other intellectual property (the "Intellectual Property") and any reproductions of copyright works in the thesis, for example graphs and tables ("Reproductions"), which may be described in this thesis, may not be owned by the author and may be owned by third parties. Such Intellectual Property and Reproductions cannot and must not be made available for use without the prior written permission of the owner(s) of the relevant Intellectual Property and/or Reproductions.

(IV). Further information on the conditions under which disclosure, publication and commercialisation of this thesis, the Copyright and any Intellectual Property and/or Reproductions described in it may take place is available in the University IP Policy (see http://documents.manchester.ac.uk/display.aspx?DocID=24420), in any relevant Thesis restriction declarations deposited in the University Library, The University Library's regulations (see http://www.manchester.ac.uk/library/about/regulations/) and in The University's policy on Presentation of Theses.

Acknowledgement

I would like to extend my utmost gratitude to my supervisor, Dr Qiang Liu for his continuous support and guidance throughout my PhD study. He has been a shining light of wisdom, knowledge and persistence to me. I would like to also express my utmost gratitude to my co-supervisors Prof Zhongdong Wang and Prof Paul Jarman, and a special thank you to Prof Peter Crossley for their inspiration, help and encouragement along my PhD research journey. The knowledge, guidance and advice from them made my work infinitely better than it would have otherwise been.

I would also like to thank the sponsors in the Transformer Research Consortium for providing me a full PhD scholarship. It is a real pleasure to work with all the experts: Luke Van Der Zel and Timothy Traymond from EPRI, Attila Gyore, James Reid, Mark Lashbrook, Muhammad Daghrah and Russel Martin from M&I, Gordon Wilson and Ruth Hooton from National Grid, Andree Hiker and Ed. Van Schaik from Shell, Luc Dorpmanns and Mark Wilkinson from SGB-Smit, David Walker from Scottish Power, Christoph Krause and Massimo Negro from Weidmann. Thanks a lot for your financial and technical contributions.

I wish to express my thanks to Dr Xiang Zhang. The exceptionally knowledgeable and generous sharing always helped me finding the flaws in my work. Without his help, I could not understand the whole background as fast as I did. I also wish to extend my gratitude to Dr Shanika Matharage and Mr Berihu Mebrahtom for their help on my experiments.

PhD is a long journey and mine would not have been as smooth as I wanted it to be without the friendship of Mr Hang Xu, Mrs Shuyang Shen, Mr Haichuan Yu, Ms Gechen Bian, Dr Xiaohan Li, Dr Bozhi Cheng, Dr James Hill, Dr Yiming Huang, Dr Donglin Liu, Mr Thathsara Herath, Dr Zongwen Yan, Ms Ziye Guo, and Dr Mingyu Han.

Last but not least, my acknowledgement would be incomplete without expressing my sincere thanks to my parents and my family for their selfless and continuous love, support and encouragement, and to my beloved partner Dr Chenning Wu for her faithful love, inspiration and care.

Chapter 1 Introduction

1.1 Motivation

Since the beginning of the first industrial revolution in 1760s, the average global temperature has been increasing as reported in [1-3], and the threat of average temperature rise to the society has been recognised globally. Hence, at the 26th United Nations Climate Change conference (COP26) in November 2021, agreed by 197 countries within the United Nations Framework Convention on Climate Change (UNFCCC), the global temperature rise should be maintained ‘well below 1.5 ℃ above pre-industrial levels’ [4] instead of ‘below 2 ℃ above pre-industrial levels’, which was signed in the Paris Climate Agreement [5] (on 4th November 2016).

The unexpected increase of global temperature is the result of greenhouse gas emission to the atmosphere, which is mainly from the carbon dioxide. Therefore, over 140 countries in UNFCCC pledged to reach net-zero emissions, which are related to 90% of global Gross Domestic Product (GDP) [6]. The UK government also sets out various policies for decarbonising all sections of the economy to meet the carbon ‘Net Zero’ target by 2050 [7, 8]. To meet such target, the UK government plans to reduce the emissions by 78% by 2035 [7, 8].

The emissions come from various sources. As documented in [8], the emission can be grouped into different categories, as: (1) transportation, including international aviation and shipping (2) electricity or power generation (3) heating and cooling of the buildings (4) agriculture (5) industry (6) waste and (7) fluorinated gases. One of the most efficient methods to reduce the emissions is through ‘electrification’ of other uses of the energy [8-10], in which the energy for transportation, heating and cooling will be from the electricity rather than the fossil fuel. However, such a large scale of electrical energy for transport and heat would phenomenally increase the demand of the electrical power network. As reported by the Committee for Climate Change (CCC) in 2018 [11], the electricity demand in the UK will be at least doubled by 2050, as a result of ‘the electrification of other energy sectors’. To further reduce the emissions from the electricity, the fossil fuel used in the thermal power stations will be replaced by the renewable energy, e.g., wind, solar, waves, biomass and hydro. The electrification and the integration of the renewable energy will lead to a higher and more dynamic loading for the electricity network in the forthcoming future.

The thermal issue has been identified as one of the main constraints in the transmission system in the UK, as reported by National Grid Electricity System Operator (NGESO) in its Electricity Ten Year Statement [12] in 2021.

The electricity networks are ageing infrastructures in some of the developed countries. Specifically, in the UK, the majority of the electricity transmission networks were commissioned in the 1960s [13-15]. Taken transformers as an example, a large proportion (over 50%) of the transformers in the UK are over 40 years old [15], and some are even more than 50 or even 60 years old (a survey conducted from three utilities in the UK, as National Grid, Scottish Power and UK Power Networks). Normally, the lifetime of the transmission and distribution power transformers are around 45 years and 60 years, respectively [13-15]. The longer serving time of a transformer in the UK is mainly because they are normally operated well below the rated load condition due to the double-circuit transmission system. However, higher and more dynamic loadings are expected due to the electrification, which will lead to a higher operating temperature, as well as a more severe thermal stress. Both can result in a shortened lifetime, or even worse, a premature and unexpected failure. It should be noted that the replacement of most of the network components or even a part of the electricity network is feasible however due to the tight timeframe, which is often related to global production capability, availability of material resource, transport capability and etc, careful and advanced planning is needed which is not only due to finance.

To better cope with the thermal issues of the transformers, an accurate temperature prediction would help the transmission owners to understand the headroom of the loading capacities, which contributes to release the further/potential capacities and manage the short-period overloading. Moreover, due to the environmental concern, the alternative insulating liquids, e.g., ester liquids, have become more and more popular to replace the conventionally used mineral oil. The alternative insulating liquid can also be used to retro-fill the aged transformers to extend its lifetime. Ester liquids are biodegradable and fire resistant, however they are quite viscous as compared to the hydrocarbon mineral oil. The performances of different insulating liquids can be investigated by an accurate and reliable thermal model.

The importance of the temperature predication, as well as the thermal modelling, of power transformers has already been identified by transformer operators and manufacturers. So far, there have been four Cigre Working Groups (WG) assembled, i.e., WG 12.09, WG A2.24, WG A2.38 and WG A2.60, to enhance the understanding of the power transformer thermal behaviour either by the experiments or the modelling. The last working group, WG A2.60, was assembled in 2019, with a focus of dynamic thermal modelling. The outcome of this working group has not been published yet however the technical brochure is expected to be in 2023. The work from the other three WG are introduced herein.

In 1995, WG 12.09 published its technical brochure named 'Thermal aspect of Transformers' [16]. It covered mainly on the experimental work, including the procedures of the heat run test, direct measurements of the hot-spot temperatures, and how to experimentally determine the hot-spot factor and how to analytically determine the hot-spot factor. Its contents of the experimental determination of the hot-spot factor will be further discussed in Section 2.1.6, where the calculated hot-spot factors from the experiments will be discussed and the possible causes of the errors in the data will be explained.

WG A2.24 published its technical brochure, namely 'Thermal Performances of Transformers' in 2009 [17]. The work mainly focused on thermally induced ageing and failure mechanisms, which is not the focus of this PhD project. It contained very limited information on how to calculate the liquid temperatures and the hot-spot temperature in a transformer.

WG A2.38 compared different thermal modelling approaches and published its technical brochure, i.e. 'Transformer Thermal Modelling' in 2016 [18]. Different modelling approaches were introduced by their principles, advantages and the drawbacks. Especially for the steady-state condition, among all the transformer thermal models, the Computational Fluid Dynamics (CFD) model was reported to be more accurate than the Thermal-Hydraulic network model (THNM), as a more detailed and complex flow phenomena can only be captured by the CFD model.

Also found in [18], in either the winding only or radiator only CFD simulations, the input conditions, i.e. the liquid temperature and the liquid velocity (or the total liquid flow rate), were within a range mainly from the experience of transformer operation. The data pair may have a correlation to the reality. The interdependent relationship between the liquid temperature and the liquid velocity may not be important for understanding the liquid directed and forced cooled transformer, but such a relationship matters significantly for the study of a liquid natural cooled transformer. The reasons and a detailed discussion will be presented in Section 2.3 and Section 2.4 in the literature review (Chapter 2).

The interdependent relationship of the liquid temperature and the liquid velocity (or the total flow rate) of a natural cooled transformer can only be obtained by considering / modelling the liquid complete circulation from the winding to the radiator, referred to as the transformer complete-cooling-loop (CCL). The transformer CCL modelling requires in-depth understandings of both the windings and the radiators. However, as observed in [18], less efforts were made for transformer radiators than the ones for transformer windings.

1.2 Aim and Objectives

The aim of this PhD study is to establish experimentally verified radiator and CCL CFD models that can be used to study the impacts of various design and operational parameters on the liquid temperatures and velocities under natural cooling mode.

The aim of the study is met by achieving the following objectives:

i. Development of a CCL experimental setup which achieves the spontaneous flow in the natural cooling mode and allows the measurements of the winding, liquid, ambient and radiator surface temperatures;
ii. Analysis of the thermal experiment results under a variety of loading conditions, with different thermal heads and filled with three different insulating liquids, including a conventionally used mineral oil, a Gas-to-Liquid and a synthetic ester liquid;
iii. Establishment of a radiator CFD model, which can achieve accurate calculations of the liquid temperature distribution, the bottom liquid temperature and the total heat dissipation, as well as with an acceptable processing time;
iv. Development of a CCL CFD model, which is applicable to model liquid temperature distributions and velocities in different conditions.

1.3 Main Contribution

The results from this PhD research can be utilised by transformer operators and manufacturers to understand thermal behaviours of the liquid natural air natural cooled power transformers and develop the thermal models.

The following seven key contributions can be extracted from the thesis:

i. Development of a laboratory-scale experimental setup achieving the spontaneous flow as the same as in the liquid natural air natural cooled transformers. The winding, liquid, ambient and the radiator surface temperatures are all captured.
ii. Establishment of the full and reduced radiator CFD models. All the heat transfer processes and the cooling media are considered in the full radiator CFD model, which is experimentally verified as the reference model. To reduce the computational

efforts, the reduced radiator model is built by adopting an optimized air heat transfer coefficient equation. The validity of the model is verified by comparing with the reference model and the experimental measurements.

iii. Comparison between the optimized air heat transfer coefficient equation and the exiting equations in the literature. Only the optimized equation derived in this project can provide simulation results comparative to the measurements.

iv. Investigation of the impacts of the type of insulating liquid and the ambient temperature on the optimized air heat transfer coefficient equation. The differences of the material properties of alternative insulating liquids have negligible influence; and the effects of the ambient temperature can be resolved by transforming the equation into a dimensionless form.

v. Development of the CCL CFD model. The model is built based on the reduced radiator CFD model. The validity of the CCL CFD model is verified by the experiments in different loading conditions, under different thermal heads and filled with different insulating liquids.

vi. Analysis of liquid temperatures and velocities in different conditions. Under an increased power loss (proportional to the square of loading level), the top liquid temperature increases exponentially, and bottom liquid temperature increases linearly. The liquid velocity is proportional to the square root of the product of the total power loss and the thermal head. The liquid velocity increases by 10.8% to 33.6% (depending on the loading condition) in every 20 °C increase of the ambient temperature.

vii. Comparison of different insulating liquids. In the liquid natural cooling mode, the liquid temperatures and velocity of the Gas-to-Liquid are similar to the ones of the mineral oil. The cooling performance of the synthetic ester liquid is not as good as the mineral oil and the Gas-to-Liquid. Compared with the mineral oil, the top liquid temperature of the synthetic ester liquid is higher, and the bottom liquid temperature is lower. The liquid velocities of the synthetic ester liquid are 33.0% to 47.5% lower than these of the mineral oil under different loading conditions investigated in this thesis. It is also found that the dominating material property to the liquid velocity is the dynamic viscosity. The closer the viscosity is, the similar the liquid thermal performance will be to the mineral oil.

The work presented in this thesis has led to five peer-reviewed publications, listed in ‘Publication List’ section. Contribution i. was published in [P4]. Contributions ii, iii and iv were published in reference [P1] and [P3]. The contributions of point v, vi and vii will be published in [P2].

1.4 Outline of Thesis

The thesis has eight chapters. A brief description of each chapter can be found below.

Chapter 1 Introduction

Chapter 1 provides an overview on the thermal constraints of transformers due to the electrification in the forthcoming future. Research motivation, aim, objectives and main contributions are stated.

Chapter 2 Literature Review

Chapter 2 reviews the transformer heat transfer mechanism, the factory temperature-rise test, the temperature estimation method in the IEC standards, various thermal modelling approaches, as well as the latest CFD simulations and verification experiments for windings only, the complete-cooling-loop and radiators only. The purpose of the literature review is to help frame the problems that were previously solved by the researchers, and to identify the research gaps.

Chapter 3 Development of Complete Cooling Loop based Thermal Test Setup

Chapter 3 includes a detailed outline of how the CCL experimental setup was designed and how the temperatures were measured. The experimental plan and procedures of the temperature-rise test are explained, followed by a complete set of measurements under one tested condition demonstrating the functionality of the setup.

Chapter 4 A Full Radiator CFD Model and its Experimental Verification

Chapter 4 presents a full radiator CFD model considering all the heat transfer mechanisms and all the cooling media. The full radiator CFD simulations are verified by a set of experiments with regard to the bottom liquid temperature, the total heat dissipation, and the surface temperature distribution.

Chapter 5 A Reduced Radiator CFD Model using Optimised h_{air} Equation

Chapter 5 follows Chapter 4 by introducing an optimized modelling strategy of the radiator which adopts an air heat transfer coefficient equation to replace the detail air flow simulation, namely the reduced radiator CFD model. The validities of the reduced radiator CFD simulations are verified by the simulation results of the full radiator CFD model and the experimental measurements. The impacts of two influencing factors, i.e. ambient temperature and the material properties of different insulating liquids, on the air heat transfer coefficient equation derived are also evaluated.

Chapter 6 CCL CFD Modelling using the Reduced Radiator Model

Chapter 6 focuses on the development and the experimental verification of the CCL CFD model built upon the reduced radiator CFD model in Chapter 5. The CCL CFD simulations are verified by a set of experiments, where the ambient temperatures and the power losses of the experiments and simulation inputs are exactly matched.

Chapter 7 Liquid Temperatures and Velocity in CCL Models under Various Conditions

Chapter 7 delves into the trends of the liquid temperatures and velocities under different conditions by CCL CFD parametric sweep simulations and experiments. The effects of various parameters, including the loading condition, the thermal head, the ambient temperature and the insulating liquid type, are all investigated.

Chapter 8 Conclusion and Future Work

Chapter 8 summaries the outcomes from each chapter in the thesis. Finally, the possible future work is raised.

Chapter 2 Literature Review

This chapter provides the background for the thesis. The information herein is used to aid discussions of findings in later chapters.

A liquid-immersed power transformer is introduced from a thermal aspect, including its structure, heat generation and dissipation, and how to measure the temperatures within a transformer. The factory temperature-rise test introduced in the standards is presented by its test procedures. Also as addressed in the standard, temperature-rise results can be used to determine the hot-spot temperature within a transformer under different loading conditions. The principle and the key assumptions of the proposed determination method in the standards are also introduced.

To accurately predict the hot-spot temperature and its location, different numerical models have been developed, i.e., the electrical-thermal analogy circuit, the thermal-hydraulic network model (THNM) and the Computational Fluid Dynamic (CFD) model. The principles of different models and their development, as well as drawbacks in applications, are reviewed. The CFD is found to be the most accurate modelling approach, however its main drawback is the higher computational requirements than the electrical-thermal analogy circuit and the THNM. Therefore, rather than modelling a complete power transformer, most of the CFD models for the liquid-immersed power transformers are focused on the individual components, e.g., the winding or the radiator. The winding CFD models and the relevant experiments are presented first. The influencing factors such as different loading conditions, thermal designs and insulating material properties, are then reviewed.

Since the current research pointed out that a natural cooled transformer cannot be thermally analysed by individual components, and its liquid velocity (or total liquid flow rate) is dependent on the temperature profile of a complete-cooling-loop, which consists of both the winding and the radiator. Thus, the complete-cooling-loop models and their corresponding thermal experiments are reviewed. It has been observed that the complete-cooling-loop simulations needs experimental verification, and the accuracy of the simulation is restricted by the modelling strategy of a radiator. Therefore, the latest worldwide worth-noting work relevant to the transformer radiator thermal modelling and its thermal experiments are introduced; and particularly, the gaps in the current understanding of transformer radiator are identified, and some of these are answered in the following chapters of the thesis.

2.1 Background Knowledge of Liquid-Immersed Power Transformers

2.1.1 Introduction

The liquid-immersed power transformers are one of the key components of the electrical transmission grid, designed to step up and down the voltages to enable the long-distance transmission of the electricity. The liquid-immersed power transformers are commonly used to connect different voltage levels of the network. A typical power network in the UK is shown in Figure 2-1 [19], where 400 kV and 275 kV act as the backbone of the network. Generators are connected and their voltages at 22 kV or 13 kV are boosted through generator transformers. Closer to the customer side, the voltage is dropped to 132 kV distribution level and even further lower levels that are safe for industry or domestic use.

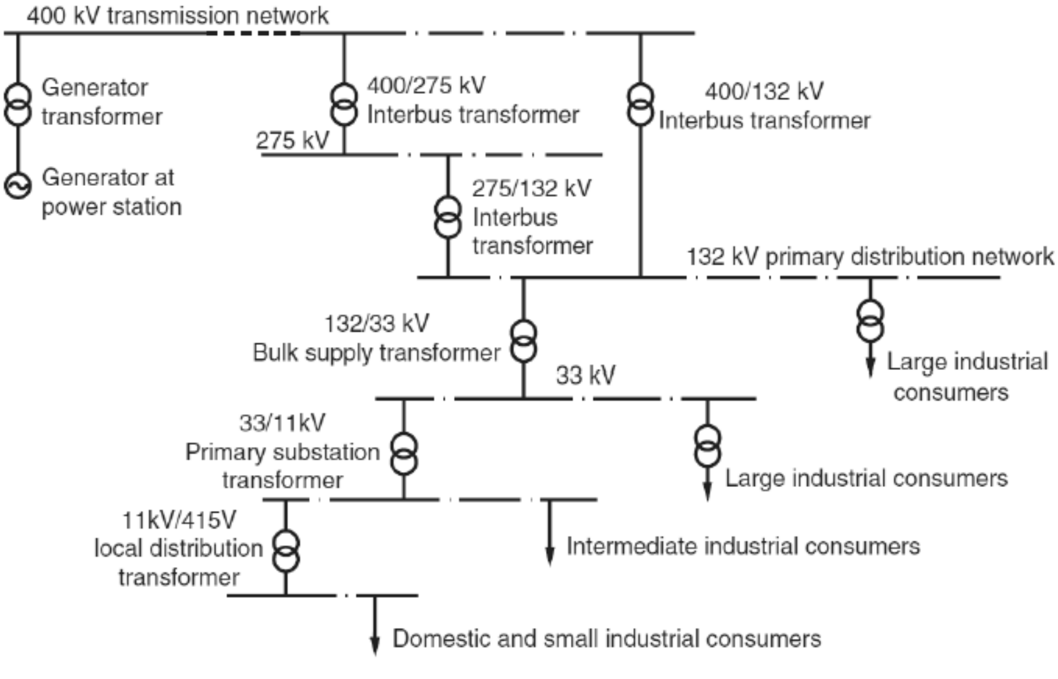

Figure 2-1 A typical power network in the UK [19]

There are two main reasons for transformer owners and operators to care about thermal behaviours of a transformer. One is related with failure mode, and the other is the lifetime. Firstly, as addressed in the IEC transformer loading guide [20], under a high-temperature event, bubbles are likely formed from the water vapour at the solid paper insulation in a power transformer. The bubbles present risks to a transformer by introducing weaknesses to the insulation system and could lead to an electrical failure of a transformer. The latest research [21, 22] indicated that the bubble inception temperature (BIT), at which bubbles appear, may be lower than the value (140 °C) reported the IEC loading guide [20]. The BIT is influenced by conditions other than the moisture content in paper, such as the degree of polymerization (DP) and the type of the insulating liquid. Therefore, to avoid the presence of bubbles, the temperature within a power transformer needs to be accurately predicted and then carefully maintained below its BIT.

Secondly, as documented in both IEC and IEEE standards [20, 23, 24], the ultimate lifetime of a liquid-immersed power transformer is assumed to be the life duration of its solid paper insulation. The expected lifetime of the solid insulation can be evaluated by its hot-spot temperature, which is referred to as the highest temperature where the solid insulation suffers the severest thermal stress within a transformer.

If the contents of moisture, acidity and oxygen of the insulating liquid in a transformer are kept the same, the ageing rate (V) of non-thermally upgraded paper (the Kraft paper) would be approximately doubled for every 6 °C temperature increase during transformer normal operation [20, 25]. At the hot-spot temperature in an 'IEC standard' transformer is assumed as 98 °C when the ambient temperature is 20 °C, and the ageing rate is expressed by Equation 2-1 [20]. For the thermally upgraded paper, the ageing rate follows the same 6 °C rule, which can be calculated from Equation 2-2 [20], in which the reference temperature is set as 110 °C.

$$V = \frac{\text{Ageing rate at } T}{\text{Ageing rate at 98 °C}} = 2^{\left(\frac{T_{hs}-98}{6}\right)} \qquad \text{Equation 2-1}$$

$$V = \frac{\text{Ageing rate at } T}{\text{Ageing rate at 110 °C}} = e^{\left(\frac{15000}{110+273}-\frac{15000}{T_{hs}+273}\right)} \qquad \text{Equation 2-2}$$

where V is the thermal ageing rate, T_{hs} is for the hot-spot temperature (°C).

IEEE loading guide also defines the 'F_{AA} (ageing accelerator factor)' in [23], which has the same meaning as the ageing rate (V) in [20]. The IEEE loading condition [23] only gives the ageing rate for the thermally upgraded paper, and the Equation 2-3 is the same as the Equation 2-2 [20]. By the integral of either the ageing rate (V) or the F_{AA}, the life consumed within a certain time can then be obtained [20, 23].

$$F_{AA} = e^{\left(\frac{15000}{383} - \frac{15000}{T_{hs}+273}\right)} \qquad \text{Equation 2-3}$$

where T_{hs} is for the hot-spot temperature (°C).

The equations 2-1, 2-2 and 2-3 are shown in Figure 2-2 when the hot-spot temperature in the range from 50 °C to 140 °C. As seen in the figure, the transformer ageing rate, or its expected lifetime, is sensitive to the hot-spot temperature. Therefore, an accurate prediction of the hot-spot temperature and its location could help the utilities safely operate a transformer under emergency loading conditions, as well as manage the transformer assets from the lifetime perspective.

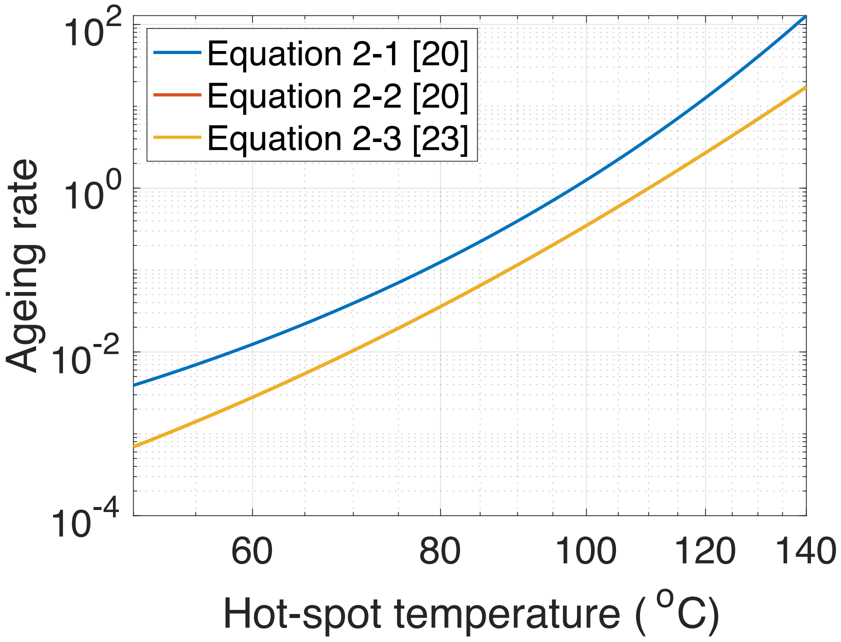

Figure 2-2 Ageing rate of the paper insulation [20, 23]

2.1.2 Transformer Structure

A liquid-immersed power transformer is designed with a complex structure, which accounts for electrical, mechanical and thermal considerations. Figure 2-3 [19, 26] shows the configuration of a liquid-immersed power transformer. All the components can be categorized as the internal and external components. Internal components are all the components inside the transformer main tank, which includes the transformer core, transformer windings, supporting structures and transformer insulations. The components outside the transformer main tank are the external components, which include cooling radiators, the conservator, other protection devices and transformer bushings. The external pump and the fan are optional to a transformer, depending on the design of its cooling system. Generally, the heat is caused by the electrical loss from the internal components, and then is carried by the insulating liquids from the internal components to the radiators, where the heat is finally dissipated to the environment. In this section, the transformer components relating to the heat transfer process are presented with their structure.

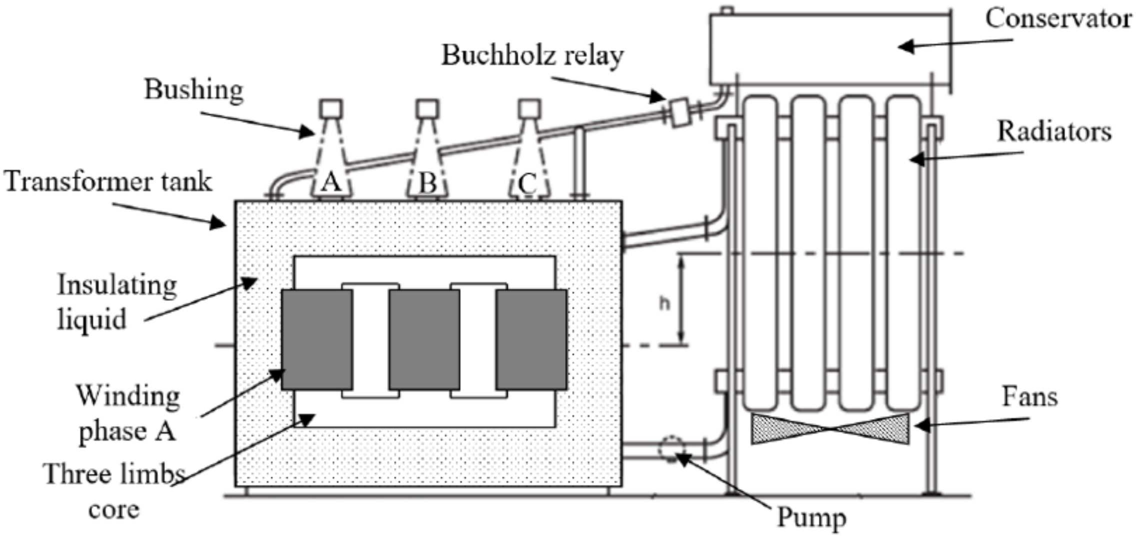

Figure 2-3 Configuration of an liquid-immersed power transformer [19, 26]

The transformer core links the primary and secondary windings via the magnetic field, and a quarter of the core in one phase is detailed in Figure 2-4. The core is composed of laminated steel sheet strips of different widths. Under the main magnetic flux, core strips will generate heat due to the no-load loss. And axial cooling duct, sometimes referred to as vertical cooling ducts, are provided for the insulating liquid to cool the core. Usually, core losses account for 10% of total transformer losses [19].

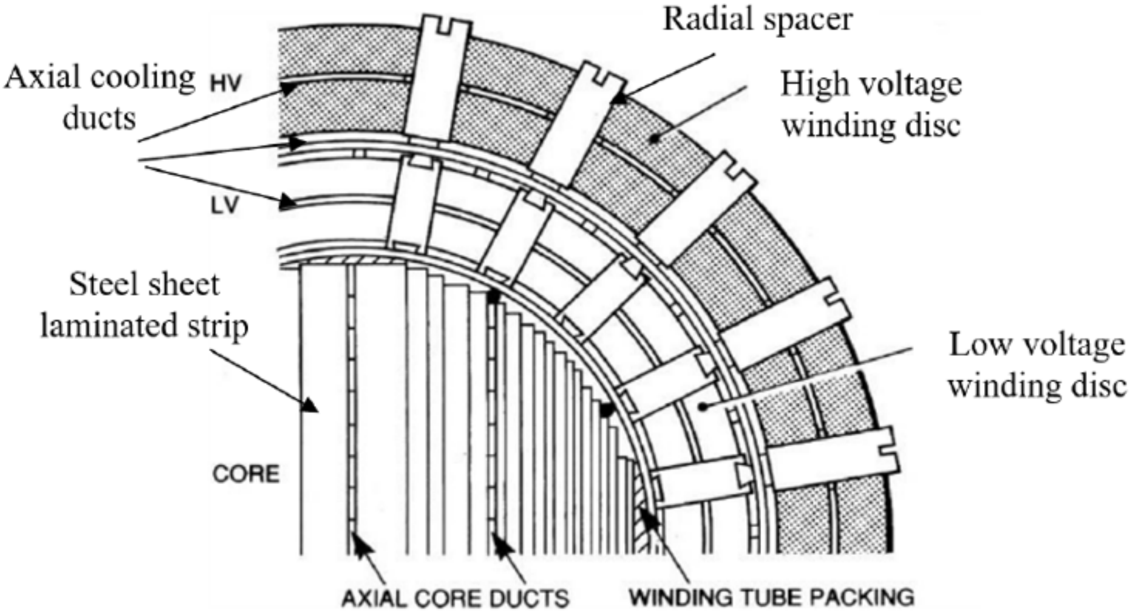

Figure 2-4 Configuration of a quarter of core and disc-type windings [19, 26]

The other key component involved in the heat transfer processes is the transformer windings, where the load loss generates most of the heat. There have been two types of the windings in liquid-immersed power transformers, i.e., the disc-type winding and the layer-type winding. The disc-type winding consists of wrapped copper turns wound over the core. A complete set of turns around the core is called a winding disc. Winding discs are separated by spacers (seen in Figure 2-4 as a top view) to allow for radial cooling ducts, which are also referred to as horizontal cooling ducts. Vertical cooling ducts are designed and placed between the low voltage and high voltage windings to create an efficient distribution of the insulating liquid flow for a better cooling of each component. In this PhD project, the disc-type winding is focused.

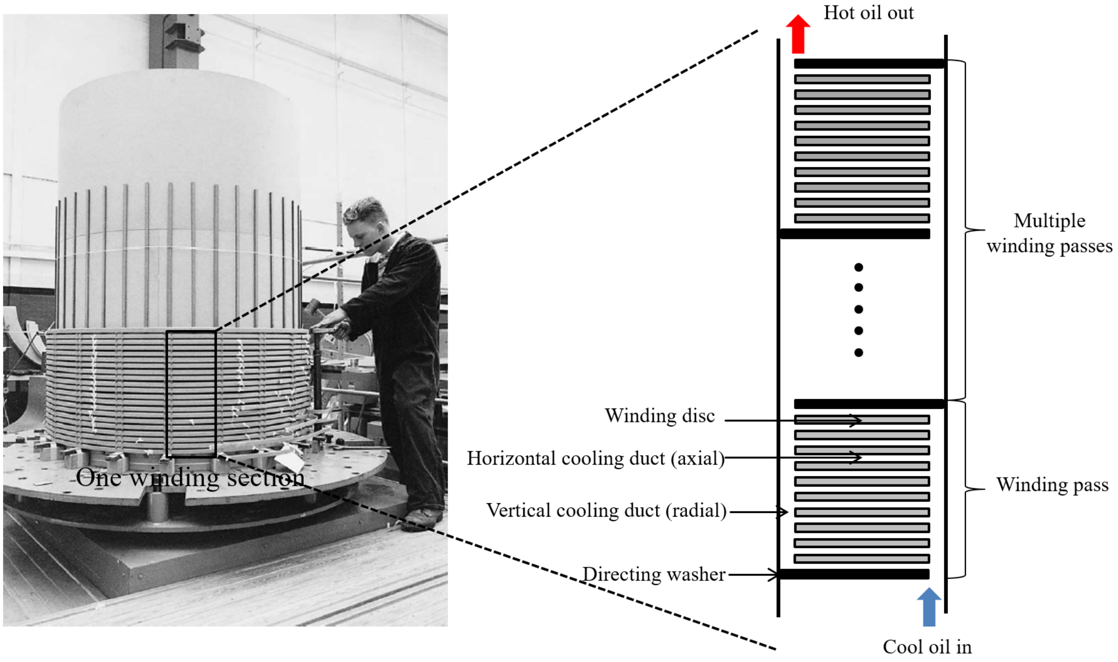

Figure 2-5 Configuration of cooling ducts within a disc-type winding [19]

The circumference of the winding shown in Figure 2-4 is separated by the radial spacers into many winding sections. It is worth noting that each winding section is hydraulically independent [19]. In each winding section, there are multiple passes, which is defined as a set of discs between two directing washers. Multiple passes within a winding section are given by a side view in Figure 2-5. The cool insulating liquid is flowing from the bottom of the winding to the top in a zig-zag fashion through both the vertical and horizontal cooling ducts.

The heat carried by the insulating liquid is dissipated through the transformer tank, the connecting pipework and radiators. Due to its large surface area, the radiator is the key component and dissipates most of the heat. A stamped-plate transformer radiator is presented in Figure 2-6, which consists of top/bottom header pipe and parallel panels. Different from the transformer core and windings, the dimensions of transformer radiators are defined and specified in BS EN standard 50216-6 [27], as following:

- Number of panels/fins in each radiator: $2-36$;
- Panel length (L): 800-3500mm, panel width (W): 520 mm;
- Thickness of the wall in each panel: 1 or 1.2 mm;
- Distance between parallel panels (s): 45 mm.

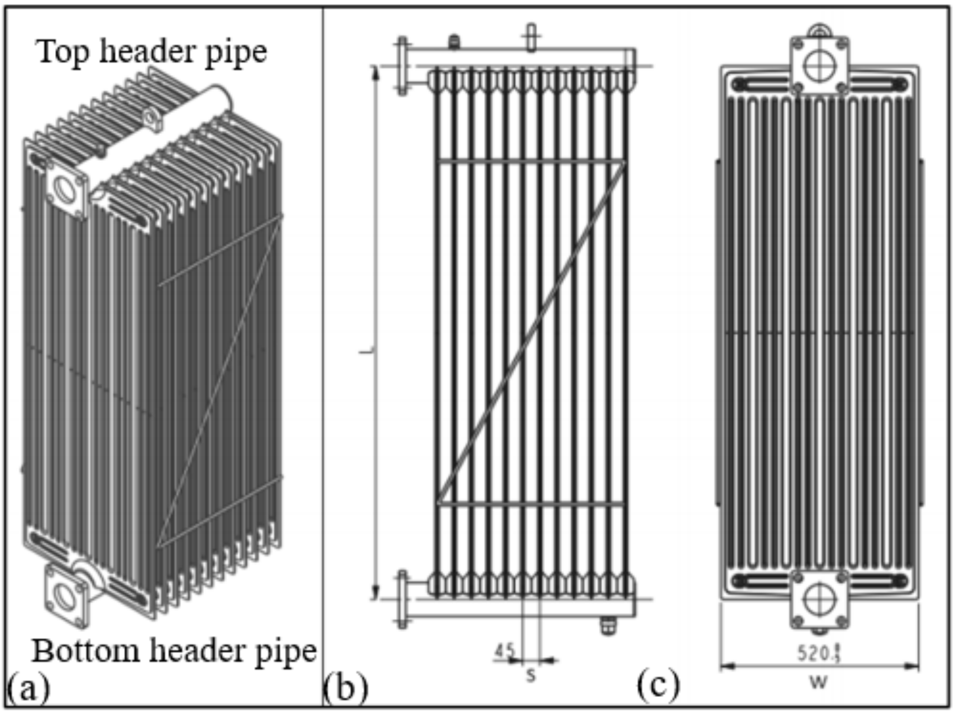

Figure 2-6 Configuration of power transformer radiator (a) radiator configuration (b) side view of radiator (c) single panel/fin of radiator [27]

2.1.3 Heat Generation and Dissipation within Transformers

The temperature change is a result of the heat generation and dissipation within a liquid-immersed power transformer. The heat generation within a transformer is caused by its electric losses. The total electric losses comprise the no-load loss and the load loss. All the losses within a transformer are shown in Figure 2-7. The no-load loss is also called the core loss or iron loss, which is caused by the eddy current at the transformer core and magnetic hysteresis. The load loss consists of the resistive loss and the stray loss. The resistive loss, also known as Joule loss or Ohmic loss, is generated by the Joule heating of the current in its conductors and other current carry parts. The stray loss is induced by the magnetic leakage flux at all the metallic components within the transformer tank. Particularly, the stray loss in the winding is also named the eddy current loss. Commonly, the load loss can be measured from a short-circuit impedance test, and the no-load loss can be obtained by an open circuit impedance test.

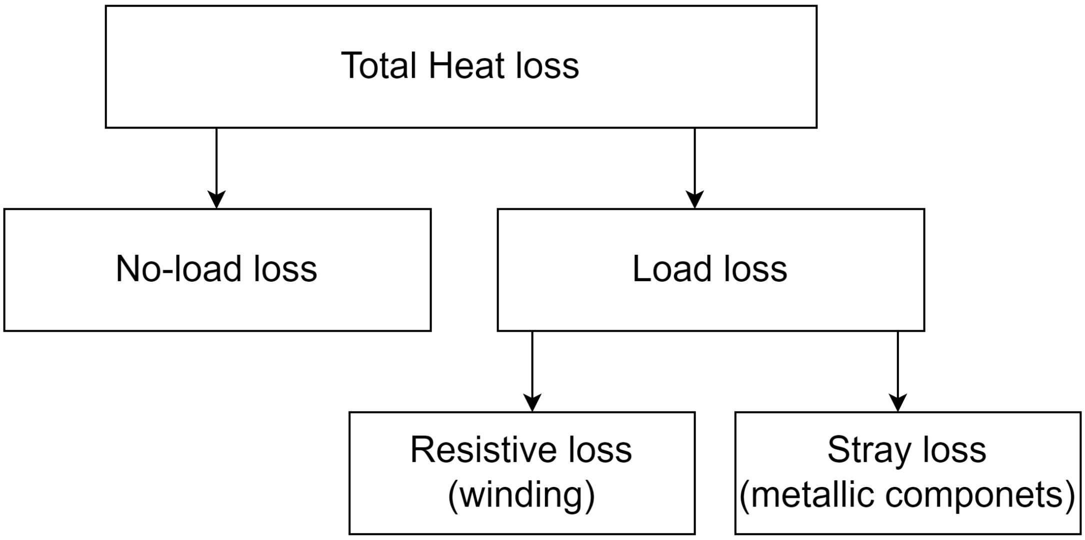

Figure 2-7 Transformer losses clarification

The resistive losses can be calculated by I^2R (I is the current passing through the conductors (A) and R is the resistance of conductors (Ω)), whereas the calculation of the stray loss is more complex. Both analytical calculations, e.g. in [28], and finite element simulations, e.g. [29], were used to study the stray loss distribution within a transformer.

The electromagnetic field from the finite element simulations helps understand the distribution of the eddy current loss within a transformer. A two-dimensional finite element simulation was adopted to model the electromagnetic field of a 225/26.4 kV, 66 MVA transmission transformer in [28]. This study focused on the eddy current loss within the transformer windings, which was mostly found at the top and bottom of windings. An example of the losses at the top part of a winding was given in Figure 2-8. As seen in the figure, the resistive loss is uniform, whereas the effects of the eddy current loss are significant at the upper discs at the topmost winding pass.

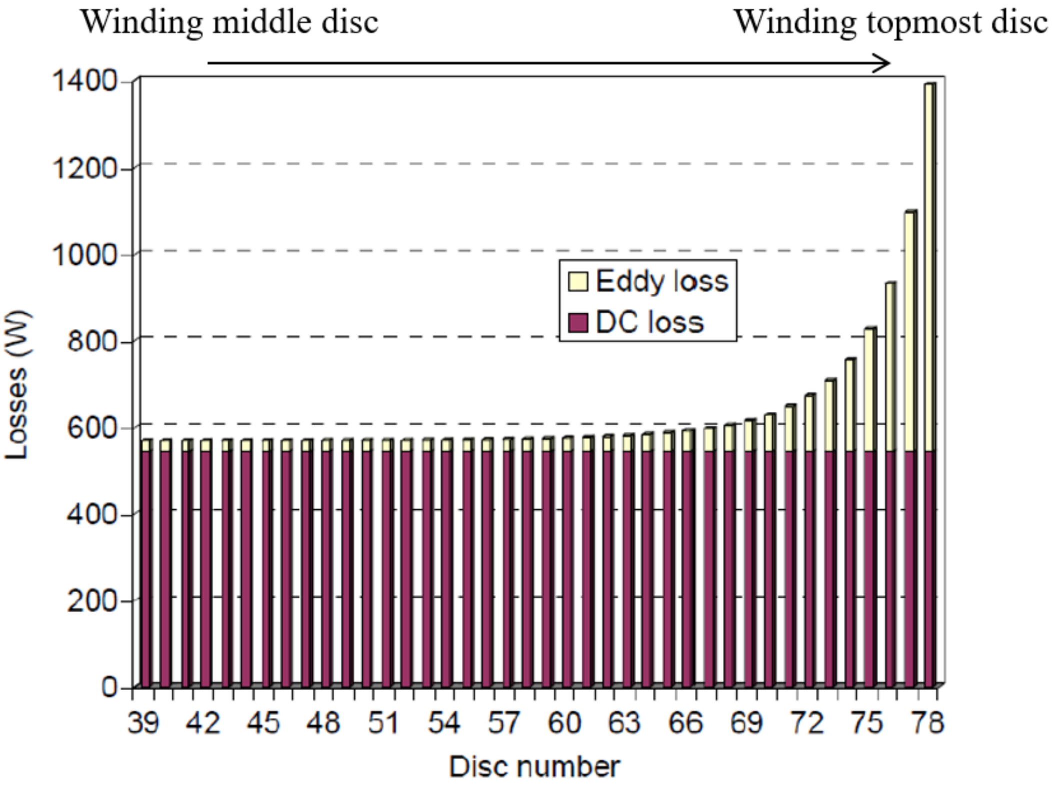

Figure 2-8 Losses (DC loss and eddy current loss) of a transformer LV winding [28]

The heat generated from the electric losses within the transformer internal components is transferred to the surrounding insulating liquid flow. Then the heat is carried by the liquid flow from the internal components to the radiators, where the heat will be dissipated to the environment. The temperatures of the internal components, i.e., the core and windings, are dependent on the insulating liquid flow distribution. Thus, an advanced understanding of the liquid flow within the transformer can benefit the prediction of its temperature profile. The liquid flow distribution is influenced by the cooling mode. In [24], methods of cooling for the liquid-immersed transformer have been identified by a four-letter designation as follows:

First letter: internal cooling medium

- O: mineral oil or synthetic insulating liquid with fire point less than 300 ℃
- K: insulating liquid with fire point more than 300 ℃

Second letter: liquid circulation mechanism for internal cooling medium

- N: natural thermosiphon flow through cooling equipment and in windings
- F: forced circulation through cooling equipment, thermosiphon flow in windings

- D: forced circulation through cooling equipment, directed from the cooling equipment into at least the main windings

Third letter: external cooling medium

- A: air
- W: water

Fourth letter: circulation mechanism for external cooling medium

- N: natural convection
- F: forced circulation (fans, or pumps)

In order to drive the insulating liquid into the winding, sometimes additional pumps can be used, in which case the cooling mode is a forced cooling mode (OF/KF/OD/KD). Otherwise, the insulating liquid is driven by its buoyancy pressure, so-called natural thermosiphon flow (ON/KN). Similarly, once additional fans are installed to facilitate the cooling of external radiator, such transformers are in the air forced (AF) cooling mode.

The liquid natural air natural (ONAN/KNAN) cooling mode is taken as an example to illustrate the complete-cooling-loop of the insulating liquid within a transformer in Figure 2-9. The winding disc is presented as a block, the heat generated from the electric losses is transferred from the centre to its surface by thermal conduction. As seen in Figure 2-9, two vertical cooling ducts at the left and right sides of the winding, and they are cross-linked with an array of horizontal cooling ducts. All the ducts compose a network to maximize the conduct-to-liquid contacting surface. When the cool insulating liquid (shown as blue in Figure 2-9) flows through such a network, the winding is cooled down by transferring the heat to the liquid via thermal conduction and convection. Consequently, the liquid becomes warmer (shows as red in Figure 2-9) and merges at the winding top, it carries the heat out of these internal components. Then, the hot insulating liquid transfers its heat to the radiator surface via the thermal conduction and convection. The heat is finally dissipated to the environment by the thermal conduction, air convection and radiation.

It should also be noted that most of the power transformers are designed with alternative cooling modes instead of a single cooling mode [30]. The power transformers are installed with extra pumps or fans, which are switched off for a low loading condition and back on for a high loading condition. In the UK, most of the power transformers are operated in an ONAN cooling mode.

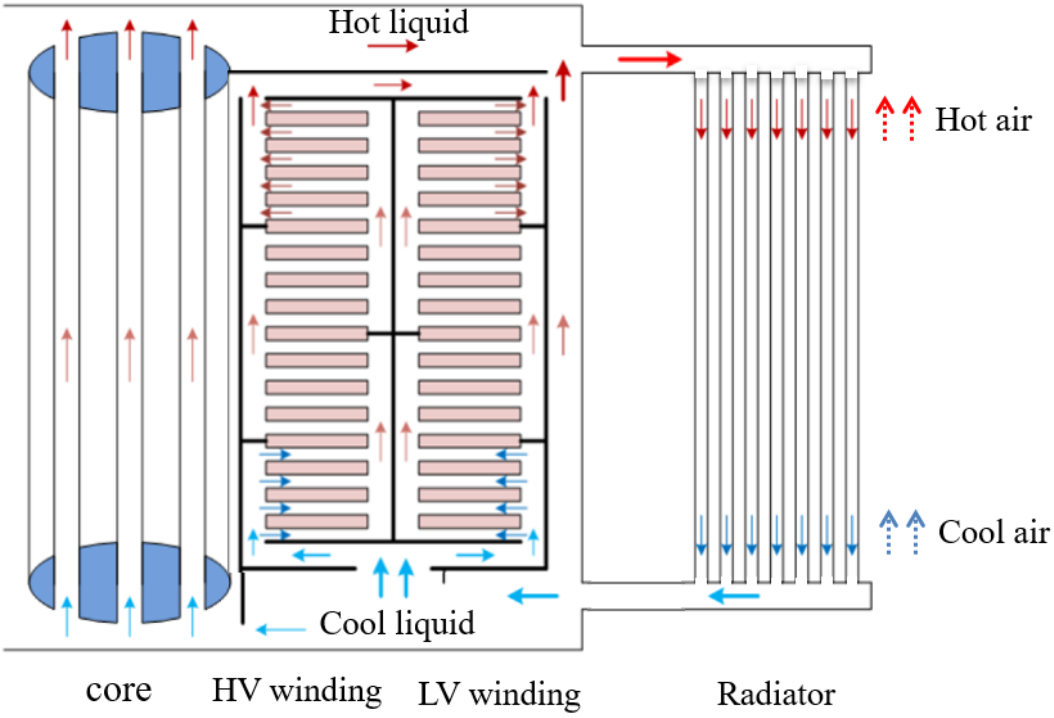

Figure 2-9 Configuration of a transformer complete-cooling-loop in ONAN/KNAN cooling mode

2.1.4 Factory Temperature Rise Test

Transformer manufacturers need to conduct a factory temperature rise test to ensure that the key parameters of temperatures within a transformer are lower than the temperature limits specified in the standards. The limits in the IEC standard 60076-2 [24] are presented in Table 2-1.

Table 2-1 Temperature limits in IEC standard 60076-2 [24]

Variable	Temperature limit (℃)
Top liquid temperature rise over ambient temperature (ΔT_{top})	60
Average winding temperature rise over ambient temperature (ΔT_{avw})	65 (liquid natural cooling mode) 70 (liquid forced and directed cooling mode)
Hot-spot temperature rise over ambient (ΔT_{hs})	78

2.1.4.1 Test Procedure and Measurements

The factory temperature rise test should be conducted at the rated loading scenario. To reflect the total loss within a transformer in its rated condition, i.e. the summation of both the no-load loss and the load loss, the current injected into the transformer using the short-circuit method should be slightly higher than the rated current, as expressed by Equation 2-4.

$$\text{Test current} = \text{Rate current} \times \sqrt{1+\frac{\text{iron loss}}{\text{hot copper loss}}} \qquad \text{Equation 2-4}$$

where hot copper loss refers to the copper loss at the temperature when the transformer is operated at the rated loading condition in the steady-state condition.

The procedures of the temperature-rise test are outlined as follows:

1. Measure the winding resistance at the ambient temperature;
2. Inject a current calculated from Equation 2-4. Once the top and bottom liquid temperatures reach the steady-state condition, which is defined as the variation of the temperature is no larger than 1 K/hour;
3. The injecting current is then reduced from the one in the step 2 to the rated current. The condition needs to be maintained for 1 hour, and the temperature measurements should be taken at least every 5 minutes.
4. After 1 hour, the winding resistance is suggested to be measured immediately.

The measurements from the procedure above are top and bottom liquid temperatures (T_{top} and T_{bot}), and winding resistances. The winding resistances are used to determine the winding temperature. Since the winding temperature is in a linear relationship with the resistance of a conductor, it can be calculated from Equation 2-5 and Equation 2-6 for copper conductor and aluminium conductor, respectively [24].

$$T_{avw-copper} = \frac{R_2}{R_1}(235 + T_{amb}) - 235 \qquad \text{Equation 2-5}$$

$$T_{avw-aluminium} = \frac{R_2}{R_1}(225 + T_{amb}) - 225 \qquad \text{Equation 2-6}$$

where $T_{avw-copper}$ and $T_{avw-aluminium}$ are the average winding temperatures (°C) of the copper and aluminium conductor, respectively; R_1 is the winding resistance measured in step 4 (Ω), R_2 is the winding resistance measured at the ambient temperature (Ω), T_{amb} is the ambient temperature (℃).

If the hot-spot temperature is directly measured, it should be taken as the highest reading during step 1 to 4. Otherwise, it can be calculated from a thermal diagram shown in Figure 2-10.

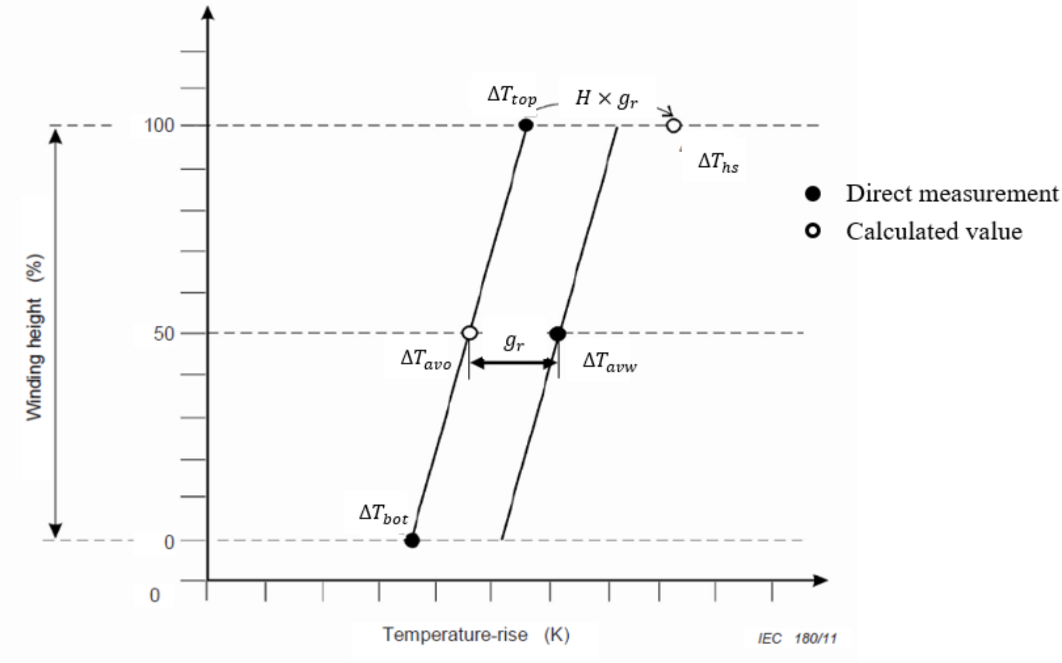

Figure 2-10 Thermal diagram of power transformer from IEC standard [24]

In the thermal diagram, there are two solid straight lines in parallel. The left line represents the liquid temperature rise, and the right line is the winding temperatures measured from winding bottom to the top. The black solid point represents the direct measurements in the temperature-rise tests, i.e., top and bottom temperature rise over ambient temperature (ΔT_{top} and ΔT_{bot}) and winding average temperature rise over ambient temperature (ΔT_{avw}).

The assumptions of the thermal diagram can be summarized as:

- The increase of the insulating liquid temperature from the winding bottom to the top is linear, and the average liquid temperature rise (ΔT_{avo}) is the average of top and bottom liquid temperature rise ($\Delta T_{avo} = (\Delta T_{top} + \Delta T_{bot})/2$);
- The temperature gradient between the average insulating liquid (T_{avo}) and the winding (T_{avw}), namely winding-to-oil gradient (g_r), remains the same at all heights of the winding;

- The hot-spot temperature is assumed to be at the winding top, which is, however, higher than the summation of the temperature gradient and top liquid temperature ($T_{top} + g_r$), mainly due to the eddy current loss.

The hot-spot temperature can be estimated by Equation 2-7 [24].

$$T_{hs} = T_{amb} + \Delta T_{top} + H \times g_r \qquad \text{Equation 2-7}$$

where T_{hs} is the hot-spot temperature (°C), T_{amb} is the ambient temperature (°C), ΔT_{top} is the top liquid temperature rise over ambient temperature (K), H is the hot-spot factor, g_r is the temperature gradient between the winding and insulating liquid (°C).

In the IEC standard [24], the hot-spot factor (H) is specified as:

- $H = 1.1$ for distribution transformer;
- $H = 1.3$ for medium or large power transformer.

2.1.4.2 Recommendations for Measurement of Key Temperatures [24]

The measurements of the liquid temperatures are influenced by the liquid flow, and the measurement of ambient temperature is affected by the air flow. Therefore, the sensor locations and quantities for such measurements are specified in [24].

- Top liquid temperature measurement

The top liquid temperature is measured by immersing the temperature sensors into the liquids at the top of the transformer or in oil pockets. In [24], a specific sentence is given as ‘the position of the sensors should be chosen to present the top-liquid temperature possibly in correspondence to the wound columns’, which highlights the difficulty in interpretation of how to measure the top liquid temperature. If more than one oil pocket is used, the readings of the sensors shall be averaged in order to obtain a representative temperature value. Moreover, ‘by agreement between manufacturer and purchaser, the top-liquid temperature can be determined assuming as the average of the indications of the pockets placed on the cover and the temperature of the liquid of the inlet of the cooling equipment’.

- Bottom liquid temperature measurement

The bottom liquid temperature is identified as the liquid temperature entering the winding. The bottom liquid temperature shall be determined by sensors placed at the return headers from coolers or radiators. Same as the top liquid temperature, more than one sensor should be used and the reading average is assumed as bottom liquid temperature.

- Ambient temperature measurement

The ambient temperature should be measured with at least four sensors and the average of their readings is assumed as the ambient temperature. For an air natural cooled transformer, the sensors should be placed at a level about halfway up to the cooling surfaces. The sensors shall be distributed around the tank, about 2 m away from the perimeter of tank and cooling surfaces, and protected from direct heat radiation. For forced air cooled transformers, the sensors should be placed 0.5 m above the ground level. In the case of separate cooling equipment placed at a distance of at least 3 m from the transformer tank, the ambient temperature shall be measured around the cooling equipment applying the same rules given above.

'Attention shall be paid to possible recirculation of the hot air. The transformer should be placed so as to minimize obstructions to the air flow and to provide stable ambient conditions. Precautions should be taken to minimize variations of cooling-air temperature, particularly during the last part of the test period when steady state conditions are approached.' [24]

2.1.5 Hot-spot Temperature Estimation

If the hot-spot factor (H) of a power transformer is obtained, the top liquid temperature (T_{top}) and the hot-spot temperature (T_{hs}) in a steady-state condition under different loading scenarios can be determined from Equation 2-8 and Equation 2-9 proposed in IEC standard [24].

$$\Delta T_{top} = \Delta T_{top-rate} \times (\frac{1 + R \times K^2}{1 + R})^x \qquad \text{Equation 2-8}$$

$$\Delta T_{hs} = \Delta T_{top} + H \times g_r \times (K)^y \qquad \text{Equation 2-9}$$

where ΔT_{top} is the top liquid temperature rise over ambient temperature (K), $\Delta T_{top-rate}$ is the top liquid temperature rise over ambient temperature (K) at the rated loading condition, R is the ratio of load loss at the rated load to the no-load loss, K is the loading level, ΔT_{hs} is the hot-spot temperature rise over ambient temperature (K), H is the hot-spot factor, g_r is the temperature gradient between the insulating liquid and the winding, x and y are the liquid and winding exponents.

There are three unknown parameters in Equation 2-8 and Equation 2-9, i.e. x, y and H. In the IEC standard [24], some recommended values in Table 2-2 are given for the liquid and winding exponents. As seen in Table 2-2, x is mainly affected by the liquid cooling mode, and y is dependent on the transformer power rating and winding design (e.g. directed liquid flow or not). Another way to identify an individual transformer's liquid and winding exponents is given in IEEE loading guide [23], the temperature-rise tests are suggested to be conducted at three different loading levels, i.e. 0.7 p.u., 1.0 p.u. and 1.25 p.u., to derive the x and y components from the measurements. The validity range of such values determined by the tests have not yet been verified, especially for the extremely low and high loading conditions. In addition, whether the liquid and winding exponents (x and y) would change or not when a transformer is retro-filled with another insulating liquid, has not been clarified in the standard. Therefore, this point has been identified as one of the research questions in this PhD thesis.

Table 2-2 Recommended values of x and y for exponential equations in [24]

Characteristic	Small transformer	Medium and large power transformers					
	ONAN	ONAN	ONAN	ONAF	ONAF	OF	OD
Liquid exponent x	0.8	0.8	0.8	0.8	0.8	1.0	1.0
Winding exponent y	1.6	1.3	1.3	1.3	1.3	1.3	2.0

The hot-spot factor (H) is normally assumed constant, as $H = 1.1$ for distribution transformers, and $H = 1.3$ for medium size power transformers under all loading conditions [24]. However, this constant assumption has been challenged by recent research [16].

2.1.6 Hot-spot Temperature Measurements

Because the accuracy of the hot-spot temperature estimated by the equations in IEC standard [24] is restricted by the above assumptions, the Fibre Optics Temperature Sensor (FOTS) has been introduced to directly measure the hot-spot temperature. Comparing with other types of temperature sensors, the FOTS is more immune to the electromagnetic interferences within a transformer.

In 1994 [31], six FOTS were installed in a 240 MVA autotransformer and tested for their functionalities of winding temperature measurement. The measurements matched the calculations in the design process. Since then, FOTSs have gained popularity in measuring the liquid and winding temperatures in temperature-rise tests. One of the work was published in [32], where 28 FOTSs were adopted to measure the bottom and top liquid temperatures, liquid temperatures at vertical cooling ducts, and the low voltage and high voltage winding temperatures. The work tested the effects of the sensors' locations on the measurements, and it was found that the liquid temperature should be measured as close as possible to the winding top. Another study [33] comprehensively analysed the performances of the FOTS under different installations and operational conditions, and concluded that a larger temperature variation would occur in an ON cooling mode due to its more complex liquid flow distribution during the measurements.

In 1995, a Cigre WG 12.09 [16] conducted an ambitious project on thermal aspect of transformers by measuring the hot-spot temperatures of 34 power transformers across 7 countries, i.e. Australia, Austria, Canada, Finland, France, Sweden and the USA, in order to determine maximum safe operating temperatures under emergency conditions. These transformers were all medium and large power transformers, with different types of designs, and they were tested under different loading conditions. In total, 60 sets of the temperature-rise tests were obtained. [16] summarizes the inverse accumulative distribution (probability) of the calculated hot-spot factors. The calculated hot-spot factors based on the measurements were found spread in the range from 0.51 to 2.06, among which any number below the unity was mainly due to the unreliable measurements as reported in [16]. Indeed, the accuracy of hot-spot temperature measurements using FOTSs is dependent on the locations of the sensors.

Although the application of the FOTS enables the direct hot-spot temperature measurement which helps advance the thermal design and thermal management of a power transformer, an understanding of the hot-spot temperature and its location is still needed, and this requires the development of the thermal modelling of the transformers.

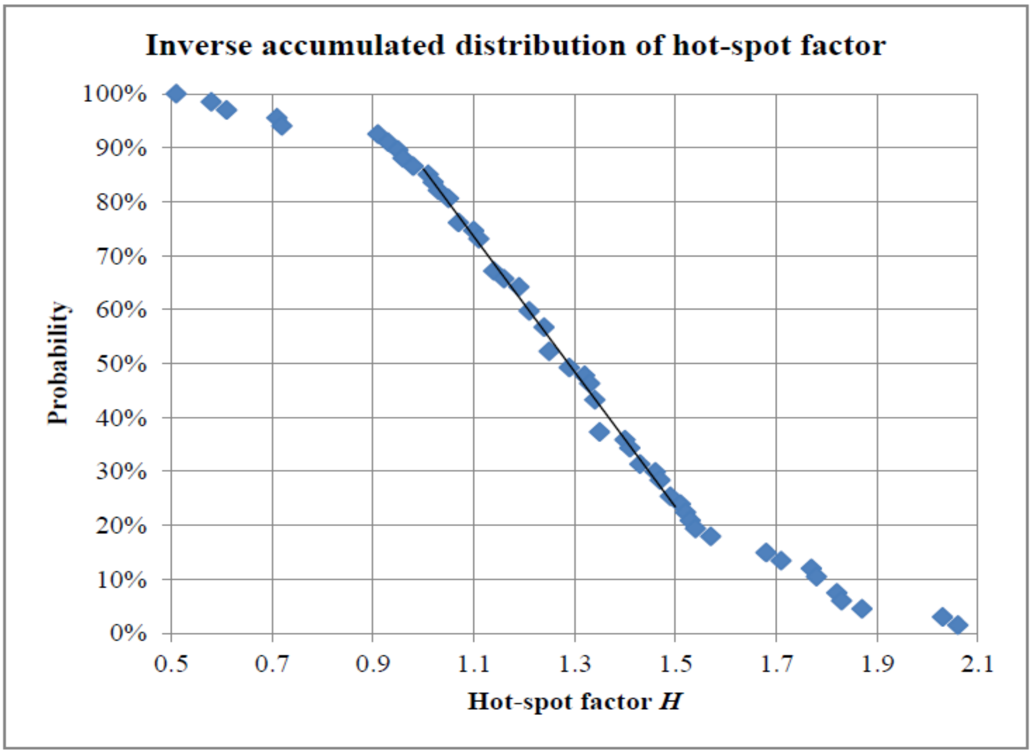

Figure 2-11 Inverse accumulated distribution of hot-spot factors derived from different transformers under different loading conditions (34 power transformers under 60 loading conditions) [16]

2.2 Thermal Modelling Approaches

In the light of above, numerical modelling, as an alternative solution to determine the hot-spot temperature and its location, has gained widespread attentions in the last few decades, especially with the recent advance in computation. In this section, the principle, main achievements and limitations of three popular modelling approaches are reviewed.

In 2001, a modelling approach, the electrical thermal analogy circuit, was proposed by G. Swift and T.S. Molinski [34, 35] for calculating the hot-spot temperature and the liquid temperatures in the steady-state condition under various loading conditions. This method modelled the transformer components and its insulation system as the lumped elements of thermal resistances and thermal capacitances, and it split the whole heat transfer processes into a winding-to-oil circuit and an oil-to-ambience circuit. The similar modelling approaches can also be found in [36], which were used to study the transformer thermal performance under a dynamic loading condition. The electrical thermal analogy circuit is straightforward, but the limitations are also obvious as outlined below:

- Cannot predict the hot-spot temperature location;

- Cannot determine the key model parameters, i.e., thermal resistances and capacitances, based on the design data. (a transformer needed to be built first, and the temperature-rise test result is needed to obtain such parameters)

The other two widely used modelling approaches, i.e., the Thermal-Hydraulic network model (THNM) and the Computational Fluid Dynamics (CFD) model, can predict the hot-spot temperature and its location. Moreover, the same principles can be applied to an individual transformer if the geometries of the transformer are known. Thus, these two modelling approaches are then reviewed in detail.

2.2.1 Thermal-Hydraulic Network Models

The THNM approach has become a popular numerical tool in the transformer industry since 1980 [37]. The THNM consisted of a thermal network model and a hydraulic network model, was firstly introduced by A. J. Oliver in [37], where a THNM model was built for the low voltage winding of a 240 MVA transformer. Detailed insulating liquid flow and winding temperature distribution within the winding were obtained from simulation. The hot-spot temperature was observed at the middle of the top pass due to a non-uniform oil flow distribution, which was otherwise always assumed at the topmost disc of a winding [24].

Since then, various THNM approaches have been developed for the transformer winding [37-43], the radiator [44] and its complete-cooling-loop [45]. In [45], a joint global-internal HST prediction model was proposed. The global model calculated the oil flow portion in each transformer component whilst the internal model calculated the HST and its location following the input flow rate provided by the global model. The simulation results were verified by 22 transformers under 46 loading conditions with FOTS measurements. A good agreement was found between the simulations and the experimental measurements. In [39], the THNM approach was applied to study the effects of different geometric parameters on the winding thermal design, including the number of disc per pass, the number of turns per disc, the thickness of paper insulation and the height of the horizontal cooling duct.

To better explain the principles of the THNM, the model built based on a transformer winding in [38] is taken as an example. The hydraulic network is shown in Figure 2-12, where a three-disc winding pass is shown in (a), and its hydraulic components are presented in (b). As seen in Figure 2-12 (a), one winding pass can be represented by 8 nodes and 12 oil paths, designated by red circles and blue arrows respectively. At each node, the conservation of mass is applied, which suggests that the total mass flowing into each node is equal to the one flowing out. Four oil paths surrounding one disc are considered as an oil circuit, and the summation of the pressure drop of a circuit is zero because of the conservation of the momentum. The input of the hydraulic model is the velocity at the bottom inlet oil path, and then the velocities at all other 11 oil paths can be solved by mass conservation equations of 8 nodes and momentum conservation equations of 3 oil circuits.

To better study the pressure drop at each node and along each oil path, both the major pressure drop caused by frictional loss (R_{af} and R_f) and the minor pressure drop occurred at junctions (corner junction loss R_C and splitting junction loss R_s) should be considered, as shown in Figure 2-12 (b). As highlighted in [42, 43], the minor pressure had a significant influence on the calculations of THNM in liquid natural cooling mode. Additionally, the pressure drop due to gravity ($\rho g \Delta H$) should also be accounted for in the THNM.

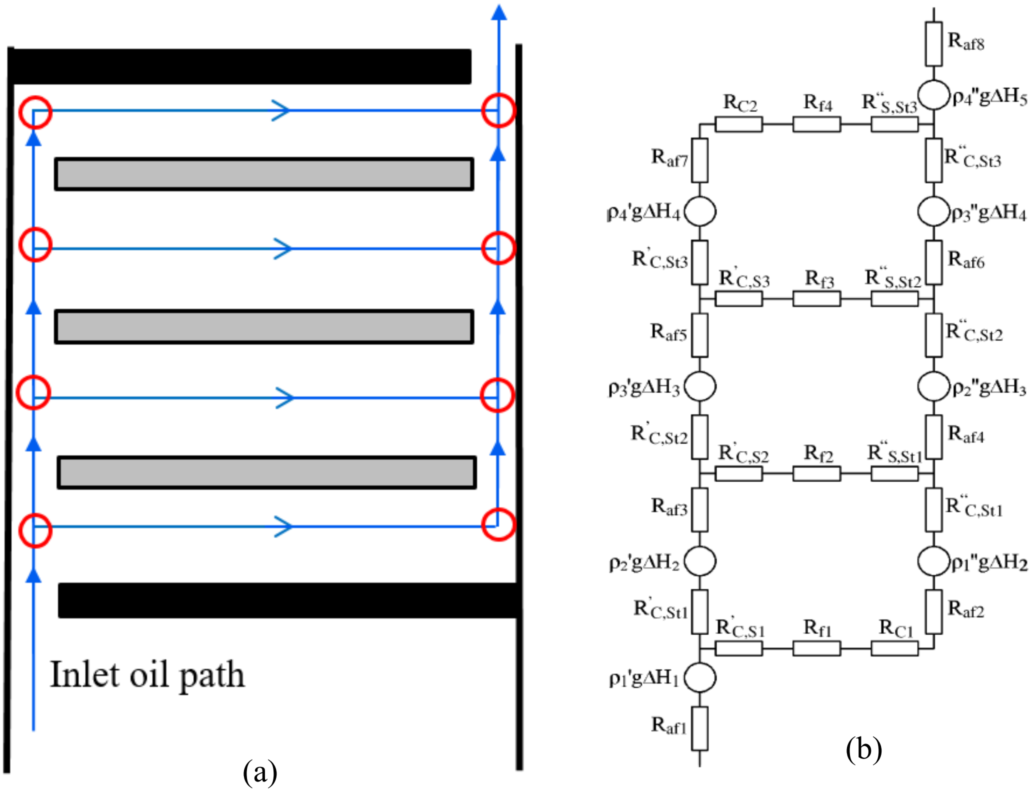

Figure 2-12 Hydraulic network within a 3-disc winding pass (a) configuration of a 3-disc winding pass (b) hydraulic components of a pass [38]: R_{af} for frictional loss at axial cooling duct, R_C for corner resistance, $R'_{C,S}$ and $R'_{C,St}$ for branching resistance at corner, $R''_{C,S}$ and $R''_{C,St}$ for merging resistance at corner, $\rho g \Delta H$ for pressure drop due to gravity

Figure 2-13 demonstrates the thermal network model in [38] by using the 3-disc winding pass. Each winding disc is represented by five conductors, as shown in Figure 2-13 (a). The temperatures of these conductors are noted as from $\theta_{Cu,1}$ to $\theta_{Cu,5}$, following the flow direction. The temperatures will be calculated from the conservation equation of the energy by using thermal resistances. Take the first conductor as an example, the heat loss generated ($P_{\gamma 1}$) is equal to the heat dissipated through the top, bottom, left cooling liquids (temperature as θ_{t1}, θ_{b1} and θ_{in} respectively), and the right-hand side conductor ($\theta_{Cu,2}$). The thermal resistance of the liquid thermal convection is expressed by R_a in Figure 2-13 (b). R_{at1}, R_{ab1} and R_{ain} are used to label the convective resistance of top, bottom and left-hand side liquids of the first conductor, respectively. The thermal resistance of the paper thermal conduction is defined by $R_{\lambda r}$.

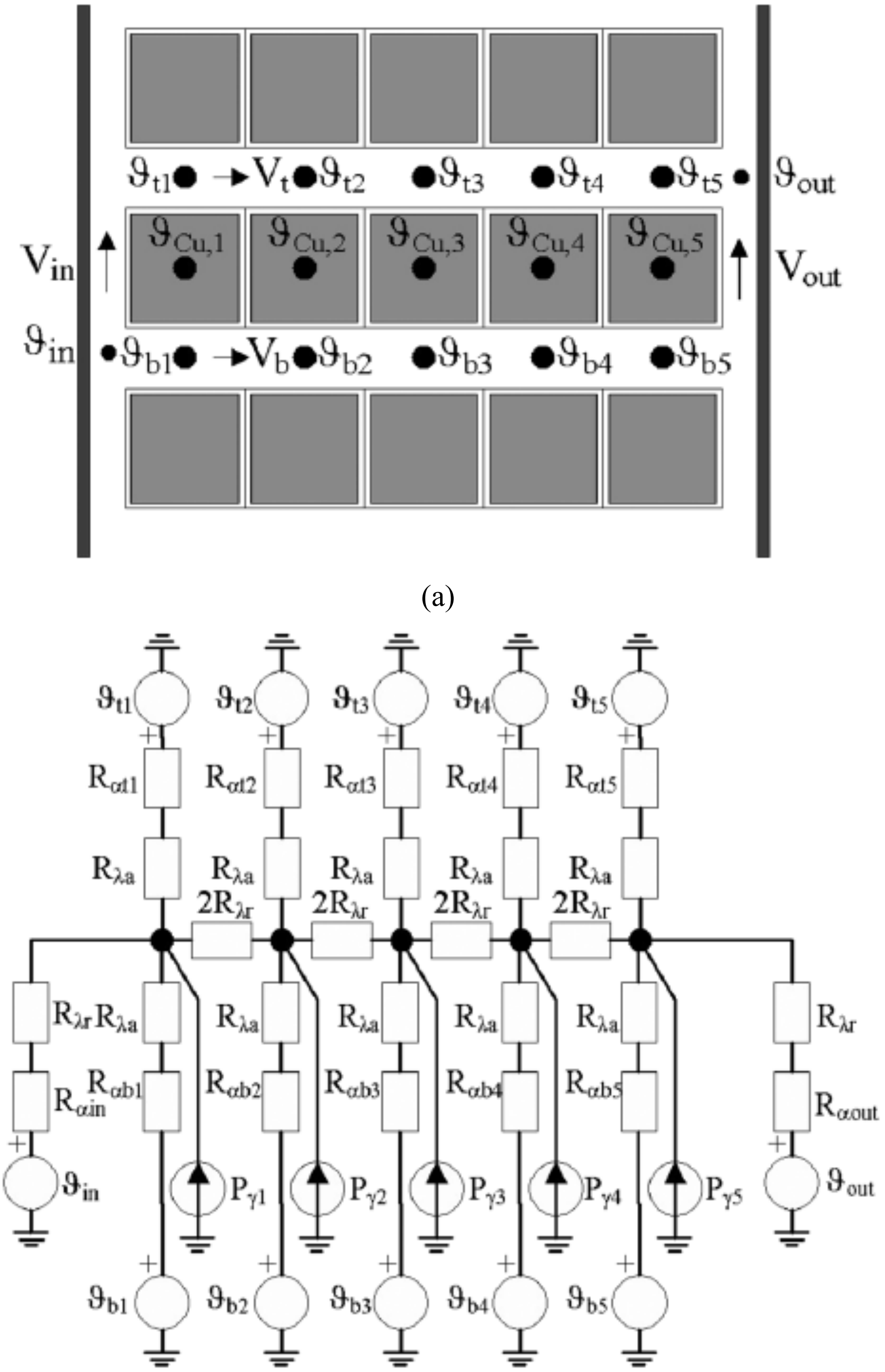

(a)

(b)

Figure 2-13 Thermal network within a 3-disc winding pass (a) configuration of a 3-disc winding pass (b) thermal network of 5 winding turns within a disc [38]: θ_{Cu} for winding conductor temperature, θ_t for top liquid temperature, θ_b for bottom liquid temperature, P_γ for heat loss in each conductor, R_{at} top liquid convective thermal resistance, R_{ab} for bottom liquid convective thermal resistance, R_{ain} and R_{aout} for left and right hand side oil convective thermal resistance respectively, $R_{\lambda r}$ for paper conductive thermal resistance

Overall, the THNM is established upon the conversation of mass, momentum and energy. Specifically, the conservation of mass and momentum is applied in the hydraulic network model to solve the liquid velocity at each oil path. And the conservation of energy is employed in the thermal network model to solve the winding and liquid temperatures at each node. The hydraulic and thermal networks are coupled with the materials properties of the insulating liquid, i.e., the thermal conductivity, the density, the dynamic viscosity and the specific heat capacity, which are temperature dependent and can affect the pressure drop in the hydraulic network model.

In the iterative calculations of the hydraulic and thermal networks, the simulation results are highly dependent on the coefficients of the pressure drop in the hydraulic network and the heat transfer in the thermal network. To improve the accuracy of the THNM, the coefficients were obtained from experiments [46, 47] or CFD calibration [48-51]. The heat transfer coefficient can be easily computed from the CFD calibration by using only one horizontal duct, as suggested in [48] and [50]. However, the coefficient of pressure drop is more complex that includes the major and minor pressure loss of different geometries [51].

Through the CFD calibration, the THNM has become more accurate and is capable to predict the complex liquid flow phenomena, such as the reverse flow in OD/KD cooling mode[52]. However, in [28] and [53] the THNM has been observed some inaccuracies under certain conditions in the thermal studies of ON/KN cooled transformers. This is mainly caused by its assumptions as outlined:

- The THNM model is always built based on a two-dimensional (2D) geometry, and the oil flow and temperature distributions are assumed as axis-symmetric;
- Insulating liquid flow is mixed at each node considering both hydraulic and thermal aspects, and assumptions are made such that the flow velocity and temperature profiles are uniform or fully-developed.

In an ON/KN cooled transformer, the winding temperature and the insulating liquid flow are strongly coupled, and the insulating liquid is kept being heated by the surrounding winding surfaces. Therefore, the temperature of the insulating liquid is more likely to be in a three-dimensional (3D) distribution, and the profile of the liquid is hardly uniform nor fully-developed due to continuous heating. This is why there was a discrepancy between the THNM calculations and experimental measurements in [53]. As concluded in [53], the mismatch of the winding temperatures between the THNM and the experiments was mainly because some of the localised liquid flows were neither uniform nor fully-developed. To better capture the characteristics of the localised flow, a CFD simulation was conducted in [53], by which a complex flow phenomenon, namely the hot-streak, was observed. Evidently, the CFD simulation results matched better with the experimental measurements than the THNM in [53]. This conclusion was further confirmed by the work in [28].

2.2.2 CFD Models

To better capture the flow characteristics, the CFD has been introduced into the thermal modelling of liquid-immersed power transformers. The CFD model uses e.g. finite element method, finite volume method or finite difference method to solve the governing differential equations for the fluid flow and the temperature, as expressed by Equation 2-10 to Equation 2-12.

$$\rho \nabla \cdot \vec{u} = 0 \qquad \text{Equation 2-10}$$

$$\rho (\nabla \cdot \vec{u}) \vec{u} = -\nabla p + \nabla \tau + \rho \vec{g} \qquad \text{Equation 2-11}$$

$$\rho c_p \vec{u} \nabla T = \nabla \cdot (k \nabla T) + P \qquad \text{Equation 2-12}$$

where ρ, c_p and k are the density (kg/m^3), specific heat capacity ($J/(kg \cdot K)$) and thermal conductivity ($W/(m \cdot K)$) of the material, respectively; p is the pressure (P_a); τ is the viscous shear stress tensor ($kg/(m \cdot s)$); $\vec{g}$ is the gravity vector (m^2/s); $\vec{u}$ and T are the fluid velocity (m/s) and temperature (K), respectively, P is the heat source (W).

Equation 2-10 implements the continuity of mass conservation. Equation 2-11 is the Naiver-Stokes equation for the momentum conservation, where the left-hand side represents variation of momentum which comprises the mass flow and the velocity, and the right-hand side terms are the static pressure variation, the viscous stress variation and the buoyancy force, respectively. Equation 2-12 demonstrates the energy conservation, where the left-hand term represents the heat dissipation by the convection, and the right-hand side terms represent thermal conduction and the external energy resource, respectively.

As discussed previously in Section 2.2.1, the liquid flow in the THNM is modelled as either a uniform or a fully-developed distribution in each oil path. Such approximations will bring the uncertainties into the simulations. On the contrary, the CFD model can describe a more realistic flow and temperature profiles of the insulating liquid. The example of the liquid flow and temperature profiles from the CFD simulations is shown in Figure 2-14 (a) [54] and (b) [55], respectively.

As seen in Figure 2-14 (a) [54], the complex flow phenomena, i.e. the reserve flow and hot-plumes, where a small transverse flow or a flow stagnation occurs, were observed. Such flow phenomena result in a non-uniform flow distribution within the winding, and a lack of the insulating liquid in the horizontal cooling duct causes a localised overheating. The identification of these phenomena is vital to predict the hot-spot temperature and its location, and it can only be acquired from CFD modelling. Figure 2-14 (b) [55] presents a complex temperature distribution, i.e. the hot-streak. The hot-streak is a hot liquid layer forming on the surfaces of winding discs, and which is hotter than the surrounding liquid. The hot-streak is mostly observed in ON/KN cooling mode [56], as it is a result of a strong coupling of the winding temperature and the insulating liquid flow.

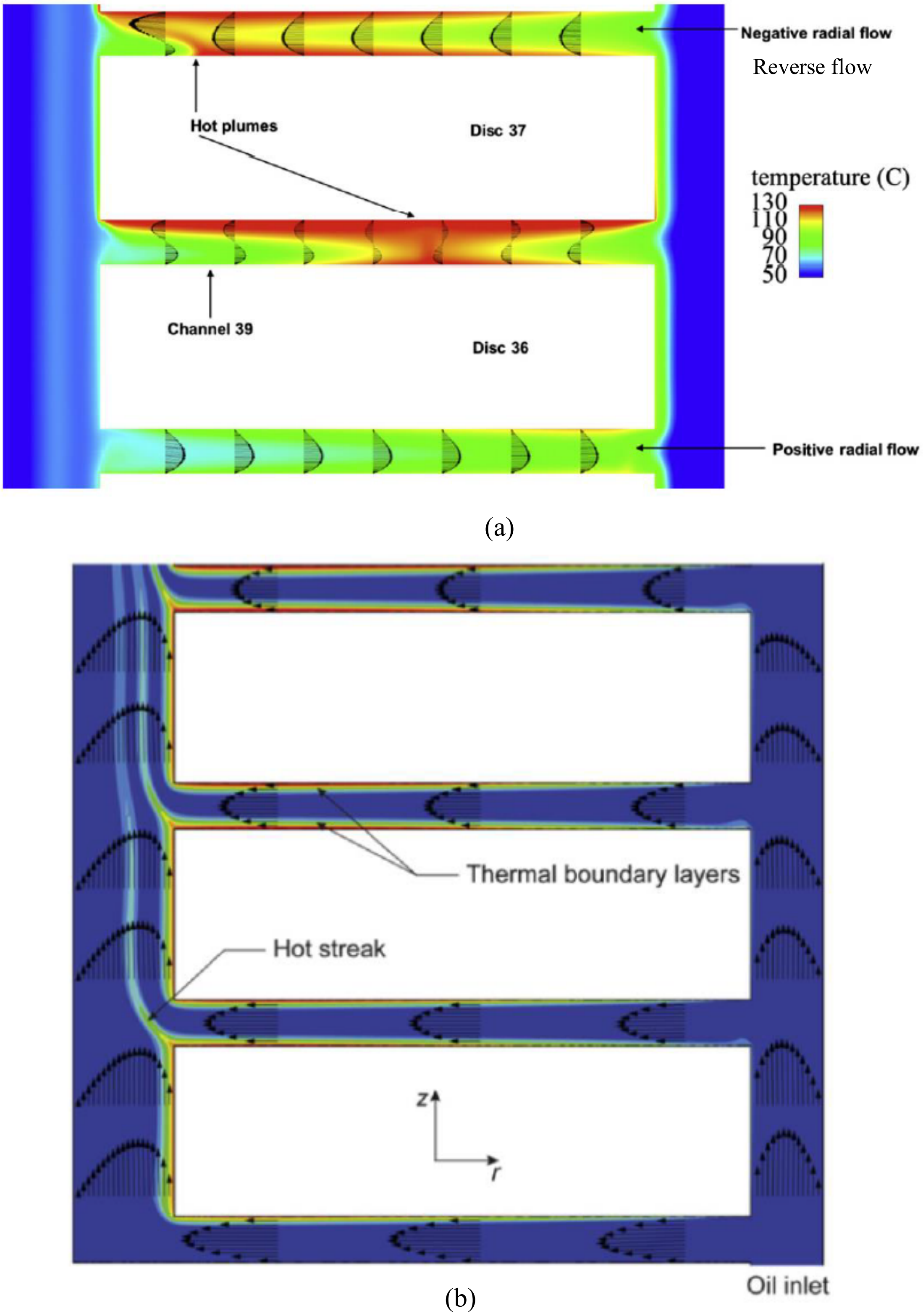

(a)

(b)

Figure 2-14 Temperature and flow profile of insulating liquid in literature: (a) temperature profile [54] (b) liquid temperature profile [55]

The overlook of the flow and temperature characteristics will lead to an unreliable prediction of the temperature profile within the transformer. As such characteristics can only be accurately modelled in the CFD simulation, it has been recognized as a powerful tool in the transformer industry. However, due to the need for discretizing the whole calculation domains into small mesh elements, the processing time of the CFD simulation is much longer than the THNM, which hinders it to model a complete transformer. Therefore, in the literature, the CFD models have mostly been used to study the thermal behaviour of an individual component, e.g., a transformer winding or a transformer radiator.

2.3 Thermal Studies of Transformer Windings

This section focuses on the CFD models of windings and the experimental verification work. Most of the CFD models are input with the bottom liquid temperature and flow velocity (or the total liquid flow rate) at the winding inlet; and a reference pressure needs to be set at the winding outlet, always as zero. The electric loss distribution is the model input, but is optional. The inputs and their boundary settings are demonstrated by a 2D winding CFD model in [57] as shown in Figure 2-15.

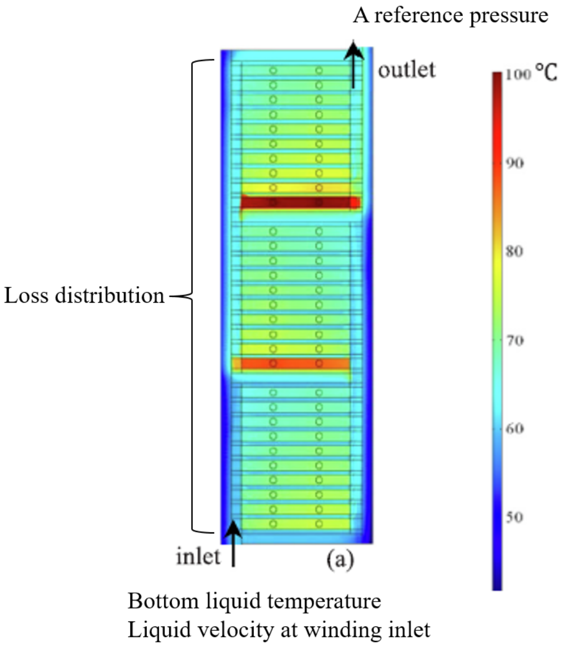

Figure 2-15 Input and boundaries of winding CFD model [57]

It is worth mentioning that the liquid flow distribution in the OD/KD cooling mode is dominated by the pressure generated from the external pump, whereas the insulating liquid flow distribution is primarily coupled with the winding temperature distribution in the ON/KN cooling mode. Therefore, the simulations and experiments in an OD cooling mode can be conducted under either an isothermal or a non-isothermal condition, whereas those in an ON cooling mode should be implemented under the non-isothermal conditions only. This is why in the OD/KD modelling and experiments, the electric loss can be neglected, and only the flow distribution is studied. The review of the CFD modelling and thermal experiments is grouped by the cooling modes below. In each cooling mode, the review includes the winding behaviour in different loading conditions and thermal designs, as well as the thermal performances of alternative insulating liquids. Moreover, the model approximations and its experimental verification will also be introduced.

2.3.1 Thermal Studies in OD Cooling Mode

The OD cooling mode can be simulated or experimentally investigated by either an isothermal condition or a non-isothermal condition. The isothermal condition helps study the flow distributions, whereas the non-isothermal condition contributes to both flow and temperature distributions.

To understand the liquid flow distribution within a disc-type winding, a two-dimensional (2D) CFD model in [58] was adopted in an isothermal condition. By a parametric study of the model inputs, i.e., the bottom liquid temperature and total liquid flow rate, the Reynolds number (R_e) was found as a key parameter dominating the liquid flow distribution. The CFD simulation results indicated that a higher Reynolds number, which was caused by a higher total liquid flow rate, would lead to a non-uniform liquid flow distribution within the winding. The non-uniform oil flow distribution further resulted in a starvation of the insulating liquid at the bottom disc of a pass, and hence, caused localised overheating. The insights and the correlation equations provided in [58] were verified by a set of experiments in [59].

The temperature distribution of a disc-type winding was simulated by a two-dimensional (2D) CFD model under the non-isothermal condition in [60]. It is worth emphasizing that the OD/KD cooled winding geometry can be simplified as a homogenous copper block due to a weak relationship between the winding temperature and insulating liquid flow distribution. By a CFD parametric study, it was found that the Reynolds number (R_e) and the Prandtl number (P_r) were the contributing parameters that affect the hot-spot temperature within the winding. The Reynolds number (R_e) influences the liquid flow distributions, and the Prandtl number (P_r) governs the material properties of an insulating liquid. The same modelling methodology in [60] was verified by the experiments in [57].

The loading conditions of an OD cooled disc-type winding were comprehensively simulated by varying the bottom liquid temperature and the liquid flow rate [58, 60], and these parameters were also experimentally investigated in [57]. The winding CFD model is also used to study different OD/KD winding thermal designs, as well as the thermal performances of alternative insulating liquids. The dimensional analysis in [58] also highlighted the key geometric parameters, which is the ratio of the height of the horizontal cooling duct (the radial oil duct shown in Figure 2-5) to the width of the vertical cooling duct (the axial oil duct shown in Figure 2-5). The CFD simulation results also indicated that the higher the horizontal cooling duct, the more non-uniformity the liquid flow distribution is. A wider vertical cooling duct would generate a more uniform liquid flow distribution, and hence, a better cooling condition within the winding. The similar conclusions drawn from the reference [58] were also confirmed by the experiments in [57] and [61].

As known, the washers inserted between the winding passes help form a zig-zag oil flow fashion in the winding. For a fixed number of winding discs, different arrangements of passes were experimentally studied in [60] and [61] and simulated in [62]. It was concluded that an increasing number of passes resulted in a more uniform oil flow distribution within each pass, and hence, a lower winding temperature. However, more passes within a winding would increase the pressure drop of the winding. Therefore, in the thermal designs of an OD/KD winding, a trade-off between the pressure drop and winding temperature needs to be considered.

The thermal performances of different alternative insulating liquids were also studied by both the experiments and CFD simulations. Three different types of the insulating liquids, i.e. a mineral oil, a Gas-to-Liquid, and a synthetic ester liquid, were studied in [57].Given the same bottom liquid temperature and the same liquid velocity, the winding temperature of synthetic ester was the lowest among these three. The lower temperature is because of a higher viscosity of the synthetic ester, which results in a lower Reynolds number, and hence, a uniform liquid flow distribution. It should also be noted that the pressure of the synthetic ester is the largest for all three liquids when the liquid temperature and the total liquid flow rate are kept the same [57]. The same conclusion was also found in [63], in which the liquid flow distributions were modelled by a 2D CFD model.

The model approximation also plays an important role in CFD modelling of an OD/KD cooled winding. Commonly, the 2D model was selected to replace the complex 3D simulation, as demonstrated in [57, 58, 64, 65]. In [66], the 2D and 3D CFD simulation results were compared with the experiments, and it was found that both 2D and 3D CFD simulation results were comparable to the experimental measurements. However, in [57], more scenarios were simulated, and it was found that the simulation results from a 2D CFD winding model matched well with the one from a 3D CFD winding model if no reverse flow was present. Once reverse flow occurred, a large temperature difference, 20.1 K [57], was found between the 2D simulation results and the experimental measurements. The appearance of the reverse flow can be found under a high Reynolds number, and the threshold of the Reynolds number is dependent on the winding geometries. It is also worth mentioning that the maximum temperature difference between the simulation results from the 3D CFD model and the experimental measurements was only 1.6 K for all the cases.

In summary, the thermal behaviour of the disc-type winding was comprehensively studied with different loading conditions, different geometries, as well as different insulating liquids.

2.3.2 Thermal Studies in ON Cooling Mode

In an ON/KN cooled winding, the liquid flow distribution within the winding is driven by the thermosiphon pressure. The thermosiphon pressure is generated due to the reduction of liquid density, which can be changed as a result of the hot winding conductors. Therefore, to accurately estimate the winding temperatures in an ON/KN cooled winding, the winding temperature should be coupled with the insulating liquid flow and its temperature.

Six 2D winding models in an ON cooling mode were compared to validate different approximations in [55]. The models and their approximations were outlined as:

- Benchmark model (CHT: conjugate heat transfer): including both the insulating liquid and winding domains with full geometric characteristics;
- CHT with Boussinesq approximation: the only difference compared with the CHT model is the application of a Boussinesq approximation, in which the liquid density is only changeable in the conservation equation of momentum (in Equation 2-11);
- CHT without buoyancy force: neglects the buoyancy force in the conservation equation of momentum (Equation 2-11);

- CHT without heating: there is no heat source input in the winding, which is simulated as an isothermal condition;
- CHT without winding domain: only the insulating liquid domain is simulated, and the loss distribution is transformed to an equivalent heat flux on each disc surfaces;
- CHT with whole disc: a simplification of the winding geometry, where the winding disc is simulated as a homogenous copper block rather than multiple conductors, is implemented.

The geometric simplification is very practical in the CFD modelling, as such simplifications could significantly reduce the computational efforts by having less mesh elements. To clearly explain the geometric simplification detail [55], Figure 2-16 takes a 3-conductor as an example to shows the geometric difference between the 'CHT' and the 'CHT without whole disc'.

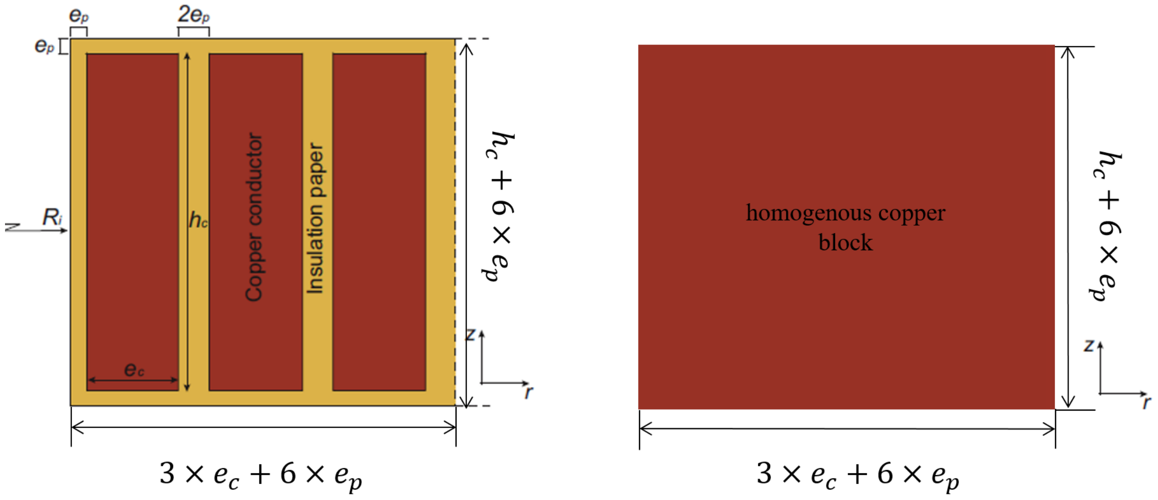

(a) (b)

Figure 2-16 Configuration of a 3-conductor winding disc in two 2D CFD models in [55] (a) geometry of the 'CHT' (b) geometry of the 'CHT without whole disc': e_c is the thickness of the conductor, e_p is the thickness of the solid paper insulation, h_c is the height of the conductor

As observed from Figure 2-16, the full winding geometry takes into account each individual conductor as well as the paper insulation in 'CHT', whereas in 'CHT with whole disc' the winding disc is merely modelled as a homogenous copper block whose height and thickness are as the same as the ones in 'CHT'. It is worth noticing that the 'CHT without winding domain' models the winding using the same geometry as shown in Figure 2-16 (b).

The simulation results in [55] indicated that the isothermal assumptions (CHT without heating) for ON cooled winding was not valid. And there was a large discrepancy between the benchmark model (CHT) and the ‘CHT without buoyancy force’, which proved that the buoyance force cannot be neglected in the ON/KN simulations. Moreover, as concluded in [55], the Boussinesq approximation was validated in the winding CFD simulation in an ON cooling mode.

The simulation results from another two CFD models in a non-isothermal condition, i.e. ‘CHT’ and ‘CHT without winding domain’, matched well in terms of the insulating liquid flow distribution and winding surface temperature. Such finding is deemed important, because this modelling approximation can be used to simplify a complex winding model if only the liquid temperature and flow distributions are required.

As for the winding geometry, modelling the whole disc as a block (CHT with whole disc) significantly affected the winding temperature distribution, which was predicted 6 ℃ lower than the one calculated in the benchmark model (CHT). This was because the copper block tends to have a uniform temperature within a disc due to its high thermal conductivity (385 $W/(m \cdot K)$). Therefore, the heat flux on the disc surfaces was changed to uniformize the temperature inside the whole disc, and then brought discrepancies in the simulation results.

In addition, the importance of the input liquid flow and temperature profiles was highlighted in [55], both uniform profiles and non-uniform profiles had a significant influence on the winding temperature distribution. The same conclusion was also given in [54].

Another approximation made for the winding CFD model in an ON/KN cooling mode is related to the winding axisymmetric geometry. In other words, whether the ON/KN cooled winding can be modelled as a 2D or a 3D scenario? Therefore, a 3D CFD model, a 2D CFD model and the experimental measurements were compared in [67]. It was found that the liquid flow and temperature distributions were not axisymmetric, and using a 2D CFD model could result in a less accuracy.

To improve the accuracy of the 2D winding CFD, two suggestions were made in [67]:

- The radial spacers were not accounted for in the 2D simulations, and therefore, a correction factor should be applied to compensate for the effects of radial spacers on the covered disc surface area and the change of liquid velocity (or total liquid flow rate);

- By matching two dimensionless number, i.e., the Reynolds (R_e) number and the Richardson number (R_i), the dimensionless flow and temperature distributions from a 2D model can have a good agreement with the results in a 3D model.

[65] also conducted a comparison between a 2D winding CFD model and a 3D winding CFD model. If there was no reverse flow, the results of these two models matched well, with the temperature difference being less than 1 K However, a large temperature difference was observed if a reversed flow was present.

Different thermal designs were also simulated and experimentally investigated in the ON/KN cooled winding. In [26], the effects of the width of the vertical cooling duct, the height of the horizontal cooling duct and the number of the passes were experimentally examined. It was found that the height of the horizontal cooling duct made a significant impact on the liquid flow and winding temperature distributions under three different investigated liquid velocities. More passes within a fixed number of winding discs could produce a more uniform liquid flow distribution, and thus, lower winding temperatures, with a cost of higher pressure loss.

It should be noticed that both input of the bottom liquid temperature and liquid velocity at the winding inlet in the simulations of [55], [65] and [67] were within a range based on industrial experience of transformer operation. Each parameter range has been scanned, but the data pair may have no correlation to reality. So are the experimental conditions in [26] and [68] in terms of bottom liquid temperature and the flow rate. The sketch of the experimental setup was shown in Figure 2-17, where the bottom liquid temperature and the liquid velocity in the ON/KN experiments were controlled by an external heater and pump, receptively.

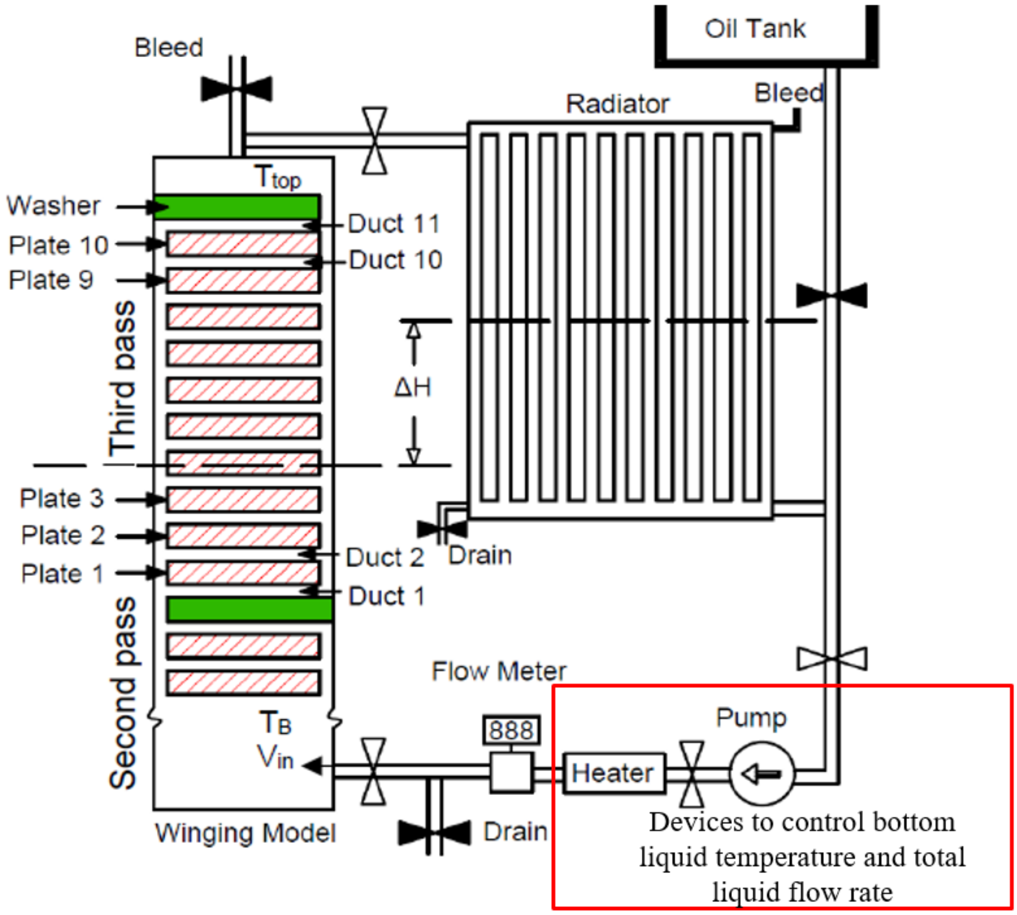

Figure 2-17 Sketch of experimental setup in [68]

The thermal performances of alternative insulating liquids in an ON/KN winding were also studied previously. Particularly, dedicated CFD simulations [69-73] and laboratory-scale experiments using a test rig[68] were performed to explore the winding temperatures when filled with different insulating liquids. In these studies, the bottom liquid temperature and the liquid velocity were kept the same, and the results have identified that the ester liquid could result in a lower winding temperature than mineral oil.

However, an opposite conclusion has been drawn when an ON/KN power transformer is used to compare different insulating liquids. In [74], a 154/22.9 kV, 15 MVA transformer was filled with natural ester and mineral oil, respectively. Under the rated condition, the hot-spot temperature of high voltage winding with natural ester was 9.8 °C higher than that of mineral oil, and this difference was 15.7 °C for the low voltage winding. Moreover, similar results were also observed in a 141/13 kV, 50 MVA transformer retro-filled with natural ester in [75]. In the ONAN/KNAN cooling mode, the hot-spot temperature was found 8 °C higher than when filled with mineral oil. The conclusion drawn from the tests of the power transformer is opposite to the laboratory-test, simply because the use of the ester liquid results in the different liquid velocity and bottom liquid temperature than the mineral oil.

In summary, the winding CFD models in an ON/KN cooling mode have been established, and the methodology has been validated by the experiments. However, to study an ON/KN cooled winding under different loading conditions, the inter-dependent relationship between the bottom liquid temperature and liquid velocity needs to be obtained. This also helps the transformer retro-filling studies.

2.4 Transformer Complete-Cooling-Loop Studies

In an ON/KN cooled transformer, the liquid velocity at the winding inlet is dependent on the liquid temperature distribution within its complete-cooling-loop (CCL), from the windings to the radiators. Therefore, the relationship between the liquid temperature and liquid velocity, and the loading conditions can only be obtained by investigating a transformer liquid complete-cooling-loop (an example shown in Figure 2-9). However, little work has been done in this area both experimentally and numerically. This is partly because much more computational efforts are needed than the winding only models.

In the winding focused experiments, the liquid velocity (or total liquid flow rate) could be controlled by an external pump or a valve (e.g. Figure 2-17 in [68]), whereas a spontaneous liquid flow needs to be achieved through a CCL experimental setup, such a CCL experimental setup in an ONWF cooling mode was achieved in [76]. The setup consisted of a winding assembly, connecting pipework, a radiator, and a water cooling system, shown in Figure 2-18. The liquid flow velocity was measured at the 'measuring point' by a laser Doppler Velocimetry. The measurements indicated that the liquid velocity increased proportionally to the square root of the total power loss within the winding and to the thermal head (shown as ΔH in Figure 2-18).

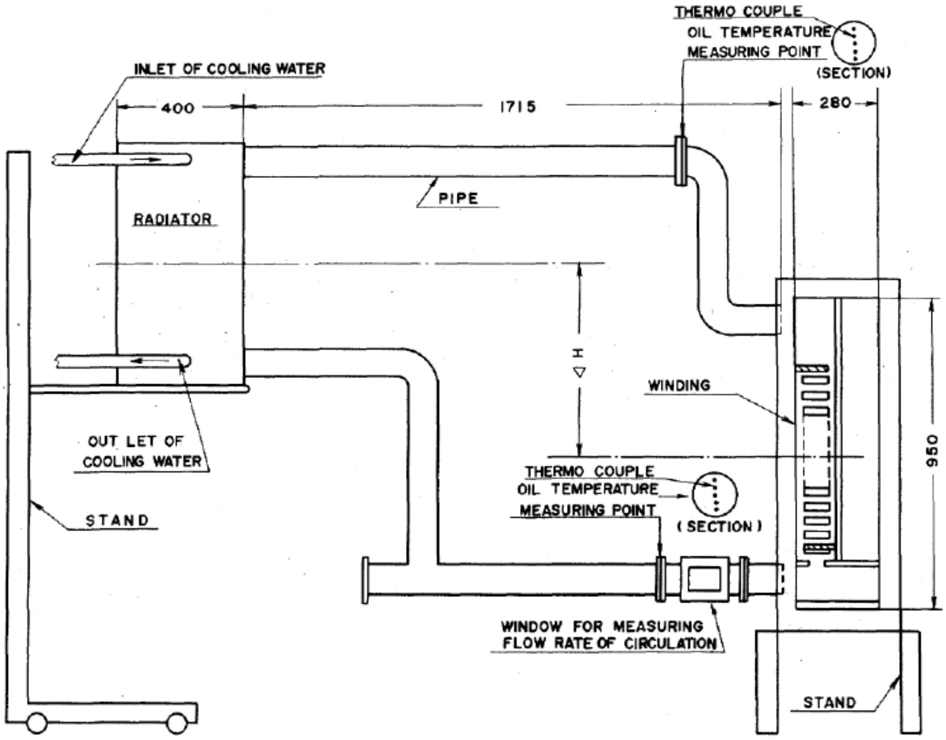

Figure 2-18 Experimental setup in [76]

Based on the findings of the ONWF experiments in [76], an analytical equation was proposed to estimate the ratio of the liquid velocity of an alternative liquid to the a mineral oil in [38], [72] and [73]. The analytical equation to calculate the liquid velocity simplified the liquid temperature within the CCL as a one-dimensional case, and was based on the pressure equilibrium. As seen in Figure 2-19, the bottom, top of the winding are referred to as point A and B, whereas the point C and D represent the radiator inlet and outlet. If the heat dissipation through the connecting pipes is neglected, the temperature at points A and D are the same, as the bottom liquid temperature. And top liquid temperature is also the same at points B and C.

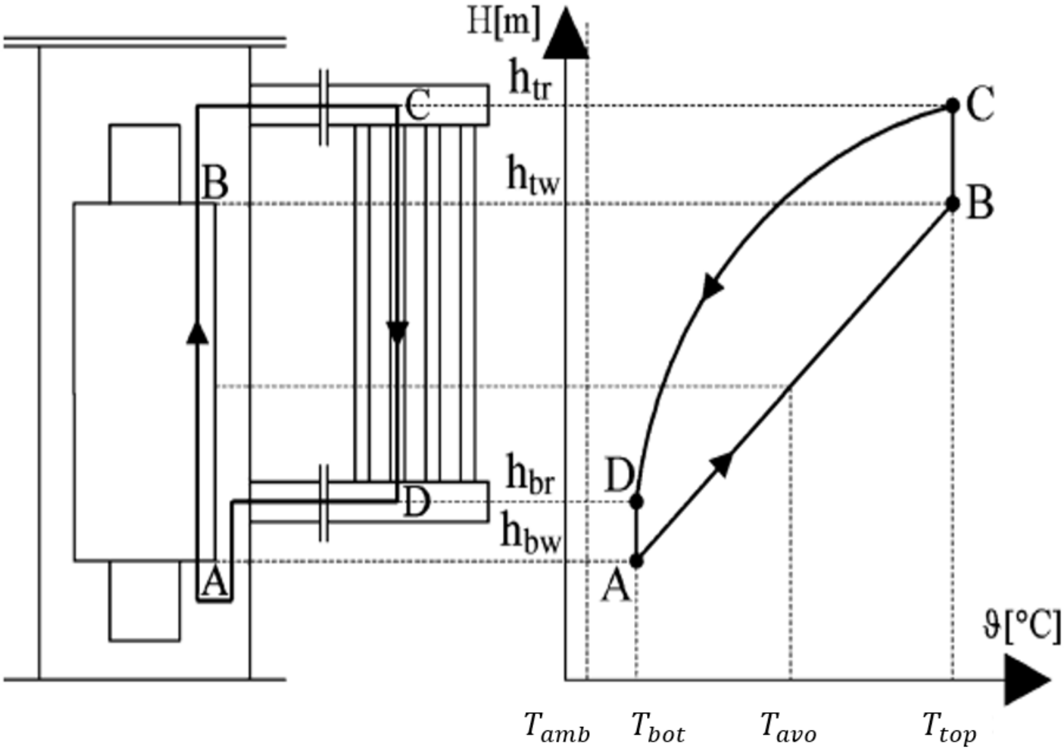

Figure 2-19 Liquid temperature distribution in the one-dimensional complete cooling loop [38]

In a CCL of a liquid natural cooled transformer, the liquid driving force is caused from the thermosiphon pressure (P_T). If the liquid temperature in both the winding and the radiator can be simulated as a linear distribution, the therosiphon pressure can be calculated from Equation 2-13 [38].

$$P_T = \rho_{avo} \cdot g \cdot \beta \cdot \Delta T_{oil} \cdot h \qquad \text{Equation 2-13}$$

where P_T is the thermosiphon pressure (P_a), g is the gravity accelerator (m^2/s), β is the thermal expansion coefficient ($1/K$), ΔT_{oil} is the liquid temperature rise ($T_{top} - T_{bot}$) (K), h is the thermal head (m).

In the CCL of the insulating liquid, the pressure loss is caused by the liquid flowing through the winding, the radiator and the connecting pipework. The pressure loss consists of the major pressure loss in the CCL due to the friction, and the minor pressure loss in the winding because of the liquid splitting or re-joining. It was believed in [38, 72] that the pressure loss within the CCL can be calculated as the major pressure loss from Equation 2-14 [77].

$$P_L = \frac{C}{Re}\frac{L'}{H'}\frac{\rho_{bot}{v_{oil}}^2}{2} \qquad \text{Equation 2-14}$$

where P_L is the major pressure loss (P_a), C is a geometry related constant [77], Re is the Reynold number, L' and H' are for the equivalent length (m) and hydraulic diameter (m) of the CCL, v_{oil} is the velocity at the winding inlet (m/s), ρ_{bot} is the liquid density at the winding bottom (kg/m^3).

The liquid velocity under the steady-state condition is the result of the pressure equilibrium, and in which the thermosiphon force (P_T) is equal to the pressure drop (P_L). Hence, the liquid velocity can be estimated from Equation 2-15 [72].

$$\mathrm{v}_{oil} = C_g\sqrt{\frac{\rho_{avo}\cdot g\cdot \beta}{\mu\rho_{bot}C_p}}\cdot\sqrt{h}\cdot\sqrt{P} \qquad \text{Equation 2-15}$$

where v_{oil} is the liquid velocity at the winding inlet (m/s), C_g is the geometric characteristic of the CCL, ρ_{avo} is the liquid density reference temperature as the average liquid temperature (kg/m^3), g is the gravity accelerator (m^2/s), β is the thermal expansion coefficient ($1/K$), μ is the dynamic viscosity ($kg/(m\cdot s)$), ρ_{bot} is liquid density reference temperature as the bottom liquid temperature (kg/m^3), ρ_{avo} is liquid density reference temperature as the average liquid temperature (kg/m^3), C_p is the specific heat capacity ($J/(kg\cdot K)$, P is the power loss within the transformer (W), h is the thermal head (m).

The main assumptions in this analytical equation in [38], [72] and [73] are as follows:

- The liquid temperatures in the winding and the radiator are in a linear distribution manner;
- The geometric characteristic (C_g) for a specific transformer is the same, though it is filled with different liquids.

It should be noted that the validity of the assumptions are yet to be verified by the experiments. To quantitatively determine the interdependent relationship between the bottom liquid temperature and liquid velocity, as well as the hot-spot temperature, CCL CFD models were developed in [78] and [79].

A pioneering paper of CCL CFD modelling was published in 2018 [78], in which both a CCL experimental setup, and a 3D CCL CFD model were both developed based on one phase of a 225/26.4 kV, 66 MVA ONWN power transformer.

Figure 2-20 shows a front view of the CCL experimental setup in [78]. In the experiment, the Nitrogen was used to allow the insulating liquid expansion due to its temperature rise (oil shown as yellow area in Figure 2-20), and the water was used to cool the radiator. In the CCL CFD model, the Nitrogen and water cooling were not considered. The model included the insulating liquid domain, the winding domain and the radiator domain. The input of the model was the volumetric heat loss within the winding, and the boundary condition was the radiator surface temperatures that were taken from the experimental measurements.

By comparing with the experiments under two loss distributions and in four different geometries (8 conditions in total), the mass flow rates obtained from the CCL CFD simulations were underestimated by from 11% to 42%. The underestimated mass flow rates caused an overestimation of the hot-spot temperature from 3.7 ℃ to 35.9 ℃ at the winding.

To find out the limitation of this CCL CFD model, a 3D winding model was also built in [78]. By inputting the total liquid flow rate and the bottom liquid temperature directly from the experimental measurements, the differences of the winding temperatures, including the hot-spot temperature and the average temperature, between the 3D simulations and measurements were less than 2.9 ℃, under all 8 investigated conditions. Clearly, the deviations of winding temperature estimation in the CCL CFD model were caused by the underestimation of the liquid velocity / total liquid flow rate, and the inaccuracy of which was mainly due to the boundary condition on the radiator side [78].

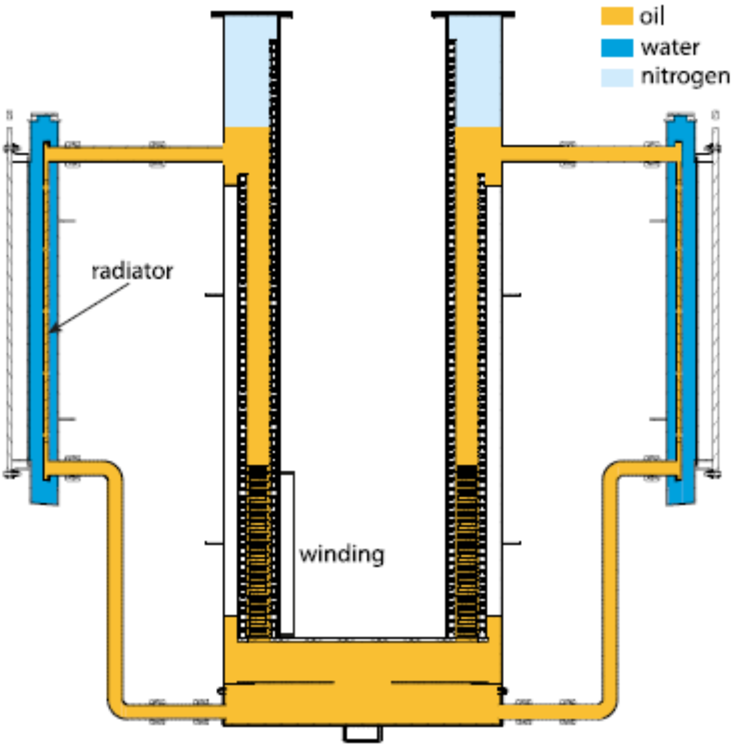

Figure 2-20 A front view of CCL experimental setup in [78]

Another CCL CFD modelling strategy was proposed, namely ‘EMAG-CFD-CFD’, to simulate a 33/6.9 kV, 8.5 MVA liquid-immersed transformer in [79] by two steps. Firstly, the loss distribution was obtained by simulating the electromagnetic field within the transformer. Secondly, the volumetric loss was input into a coupled CFD-CFD model, consisted of the ‘Windings CFD model’ and the ‘Tank CFD model’ as shown in Figure 2-21. The 3D winding CFD model solved the liquid flow and the winding temperatures within the high voltage and low voltage windings. The tank CFD model solved the liquid temperatures within the tank except for winding parts, and coupled with a reduced radiator model, as developed in [80].

The construction of the transformer CCL by using the coupled CFD-CFD model provided an insight on studying the heat transfer processes through a coupling mechanism rather than as a whole in one go. The coupling of the winding and the tank CFD models and the radiator model was achieved by iteratively updating the mass flow rate and the liquid temperatures at the winding bottom and top, and at the tank inlet and outlet, as shown in Figure 2-21.

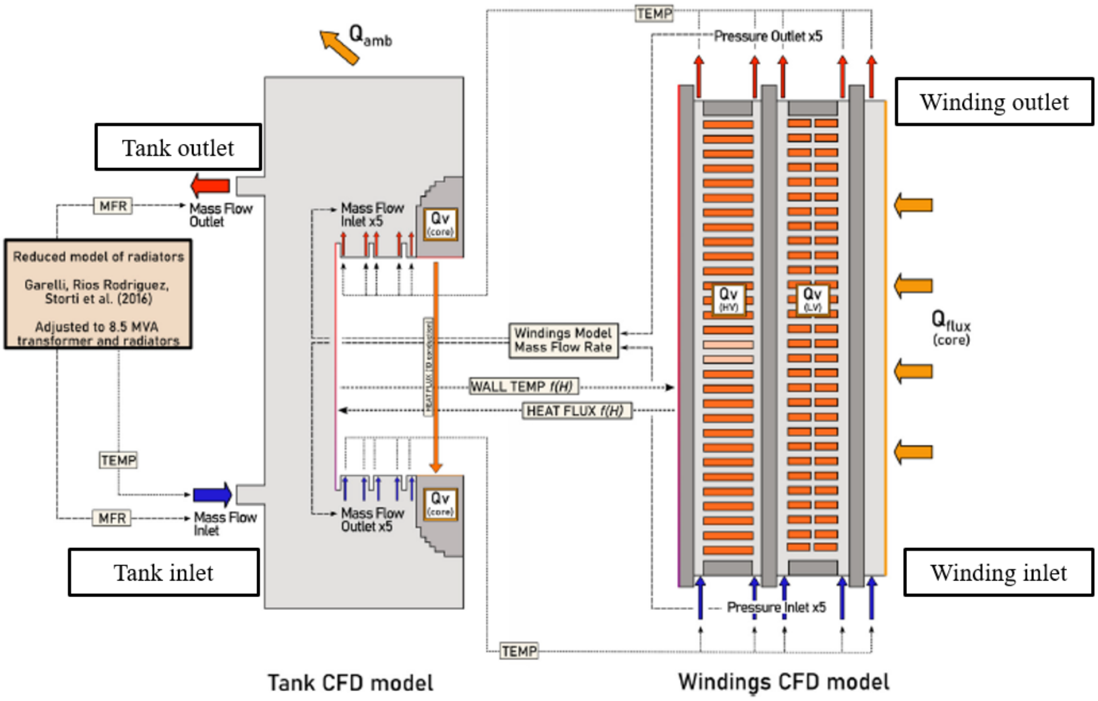

Figure 2-21 Principle of EMAG-CFD-CFD CCL modelling strategy in [79]

One of the main approximations in the CFD models in [79] was that the winding in [79] was simulated as a homogenous copper block. It was claimed that such approximation was proven by additional 2D winding only simulations. However, this was opposite to the conclusion in [55]. Therefore, the modelling strategy should be verified by a set of well-designed experiments.

In the light of above, there has been limited work done for a transformer CCL in an ONAN/KNAN cooling mode both numerically and experimentally. The present work pointed out that the accuracy of the CCL CFD simulation was affected by the estimation of liquid temperature distribution within the radiator. An advanced modelling strategy and suitable boundary conditions of the radiator are required for the CCL CFD model. Moreover, to build a reliable CCL CFD model with a reasonable processing time, the heat transfer processes in individual components can be modelled individually. But each model approximation needs to be carefully verified, and such a simulation work requires validation by a CCL experimental setup.

2.5 Transformer Radiators

As indicated in [78], the accuracy of the CCL CFD model is affected by how the transformer radiator is modelled. Therefore, the radiator CFD models and their boundary conditions are reviewed in this section.

As introduced in 2.1.2 and 2.1.3, the insulating liquid transfers the heat to the radiator wall, where the heat is mostly dissipated to the environment by air convection. The liquid temperature is vital to determine the liquid velocity (or the total liquid flow rate) of an ON/KN cooled transformer, therefore, most of the modelling approximations are made for the air convection.

By the means of simulating air convection effects, the radiator models can be categorized in two groups:

1) Modelling the detailed air flow and temperature profiles to determine the air convection effect;
2) Excluding the simulation of an air flow by using the air heat transfer coefficients based on the Newton's law of cooling.

2.5.1 Radiator Models including Air Flow Simulation

The temperature and flow distributions of the air around a transformer radiator were modelled in [80-88]. Some work [81, 88], focused on an AF cooling mode and studied the optimal fan arrangement to maximize the radiator cooling capacities.

The thermal behaviour of the transformer radiator in an AN cooling mode was modelled in [80, 82-87], and the simulation results were verified by the experiments in [80, 83, 84, 87]. These studies mostly focused on the model development and verifications.

In the experimental verification, most of the simulation results were validated by the global parameters, the bottom liquid temperature and the total heat dissipation. The differences of the global parameters between the simulations results and experimental measurements of radiator in the literature [80, 83, 84, 87] were summarized in Table 2-3.

Table 2-3 Differences between radiator simulation results and measurements in literature [80, 83, 84, 87]

Reference	Difference between the simulation results and experimental measurements		
	Bottom liquid temperature	Total heat dissipation	Surface temperature measurement
[80]		$< 30\%$	$< 5.5\ K$
[83]	$1.3\ K < \Delta T_{bot} < 1.7\ K$	$< 14.5\%$	
[84]		$< 8.2\%$	
[87]		$< 6.1\%$	

In [80], a reduced radiator modelling strategy was proposed with four steps. Firstly, only one radiator panel was simulated in a 3D CFD simulation, which was placed in the free space without any panels around. Then, in the second step, the surface temperature of the simulated panel in the first step was extracted and set the same for all the other panels of a radiator. Thirdly, the air flow around the radiator was simulated with the fixed radiator surface temperature profile, and an air heat transfer coefficient was then obtained. In the fourth step, the air heat transfer coefficient was input to an analytical equation to estimate the liquid temperature within the radiator. For the radiator simulation in step 3 in [80], all the radiator panel was simulated in the same way as the single panel in step 1, where there were no parallel panels to restrict the air flow. However, in a multiple-panel radiator, most of the panels are placed in parallel, and where the air flow between the parallel panels is restricted. This is why the radiator model in [80] overestimated by an approximately 30% of the total heat dissipation. The surface temperatures were also used to verify the model in [80], by considering six different locations, and the differences between the CFD simulation and the experimental measurement were from 0.9 K to 5.5 K.

A 3.3-meter-high 40-panel radiator was directly simulated in [83] with four different mass flow rates from $1 \times 10^{-3}\ m^3/s$ to $4 \times 10^{-3}\ m^3/s$. Under four investigated conditions, the maximum difference of the bottom liquid temperature between simulations and experiments was 1.7 K, and the mismatch of the total heat dissipation was within 14.5%. In [87], a 3.5-meter-high 30-panel radiator was taken to compare different radiator CFD modelling strategies. Due to the large size of the radiator, air flow was assumed as in a turbulent flow regime. The results of four turbulent flow models were then compared with the experimental measurements, and it was found that the standard $k - \varepsilon$ model provided the minimum discrepancy, 6.1%, between the simulation and experiment. It is worth noting that the Boussinesq approximation in air flow simulation was also experimentally verified in [87].

Simulation work in [85] highlighted the importance of the radiation effect in the radiator modelling. By comparing the simulation results with and without radiation based on a 2.5-meter-high 27-panel radiator, it was found that the radiation contributed a 25.1% of total heat dissipation. Mostly importantly, the radiation was pronounced on the outwards facing surfaces. However, since the radiation is mostly on the radiator outwards facing surface, the ratio of the radiative heat dissipation to the total heat dissipation should be approximately equal to the ratio of the outwards facing surface area to the radiator total surface area, which is 3.7% in [85]. The conclusions in [85] were obtained from the CFD simulations only, and an experimental verification is hence suggested.

Different radiator models, including a distributed air flow and temperature simulation, were developed. Different modelling strategies were verified by the corresponding experiments. The accuracy of the predictions of global parameters were acceptable. However, less work was carried out on surface temperature measurements that were meant to represent the liquid temperature distribution within a radiator.

2.5.2 Radiator Models excluding Air Flow Simulation

The radiator CFD model including the air domain is very time consuming, one case in [86] was processed for more than 500 hours. The long processing time hinders the application of the radiator model including air flow simulation, and makes it impractical to be implemented in a transformer CCL CFD model.

Therefore, according to the Newton's law of cooling, the radiator was modelled by using air heat transfer coefficients to replace the air flow simulation, as in [80, 83, 89]. In [83], the simulation results of the radiator model, excluding air flow simulation, were compared with the experimental measurements as shown in Table 2-4. As seen in Table 2-4, the difference of the liquid temperature rise between the calculations and measurements was in the range from 1.3 K to 3.1 K, and the mismatch of the total heat dissipation was less than 26.9%.

Table 2-4 Radiator model excluding air domain simulation results and experimental verification in [83]

	Variable	Liquid flow rate (m^3/s)			
		1×10^{-3}	2×10^{-3}	3×10^{-3}	4×10^{-3}
Radiator model excluding air domain	Liquid temperature rise ΔT_{oil} (K)	12.8	6.7	4.5	3.4
	Air heat transfer coefficient h_{air} ($W/(m^2K)$)	3	3	3.1	3.1
	Total heat dissipation P (kW)	22.5	23.5	23.9	24.1
Experimental measurements	Liquid temperature rise ΔT_{oil} (K)	15.9		6.1	4.7
	Air heat transfer coefficient (calculated from measurements) h_{air} ($W/(m^2K)$)	3.9		4.1	4.3
	Total heat dissipation P (kW)	27.4$\pm$1.7		32.4$\pm$1.8	33.0$\pm$1.6

As concluded in [83], the discrepancies between calculations and experiments were mainly caused by the adoption of air heat transfer coefficients, which were calculated from the empirical equations. A similar conclusion was made in the investigated condition in [80], the air heat transfer coefficient extracted from a CFD model including air flow simulation was 29.5% larger than the one from empirical equations. The lack of heat coefficient equations that are specifically derived for transformer radiators has compromised the accuracy of radiator model excluding air flow.

In addition, some of the radiator models excluding air flow employed two air heat transfer coefficients, e.g. [83], and others adopted only one air heat transfer coefficient [80, 89] to represent the air flow simulation. There has been no justification on the minimum number of air heat transfer coefficients required in the radiator model excluding air flow.

2.6 Summary

In this chapter, a literature review on transformer heat transfer mechanisms, factory temperature-rise tests, the temperature estimation methods in the IEC standards, and various thermal modelling approaches has been conducted. Furthermore, the latest CFD simulations and verification experiments for windings only, the complete-cooling-loop and radiators have also been assessed. The conclusions and the research gap identified from the critical review can be summarized as follows:

1. The expected lifetime of a liquid-immersed power transformer primarily depends on its temperature profile as the solid paper insulation at the hottest spot undergoes the severest thermal stress. To operate transformers safely and optimize the asset lifetime, an accurate thermal model is required to predict the hot-spot temperature and its location under different operational conditions.
2. There have been three commonly used modelling approaches, i.e., electrical thermal analogy circuit, Thermal-Hydraulic Network model (THNM) and Computational Fluid Dynamics (CFD) model. The main drawback of the electrical thermal analogy circuit is that the hot-spot location cannot be predicted; and the THNM loses its accuracy when complex flow phenomena occur, especially in the liquid natural (ON/KN) cooling mode. The CFD modelling is the most accurate, whose application, however, is limited by its high computational requirement and long processing time. Therefore, the CFD modelling was applied to simulate individual components, e.g., the winding and the radiator, rather than a complete liquid-immersed transformer.
3. Comprehensive CFD simulations and experiments have been carried out for the OD/KD cooled transformer windings to investigate their thermal behaviours under different loadings, thermal designs and filled with different insulating liquids. In the OD/KD thermal studies, different loadings are represented by varying the bottom liquid temperature and the total liquid flow in a certain range. The same strategy was also used for the ON/KN cooled windings to study their

thermal designs. Within both OD/KD and ON/KN cooled windings, a wider vertical cooling duct or a lower horizontal duct provides a more uniform liquid flow distribution. Lower number of the discs per pass also generate a more uniform liquid flow distribution but at a cost of increased pressure losses. Winding only CFD models were also verified by the experiments.

4. To study an ON/KN cooled transformers under different loading conditions, an interdependent relationship between the bottom liquid temperature and the liquid velocity under different conditions is required. Such relationship can only be obtained by a liquid complete-cooling-loop (CCL) which accounts for both the winding and the radiator. However, it has yet been established a CCL experimental setup of an ONAN/KNAN transformer, nor an experimentally verified CCL CFD model. One of the main limitations of CCL CFD is the thermal modelling of the radiator, and an accurate liquid temperature estimation within the radiator can improve the CCL CFD.
5. Different radiator CFD models were developed and verified by the experiments through global parameters, i.e., the bottom liquid temperature and the total heat dissipation. Another key parameter in the simulation, i.e., the liquid temperature distribution, can be verified by measuring the surface temperatures, but little work has been done in this area. Moreover, a detailed radiator CFD model including air simulation which requires exceedingly long computational time; and therefore, empirical equations of an air heat transfer coefficient were used to achieve a fast calculation. However, large discrepancies were found between the calculations adopted with empirical equations and the experimental measurements. This is because the empirical equations were not specifically developed for a transformer radiator. Moreover, the minimum number of air heat transfer coefficients required in the radiator model excluding air flow has not been justified. Therefore, in the radiator thermal studies, a model with accurate liquid temperature estimation and less processing time is needed to be implemented in a CCL CFD model.

Chapter 3 Development of Complete Cooling Loop based Thermal Test Setup

As previously introduced, most of the experimental setups published in the literature mainly focused on individual components, and controlled the liquid velocity / the total liquid flow rate using a pump. Such studies are reasonable for liquid directed and forced (OD/KD) cooling mode, where the liquid velocity is indeed controlled by the pump, and thus known. However, it is not the case for liquid natural (ON/KN) cooling mode, where the liquid velocity (or total liquid velocity) is dependent on the liquid temperature distribution within a transformer CCL. A CCL experimental setup of an ONAN/KNAN transformer has yet been established in the existing studies.

In this chapter, a laboratory-scale experimental setup based on the CCL has been developed to study an ONAN/KNAN cooled transformer, where various factors including operating conditions, thermal head and insulating liquid type are considered. The design and construction of the CCL experimental setup are presented in Section 3.1 by introducing the main components. Next, the plan and procedures of the temperature-rise experiment are introduced in Section 3.2. Sections 3.3 shows a complete set of measurements under a tested condition to demonstrate the functionality of the experimental setup in terms of winding, liquid, radiator surface temperatures, liquid velocity at the winding inlet and total liquid flow rate at the radiator top. The repeatability tests are conducted and discussed in the Section 3.4.

3.1 Design and Construction of CCL Experimental Setup

The schematic diagram and a photo of the CCL experimental setup are shown in Figure 3-1. The experimental setup consists of a disc-type modularised winding assembly, a 4-panel transformer radiator, connecting pipework, variable AC power supplies, a temperature measurement system, and the other accessories, including an oil expansion vessel, an oil tank and a transparent box.

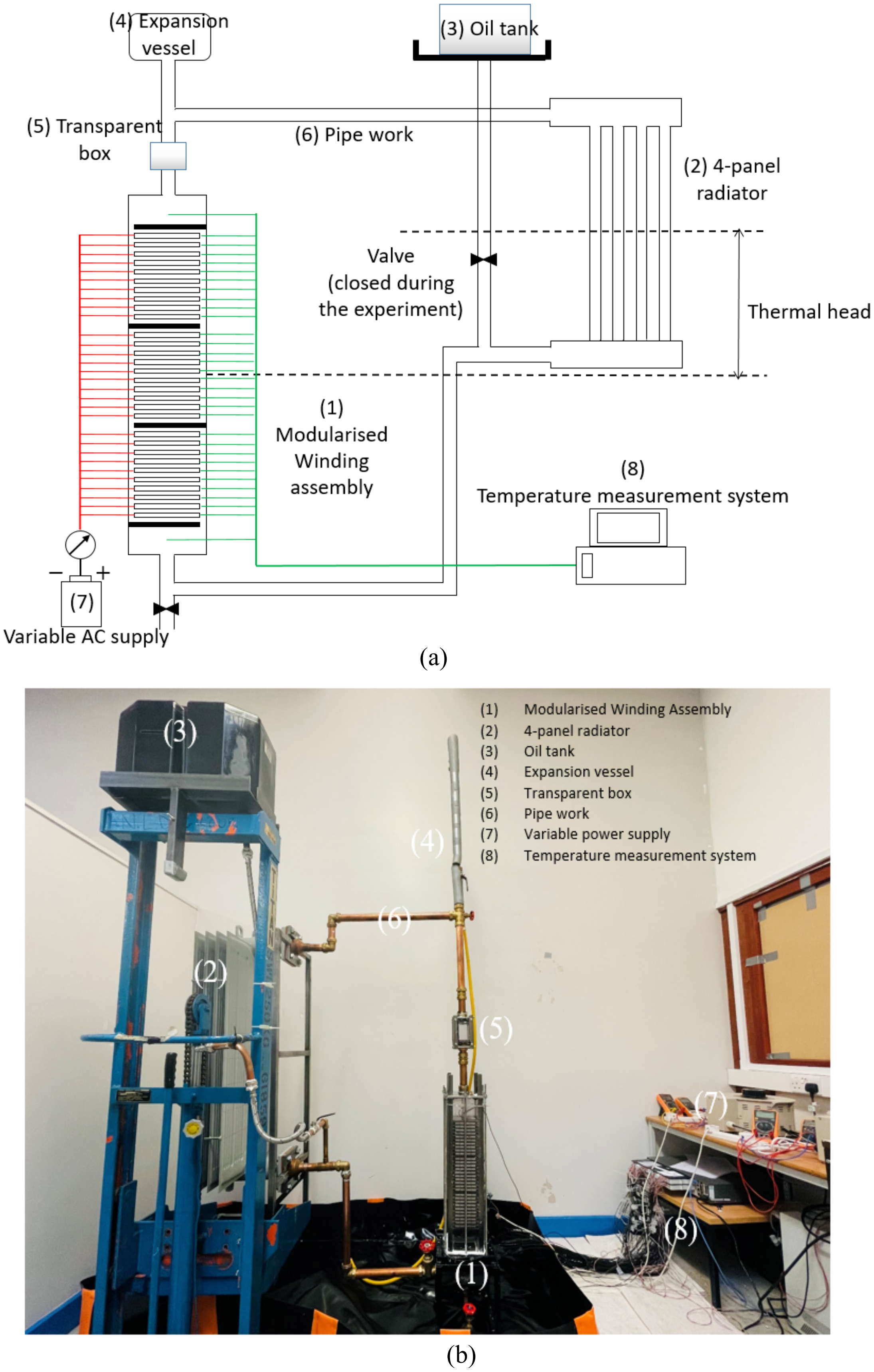

Figure 3-1 Complete-cooling-loop (CCL) experimental setup (a) a schematic diagram (b) a photo

The winding assembly is designed to represent a section of the disc-type transformer winding, and the radiator is then scaled down to 4-panel 1-meter-high accordingly. The temperature measurement system is used to record the winding, liquid and ambient temperatures from a cold start until reaching the steady-state condition. The expansion vessel is designed to store the expansion of the insulating liquid during the temperature-rise test. The oil tank on the top is used to fill the testing liquid into the system. The transparent box allows the liquid velocity (or total liquid flow rate) to be measured by a laser system.

3.1.1 Modularised Winding Assembly

Majority of the electric loss within a transformer is the resistive loss occurred at the windings. Therefore, during the temperature-rise experiment, the winding is injected with different powers to simulate various loading conditions. As introduced in Section 2.1.2, the transformer windings are divided by the spacers into many sections, and each section is thermally and hydraulically independent [19]. Thus, in the experimental setup, only one section is included, whose thermal behaviour is regarded as a representation of the whole transformer winding.

In the power transformer, each section of the winding is in a circular shape. Due to the presence of the core, the inner and outer radius of the cylinder winding are close, e.g. 750 mm and 839 mm in [64], respectively. Therefore, in the laboratory-scale experimental setup in the literature, the circular winding section was built either as a trapezium shape, e.g. in [64], or a rectangular shape, e.g. in [57, 65]. Particularly, the approximation of rectangular winding was verified by using a CFD model in [90], where the winding temperature and flow distributions within a rectangular winding and a circular winding were the same. Therefore, in the experimental setup in this thesis, the winding section is built in a rectangular shape.

Each winding section of a power transformer consists of multiple disc segments along the winding height. Each disc segment comprises multiple winding conductors wrapped with paper insulation placed in parallel. In the light of above, in the winding assembly of the CCL experimental setup, modularised winding discs are employed. This modularised design makes sure that every disc is manufactured the same. A modularised winding disc is described in Figure 3-2 (a), where the winding disc is made up of 4 aluminium bars wrapped with the Kraft paper placed in parallel.

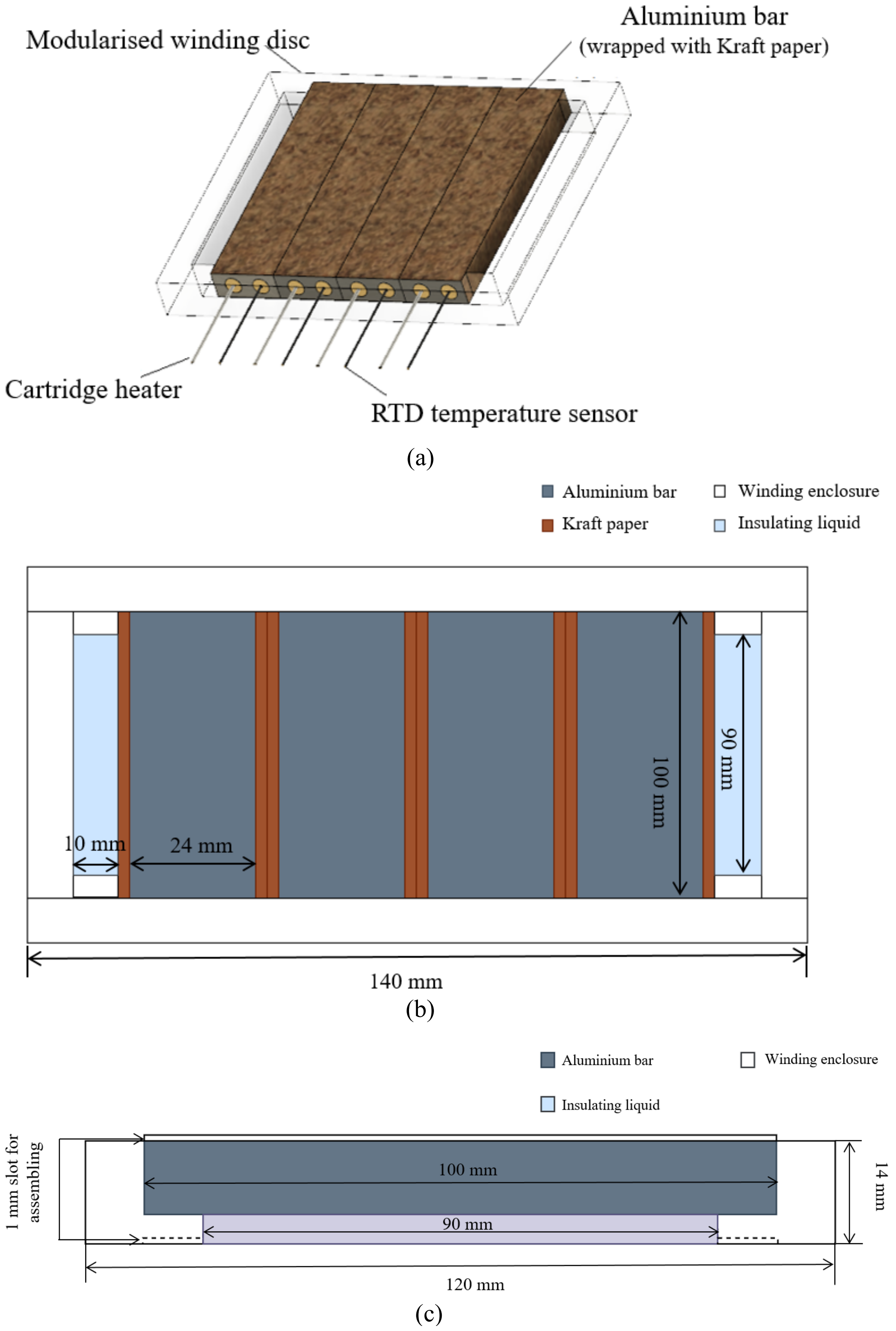

Figure 3-2 Configuration of a modularised winding disc (a) three-dimensional drawing (b) top view (c) side view

A top view and a side view of the modularised winding disc are illustrated in Figure 3-2 (b) and (c), respectively, to model the aluminium bar, the paper insulation, the liquid cooling ducts and the winding enclosure. The dimensions of each aluminium bar are $100 \times 24 \times 10\ mm$ (length, width and height), and the thickness of the paper insulation is $0.5\ mm$. In each modularised winding disc, the dimensions of the vertical cooling duct are $90 \times 10\ mm$ (length and width); and the dimensions of the horizontal cooling duct are $100 \times 4\ mm$ (width and height). As given in Figure 3-2 (c), a $1\ mm$ slot is designed to help assembling the winding discs without any shifting.

To simulate the heat loss in each conductor, a cartridge heater is embedded in each aluminium bar. In addition, a Resistance Temperature Detector (RTD) sensor is also inserted in the aluminium bar to measure the temperature. A total of 30 modularised winding discs, including 120 aluminium bars, are produced. The resistance of each cartridge heater is 500 Ohm with $\pm 5\%$ deviations.

In the transformer winding design, spacers are used to create multiple passes within a winding and to form a zig-zag liquid flow pattern to improve the cooling efficiency. Therefore, in the CCL experimental setup, the 30 modularised winding discs are evenly separated into three passes by using four washers. The horizontal cooling duct between the winding disc and the washer is kept the same as $4\ mm$, the design of the washer is presented by a configuration of a side view in Figure 3-3. As seen in the figure, in each washer, a 2 mm spacer is also designed and built with same material as the winding enclosure. In addition, the slots are also considered in manufacturing the washer to avoid any shifting.

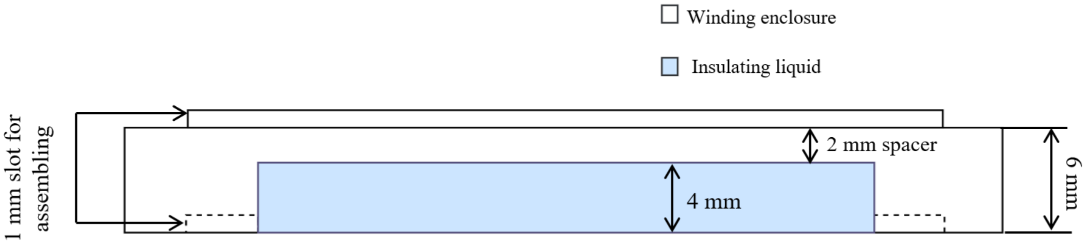

Figure 3-3 Side view of the configuration of a washer

The three-dimensional drawing and a photo of the winding assembly are shown in Figure 3-4, where 30 modularised winding discs and 4 washers are assembled with two buffer zones at the top and bottom. The buffer zones are designed for the insulating liquid mixture, which help the liquid temperature measurement. Also seen in Figure 3-4, two stainless steel plates and 8 threaded rods are applied to ensure the stability of the winding assembly, and to minimise the geometric deviations during the assembling process.

It is also worth mentioning that the winding assembly and the transparent box are both manufactured from polycarbonate (Lexan* 9030), whose transparency is sufficient for measuring the liquid velocity and its flow profile by using an additional laser system.

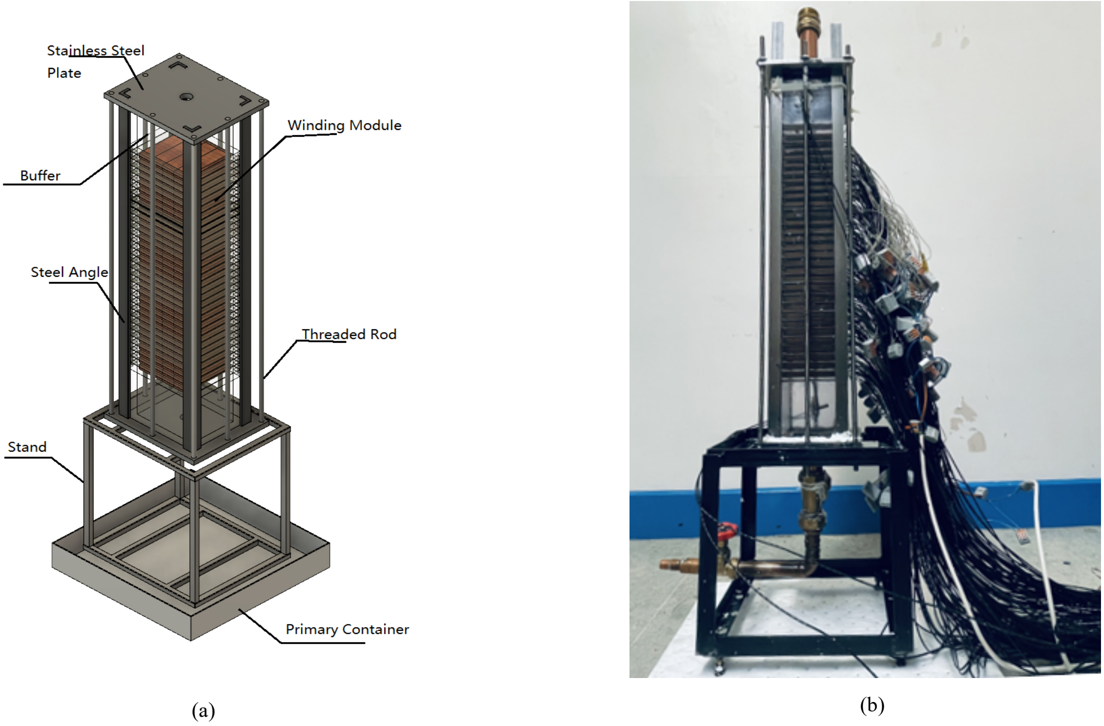

Figure 3-4 3D drawing and photo of modularised winding assembly (a) a 3D drawing (b) photo

3.1.2 4-Panel 1-Meter-High Transformer Radiator

As the winding assembly is only a section of the transformer winding, the size of the radiator is therefore scaled down accordingly. The objective of the radiator selection is to make sure that the temperature measurements in the experiments are in a typical range, as the same as a power transformer. The typical range of key temperatures, including top liquid temperature rise over ambient (ΔT_{top}), liquid velocity at winding inlet (v_{oil}) and the liquid temperature rise (ΔT_{oil}), are given in Table 3-1.

Table 3-1 Typical range key parameters / measurements of experiments

Key parameter	Typical range	Reference
Top liquid temperature rise over ambient temperature (ΔT_{top})	$\Delta T_{top} < 60\ K$	IEC standard 60076-2 [24]
Liquid velocity at winding inlet (v_{oil})	$0.01 < \mathrm{v}_{oil} < 0.05\ m/s$	Published papers [40, 41, 65, 91]
Liquid temperature rise ($\Delta T_{oil} = T_{top} - T_{bot}$)	$15\ K < \Delta T_{oil} < 25\ K$	Experience from transformer industry

The area of the radiator surfaces can be estimated by the Newton's cooling law, as given in Equation 3-1 [92].

$$A = \frac{P}{h_{air}(T_w - T_{amb})} \qquad \text{Equation 3-1}$$

where A is the radiator surface area (m^2), P is the heat injection from the winding assembly (W), h_{air} is for the air heat transfer coefficient $(W/(m^2K))$, T_w is for the average radiator surface temperature (°C), T_{amb} is for the ambient temperature (°C).

For all the investigated experimental conditions, P is changed from 200 W to 1400 W, h_{air} is in the range from 3 $W/(m^2K)$ to 7 $W/(m^2K)$ [93], T_w is varied from 40 °C to 70 °C, and T_{amb} is set as 20 °C. In the calculations by using Equation 3-1, it should be noted that the higher T_w is, the higher h_{air} should be applied. According to the ranges of all above parameters, the surface area of the radiator for the experimental setup is estimated in the range from 3 to 4 m^2. In addition, a preliminary study by using a 3D CFD simulation was carried out to help select the radiator. The CFD simulation results indicated that a 4-panel 1-meter-high radiator would satisfy the objectives.

To study the effect of the thermal head of an ONAN/KNAN power transformer, a supporting frame is built to lift the radiator up and down. The schematic diagram and a photo of the supporting frame are shown in Figure 3-5 (a) and (b), respectively. The geometry is designed in the way that clear pathways for air to flow through the structure with the least obstruction, and hence minimize the restrictions of airflow.

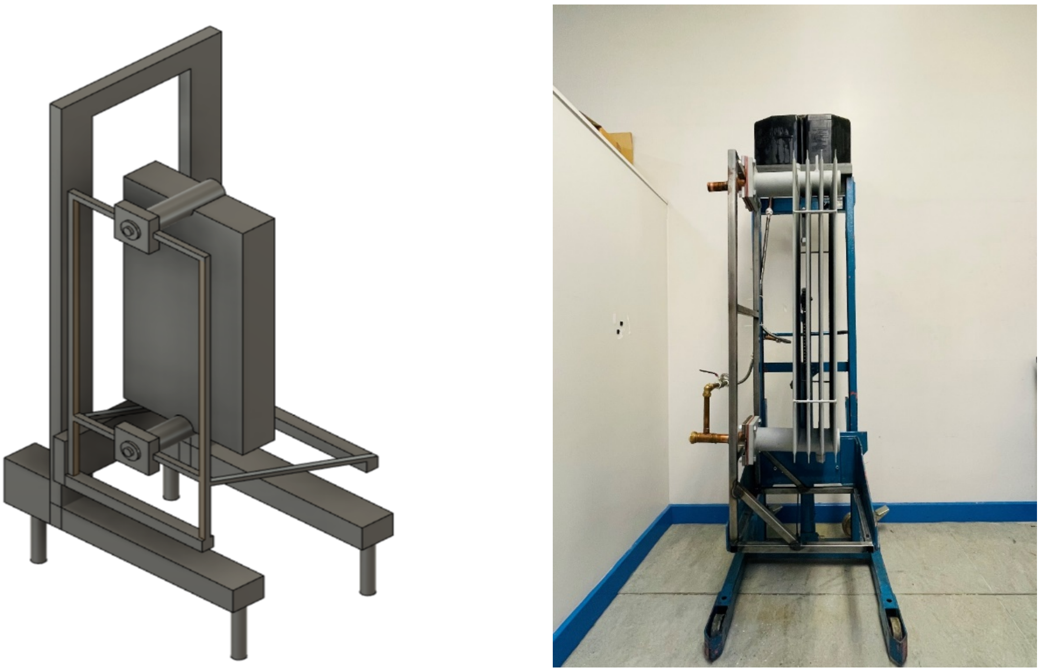

(a) (b)

Figure 3-5 Radiator supporting frame (a) a 3D drawing (b) a photo

3.1.3 Temperature Measurement System

The temperature measurements in the CCL experiments can be categorized into four groups: winding temperatures, liquid temperatures, ambient temperatures and radiator surface temperatures. The winding, liquid and ambient temperatures are measured by the Resistance Temperature Detectors (RTD), i.e., PT 100 sensors (4-wire connection), which measure the temperatures by sensing the resistance change of the platinum. The radiator surface temperature is measured by an infrared thermometer, i.e., FLUKE 568. The accuracy of the RTD sensor is $\pm(0.15 + 0.2\%)$ ℃. According to the temperature range of each category, the accuracy and the number of sensors for each kind of the measurement are summarized in Table 3-2.

Table 3-2 Measurement objects and sensor accuracy

Measurement objects	No. of sensors	Accuracy
Winding temperature	120 RTD sensors	±0.40 °C
Liquid temperature	4 RTD sensors	±0.35 °C
Ambient temperature	4 RTD sensors	±0.15 °C
Radiator surface temperature	Infrared thermometer	±0.8 °C

3.1.3.1 Temperature Sensor Stability

Before conducting the experiments, the stability of all 128 RTD sensors are tested by using a water bath. The stability tests are conducted three times with different temperatures, as the 60 °C, the 75 °C and the 90 °C.

In each stability test, after the temperature of the water bath stabilises, all the 128 RTD sensors are immersed in the water at the same location. Each sensor takes measurements 20 times, with a time interval of 2 minutes.

The results of the stability test under 75 °C is taken as an example. The average values of 20 measurements of individual sensors are plotted in Figure 3-6. The error bar represents the span of all 20 readings of a sensor. As observed in the figure, the measurements of all 128 sensors is around 75 °C, and the maximum spread of RTD measurements of individual sensors is less 0.4 °C. The same results are also observed in the stability tests under 60 °C and the 90 °C.

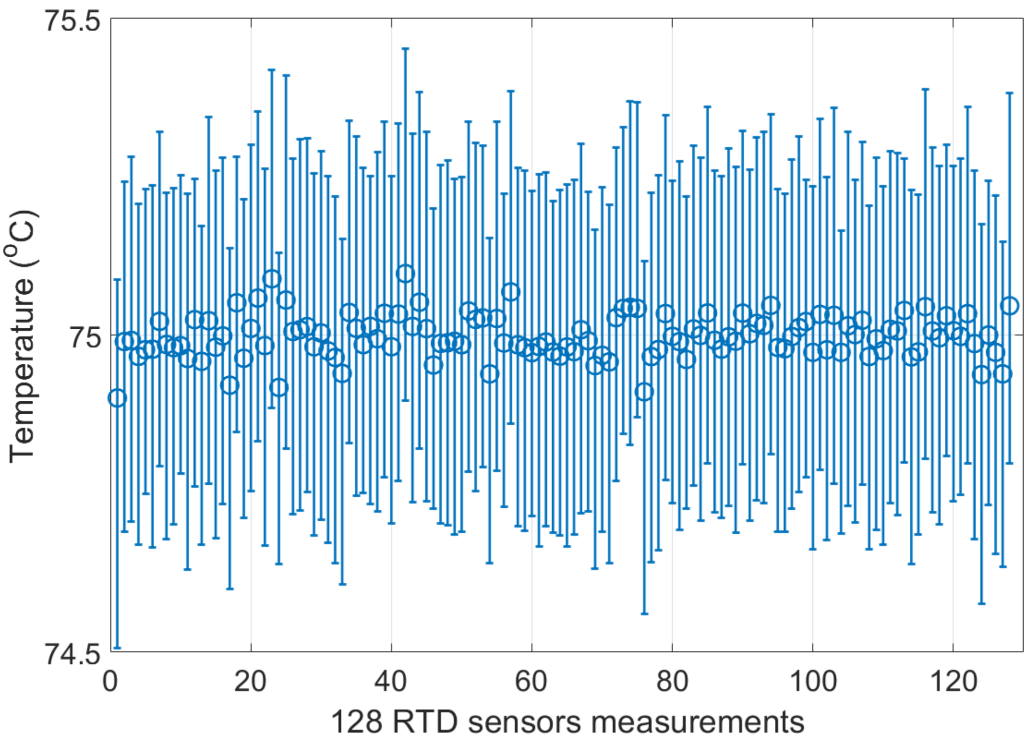

Figure 3-6 RTD sensor stability test under 75 °C

3.1.3.2 Winding and Liquid Temperature Measurements

As introduced in Section 3.1.1, a configuration of the winding assembly is shown in Figure 3-7. The winding temperature is measured by a RTD sensor in each aluminium bar.

Since there are 30 modularised winding discs, which include 120 aluminium bars, and hence, 120 RTD sensors are used to measure the winding temperature distribution in total.

The top and bottom liquid temperatures are also measured by the RTD sensors. Two sensors are placed at the middle of buffer zones, with one at the top and the other at the bottom, namely $T_{top-mid}$ and $T_{bot-mid}$, as shown in Figure 3-7. Another two sensors are placed at the inlet and outlet of the winding, shown as $T_{top-outlet}$ and $T_{bot-inlet}$ in Figure 3-7. The average of the two RTD sensor readings in the same buffer zone are considered as the top / bottom liquid temperature, i.e. T_{top} is the average of $T_{top-mid}$ and $T_{top-outlet}$, and T_{bot} is the average of $T_{bot-mid}$ and $T_{bot-inlet}$.

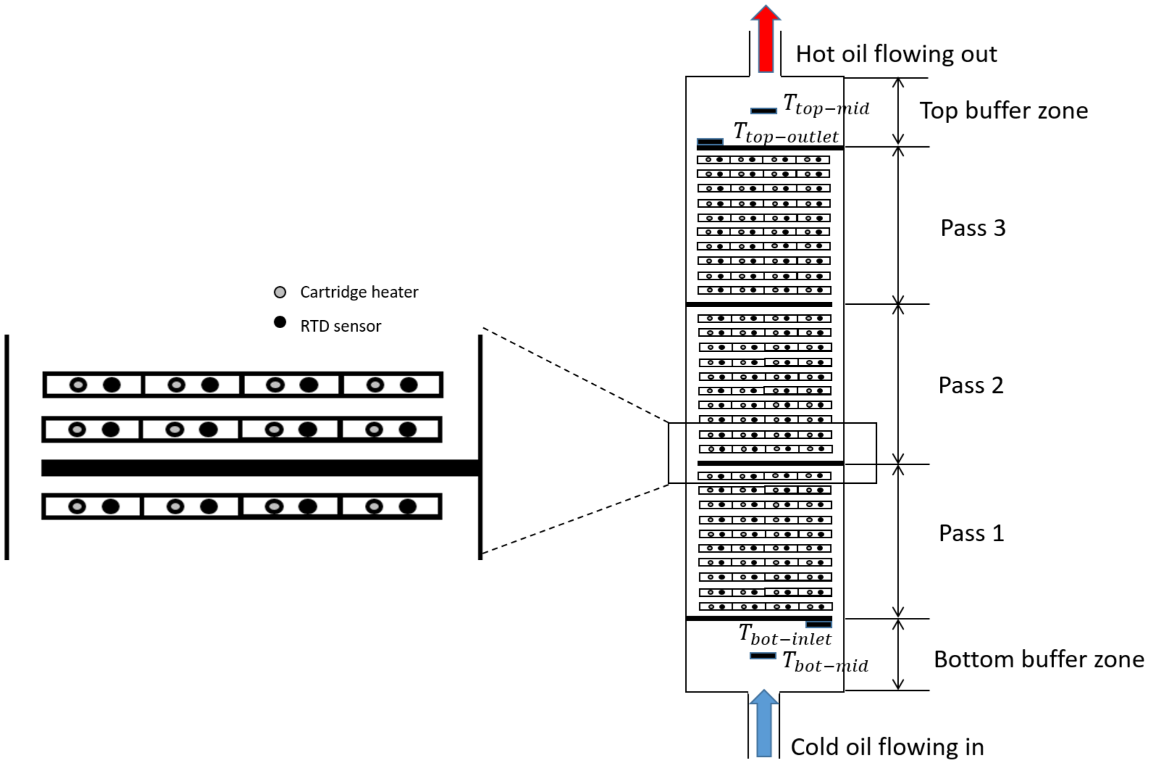

Figure 3-7 Configuration of winding assembly

3.1.3.3 Ambient Temperature Measurement

As addressed in IEC standard 60076-2 [24], the ambient temperature is supposed to be measured by at least 4 sensors. Especially for an air natural (AN) cooled power transformer, the sensor should be placed at 2-meter away to the halfway up to the cooling surfaces. However, due to the limitation of the lab room size, the sensors are placed less than 2 meters away from the radiator surfaces.

The layout of the lab room and the main components of the CCL experimental setup are illustrated in Figure 3-8. The winding and the radiator are placed in the middle of the lab room, and there are four RTD sensors used to measure the ambient temperatures. Three out of four are placed from 1 to 1.3 meter away to the halfway up to the cooling surfaces as shown as red cross in Figure 3-8, namely sensor 1, sensor 2 and sensor 3. The remaining, i.e. sensor 4 shown as the blue cross in Figure 3-8, is placed on the ground right under the radiator.

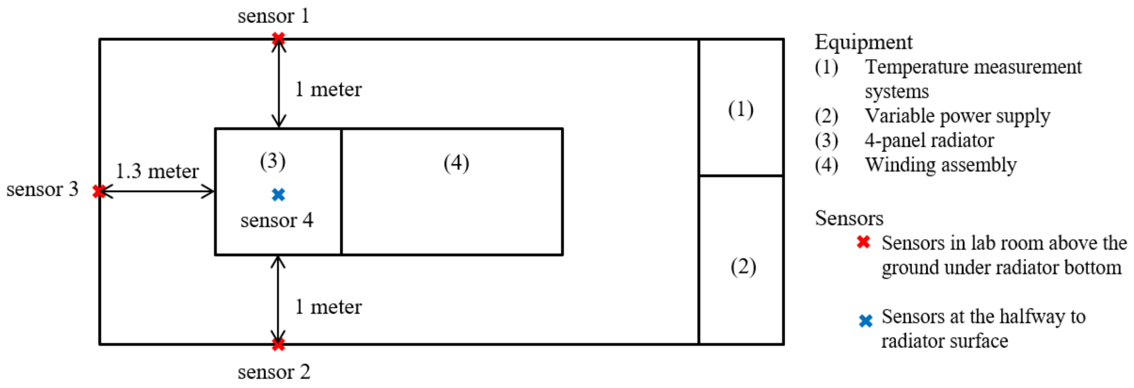

Figure 3-8 Lab room layout

To examine whether the sensors would be influenced by the temperature-rise test, a preliminary test was conducted with the highest power loss. The ambient temperature measurements of the preliminary test are shown in Figure 3-9. The power loss was injected from the first minute, and the winding and liquid temperatures became stable after 240 minutes. It can be seen in Figure 3-9 that the measurements of all four sensors are similar (the difference between the measurements of any two sensors is within 0.4 K), and the changes of the ambient temperature during the temperature-rise test is less than 1 K. Therefore, the sensors placed at the present locations are capable of accurately measuring the ambient temperature, though the distances between the radiator surfaces and sensors are less than 2 meters. The conclusion is also confirmed by the air temperature simulations of the full radiator CFD model, which will be shown in Section 4.2.1.

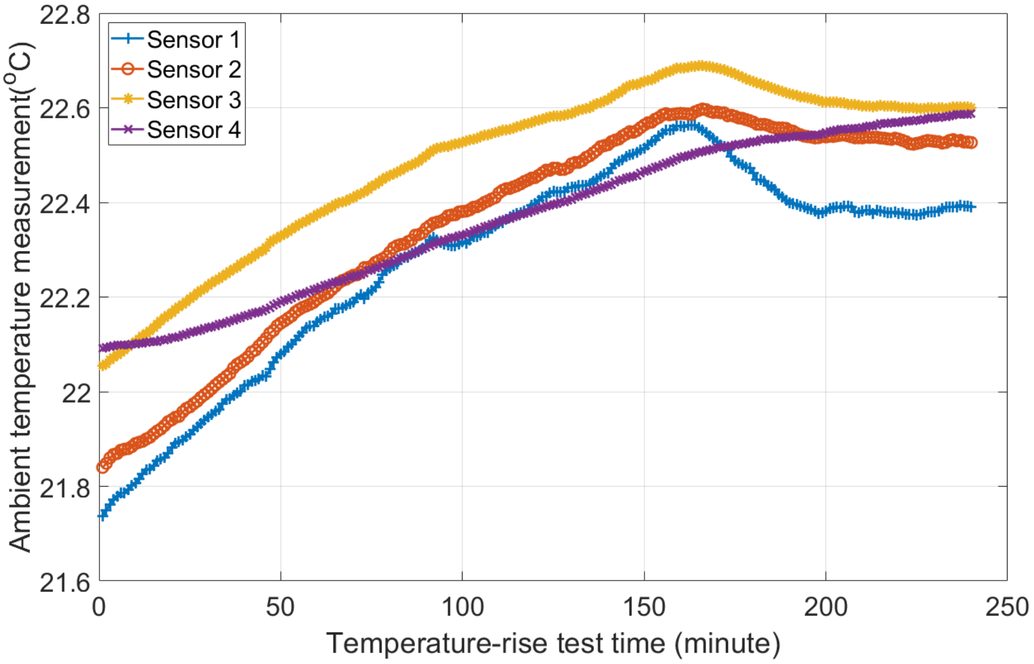

Figure 3-9 Ambient temperature measurements in a preliminary test under the highest power loss

Suggested by the IEC standard 60076-2 [24], the readings of all four RTD sensor are averaged to represent the ambient temperature in the steady-state condition.

3.1.3.4 Radiator Surface Temperature Measurement

To study an ONAN/KNAN cooled transformer, the liquid temperature distribution along the radiator height is of great importance in determining the liquid velocity (or total liquid flow rate). However, the liquid within a radiator cannot be accessed directly, and hence, cannot be measured. Therefore, instead of measuring liquid temperatures, the radiator surface temperatures are measured on two radiator outwards facing surfaces, namely ‘front outwards facing surface’ and ‘back outwards facing surface’ shown in Figure 3-10 (a), by using an infrared thermometer (Fluke 568), with an accuracy of ±0.8 °C in the measurement range from 10 to 80 °C. Each surface is marked with eleven horizontal points at nine different vertical heights from the radiator bottom to the top, i.e., from 0.1 meter to 0.9 meter with an interval of 0.1 meter. The back outwards facing surface is taken as an example to depict the measurement positions, three out of nine vertical heights are shown in Figure 3-10 (b). There are, in total, 198 positions measured.

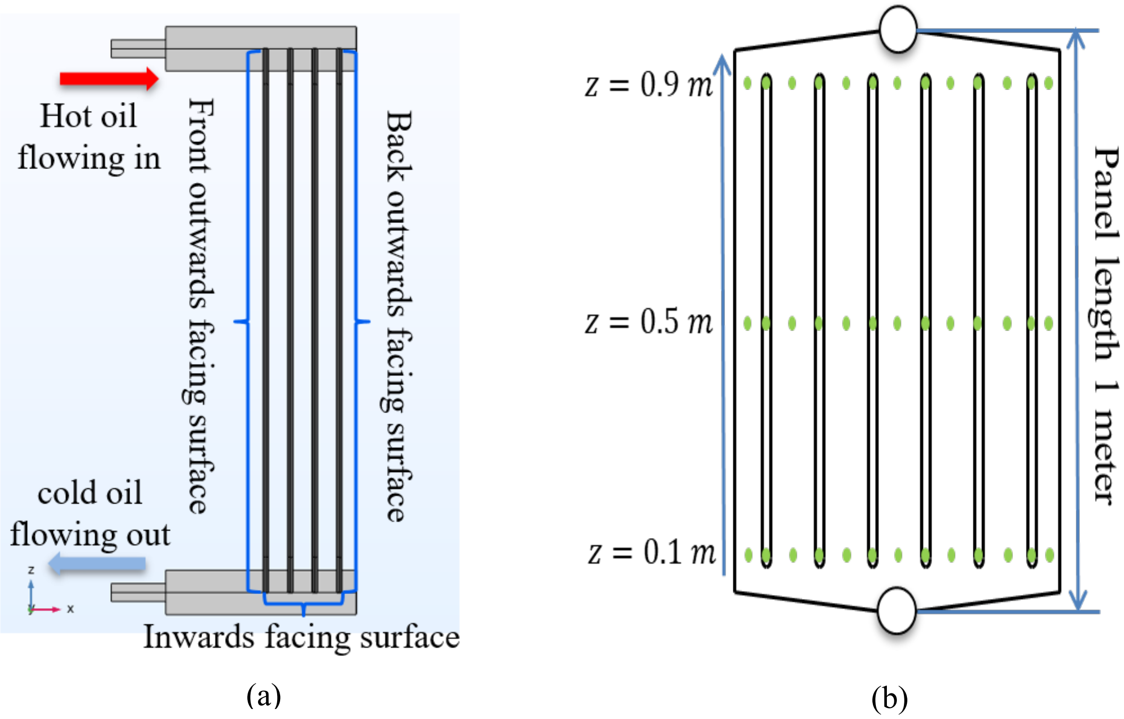

Figure 3-10 Configuration of radiator and measurements on radiator surface (a) Side view of the transformer radiator (b) Radiator surface measurements on outwards facing surface

3.2 Experiment Plan and Procedure

The CCL experimental setup is developed to study the thermal performance of an ONAN/KNAN power transformer under different conditions. In this section, an experimental plan is introduced in terms of all the testing parameters, including the loading condition, the thermal head and the insulating liquids. Moreover, the procedure of a temperature-rise test is also presented in full details.

3.2.1 Experiment Plan

The loading conditions of a power transformer can be represented by the current density in the conductors, which is commonly in the range from 2 to 5 A/mm^2 [19]. Accordingly, the heat flux and the power losses under such current densities are calculated and given in Table 3-3. There are in total seven power injections, i.e. from 200 W to 1400 W, included in the experiments to simulate the loading condition of from 0.5 p.u. to 1.3 p.u..

Table 3-3 Power injection conditions for complete-cooling loop temperature-rise tests

Current density (A/mm²)	2.0	2.8	3.5	3.9	4.5	4.9	5.3
Heat flux (W/m²)	303	607	910	1213	1517	1820	2123
Power injection (W)	200	400	600	800	1000	1200	1400
Loading condition (p.u.)	0.5	0.7	0.9	1.0	1.1	1.3	1.3

Three thermal heads will be studied in the temperature-rise experiments, as 0.3 m, 0.5 m and 0.7 m. Moreover, three insulating liquids are also investigated in this PhD project, which are mineral oil (Nytro Gemini X), Gas-to-Liquid (Diala S4 ZX-I) and synthetic ester liquid (MIDEL 7131).

With the same thermal head and insulating liquid, seven experiments of different loading conditions are planned. However, for the Gas-to-Liquid and synthetic ester liquid, the experiments under 1400 W power injection with 0.3 m thermal head are not completed, because the hottest temperatures during the two experiments were observed to be more than 125 ℃, which is the Heat Deflection Temperature of the winding enclosure. Therefore, except for those two experiments, in total, there have been 61 sets of experiments conducted in this PhD project.

3.2.2 Experiment Procedure

Prior to the start of the experiments, a leakage-free check needs to be firstly conducted by three steps as follows:

1. Connect individual components by the pipework;
2. Fill the system with the testing liquid from the oil tank at the top;
3. Inject the highest power injection (1400 W), and run for 6 hours.

It is also worth noting that the leakage-free check also helps remove the air bubbles, which is normally generated in the liquid filling process (step 2). During all three steps above, an oil absorbent pad is placed under the experimental setup to help observe any liquid leakage. If no leakages are detected, the experimental setup (connecting pipes and the winding assembly) are then wrapped with the thermal insulation materials as show in Figure 3-11. This ensures that most of the heat is dissipated by the transformer radiator, and only a negligible proportion of heat can be dissipated by the other components. Such design benefits the verification of modelling work in the next chapters.

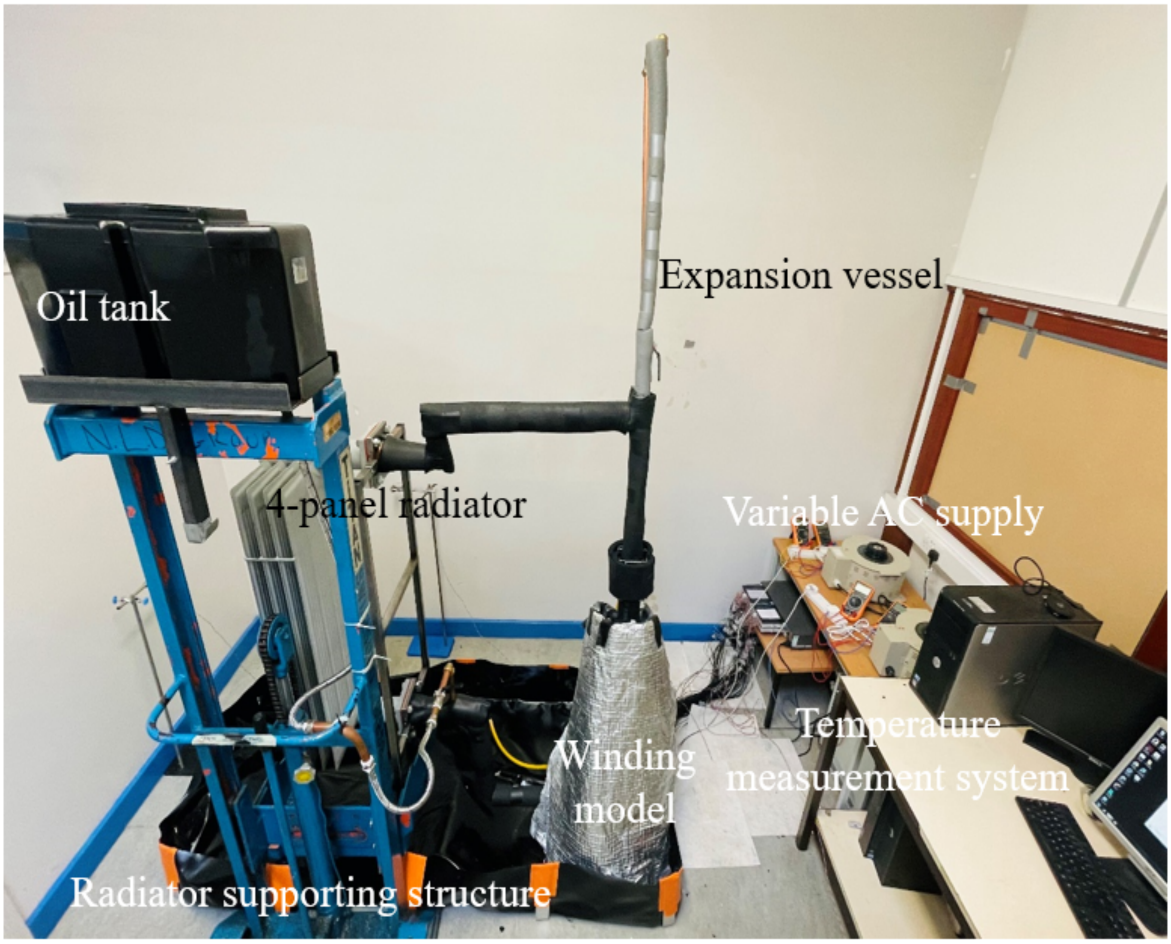

Figure 3-11 Experimental setup wrapped with thermal insulation material

Next, the temperature-rise test is conducted as the follows:

- Turn the temperature measurement system on, and check all 128 RTD sensors;
- Inject the power losses from the variable AC supply, record the power injection by the digital multimeters;
- Record the winding, liquid and ambient temperatures using a multiplexer ‘Keithley T 3700AS-901-01D’, and each sensor is recorded every minute;
- Monitor the winding and liquid temperatures. If the system reaches the steady-steady condition (the temperature changes within 1 hour are less 1 K), then the radiator surface temperature is measured by an infrared thermometer (Fluke 568);
- Measure radiator surface temperatures on two outwards facing surfaces three times, with the time interval between two measurements is 10 minutes;

- After the surface temperature measurements are taken, turn the power off.

To ensure that no mixture of insulating liquids, after all 7 loading conditions are considered, the experiments using other thermal heads need to be conducted first, and then move onto the experiments of different insulating liquids. The procedures are as the following:

- Replace the connecting pipe of the experimental setup by new ones;
- Run the experiment under 1400 W power injection with the next testing insulating liquid for a whole week to thoroughly flush the experimental setup;
- Dispose the flushing liquid;
- Fill the system with the new testing liquid, and repeat the test procedures from the leakage-free check.

It should be noted that the leakage-free check is conducted every time if either the thermal head or the insulating liquid changes.

3.3 Functionality of the CCL Experimental Setup

One set of the experimental measurements, under an 800 W power injection with a 0.5m thermal head and mineral oil coolant, is taken as an example to demonstrate the functionality of the CCL CFD experimental setup.

Firstly, the dynamic temperature measurements are presented, and the data processing technique to obtain the temperature in the steady-state conditions is introduced. Next, the winding and radiator surface temperature distributions are measured, followed by the liquid temperatures and its velocity calculation.

3.3.1 Steady-State Condition

The dynamic temperature profiles of the example condition are depicted in Figure 3-12 (a), where the winding, liquid and ambient temperatures are measured by 128 RTD sensors. The key parameters in the temperature-rise test are the hot-spot temperature, top and bottom liquid temperatures, whose dynamic temperature profiles are shown in Figure 3-12 (b). The top liquid temperature increases faster than the bottom liquid temperature from the beginning of the temperature-rise test until the thermosyphonic liquid flow is fully established.

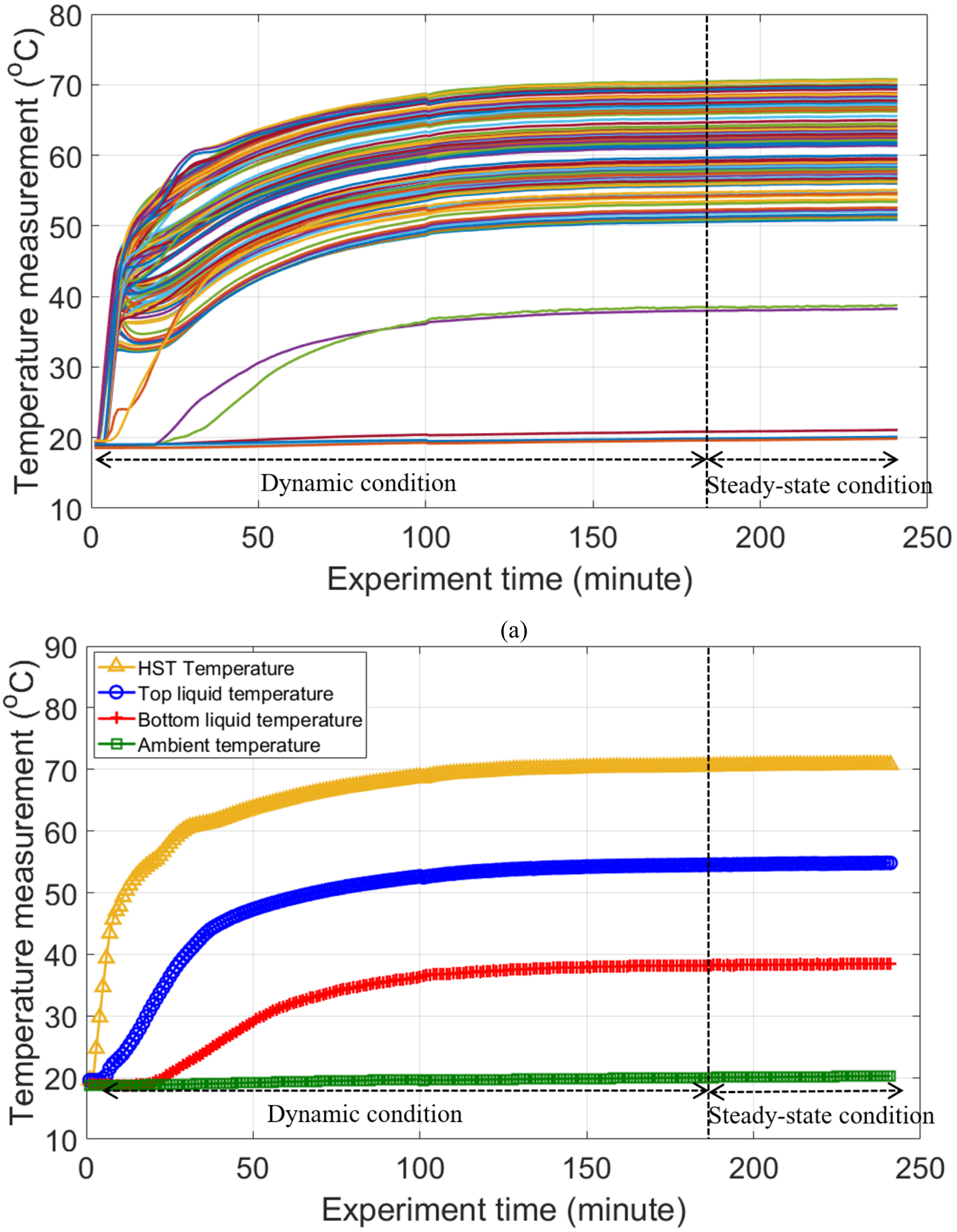

(a)

(b)

Figure 3-12 Temperature measurements in the temperature-rise test under example condition (a) all RTD sensors (b) key temperatures

According to IEC60076-2 [24], the criterion of the steady-state condition is that the temperature change within 1 hour is less than 1 K. Therefore, in each temperature-rise test, the temperature measurements of all sensors have been checked to ensure that the temperature fluctuation in the last hour is within 1 K. The measurements of each sensor in the last one hour are averaged to represent its temperature in the steady-state condition.

3.3.2 Winding Temperature Distribution

In the disc-type winding assembly introduced in Section 3.1.1, each modularised winding disc consists of 4 bars, named from ‘bar 1’ to ‘bar 4’ along the nominal liquid flow direction. The winding discs are named from disc 1 to 30 from the lowest disc at pass 1 to the topmost disc at pass 3. The complete temperature profile of the winding, consisting of all the temperature measurements of 120 aluminium bars in the steady-state condition, is shown in Figure 3-13 under the example testing condition.

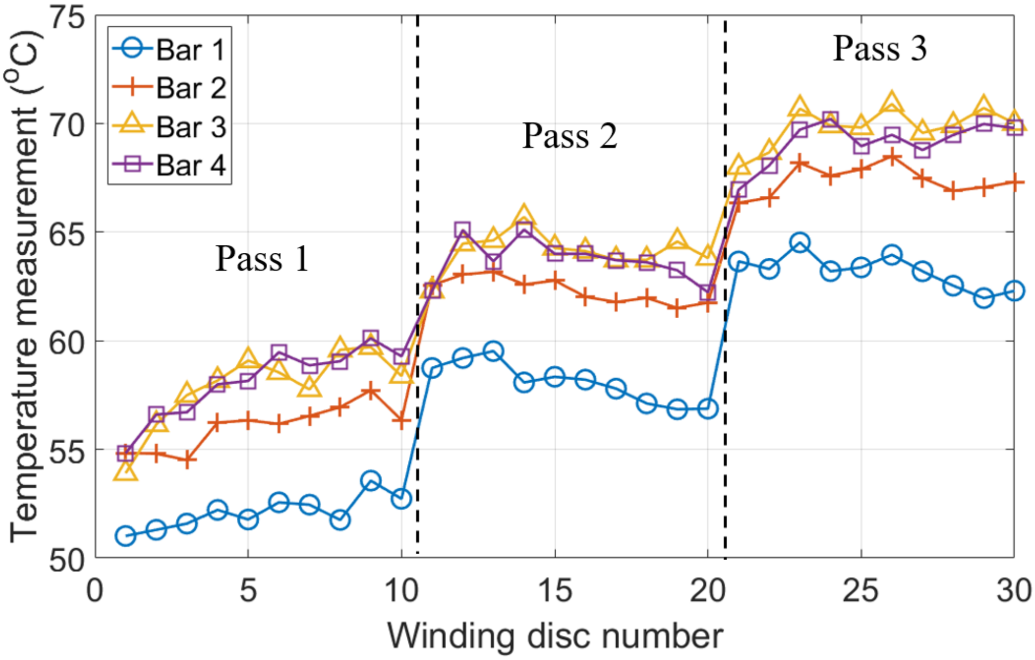

Figure 3-13 Winding temperature profile under example condition

The winding temperature distribution in each winding disc helps understand the localised liquid flow phenomena, especially for the reverse flow condition. A decreasing trend of temperature distribution from ‘Bar 1’ to ‘Bar 4’ in a winding disc indicates the presence of the reverse flow in the corresponding horizontal duct, whereas an increase of temperature concerning the winding disc number indicates the expected nominal liquid flow.

Moreover, the mean and maximum temperature of the 4 bars in one winding disc, have been shown in Figure 3-14, which facilitates the understanding of the overall liquid flow distribution and the hot-spot location under different conditions.

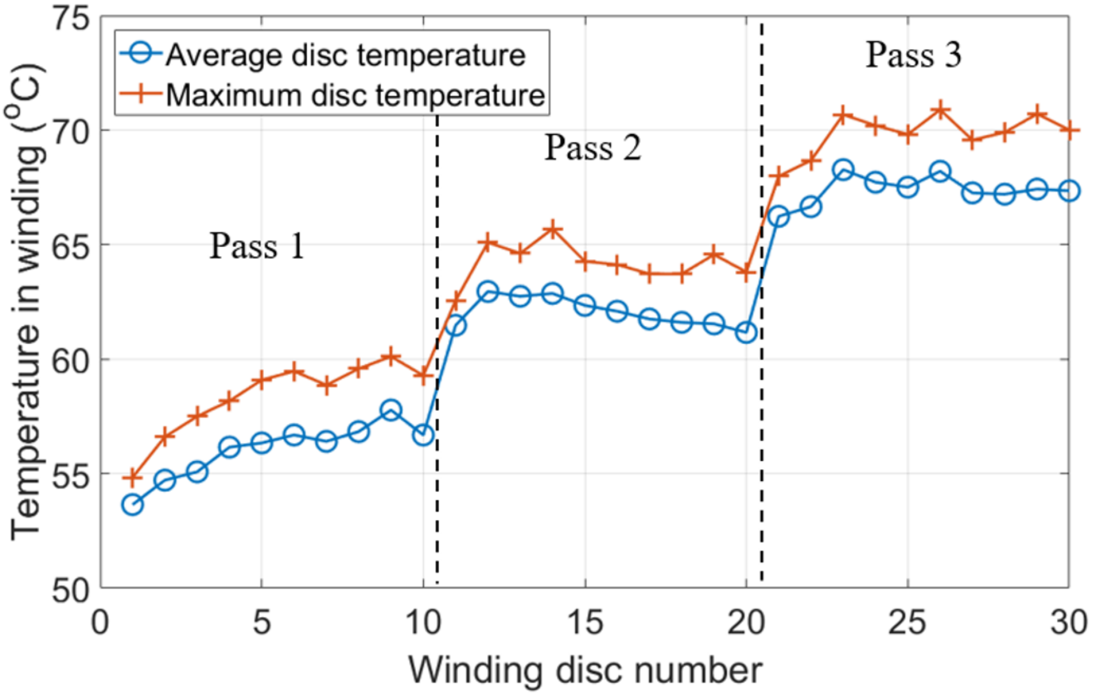

Figure 3-14 Winding temperature profile under example condition

3.3.3 Liquid Temperature and Velocity

As previously introduced, the top and bottom liquid temperatures are measured by four RTD sensors placed in the buffer zones. Two sensors ($T_{top-outlet}$ and $T_{top-mid}$) are placed in the top buffer zone for top liquid temperature measurements; the other two ($T_{bot-inlet}$ and $T_{bot-mid}$) are placed in the bottom buffer zone to measure the bottom liquid temperature. The average of the two RTD sensor readings in the same buffer zone are used to represent the top / bottom liquid temperature. The top and bottom liquid temperatures under the example condition are given in Table 3-4.

Table 3-4 Top and bottom liquid temperature measurements under the example condition

Power injection	Top liquid temperature			Bottom liquid temperature		
	$T_{top-outlet}$ (°C)	$T_{top-mid}$ (°C)	T_{top} (°C)	$T_{bot-inlet}$ (°C)	$T_{bot-mid}$ (°C)	T_{bot} (°C)
800 (W)	55.2	54.7	55.0	38.4	38.9	38.5

The liquid velocity, as well as the total liquid flow rate, is important to study the thermal behaviour of an ONAN/KNAN transformer, in particular when comparing the effect of different insulating liquids. However, there has been a lack of commercial flow meter that can not only accurately measure the flow rate in a range between 1×10^{-5} to 5×10^{-5} m^3/s, but also have a negligible influence on the pressure drop during the experiments. Therefore, the total liquid flow rate at the radiator top is determined from the temperature measurements via the liquid energy conservation Equation 3-2. The liquid velocity at the winding inlet can be also calculated from Equation 3-3.

$$Q_{oil-top} = \frac{P}{\left(T_{top} - T_{bot}\right) C_p \rho_{top}} \qquad \text{Equation 3-2}$$

$$\mathrm{v}_{oil} = \frac{P}{\left(T_{top} - T_{bot}\right) C_p \rho_{bot} A_{bot}} \qquad \text{Equation 3-3}$$

where $Q_{oil-top}$ is the total liquid flow rate (m^3/s), P is the power injection in the temperature-rise test (W), T_{top} is the top liquid temperature (°C), T_{bot} is the bottom liquid temperature (°C). C_p is the specific heat capacity ($J/(kg \cdot K)$), and ρ_{top} and ρ_{bot} are the liquid density (kg/m^3) at the radiator top and winding inlet, respectively. The reference temperature of the C_p and ρ is the average liquid temperature ($(T_{top} + T_{bot})/2$). v_{oil} is the liquid velocity at the winding inlet (m/s), and A_{bot} is the liquid inlet surface area at the winding bottom (m^2).

The total liquid flow rate is commonly used in the study the radiator, as input in the radiator models in Chapter 4 and 5. As for the CCL or winding only CFD simulations, the liquid velocity is preferred, which will be discussed in Chapter 6 and 7.

3.3.4 Radiator Temperature Measurements

The radiator surface temperature measurements under the example condition are plotted in Figure 3-15. All the 198 points on outwards facing surfaces, i.e. radiator front and back outwards facing surfaces, are shown in Figure 3-15 (a) and Figure 3-15 (b), respectively. The error bar represents the standard deviation among three sets of measurements. The maximum value of the error bars under the example condition is 0.6 K.

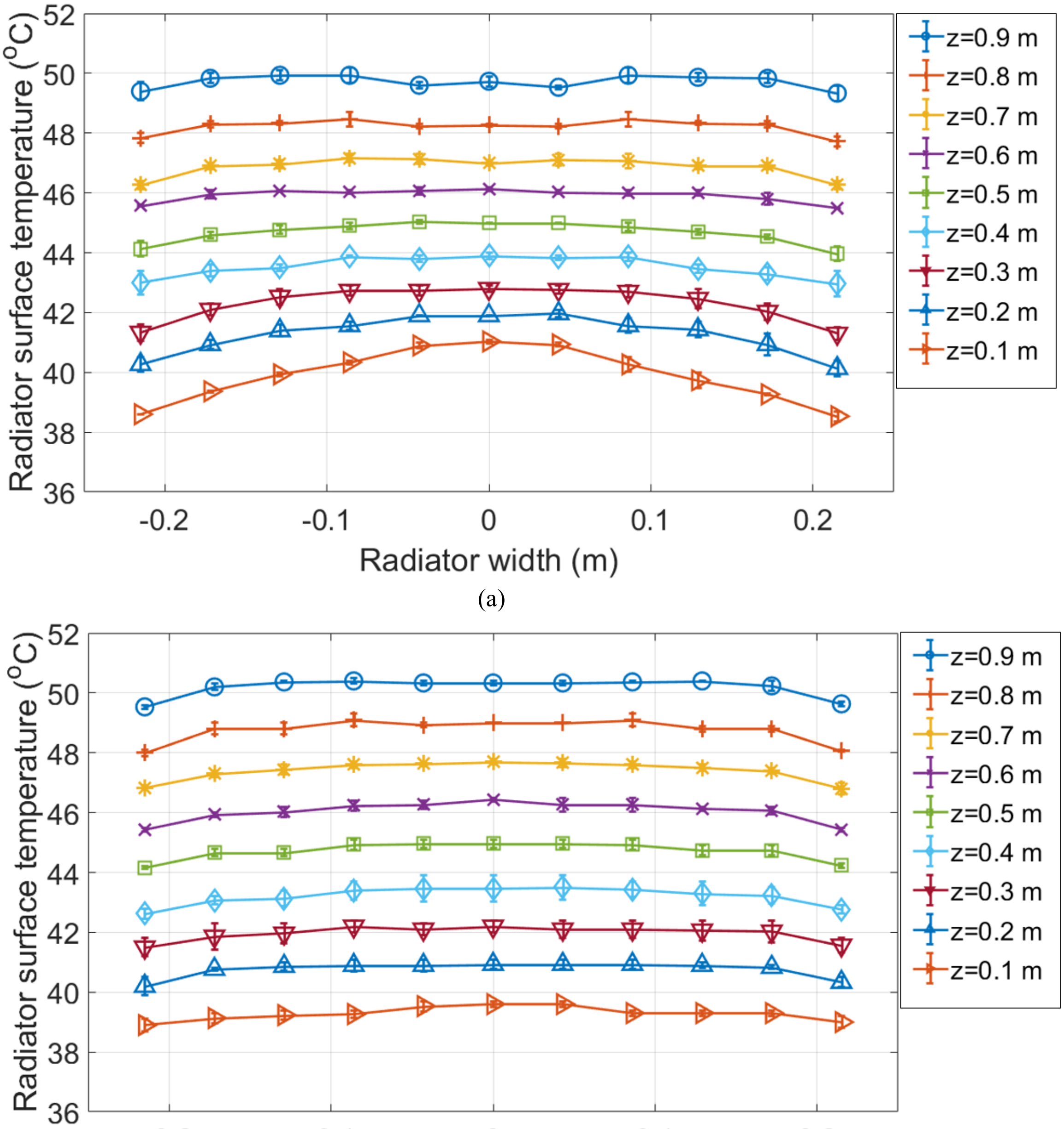

(a)

(b)

Figure 3-15 Radiator surface temperature measurement under example condition (a) front outwards facing surface (b) back outwards facing surface

The radiator surface temperature measurements at the same vertical height can be averaged to represent the liquid temperature distribution. Such distribution helps understand and estimate the liquid velocity (or total liquid flow rate) of an ONAN/KNAN cooled transformer. The surface temperature distribution along the vertical direction of the example condition is shown in Figure 3-16, where the surface temperature is approximately in a linear relationship with the radiator vertical height.

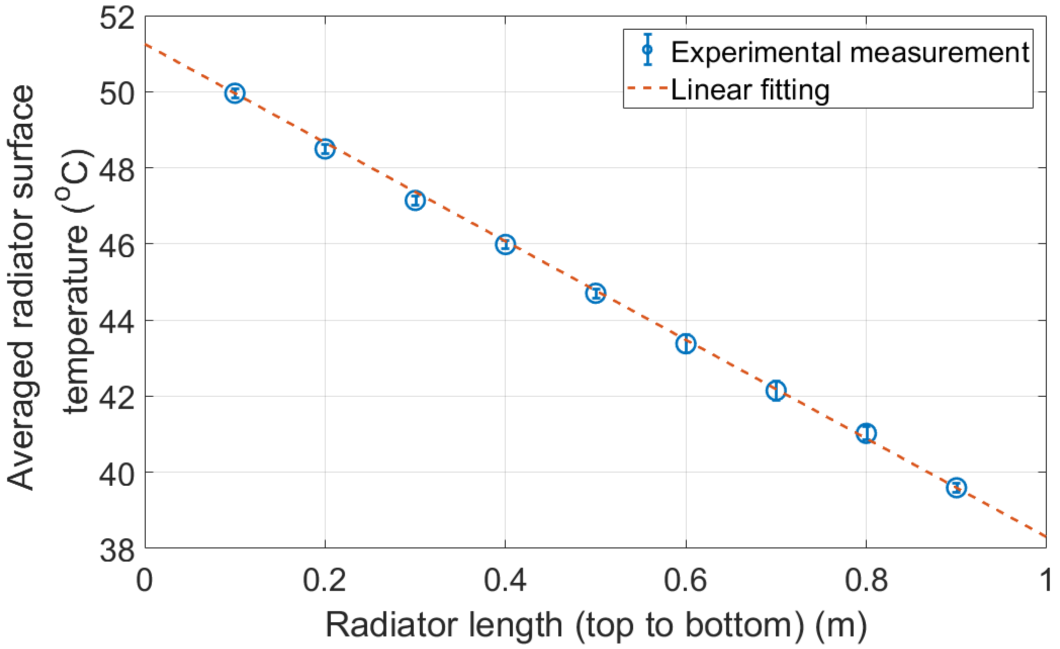

Figure 3-16 Radiator surface temperature distribution along the radiator height under example condition

3.4 Repeatability Tests

Three repeatability tests were conducted under an 800 W power injection with thermal head of 0.5 m and coolant as a mineral oil on three different days.

The measured ambient temperatures in three tests were found varied slightly. Therefore, the temperature rises over ambient temperature ($\Delta T = T - T_{amb}$) are used in the comparison instead of the absolute temperature measurements. The liquid temperature rises over ambient temperature (ΔT_{top} and ΔT_{bot}), total liquid flow rate at the radiator top and the liquid flow velocity at the winding inlet in the repeatability tests are summarized in Table 3-5.

Table 3-5 liquid temperature rise, total liquid flow rate and liquid flow velocity in three repeatability tests

Test No.	$P\ (W)$	T_{amb} (°C)	$\Delta T_{top}\ (K)$	$\Delta T_{bot}\ (K)$	$Q_{oil-top}\ (m^3/s)$	$v_{oil}\ (m/s)$
Test 1	805	21.0	34.5	18.2	3.2×10^{-5}	0.035
Test 2	800	20.4	34.6	18.3	3.2×10^{-5}	0.035
Test 3	813	22.5	34.6	18.4	3.2×10^{-5}	0.036

As seen in the table, variations of liquid temperature rise among three individual tests are less than 0.2 K. The calculated liquid flow rate is exactly the same, and the relative differences of the liquid velocity are less than 2.8% in the repeatability tests.

The winding and radiator surface temperature distributions are also compared in the repeatability tests. Figure 3-17 shows the maximum winding temperature rises in each disc, and the maximum difference of the temperature rise of each disc among three tests is less than 0.4 K. The average radiator surface temperature distribution along radiator height is show in Figure 3-18, where the changes of temperature rise at the same height are within 0.8 K.

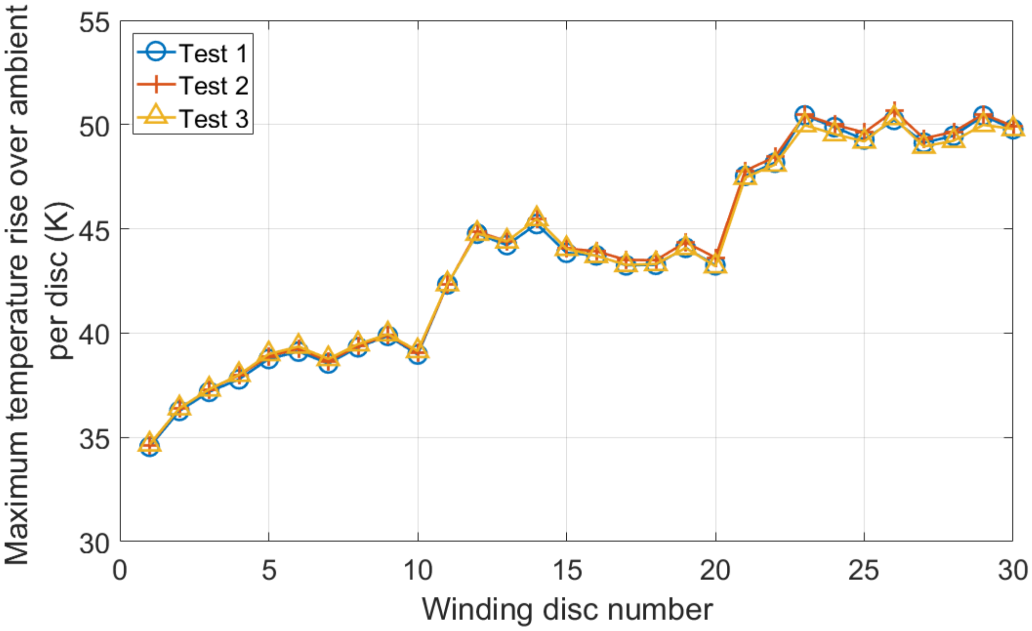

Figure 3-17 Maximum winding temperature in each winding disc of repeatability tests

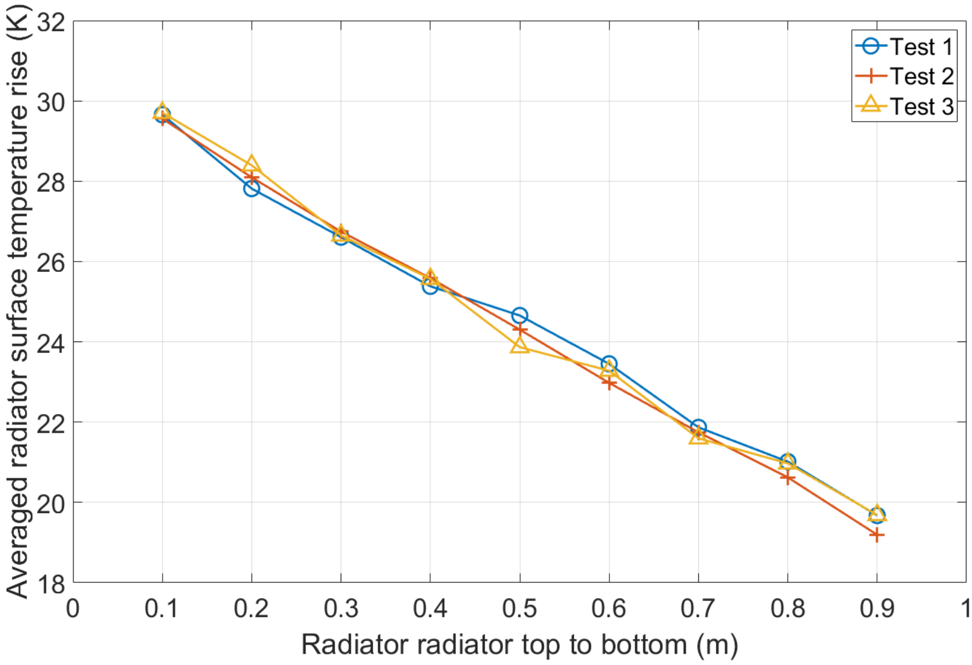

Figure 3-18 Radiator surface temperature distribution along the radiator height of repeatability tests

From the results shown in Table 3-5, Figure 3-17 and Figure 3-18, it can be concluded that the temperature measurements of the CCL experimental setup are repeatable and reliable.

3.5 Summary

A CCL experimental setup has been developed to investigate the thermal behaviour of a liquid-immersed power transformer in an ONAN/KNAN cooling mode. The CCL experimental setup includes a section of the transformer winding, a 4-panel 1-meter radiator and a temperature measurement system. In the temperature-rise experiment, the winding, liquid and ambient temperatures are measured and recorded by 128 RTD sensors from a cold start to the steady-state condition. The temperature of each RTD sensor is recorded every minute. The radiator surface temperature is measured by 198 positions three times under the steady-state condition.

In total, 61 sets of experiments are designed, and loading conditions, thermal head and insulating liquid materials are all considered. One set of the experimental measurements is used to illustrate the data processing procedure, and the winding, liquid, and radiator surface temperatures under the steady-state condition are presented. Among three repeatability tests, the changes of the liquid, winding and radiator surface temperature measurements are less than 0.2 K, 0.4 K and 0.8 K; the differences of the total liquid flow rate at the radiator top and flow velocities at the winding inlet are within 2.8%.

Chapter 4 A Full Radiator CFD Model and its Experimental Verification

As indicated in the literature review, the main limitation of the present CCL CFD model is resulted from the radiator modelling. The liquid temperature in the radiator determines the thermosiphon pressure in the CCL, and thus, an accurate calculation of it can contribute to a reliable estimation of the liquid velocity (or total liquid flow rate) within the CCL. However, there has been a lack of accurately verified radiator CFD models in the published work.

Therefore, this chapter focuses on the establishment of a full radiator CFD model and its experimental verification. The heat transfer processes are reviewed and carefully studied, and the development of a full radiator CFD model considering all the heat transfer mechanisms and cooling media is presented in Section 4.1. Subsequently, in Section 4.2, the data processing strategy and the full radiator CFD simulation results are shown. Next, the experimental verification of the full radiator CFD simulation is focused in Section 4.3 in terms of global parameters and the surface temperature distributions.

4.1 Full Radiator CFD Model including Air Domain

Three heat transfer mechanisms, conduction, convection, and radiation are involved in heat dissipation process of transformer radiators. The conduction occurs in the radiator wall, where the three-dimensional thermal conduction was suggested in [94]. The convection exists in both the internal hot insulating liquid and the external cooling air. The radiation can mostly be found on the outwards facing surfaces, as discovered in [85]. All three heat transfer mechanisms and the cooling media are considered and included in the full radiator CFD model.

4.1.1 Model Geometry

The model geometry is based on the 4-panel 1-meter-high transformer radiator introduced in the Section 3.1.2. The radiator consists of top and bottom header pipes, as well as four 1-meter-high panels. The configuration and geometry of the radiator in the CFD model is shown in Figure 4-1.

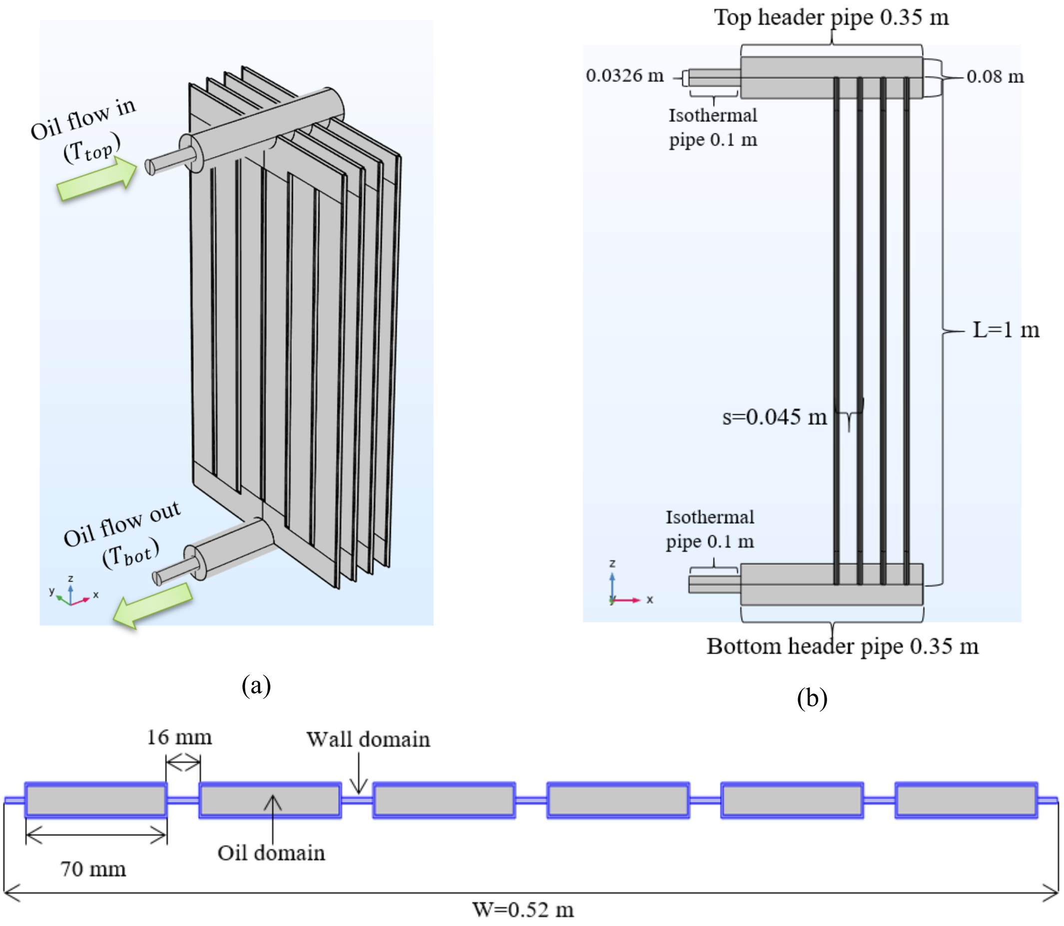

(a)

(b)

(c)

Figure 4-1 Radiator CFD model geometry (a) 3D radiator CFD model (b) Side view of radiator CFD model (c) Cross-sectional view of middle of the radiator (oil domain in grey, wall domain in blue)

The inputs of radiator CFD simulations include the top liquid temperature (T_{top}) and the liquid flow rate at the radiator top ($Q_{oil-top}$) of the insulating liquid domain. The profiles of the input liquid temperature and the flow rate affect the simulation results. As shown in the experimental setup in Figure 3-1, the connecting pipework has a smaller diameter than the top header pipe, as 0.0326 m and 0.08 m, respectively. Therefore, the temperature and the flow distributions at the beginning of top header pipe are neither fully developed nor uniform. To reflect the true boundary conditions of the insulating liquid domain, a section of connection pipe is added and modelled as isothermal pipes as shown in Figure 4-1 (b).

According to experimental conditions investigated in this chapter, the Reynolds number (R_e) is in the range from 51.2 to 479.1, under which conditions, the insulating liquid flow is in the laminar flow regime. And the entrance length of the liquid flow can be calculated by [92]:

$$L_h = 0.05R_eD \qquad \text{Equation 4-1}$$

where L_h is the entrance length of the insulating liquid (m), R_e is the Reynolds number, D is for the characteristic length of the connecting pipe (m).

Hence, considering the investigated conditions, L_h is calculated to be from 0.08 to 0.78 m. Therefore, the liquid flow would be fully developed after an entrance length of 0.78 m. The total length of the isothermal pipe connecting to the radiator top is 1.3 m, and hence, the fully developed flow can be assumed as long as the length of the isothermal pipe in the radiator CFD model is less than 0.52 m (1.3 m – 0.78 m). In this case, a 0.1 m long isothermal pipe is added in the model as show in Figure 4-1 (b). The liquid flow and temperature profiles are set as a fully developed flow.

It should also be noted that the oil channel of the radiator is simplified as the rectangular shape, as depicted in Figure 4-1 (c). The key geometric characteristics, i.e., surface area and oil volume per panel, in the radiator CFD model are matched within 0.5% difference to the radiator specification as given in Table 4-1. Moreover, the simplification of the oil channel shape is validated by additional CFD simulations. The CFD simulations of the rectangular oil channel are compared with the simulations of a more realistic design. The simulation results indicate a negligible difference in the key parameters, i.e., bottom liquid temperature and total heat dissipation. The CFD models of a different oil channel geometry and their simulation results are presented in the Appendix-1.

Table 4-1 Main geometric characteristics of 4-panel radiator and its CFD models

Geometric characteristics (per panel)	Manufacture datasheet	Radiator CFD model
Surface area (m^2)	1.12	1.13
Liquid volume (l)	3.44	3.45

4.1.2 Model Setup

As introduced, there are three processes, i.e., conduction, convection, and radiation, involved in the heat transfer within a transformer radiator. The hot insulating liquid flows from the radiator top to bottom transferring the heat to the radiator wall by conduction and convection. The wall then dissipates the heat to the ambient environment by the conduction, air convection and radiation.

To simplify the radiator CFD simulation, the conduction in the radiator wall was often neglected [80, 89]. This is because the thickness of a radiator steel wall is only 1 mm. To take the thermal conduction in the 1 mm radiator steel wall into consideration, the minimum mesh size in the CFD model will be less than 1 mm, and consequently, total mesh elements in the CFD model would greatly increase, as well as the calculating time. However, in a previous our study [94], the CFD simulations of different transformer radiator designs have confirmed that the thermal conduction in the radiator steel wall can contribute as much as 8% to 10% of the overall heat dissipation under different loading conditions. Therefore, the thermal conduction in the radiator steel wall is considered in this radiator CFD modelling. The thermal conduction in the radiator wall is simulated by Fourier's law of conduction, Equation 4-2 [95].

$$q_{cond}'' = k \frac{\nabla T}{\Delta x} \qquad \text{Equation 4-2}$$

where q_{cond}'' is the heat flux density through the radiator steel wall (W/m^2), ∇T is the temperature gradient due to the thermal conduction (K), and k is the thermal conductivity ($W/(m \cdot K)$), Δx is the wall thickness (m).

The convection effects are found in the insulating liquid and cooling air, both of which are simulated by the detailed flow and temperature distributions in the full radiator CFD simulations. The insulating liquid was modelled as a laminar flow under ON/KN cooling mode in [65, 80]. Due to the small size of the 4-panel 1-meter-high transformer radiator, the air flow is also simulated as a laminar flow which is different to the CFD simulations in the literature [80, 83], where the air around a 40-panel 3.3-meter-high radiator was considered as a turbulent flow in [83] and the air surrounding a 26-panel 1.8-meter-high radiator was simulated by the large eddy turbulent flow in [80].

The determination of an air flow regime in the natural cooling is dependent on the Rayleigh number (R_a), as documented in [92, 93]. There are two types of surfaces of a transformer radiator, i.e., outwards and inwards facing surfaces, as seen in Figure 3-10. The air on the outwards facing surfaces is heated up only by one vertical surface, whereas the air flowing between the inwards facing surfaces is heated by two parallel surfaces. Therefore, the calculations of the Rayleigh number (R_a) for the outwards and inwards facing surfaces are different, as given by Equation 4-3 and Equation 4-4, respectively. Reported in [92], the flow would be in a laminar flow regime if the Rayleigh number for outwards facing surface (Ra_L) is less than 10^9; as for the inwards facing surface, the flow is a laminar flow once Rayleigh number for inwards facing surface (Ra_s) is within 10^6.

$$Ra_L = \frac{g\beta_{air}(T_w - T_{amb}) \cdot L^3}{{\nu_{air}}^2} Pr \qquad \text{Equation 4-3}$$

$$Ra_S = \frac{g\beta_{air}(T_w - T_{amb}) \cdot S^3}{{\nu_{air}}^2} Pr \qquad \text{Equation 4-4}$$

where Ra_L is the Rayleigh number of radiator outwards facing surfaces, L is the radiator length (m), Pr is the Prandtl number, g is the gravity accelerator vector (m/s^2), β_{air} is the thermal expansion coefficient of air ($1/K$), T_w is the radiator average surface temperature (K), T_{amb} is the ambient temperature (K), ν_{air} is the kinematic viscosity of air (m^2/s), Ra_S is for the Rayleigh number of radiator inwards facing surfaces, S is the characteristic length of radiator inwards facing surfaces (m).

To determine the flow regime of the air around the 4-panel 1-meter-high transformer radiator, Ra_L and Ra_S are calculated in the ambient temperature (T_{amb}) varying from 0 to 40 °C, and the surface temperature of radiator wall (T_w) ranging between 45 and 60 °C. All the material properties of air in Equation 4-3 and Equation 4-4 are calculated by the film temperature (T_f), which is calculated as the average temperature of surface temperature of radiator wall (T_w) and ambient temperature (T_{amb}).

The ranges of the Rayleigh number of outwards and inwards facing surface (Ra_L and Ra_s) of above conditions are shown in Figure 4-2 (a) and (b), respectively. In Figure 4-2 (a), the Rayleigh number of the outwards facing surface (Ra_L) is lower than 10^9 only when the ambient temperature is as high as 40 °C and the surface temperature is more than 55 °C. For the rest scenarios in which Ra_L is over 10^9, the air flow near outwards facing surfaces is likely to be a turbulent flow. However, the Rayleigh number of inwards facing surface (Ra_S) is lower than 10^6 in all scenarios, which indicates that air flow between inwards facing surfaces should be modelled as a laminar flow. In the 4-panel radiator, there are 6 inwards facing surfaces out of total 8 surfaces. Therefore, the dominating air flow around the 4-panel 1-meter-high radiator is in the laminar flow regime. The validity of this assumption is experimentally verified in Section 4.3 by the global parameters, as well as surface temperature distributions.

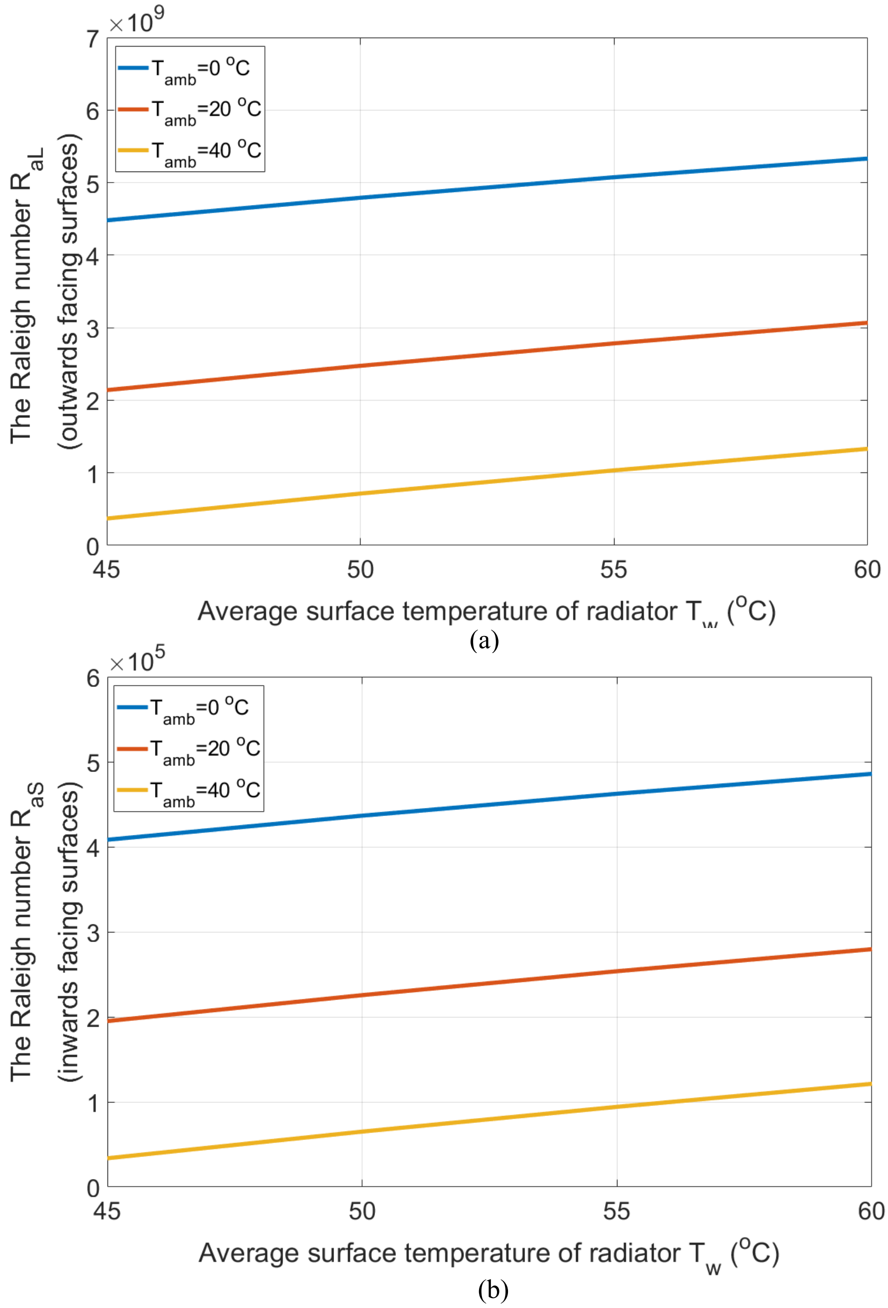

(a)

(b)

Figure 4-2 Rayleigh number (Ra_L and Ra_S) of air around 4-panel 1-meter-high transformer radiator (a) Rayleigh number of outwards facing surface (Ra_L) (b) Rayleigh number of outwards facing surface (Ra_S)

In the light of above, in the full radiator CFD models, the insulating liquid and air flows are both modelled as the laminar flows, and are simulated by conservations of mass, momentum and energy, by Equation 4-5 to Equation 4-7 [92].

$$\rho \cdot \left(\frac{\partial u}{\partial x} + \frac{\partial v}{\partial y} + \frac{\partial w}{\partial z}\right) = 0 \qquad \text{Equation 4-5}$$

$$\left\{\begin{array}{c}\left(u\frac{\partial u}{\partial x}+v\frac{\partial v}{\partial y}+w\frac{\partial w}{\partial z}\right)=-\frac{\partial p}{\partial x}+\mu\left(\frac{\partial^2 T}{\partial x^2}+\frac{\partial^2 T}{\partial y^2}+\frac{\partial^2 T}{\partial z^2}\right)\\ \left(u\frac{\partial u}{\partial x}+v\frac{\partial v}{\partial y}+w\frac{\partial w}{\partial z}\right)=-\frac{\partial p}{\partial y}+\mu\left(\frac{\partial^2 T}{\partial x^2}+\frac{\partial^2 T}{\partial y^2}+\frac{\partial^2 T}{\partial z^2}\right)\\ \left(u\frac{\partial u}{\partial x}+v\frac{\partial v}{\partial y}+w\frac{\partial w}{\partial z}\right)=-\frac{\partial p}{\partial z}+\mu(\frac{\partial^2 T}{\partial x^2}+\frac{\partial^2 T}{\partial y^2}+\frac{\partial^2 T}{\partial z^2})+\ (\rho_T-\rho_{ref})g\beta\end{array}\right\} \quad \text{Equation 4-6}$$

$$\rho C_p(u\frac{\partial T}{\partial x}+v\frac{\partial T}{\partial y}+w\frac{\partial T}{\partial z})=k(\frac{\partial^2 T}{\partial x^2}+\frac{\partial^2 T}{\partial y^2}+\frac{\partial^2 T}{\partial z^2}) \quad \text{Equation 4-7}$$

where ρ is the flow density (kg/m^3), u is the velocity x-component (m/s), v is the velocity y-component (m/s), w is the velocity z-component (m/s), p is for the static pressure (P_a), μ is the flow dynamic viscosity (P_a/s), ρ_T is the flow density at a specific temperature (kg/m^3), ρ_{ref} is the flow density at the reference temperature (kg/m^3), β is the thermal expansion coefficient $(1/K)$, g represents the gravity acceleration (m/s^2), C_p is the heat capacity $(J/(kg\cdot K))$, T is the temperature (K), k is the thermal conductivity $(W/(m\cdot K))$.

It should be noted that the Boussinesq approximation is applied to estimate the buoyancy pressure in Equation 4-6. The Boussinesq approximation used for the air flow simulation in the CFD model was experimentally validated in [87], and the application of it for the transformer insulating liquid was verified in [55].

The radiation effect of a transformer radiator is mostly found on the outwards facing surfaces, as discovered in [85]. Therefore, the radiation is only considered on two outwards facing surfaces, and is governed by the Stefan-Boltzmann law Equation 4-8 [95].

$$q_{radi}''=\varepsilon\sigma({T_w}^4-{T_{amb}}^4) \quad \text{Equation 4-8}$$

where q_{radi}'' is the heat flux by radiation effect (W/m^2), ε is the surface emissivity, σ is for the Stefan-Boltzmann constant, T_{amb} is the ambient temperature (K), and T_w is the radiator surface temperature (K).

The insulating liquid, the radiator wall and air domains are all simulated in the full radiator CFD model. The input of the insulating liquid domain are the top liquid temperature and total liquid flow rate at the radiator top, where the insulating liquid has a fully-developed temperature and velocity profile. The radiator wall is simulated as thermal boundaries between the insulating liquid and air domains. The air domain is presented in Figure 4-3, and the input of the air domain is the ambient temperature (T_{amb}) and a pressure profile.

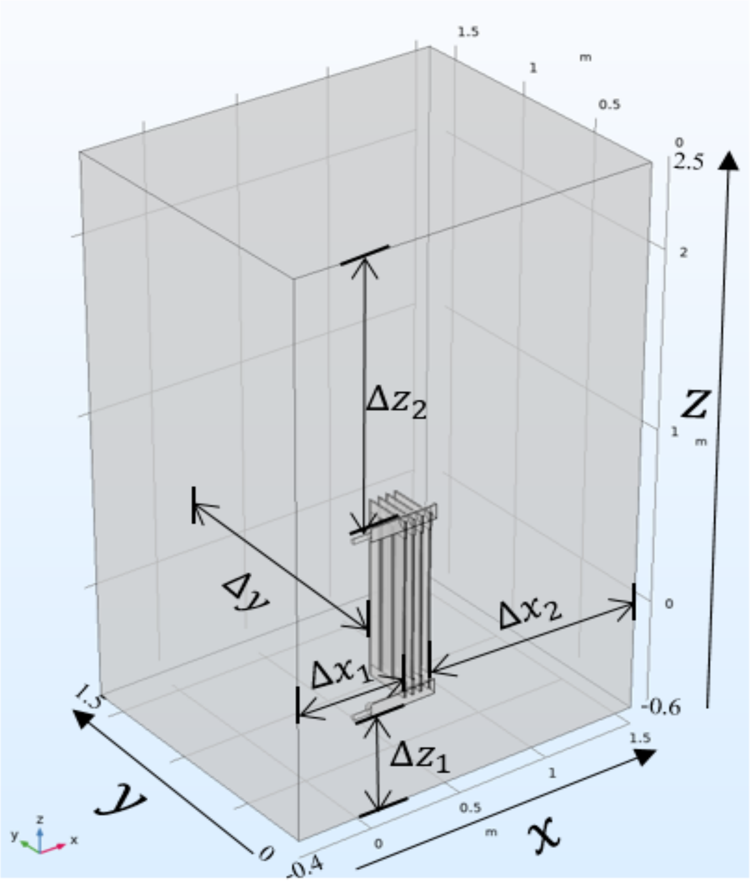

Figure 4-3 Air domain boundaries in full radiator CFD model

The bottom xy-plane is modelled as wall condition and is assigned with ambient temperature (T_{amb}), resembling the ground surface in the experiment. The xz-plane at $y = 0\ m$ is set as the symmetric boundary to save the processing time. The rest of boundaries are set as the open boundary condition. The top xy-plane is assigned with the ambient temperature and ambient pressure (p_{amb}); the vertical boundaries are assigned with the ambient temperature and pressures varying linearly from ambient pressure at its top to the ground ($p_{amb} + \rho g Z$), where g is the gravity acceleration (m/s^2), and Z is the height of the air domain (m). The boundary condition of each surface is also summarized in Table 4-2.

Table 4-2 Boundary conditions of the air domain in the full radiator CFD model

Open boundary	xy-plane at $z = 2.5\ m$	T_{amb}, p_{amb}
	xz-plane at $y = 1.5\ m$	T_{amb}, $p_{amb} + \rho g Z$
	yz-plane at $x = 1.5\ m$	T_{amb}, $p_{amb} + \rho g Z$
	yz-plane at $x = -0.4\ m$	T_{amb}, $p_{amb} + \rho g Z$
Symmetry	xz-plane at $y = 0\ m$	Temperature and flow symmetry
No-slip wall (Ground)	xy-plane at $z = -0.6\ m$	T_{amb}

All the material properties of the insulating liquid, including density (ρ), specific heat capacity (C_p), thermal conductivity (k) and dynamic viscosity (μ), are temperature dependent. Three types of the insulating liquids are studied in this PhD project, i.e. a mineral oil (NYTRO Gemini X), a Gas-to-Liquid (Shell Diala S4 ZX-I) and a synthetic ester liquid (MIDEL 7131), the temperature-dependencies of different insulating liquids from the manufacturers are given in Equation 4-9 to Equation 4-11 [96-98]. The air material properties can be calculated from Equation 4-12 [99].

$$\left\{ \begin{array}{c} \rho_{MO} = -0.658 \times T + 1064 \\ \mu_{MO} = 7.863 \times 10^{-5} \times e^{\left(\frac{632.0}{T-176.0}\right)} \\ C_{p_{MO}} = 3.950 \times T + 560 \\ k_{MO} = -7.837 \times 10^{-5} \times T + 0.1557 \\ \beta_{MO} = 7.778 \times 10^{-4} \end{array} \right\} \qquad \text{Equation 4-9}$$

$$\left\{ \begin{array}{c} \rho_{GTL} = -0.6455 \times T + 995.5 \\ \mu_{GTL} = 6.133 \times 10^{-5} \times e^{\left(\frac{749.8}{T-157.4}\right)} \\ C_{p_{GTL}} = 4.449 \times T + 871.7 \\ k_{GTL} = -8.217 \times 10^{-5} \times T + 0.1674 \\ \beta_{GTL} = 8.273 \times 10^{-4} \end{array} \right\} \qquad \text{Equation 4-10}$$

$$\left\{\begin{array}{c} \rho_{SE} = -0.7327 \times T + 1185 \\ \mu_{SE} = 6.239 \times 10^{-5} \times e^{\left(\frac{914.1}{T-162.4}\right)} \\ C_{p_{SE}} = 2.069 \times T + 1287 \\ k_{SE} = -1.236 \times 10^{-4} \times T + 0.1817 \\ \beta_{SE} = 7.790 \times 10^{-4} \end{array}\right\}$$

Equation 4-11

$$\left\{\begin{array}{c} \rho_{air} = \dfrac{M_a \times p_{amb}}{R \times T} \\ \mu_{air} = -8.4 \times 10^{-7} + 8.4 \times 10^{-7} \times T - 7.7 \times 10^{-11} \times T^2 + \\ 4.6 \times 10^{-14} \times T^3 - 1.1 \times 10^{-17} \times T^4 \\ C_{p_{air}} = 1047.6 - 0.4 \times T + 9.5 \times 10^{-4} \times T^2 - 6.0 \times 10^{-7} \times T^3 \\ +1.3 \times 10^{-10} \times T^4 \\ k_{air} = -2.3 \times 10^{-3} + 1.2 \times 10^{-4} \times T - 7.9 \times 10^{-8} \times T^2 + \\ 4.1 \times 10^{-11} \times T^3 - 3.7 \times 10^{-15} \times T^3 \\ \beta_{air} = 1/T \end{array}\right\}$$

Equation 4-12

where ρ is the density (kg/m^3), μ is the dynamic viscosity (P_a/s), C_p is the specific heat capacity ($J/(kg \cdot K)$), k is the thermal conductivity ($W/(m \cdot K)$), β is the thermal expansion coefficient ($1/K$), T is the temperature (K). The subscripts, i.e., MO, GTL, SE and air, are used to represent the mineral oil, the Gas-to-Liquid, the synthetic ester and the air. M_a is the molecular weight of air as 27.97 (kg/mol), p_{amb} is the ambient pressure as 101,325 (P_a), and R is the universal gas constant as 8.314×10^3 ($J/(mol \cdot K)$).

4.1.3 Mesh and Air Domain Size Refinement

The full radiator CFD model is simulated using the COMSOL Multiphysics (version 5.4) which solves the conservations of mass, momentum and energy with the finite element method. In the full radiator CFD simulations, the meshes consist of layers of hexahedral elements for the flow boundary layer and tetrahedral elements for the rest of flow domains, as shown in Figure 4-4. It was found that the number of hexahedral layers has negligible influence on the results of flow and temperature distributions. Therefore, 2 layers of hexahedral elements were used in all the cases.

In the full radiator CFD simulations, not only the mesh refinement study needs to be conducted, but also an air domain size refinement is required to ensure that the simulation results are mesh and air domain size independent. However, conducting a full matrix considering different meshes and different air domain sizes is too time consuming. Therefore, an alternative strategy is proposed instead of the full matrix. Firstly, the mesh refinement study is conducted under a small air domain to find out an acceptable mesh pattern. Subsequently, different air domains are simulated under the same mesh pattern, in which the minimum and maximum mesh sizes are controlled as the same.

A CFD case corresponding to the 800 W experimental condition (thermal head as 0.5 m and the coolant as a mineral oil) is taken as the benchmark case in the mesh and air domain size refinement studies. In the mesh refinement study, the tracking parameters at each mesh size (alternatively the total number of domain elements (N_{de})), are the bottom liquid temperature (T_{bot}) and the total heat dissipation (P). The results of mesh refinement study are shown in Table 4-3. According to the varying trend of the tracking parameters with the number of domain elements, 'Mesh 3' is indicated as the optimum solution (the changes temperature are within 0.1 K and the changes of the total heat dissipation is less than 0.2%), and it will be adopted for the full CFD model simulations. It should be noted that the mesh refinement study in Table 4-3 was conducted under a small air domain, as '$\Delta L \approx 0.75\ m$' in Table 4-4.

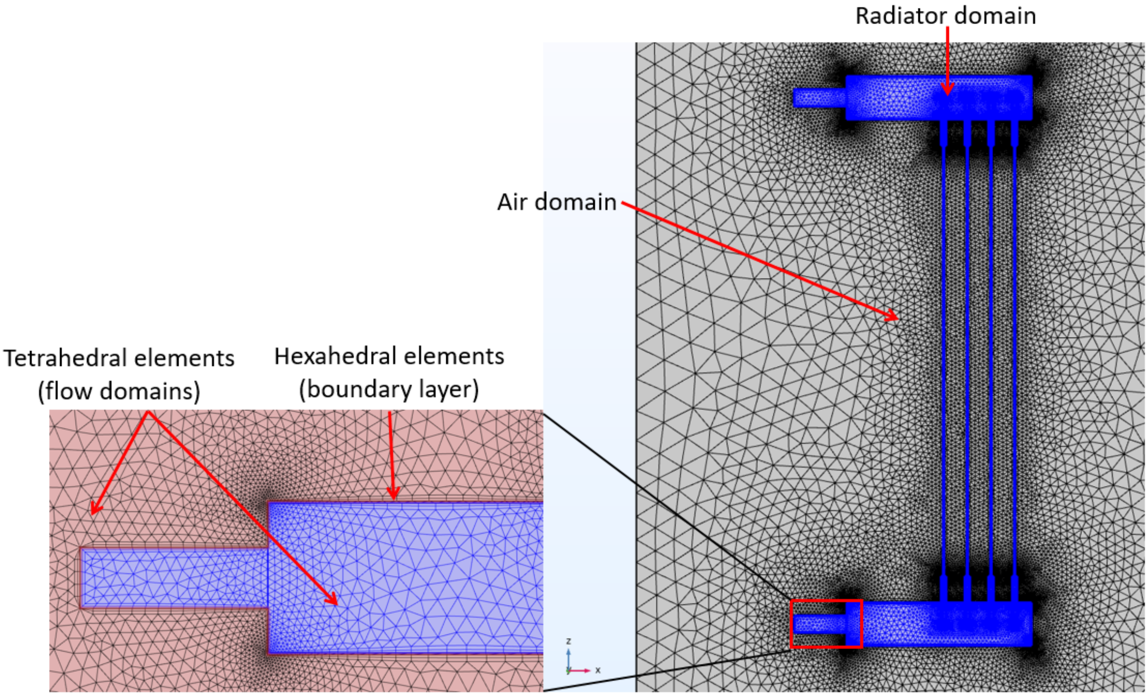

Figure 4-4 Mesh pattern of radiator CFD models (radiator domain in purple, air domain in grey)

Table 4-3 Full radiator CFD model mesh refinement results

Mesh pattern	Mesh 1	Mesh 2	Mesh 3	Mesh 4	Mesh 5
N_{de}	1,318,459	1,854,061	3,749,698	7,603,450	21,080,163
$P\ (W)$	910.6	860.5	820.0	819.4	818.2
T_{bot} (°C)	36.8	37.8	38.6	38.6	38.6

An air domain size refinement study is implemented by keeping the same minimum and maximum mesh sizes of 'Mesh 3' meshing strategy. Three different air domains are simulated, namely '$\Delta L \approx 0.75\ m$', '$\Delta L \approx 1\ m$' and '$\Delta L \approx 1.5\ m$', the number indicates the approximate distance between the surface of air domain and the radiator outwards facing surface. The air domain refinement results are given in Table 4-4. As seen in the table, the simulation results of the bottom liquid temperature (T_{bot}) and the total heat dissipation (P) are stabilized with air domain size increasing. The air domain as '$\Delta L \approx 1\ m$' is adopted for the full CFD model simulations, and Δx_1, Δx_2, Δy, Δz_1 and Δz_2, as shown in Figure 4-3, are set as 0.58 m, 1.15 m, 1.24 m, 0.60 m and 1.50 m, respectively.

Table 4-4 Air domain refinement study results

`Air domain size	$\Delta L \approx 0.75\ m$	$\Delta L \approx 1\ m$	$\Delta L \approx 1.5\ m$
N_{de}	3,749,698	4,714,982	6,912,639
$P\ (W)$	820.0	820.4	818.8
T_{bot} (°C)	38.6	38.6	38.6

4.2 Simulation Results

In this Chapter, the full radiator CFD model is used to simulate seven different loading conditions, by inputting the top liquid temperatures and the total liquid flow rates. The input are from the temperature-rise experiments with the thermal head as 0.5 m and the coolant as a mineral oil. The input conditions of the full CFD simulations are summarized in Table 4-5.

Table 4-5 Input conditions of full radiator CFD simulations

Case No.	Top liquid temperature T_{top} (°C)	Ambient temperature T_{amb} (°C)	Liquid flow rate at the radiator top $Q_{oil-top}$ $(10^{-5}\ m^3/s)$
1	32.8	20.2	1.55
2	40.2	20.0	2.22
3	51.8	24.8	2.84
4	55.0	20.4	3.17
5	62.0	20.9	3.75
6	66.6	21.2	4.05
7	76.2	25.3	4.43

In the full radiator CFD simulations, the liquid flow and temperature distributions, radiator surface temperatures and the air flow and temperature distributions are all simulated. In this section, the simulation results of Case 4 in Table 4-5 (corresponding to the 800 W power injection thermal head as 0.5 m and coolant as a mineral oil in the experiment) is taken as an example to demonstrate the simulation results, including the temperature colour contour, the flow streamlines and the temperature distributions. It is worth mentioning that the temperature and flow distributions are extracted by in-house developed MATALB programs. Next, the results of the global parameters, i.e. bottom liquid temperature and total heat dissipation, and the liquid temperature distributions from all the simulations are presented in Section 4.2.2.

4.2.1 Data Processing

As mentioned, the liquid, radiator and air domains are all modelled in the full radiator CFD model. Figure 4-5 shows the radiator temperature distribution and air flow field under the example condition (Case 4 in Table 4-5). The air flow velocity is represented by the coloured air streamlines. It is observed that the radiator temperature decreases from the top to the bottom. And also seen in the figure, the air flow around the radiator is from the bottom to the top, which leads to an increase in the air velocity along the same direction. Although most of the air flows are from radiator bottom, there still some from the side the radiator.

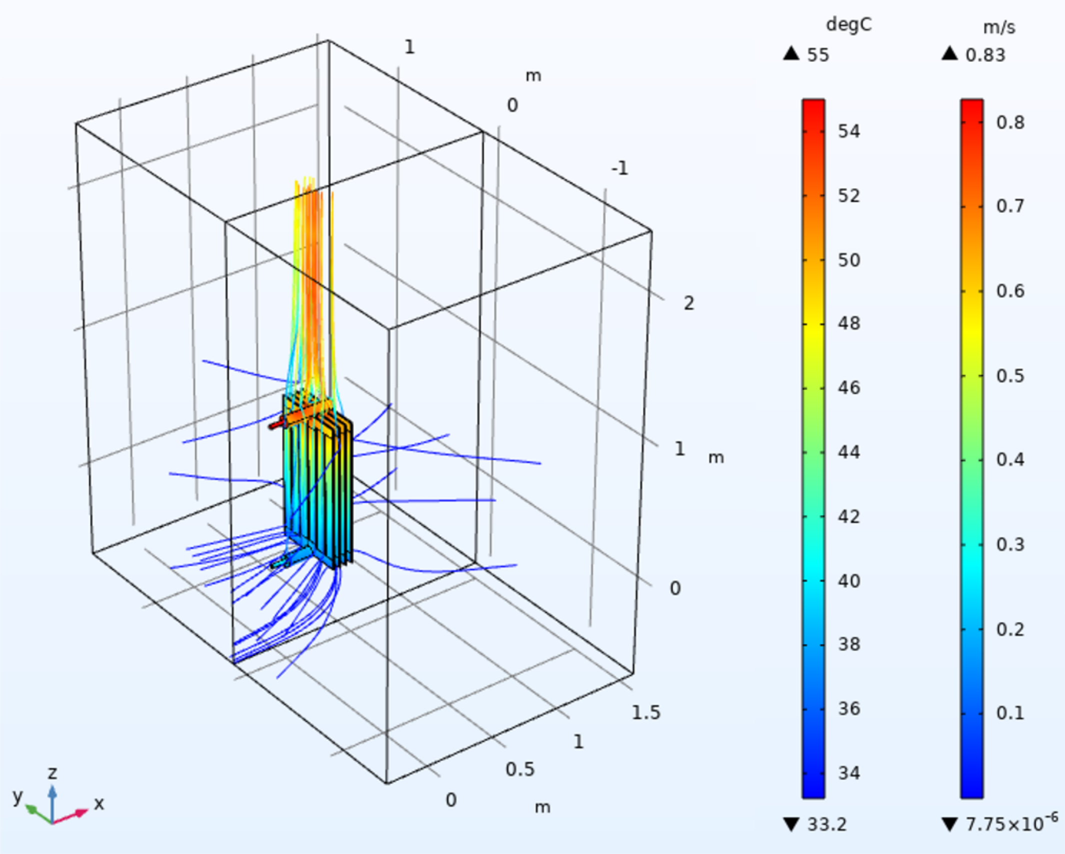

Figure 4-5 Radiator temperature profile and air flow streamlines under the example condition (Case 4 in Table 4-5)

The air temperature is also solved in the full radiator CFD model, and two slides are presented in Figure 4-6 (a) and (b), respectively. Figure 4-6 (a) shows the air temperature on a yz plane at x=0.252 m, where is the middle between the second and third radiator panel; Figure 4-6 (b) shows the air temperature on a xz plane at y=0 m, where is the middle across the radiator. As seen in both figures, air temperature changes mostly occur at either between the radiator panels or above the top header pipe. It is clearly observed that the air temperatures at 1 meter away from the radiator surface in both x and y directions are the same as the ambient temperature. The results also prove that the ambient temperature measurement method designed in Section 3.1.3.3 is reliable with respect to the number of the temperature sensors and the locations of the sensors.

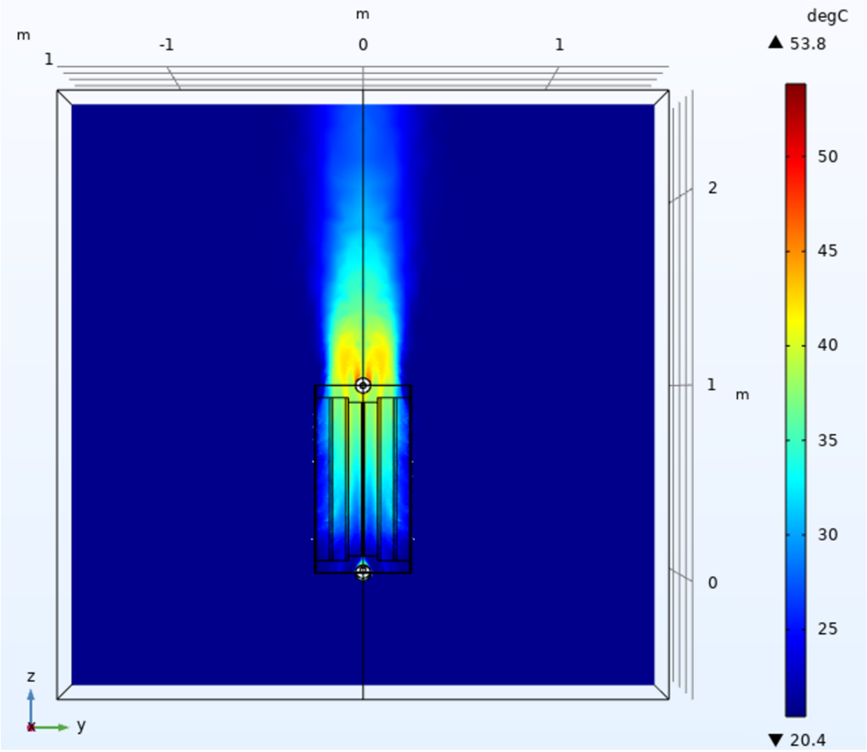

(a)

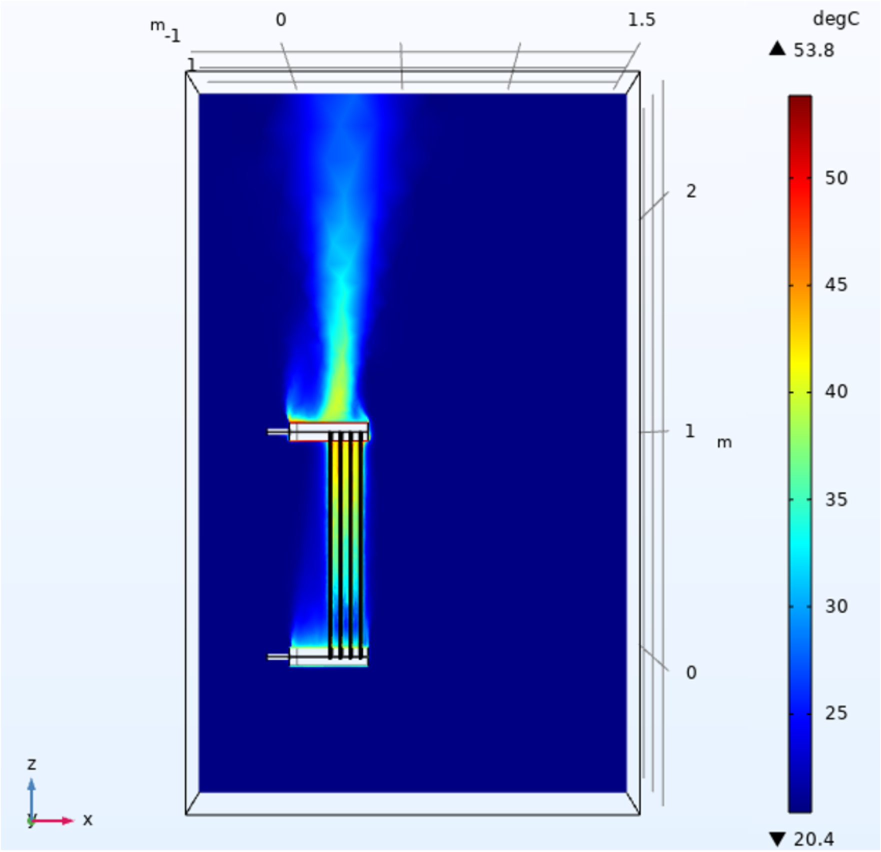

(b)

Figure 4-6 Air temperature distribution under the example condition (a) yz-plane at x= 0.252 m (b) xz-plane at y=0 m (Case 4 in Table 4-5)

The liquid flow and temperature distributions, in a vertical plane, cutting through the middle of the panel closest to the top liquid inlet, i.e. the 1st radiator panel, are shown in Figure 4-7 (a) and (b), respectively. As highlighted in both figures, each radiator panel consists of three sections, namely the top semi-circular section, the oil channel section, and the bottom semi-circular section. The top and bottom semi-circular sections are designed for mixing the insulating liquid. Due to these three different sections, a liquid flow distribution has been formed, as seen in Figure 4-7 (a), where the liquid velocity in each oil channel is different. As a result, temperature distributions in both horizontal and vertical directions (y and z directions) are produced in Figure 4-7 (b). Under the example condition, the largest horizontal temperature span from the radiator edge to the middle is 7.6 ℃; and the vertical temperature span is 20 ℃. The liquid and temperature distributions in the radiator helps understanding its convective cooling effect, which in turn help building a reduced radiator CFD model by using different air heat transfer coefficients (will be reported in Section 5.1.2).

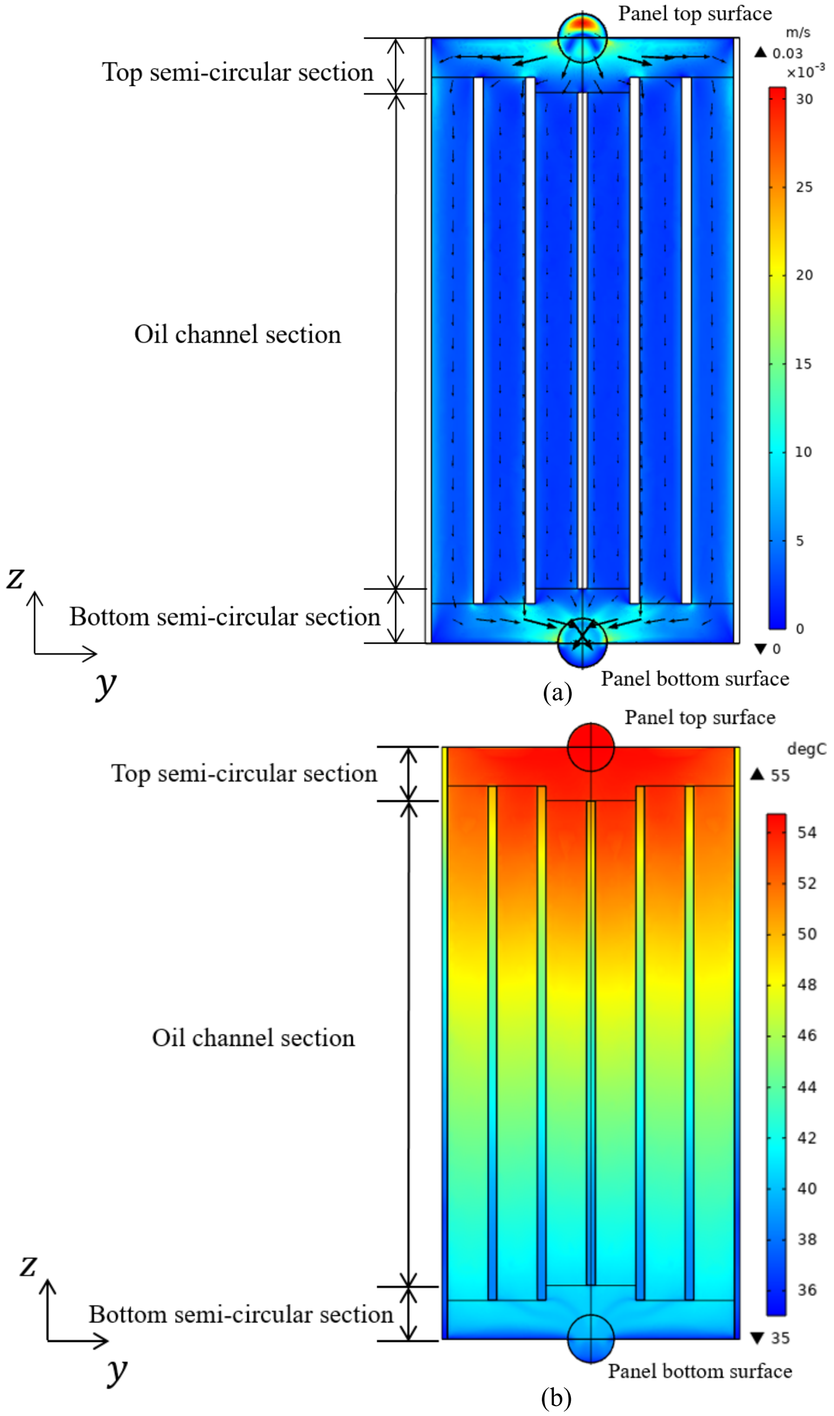

Figure 4-7 Insulating liquid temperature and flow distribution of the 1st panel under the example condition (a) flow distribution (b) temperature distribution (Case 4 in Table 4-5)

Besides the liquid flow and temperature distributions within a panel, the overall liquid temperature distribution along vertical direction of the whole radiator is also of great importance. The liquid temperature determines the thermosiphon pressure of the natural cooled transformer, which is used to estimate the liquid flow rate. Therefore, an in-house developed MATLAB code is used to extract and determine the insulating liquid and radiator surface temperatures. An example of a horizontal cross-section sliced at the middle of the radiator height is shown in Figure 4-8. The radiator panels are numbered in the ascending order, from 1 to 4, as they get further away from the insulating liquid inlet. Two oil channels of Panel 1 and Panel 2 are zoomed in in Figure 4-8 to distinguish between the highlighted insulating liquid domain and the radiator wall area.

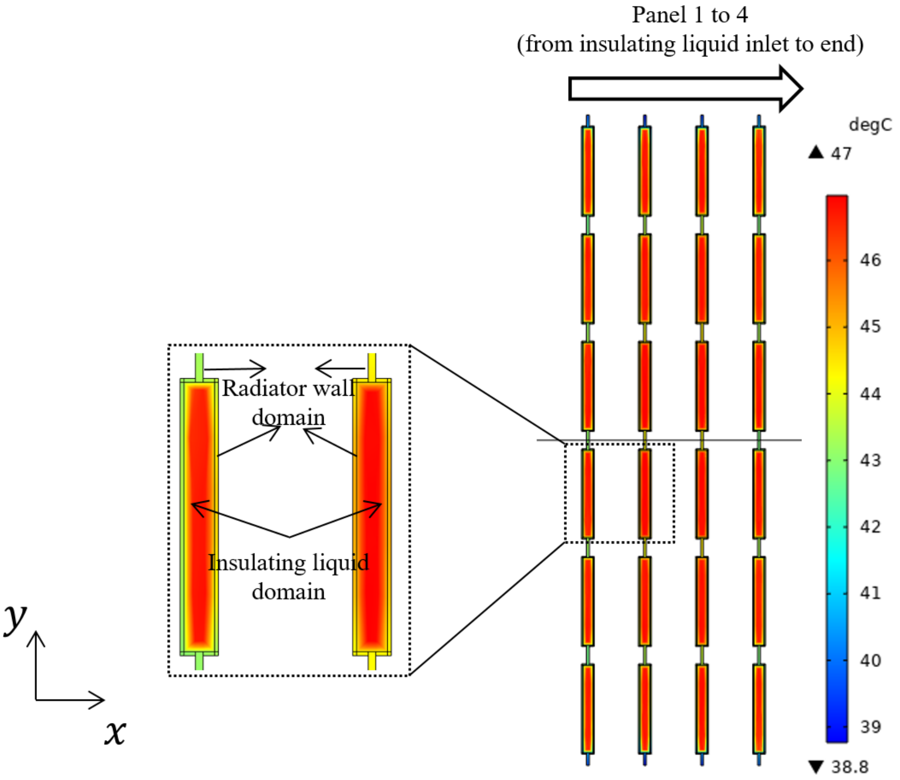

Figure 4-8 Insulating liquid temperature at the cross-sectional area at the middle height from full radiator CFD simulation (Case 4 in Table 4-5)

The liquid temperature is obtained by computing the spatial average temperature over the horizontal cross-sectional area of all 4 panels. In the x directions, temperatures from the simulation results are captured every 0.5 mm; in the y directions, temperatures from the simulation results are captured every 5 mm. Therefore, the liquid temperature of each oil channel is calculated by the temperatures extracted at 315 points (x direction: 21 points; y direction: 15 points). Similarly, the radiator surface temperature is the result of spatially averaging the temperature over the perimeter of these 4 panels (temperature extracted at 16,000 points in total). The liquid temperature distribution facilitates the calculation of total liquid flow rate of ONAN/KNAN transformers as discussed in Section 2.4; and surface temperature distribution benefits the full radiator CFD model experimental verification, which will be reported in Section 4.3.

The comparison between the liquid temperature and the radiator surface temperature is shown in Figure 4-9 under the example condition. The liquid temperature is higher than the surface temperature, as the heat is dissipated from the liquid to the radiator surface. A minor deviation between liquid and surface temperature distributions can be observed at the top semi-circular section in Figure 4-9, which is because of the liquid flow distribution shown in Figure 4-7 (b), as well as the additional cooling surfaces at the panel top and bottom. Although the temperature distributions in the top semi-circular section is slightly different, the overall trend of the liquid and surface temperature distributions are the same. Therefore, to identify the liquid temperature distribution in a radiator, the radiator surface temperature can be measured instead.

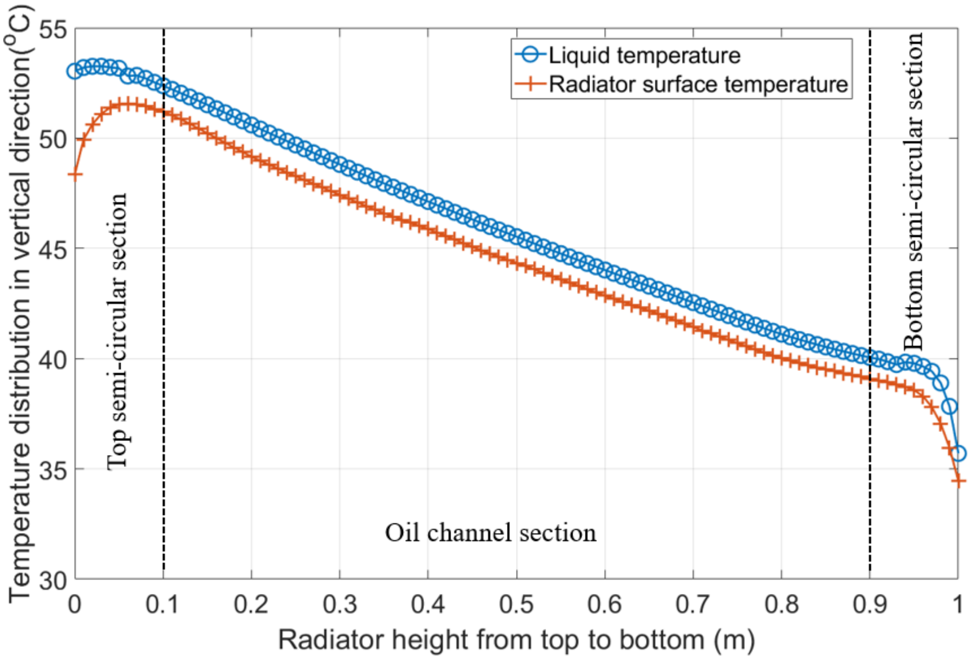

Figure 4-9 Comparison between liquid and radiator surface temperatures from full radiator CFD simulation (Case 4 in Table 4-5)

In the radiator thermal modelling, another key global parameter is the total heat dissipation (P). The total heat dissipation (P) is made up of convective heat dissipation (P_{conv}) and radiative heat dissipation (P_{radi}). The quantitative understandings of convective and radiative heat dissipations can improve the radiator thermal design. The P, P_{conv} and P_{radi} are extracted directly from CFD simulation by integrating the heat flux density on the radiator surface, as shown as the first three columns in Table 4-6. The total heat dissipation is also confirmed by the liquid energy conservation Equation 4-13. It should be noted that the bottom liquid temperature is extracted as the surface average temperature of the radiator outlet (shown in Figure 4-1).

$$P = \dot{m} C_p (T_{top} - T_{bot}) \qquad \text{Equation 4-13}$$

where P is total heat dissipation (W), $\dot{m}$ is the mass flow rate of the insulating liquid (kg/s), C_p is the specific heat capacity $(J/(kg \cdot K))$, T_{top} is for the top liquid temperature (°C), $T_{bot-ave}$ is the bottom liquid temperature at the radiator oulet (°C).

As seen in Table 4-6, the total heat dissipation estimated by Equation 4-13 has a negligible difference comparing the total heat dissipation extracted from the CFD software (COMSOL Multiphysics). In the further sections, the total heat dissipation presented is the one extracted from the CFD software (first column in Table 4-6).

Table 4-6 Heat dissipation of full radiator CFD simulation under example condition

Full radiator CFD simulation results			Estimated by energy conservation Equation 4-13
Total heat dissipation P (W)	Convective heat dissipation P_{conv} (W)	Radiative heat dissipation P_{radi} (W)	Total heat dissipation P (W)
820.4	188.3	632.2	819.1

4.2.2 Results

The global parameters, i.e., bottom liquid temperature (T_{bot}) and the total heat dissipation (P), from the full radiator CFD simulations of all seven cases are given in Table 4-7. With the increased top liquid temperature and total liquid flow rate, the total heat dissipation increases. The bottom liquid temperature should also increase from Case 1 to Case 7, however, an opposite trend is found between Case 3 and Case 4. This is due to the different ambient temperatures input in those two cases.

Table 4-7 Simulation results from full radiator CFD simulations

Case No.	Full radiator CFD model inputs			Full radiator CFD model outputs	
	Top liquid temperature T_{top} (°C)	Ambient temperature T_{amb} (°C)	Liquid flow rate at radiator top $Q_{oil-top}$ $(10^{-5}\ m^3/s)$	Bottom liquid temperature T_{bot} (°C)	Total heat dissipation P (W)
1	32.8	20.2	1.55	25.0	185
2	40.2	20.0	2.22	29.4	378
3	51.8	24.8	2.84	38.8	580
4	55.0	20.4	3.17	38.6	820
5	62.0	20.9	3.75	43.7	1066
6	66.6	21.2	4.05	47.4	1248
7	76.2	25.3	4.43	55.4	1485

The liquid temperature distributions along the vertical direction of all 7 cases are shown in Figure 4-10 (a), however, the trends under different input conditions are not clear as the ambient temperatures in all 7 cases are different. Hence, the liquid temperature rise $(T - T_{amb})$ is calculated instead and shown in Figure 4-10 (b). As seen in the figure, with a lower top liquid temperature and liquid flow rate, e.g., Case 1 in Table 4-7, the liquid temperature in the radiator is approximately in a linear relationship with radiator heights. When the top liquid temperature and the flow rate are increasing, the liquid temperature along the vertical direction shifts into an approximately exponential distribution.

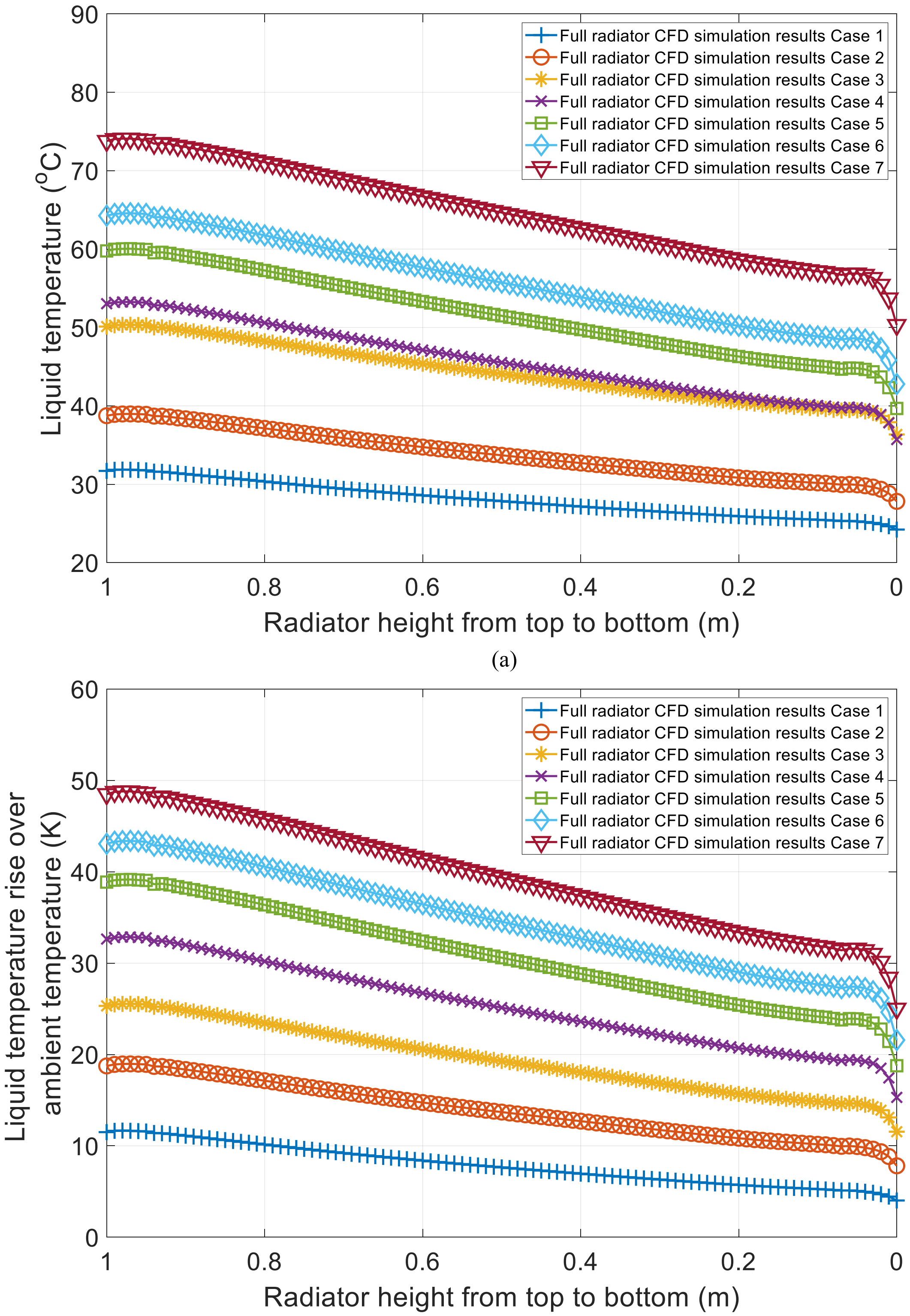

(a)

(b)

Figure 4-10 Liquid temperature distribution in the vertical direction (a) absolute temperature (b) temperature rise over ambient temperature

4.3 Experimental Verification

In this section, the full radiator CFD simulations (Case 1 to Case 7 in Table 4-7) are verified by the experimental measurements in terms of the global parameters and the radiator surface temperature distributions. The surface temperature verification of the Case 4 in Table 4-7 is presented in details in Section 4.3.1. Next, the global parameters of all the cases are compared in Section 4.3.2.

4.3.1 Verification of Surface Temperature

As introduced, the liquid temperature distribution in the radiator determines the thermosiphon pressure within a natural cooled transformer. Thus, the liquid temperature calculation in the radiator greatly influences the estimation of the liquid temperature and velocity of a liquid complete-cooling-loop. However, the liquid temperature cannot be measured directly due to the enclosure of radiator wall. As previously found out, the surface temperature has the same distribution as the liquid temperature in vertical direction, and therefore, the surface temperatures of the radiator wall are measured and used in validating the CFD simulations. As introduced in Section 3.1.3.4, there are in total 198 experimental measurement positions on two outwards facing surfaces, namely front and back outwards facing surfaces. The front outwards facing surface is the closest surface to the inlet of radiator, whereas the back one is the farthest surface away from the radiator inlet. The illustration of these two outwards facing surface can be found in Figure 3-10.

The Case 4 in Table 4-7 is taken as an example to compare the radiator surface temperatures between full radiator CFD simulations and the experimental measurements in details. The comparisons on the front and back outwards facing surface are shown by four out of nine vertical heights in Figure 4-11 (a) and (b), respectively. The error bar stands for the measurement standard deviation at each position. Comparing all 198 points and 594 measurements in Case 4, the absolute average surface temperature difference between CFD simulations and experimental measurements is 1.8 K, and the maximum difference is 2.7 K.

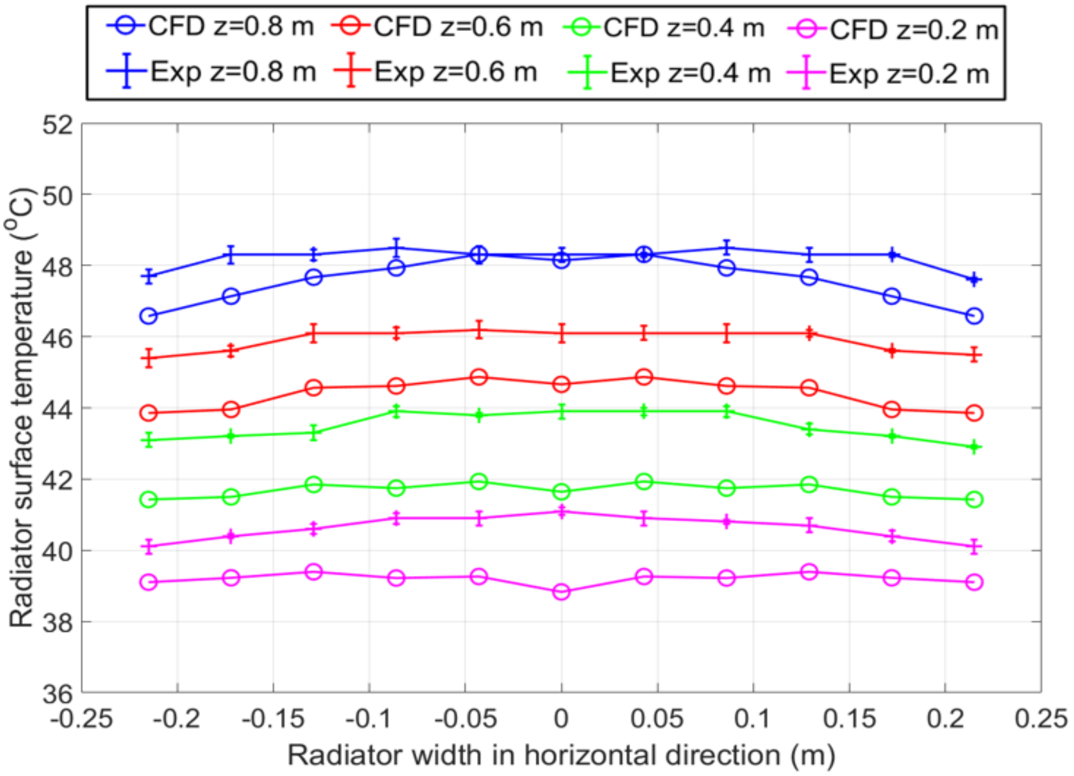

(a)

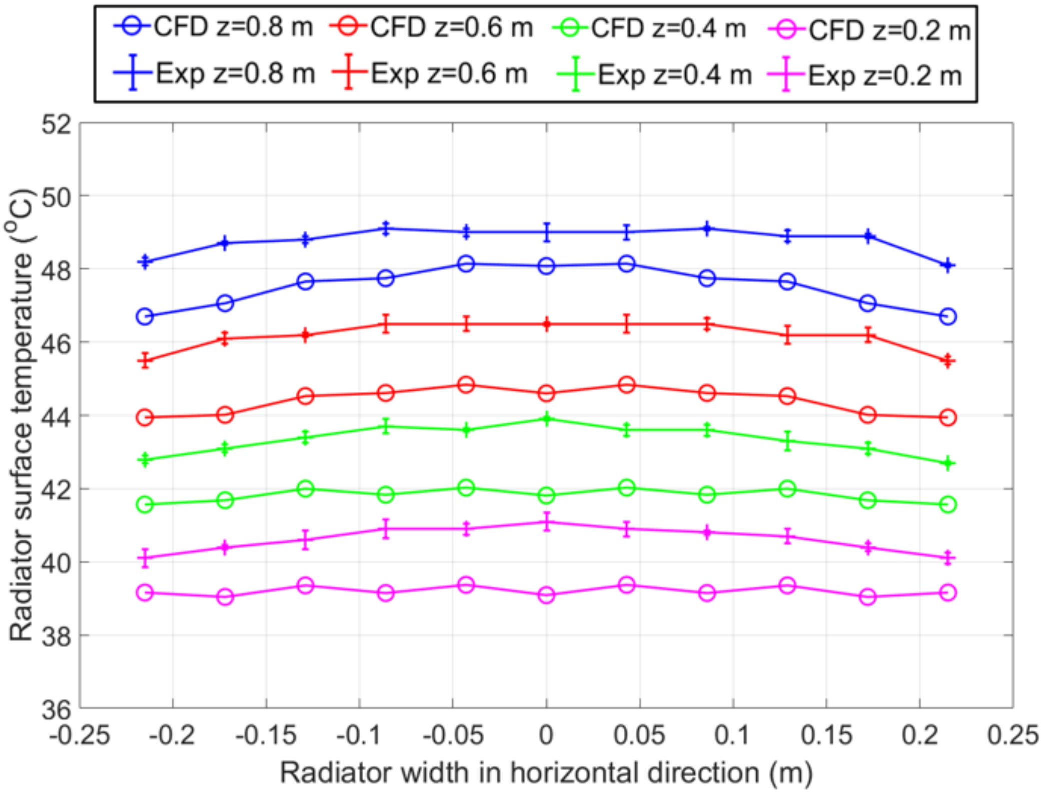

(b)

Figure 4-11 Radiator surface temperature verification of full radiator CFD simulation of Case 4 (a) front outwards facing surface (b) back outwards facing surface

In addition, the surface temperature distribution along vertical direction between the full radiator CFD simulations and experimental measurements is also compared. The measurements at the same height on individual surfaces are averaged and compared with CFD simulations with front and back outwards facing surfaces, as shown in Figure 4-12 (a) and (b), respectively. The surface temperatures calculated from full CFD simulation show the same trend as the measurements. However, minor discrepancies are observed, which are likely caused by the simplification of the oil channel shape, as shown in Figure 4-1 (c), as well as the radiator support structure in the experiment that may pose a minor influence on the air flow. Underestimated surface temperature is commonly observed for most of the CFD calculations, where a perfect air flow condition is normally assumed.

Comparing all 198 points and 594 measurements from Case 1 to 7 in Table 4-7, the absolute average surface temperature difference between CFD simulations and experimental measurements is 2.2 K, and the maximum difference is 3.3 K. These discrepancies between the simulations and experiments are lower than results reported in [80], whose maximum difference was 5.5 K.

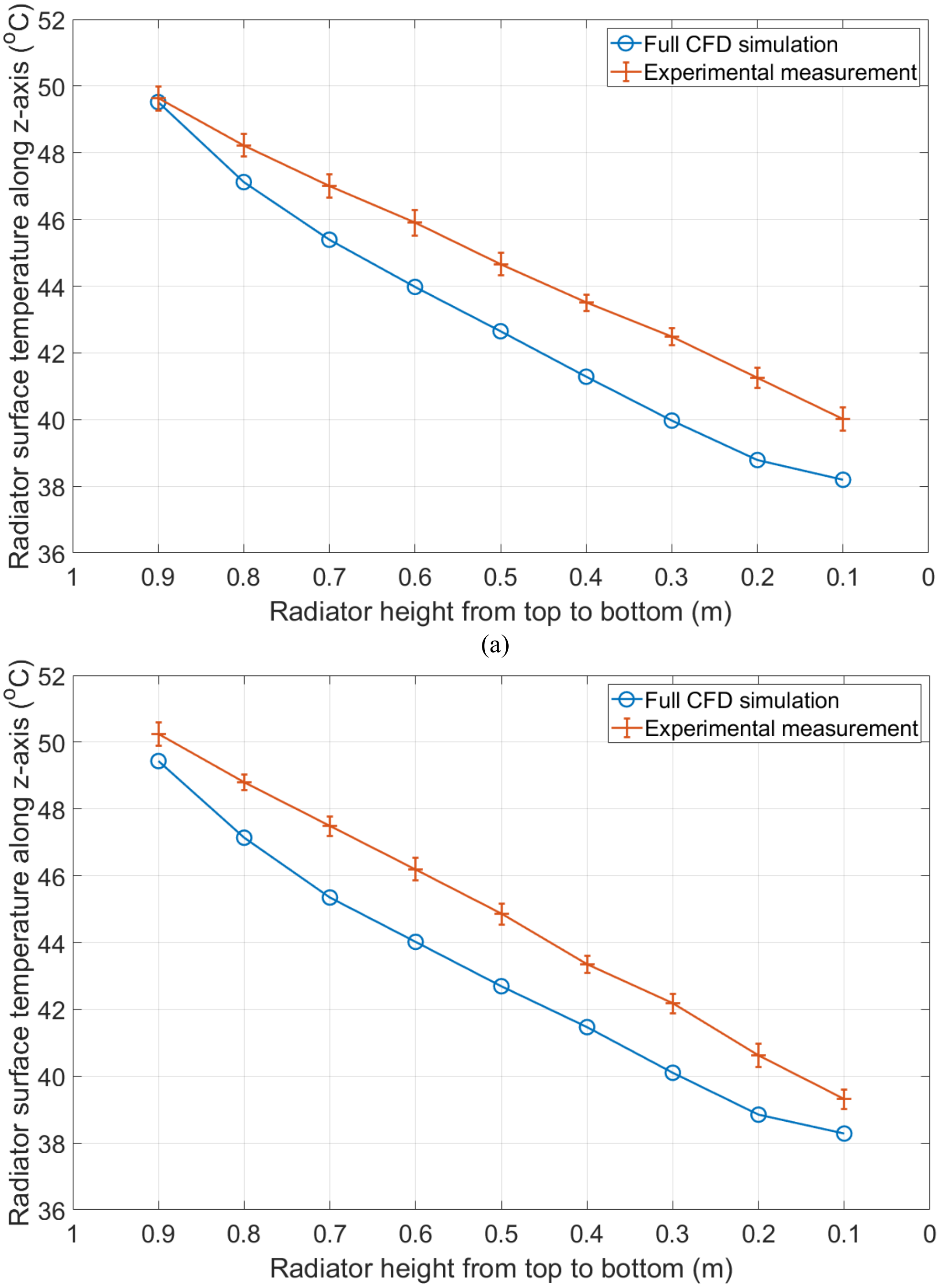

(a)

(b)

Figure 4-12 Radiator surface temperature verification in vertical direction of Case 4 (800 W) simulation result (a) front outwards facing surface (b) back outwards facing surface

4.3.2 Verification of Key Parameters

The comparison between the simulation results and the experimental measurements is given in Table 4-8. As seen in all seven cases, the differences in bottom liquid temperature between CFD simulations and experiments are within 0.9 K, and discrepancies of the total heat dissipation are within 4.3%, both of which are better than those reported in the literature [80, 83, 84, 86, 87].

Table 4-8 Comparison of full radiator CFD simulation results and experimental measurements

Case No.	Experimental measurements		Full radiator CFD simulations	
	$P\ (W)$	T_{bot} (°C)	$P\ (W)$	T_{bot} (°C)
1	190	24.3	185	25.0
2	392	28.7	378	29.4
3	600	38.1	580	38.8
4	800	38.7	820	38.6
5	1022	44.5	1066	43.7
6	1212	47.8	1248	47.4
7	1437	56.3	1485	55.4

As observed from Table 4-8, in the lower loading conditions Case 1-3, the total heat dissipation (P) in the CFD simulation are underestimated, whereas the total heat dissipation (P) are overestimated for higher loading conditions as shown in Case 4-7. This disagreement CFD simulations and their opposite trends are likely due to the following two reasons. The first is that because of a small proportion of heat dissipated by the thermal insulation material, the heat dissipation through the radiator is lower than that is measured in the experiment. The other reason is the uncertainties of the model inputs, i.e., the top liquid temperature (T_{top}) and total liquid flow rate at the radiator top ($Q_{oil-top}$). The top liquid temperature (T_{top}) is calculated as the average of top liquid temperature measurements, i.e. $T_{top-outlet}$ and $T_{top-mid}$, as introduced in Section 3.1.3.2. Total liquid flow rate ($Q_{oil-top}$) is derived from the liquid energy conservation Equation 3-2.

In the lower loading condition Case 1-3, the insulating liquid mostly flow to the middle of the top buffer zone, a similar condition was observed in [76]. Therefore, as seen in Table 4-9, the temperature measurements at $T_{top-mid}$ are higher than the one at $T_{top-outlet}$ in

Case 1-3. However, in the higher loading conditions Case 4-7, the hot-streak phenomena occurs, as reported in [65]. Hence, the temperature measured at $T_{top-outlet}$ is higher than the one at $T_{top-mid}$ in Case 4-7.

Therefore, the averaged top liquid temperature (T_{top}) is always lower than the more representative measurements, either $T_{top-mid}$ for lower loading conditions or $T_{top-outlet}$ for higher loading conditions. The bottom liquid temperature (T_{bot}) measurements, i.e. $T_{bot-mid}$ and $T_{bot-inlet}$, are not affected by the hot-streak phenomenon. As shown in Table 4-9, the bottom liquid temperature (T_{bot}) is within 0.2 K comparing with the temperature measurements at $T_{bot-intlet}$ and $T_{bot-mid}$ expect except for Case 2. Therefore, a lower top liquid temperature results in a higher calculated total liquid flow rate ($Q_{oil-top}$). A lower top liquid temperature and a higher total liquid flow rate together result in an overestimation of total heat dissipation, and thus an underestimation of bottom liquid temperature (T_{bot}).

Table 4-9 Liquid temperature measurements

Case No.	Top liquid temperature measurement		Bottom liquid temperature measurement	
	$T_{top-outlet}$ (°C)	$T_{top-mid}$ (°C)	$T_{bot-inlet}$ (°C)	$T_{bot-mid}$ (°C)
1	32.1	33.5	24.8	23.6
2	39.2	41.1	29.5	27.8
3	51.1	52.5	38.3	37.9
4	55.2	54.7	38.4	38.9
5	62.3	61.8	44.3	44.6
6	67.2	66.0	47.6	47.9
7	76.9	75.4	56.0	56.6

The effect of heat dissipation from the thermal insulation is more noticeable in lower loading conditions, and hence, the total heat dissipation is under predicted in Case 1-3. To the higher loading conditions, the effect of the second reason is more dominating, and which results in the overestimations of the total heat dissipation. It is also worth mentioning that the difference between T_{top} and $T_{top-outlet}$ under all investigated conditions is within 1.0 K, based on experimental observations given in Table 4-9. Therefore, the maximum 1 K liquid temperature difference between the full radiator CFD simulations and the experimental measurements is mainly caused by the liquid temperature measurement method.

Overall, based on the comparisons of total heat dissipation (P), bottom liquid temperature (T_{bot}) and the radiator surface temperature distribution, the results of the full radiator CFD simulations are verified by the experimental measurements and the minor differences found are acceptable. The model will be used as the benchmark model for the following simulation studies.

4.4 Summary

Due to a lack of experimentally verified radiator CFD models with great accuracy, a full radiator CFD model considering all heat transfer processes and media has been established in this chapter. The full radiator CFD model has been verified by 7 sets of experiments in terms of the bottom liquid temperature, total heat dissipation and the surface temperature distributions. The maximum difference of the bottom liquid temperature between CFD simulations and experiments is less than 0.9 K; the mismatch of the total heat dissipation is within 4.3%; the maximum deviation of radiator the surface temperature is 3.3 K. The accuracies of all three are better than the ones in the literature [80, 83, 84, 86, 87].

The full radiator CFD model constructs the understanding of the liquid temperature distribution in the radiator which cannot be measured by experiments otherwise. However, the main drawback the full radiator CFD simulation is the demanding computational efforts, which limits its feasibility in the real design and its incorporation into a CCL CFD model. Therefore, the full radiator CFD model will be applied as the benchmark model to find out a reduced radiator CFD modelling strategy in Chapter 5.

Chapter 5 A Reduced Radiator CFD Model using Optimised h_{air} Equation

The full radiator CFD simulation can accurately estimate the total heat dissipation and the liquid temperature distribution in the transformer radiator, however, the processing time and requirement of the computational memory is significantly demanding. Hence, an optimized radiator modelling strategy is needed to reduce the processing time, whilst also provides an accurate calculation of the total heat dissipation and the liquid temperature distribution.

Therefore, this chapter focuses on the development of a reduced radiator CFD model equipped with an optimised h_{air} equation that represents the detailed air flow simulation. Firstly, in Section 5.1, the methodology of the reduced radiator CFD model is introduced, and the minimum number of the h_{air} required for a reduced radiator CFD model is found out by comparing the reduced and full radiator CFD models. Next, an h_{air} equation is derived by the parametric sweep using the full radiator CFD model. Subsequently, in Section 5.2, the reduced radiator CFD model is experimentally verified, and the derived h_{air} equation is compared with the empirical h_{air} equations from [80, 83, 93-95, 100-105]. The impacts of two influencing factors, i.e., ambient temperature (T_{amb}) and the material properties of different insulating liquids, on the h_{air} equation are evaluated in section 5.3.

5.1 Development of Reduced Radiator CFD Model

The full radiator CFD simulation can accurately estimate the liquid temperature distribution and the total heat dissipation of the transformer radiator. However, one typical case of the full radiator CFD model requires approximately 50 hours, which makes it computationally challenging for being implemented in a CCL CFD model.

Therefore, the air heat transfer coefficient (h_{air}) is adopted to replace the detailed air flow simulation. This modelling strategy, i.e., reduced radiator CFD model using h_{air} to exclude the air domain simulation, is introduced in the following.

5.1.1 Modelling Methodology and Mesh Refinement Results

The reduced radiator CFD model employs the same modelling approach as the full radiator CFD model in terms of thermal conduction (Equation 4-2), convection of insulating liquid (Equation 4-5, Equation 4-6 and Equation 4-7) and radiation (Equation 4-8).

The only difference between these two CFD models is the way of modelling the air convection effect. In the reduced CFD model, the convection effect of the cooling air flow is constituted by Newton's law of cooling, shown in Equation 5-1 [95].

$$q_{conv}'' = h_{air} \times (T_w - T_{amb}) \qquad \text{Equation 5-1}$$

where q_{conv}'' is the heat flux by convection effect (W/m^2), h_{air} is air heat transfer coefficient ($W/(m^2 \cdot K)$), T_{amb} is the ambient temperature (K) and T_w is the radiator surface temperature (K).

The reduced radiator CFD model is also implemented in the COMSOL Multiphysics (version 5.4) which solves the conservations of mass, momentum and energy with the finite element method. In the CFD simulations, the meshes are consisted of layers of hexahedral elements for the flow boundary layer and tetrahedral elements for the main flow domains, which is the same as the insulating liquid and radiator domains in the full radiator CFD model shown in Figure 4-4.

Mesh refinement study was also conducted. A CFD case corresponding to the 800 W experimental condition (Case 4 in Table 4-5) is taken as the benchmark, in which the top liquid temperature (T_{top}) is 55.0 °C, ambient temperature (T_{amb}) is 20.4 °C, and air heat transfer coefficient (h_{air}) is set as 5.8 ($W/(m^2 \cdot K)$). The tracking parameters of each mesh size or number of domain elements (N_{de}) are the bottom liquid temperature (T_{bot}) and the total heat dissipation (P). The results of mesh refinement study are shown in Table 5-1. According to the varying trend of the tracking parameters against the number of domain elements, 'Mesh 8' is chosen for the reduced radiator CFD model. With further increasing mesh elements from the 'Mesh 8', the change of the total power dissipation is less than 0.1%, and the change of the bottom liquid temperature is less than 0.1 K.

Table 5-1 Radiator CFD model excluding air domain mesh refinement results

Mesh	Mesh 6	Mesh 7	Mesh 8	Mesh 9	Mesh 10
N_{de}	464,295	789,146	1,309,283	2,936,925	5,990,019
$P\ (W)$	829.8	819.7	814.7	813.8	813.5
T_{bot} (℃)	38.5	38.7	38.8	38.8	38.8

5.1.2 The Minimum Number of h_{air}

As documented in [95], based on the Newton's law of cooling, a set of heat transfer coefficients can represent the flow convection effect, and hence, replace the detailed flow simulation. Historically, one h_{air} [80, 94, 100-102] or two h_{air} [83] (one for inwards facing surfaces and the other for outwards facing surfaces), has been used to simulate the air convection for a transformer radiator in ONAN cooling mode.

However, the number of air heat transfer coefficients (h_{air}) used to represent the natural air convection in the radiator modelling is dependent on both the air and insulating liquid flows. As mentioned in [95], one convection heat transfer coefficient can be used to represent the cooling effect when the fluid is fully-developed. As seen in Figure 4-6 (a) and (b), the air is heated up from the radiator bottom header pipe and flows up to the top header pipe. Although the air flow is distorted at the top and bottom header pipes, the flow along the radiator panel is more stable and is treated as a fully-developed flow. Moreover, the air flowing along the panel still needs to be categorized into two groups: one along the outwards facing surface and the other between the inwards facing surfaces. Therefore, according to the air flow field, there are four kinds of surfaces, i.e., bottom header pipe, top header pipe, outwards facing surfaces and inwards facing surfaces. The insulating liquid flow is illustrated in Figure 4-7 (b), where the hot liquid flows from top to bottom. Similarly, the liquid flow along the panel is considered as the fully-developed flow, yet it is more distorted at the top and bottom panel surfaces. Consequently, considering both the air and oil flows, a set of 6 h_{air} can be used to represent six kinds of surfaces, as bottom header pipe, top header pipe, panel inwards facing surfaces, panel outwards facing surfaces, panel top surfaces and panel bottom surfaces.

In the literature [80, 83, 94, 100-102], there has been no detailed justification for using either one, two or more h_{air} coefficients. Therefore, the work in this section will firstly compare the applications of using 6 h_{air}, 2 h_{air}, and 1 h_{air}, to determine the minimum number of the h_{air} needed in the radiator CFD model excluding air domain. Case 4 in Table 4-5 is used to conduct this comparison, and the h_{air} of each kind of surfaces is calculated from the full CFD simulation results following Equation 5-1. Subsequently, the extracted h_{air} are input into all three radiator CFD models excluding air domain and the input h_{air} values for different kinds of surfaces are listed in Table 5-2. It can be observed that the h_{air} of the panel top and bottom surfaces are much larger than the other surfaces, which is because a more distorted either insulating liquid or an air flow. It is worth mentioning that the surface area of the top and bottom surface is as small as 0.04 m^2 in total, and the total heat dissipation by these two kinds of surface is 30.7 W.

Table 5-2 Air Heat Transfer Coefficients of Different Model Applications

Model applications	Type of surface	h_{air} $(W/(m^2K))$
Reduced CFD model with 1 h_{air}	All surfaces	5.80
Reduced CFD model with 2 h_{air}	Inwards facing surfaces	4.38
	Outwards facing surfaces	9.49
Reduced CFD model with 6 h_{air}	Bottom header pipe	4.69
	Top header pipe	5.70
	Panel outwards facing surfaces	9.48
	Panel inwards facing surfaces	4.38
	Panel top surfaces	31.27
	Panel bottom surfaces	39.24

The key parameters in an air natural cooled radiator thermal model are the bottom liquid temperature (T_{bot}), total heat dissipation (P) and liquid temperature distribution along radiator vertical direction. As the full radiator CFD model is successfully verified in Section 4.3, therefore, the liquid temperature distributions of all three applications are compared with the full radiator CFD simulation in Figure 5-1. Clearly, there is a negligible difference between three applications of using h_{air} and the full CFD model including the air domain.

To further quantitatively characterize the liquid temperature distribution along the radiator vertical direction in these three applications, the liquid temperature is integrated over the radiator height ($\int T_{oil}$). This liquid temperature integration together with the other two parameters, i.e., T_{bot} and P, are given in Table 5-3. All the key parameters calculated from the reduced CFD models using h_{air} match the values from the experimentally verified full CFD model with negligible deviations.

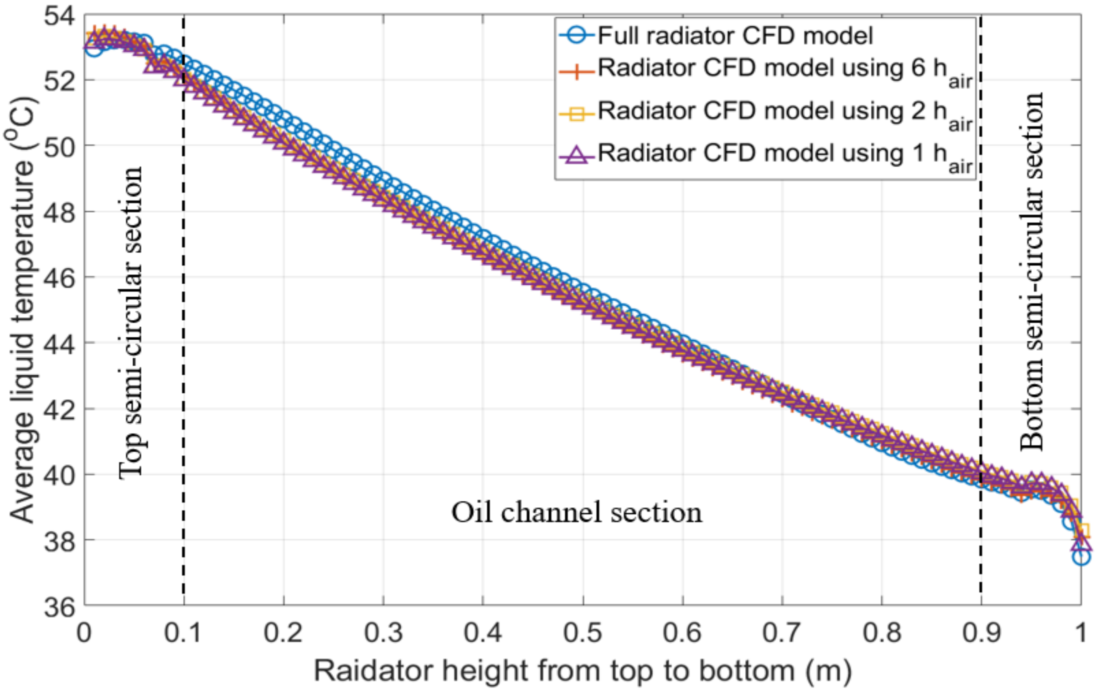

Figure 5-1 Liquid temperature distribution along radiator vertical direction

As also seen from both Figure 5-1 and Table 5-3, the reduced CFD model using 1 h_{air} has provided an acceptable accuracy comparing with the other two applications. Therefore, one h_{air} is sufficient to represent the complex air flow around the transformer radiator under one loading condition.

Table 5-3 Key parameter calculations in different model applications

Radiator CFD models	T_{bot} (°C)	P (W)	$\int T_{oil}$ (°C·m)
CFD model including air domain	38.6	820.4	45.6
Radiator CFD model using 1 h_{air}	38.8	817.1	45.4
Radiator CFD model using 2 h_{air}	38.9	810.7	45.5
Radiator CFD model using 6 h_{air}	38.8	814.7	45.4

5.1.3 Determination of h_{air} Equation

As concluded in Section 5.1.2, one h_{air} is enough to model the radiator thermal performance of one loading condition. To model the radiator under different loading conditions, an h_{air} equation for a transformer radiator should be obtained, and which can be achieved by a CFD parametric study using the full radiator CFD model that includes the air domain. It should be emphasized that the input conditions in the parametric study should be in a reasonably large range considering all operating conditions.

In an liquid natural and air natural (ONAN/OKAN) cooled transformer, the top liquid temperature rise over ambient temperature should be within 60 K [24]. If the ambient temperature (T_{amb}) is given as 20 °C, the top liquid temperature (T_{top}) should therefore vary from 40 to 80 °C. The total liquid flow rate at the radiator top ($Q_{oil-top}$) for the 4-panel 1-meter-high radiator can be found from the literature [80, 83, 94, 100-102]. Different sizes of the radiator were investigated in [80, 83, 94, 100-102], and their cross-sectional velocities were then calculated. By keeping the velocity the same, the total liquid flow rate ($Q_{oil-top}$) can then be computed from the cross-sectional area of the 4-panel 1-meter-high radiator. Therefore, the total liquid flow rate ($Q_{oil-top}$), in this study, is in the range from $3 \times 10^{-5}\ m^3/s$ to $50 \times 10^{-5}\ m^3/s$. It should be noted that the literature [80, 83, 94, 100-102] have accounted for both liquid natural air natural (ONAN/KNAN), and oil directed and forced air natural (ODAN/KDAN) cooling modes.

In total, there are 25 scenarios in the full radiator CFD parametric, and the inputs of all simulation scenarios are given in Table 5-4. The insulating liquid in the parametric study is the mineral oil, the material properties of which is given by Equation 4-9.

Table 5-4 Input conditions of parametric study

T_{amb} (°C)	T_{top} (°C)	Q_{oil} (10^{-5} m^3/s)
20	40	3, 4, 5, 10, 50
	50	3, 4, 5, 10, 50
	60	3, 4, 5, 10, 50
	70	3, 4, 5, 10, 50
	80	3, 4, 5, 10, 50

The bottom liquid temperature and the average liquid temperature of the CFD simulations are shown in Figure 5-2 (a) and (b), respectively. It can be observed that the bottom liquid increases as either the liquid flow rate or the top liquid temperature rises. Hence, average liquid temperature, which is the average of the top (T_{top}) and bottom (T_{bot}) liquid temperature, increases.

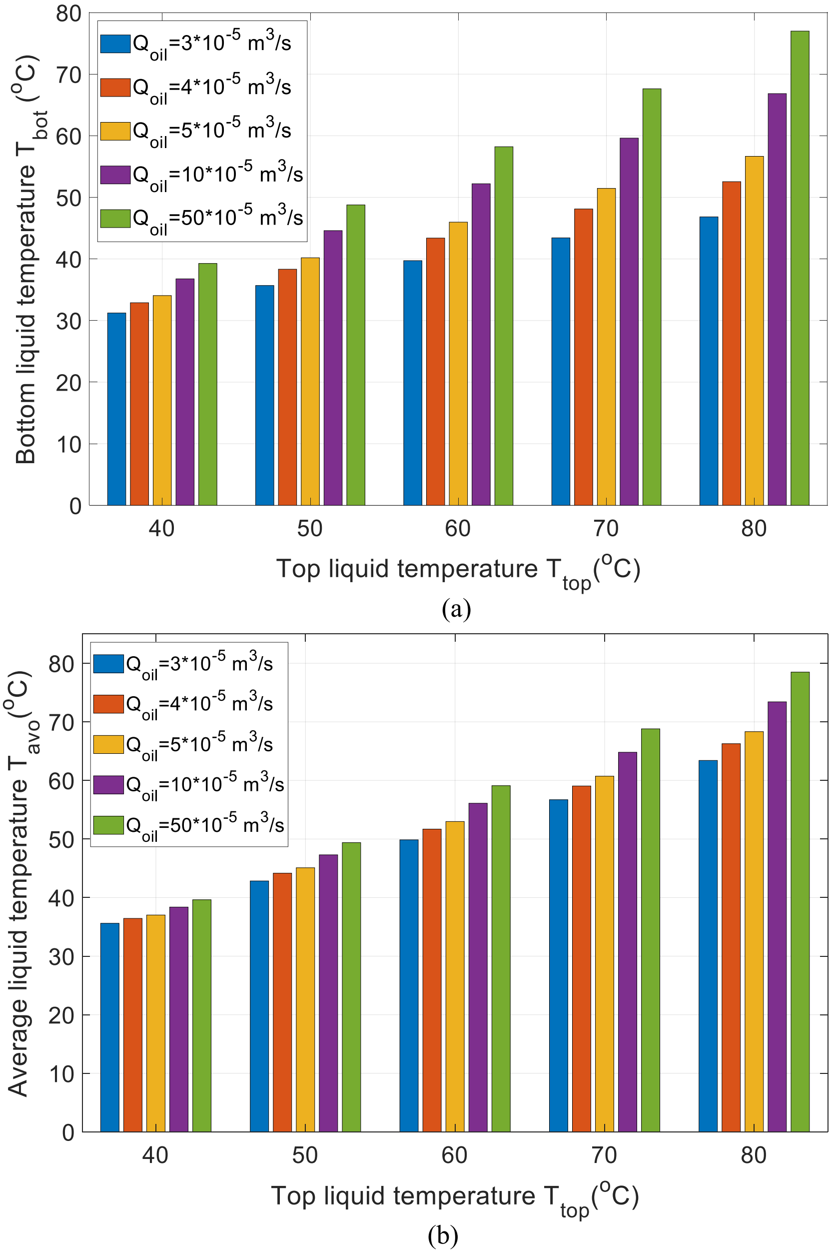

Figure 5-2 Simulation results in parametric studies (a) bottom liquid temperature (b) average liquid temperature

The total heat dissipations of the CFD parametric study (scenarios in Table 5-4) is shown in Figure 5-3. As seen in the figure, the total heat dissipation increases as the liquid flow rate rises under the same top liquid temperature, and the total heat dissipation at the same liquid flow rate is also found increasing when top liquid temperature increases.

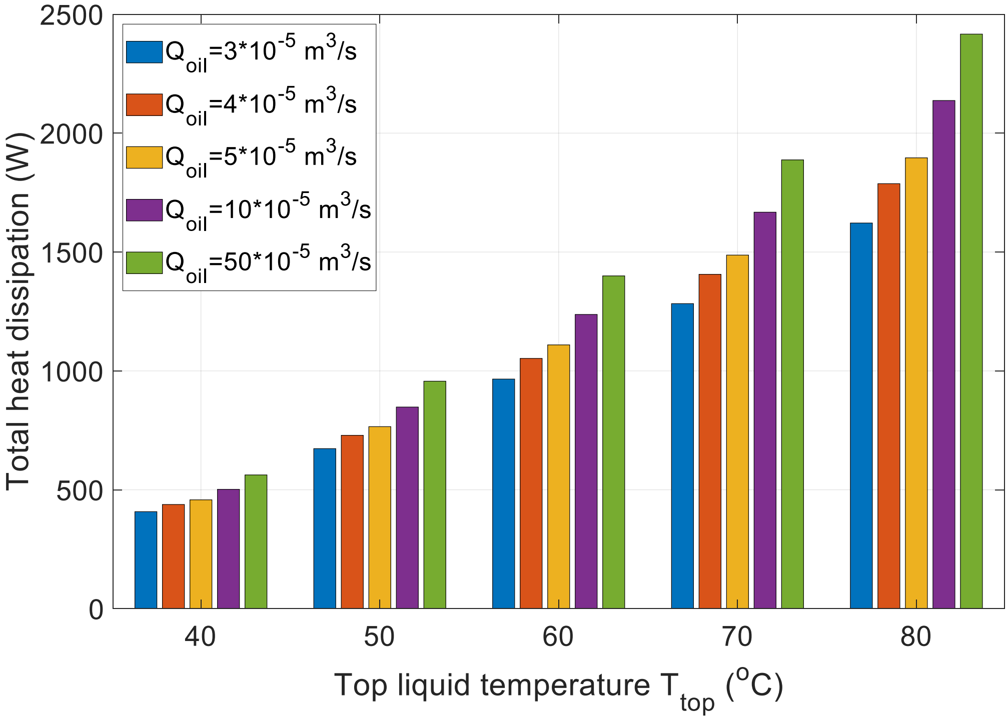

Figure 5-3 Simulation results of total heat dissipations in parametric studies

As seen in both Figure 5-2 (b) and Figure 5-3, a higher top liquid temperature or a higher liquid flow rate leads to a higher average liquid temperature and a higher total heat dissipation. The higher total heat dissipation it is, the larger the air heat transfer coefficient will be. Thus, a higher average liquid temperature results in a larger air heat transfer coefficient.

Therefore, the air heat transfer coefficient (h_{air}) is correlated with the average liquid temperature (T_{avo}) of a radiator. The equation of least-squared curve fitting is given by Equation 5-2 and plotted in Figure 5-4. The coefficient of determination (R^2) in the curve fitting is 0.98. The average and maximum absolute errors are 0.19 W/(m^2·K) and 0.30 W/(m^2·K), respectively; the average and maximum relative errors are 2.0 % and 3.6%, respectively.

$$h_{air} = 1.461 \times (T_{avo} - T_{amb})^{0.4148} \qquad \text{Equation 5-2}$$

where h_{air} is the air heat transfer coefficient ($W/(m^2 \cdot K)$), T_{avo} is the average liquid temperature in the transformer radiator (K), T_{amb} is the ambient temperature (K).

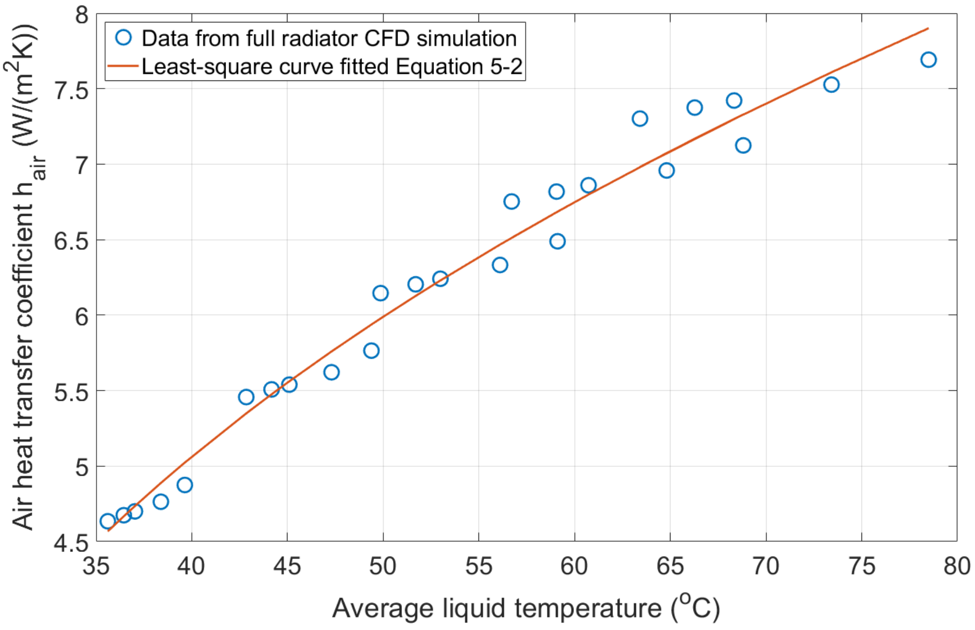

Figure 5-4 h_{air} curve fitting results from CFD parametric study

It should be noticed that the h_{air} in Equation 5-2 and Figure 5-4 is calculated from the Newton's law of cooling (Equation 5-1 [95]) using the convective heat dissipation (q_{conv}'') and the radiator surface temperature (T_w). Also reported in [95], the convective coefficient of the natural cooling mode follows an exponential relationship against the surface temperature of the heated wall. Initially, the air heat transfer coefficient (h_{air}) was correlated with the average surface temperature (T_w) of the radiator. However, there will be an iterative process between the h_{air} equation and CFD simulations in the reduced radiator CFD model. By the experience of preliminary simulations, it was found that the application of h_{air} equation correlated with radiator surface wall temperature (T_w) has a high requirement of computational resources which hinders its feasibility for the radiator thermal design and implementation into the CCL CFD model. In addition, considering that the top and bottom liquid temperatures of a transformer are generally measured in practice, the air heat transfer coefficient (h_{air}) has been instead correlated with the average liquid temperature (T_{avo}) of a radiator, which is the average value of top liquid temperature (T_{top}) and bottom liquid temperature (T_{bot}). The validity of the h_{air} equation correlated with the T_{avo} (Equation 5-2) is presented in the next section.

5.2 Application of Reduced Radiator CFD Model

A reduced radiator model has been developed by using the h_{air} equation (Equation 5-2) to replace the air domain simulation. And in the reduced radiator CFD simulations, it is vital to couple the liquid temperature distribution provided by the reduced radiator CFD model with the h_{air} equation (Equation 5-2). The process of the iteration is detailed in Figure 5-5. Firstly, the ambient temperature (T_{amb}), the top liquid temperature (T_{top}), the total liquid flow rate at the radiator top ($Q_{oil-top}$) and an initial radiator temperature profile are input into the reduced CFD model, and h_{air} is then calculated from the initial temperature profile. Following that, an iterative process takes place to update the CFD simulation and find the air heat transfer coefficient (h_{air}) until the relative tolerances of the temperature profile is less than 0.1%.

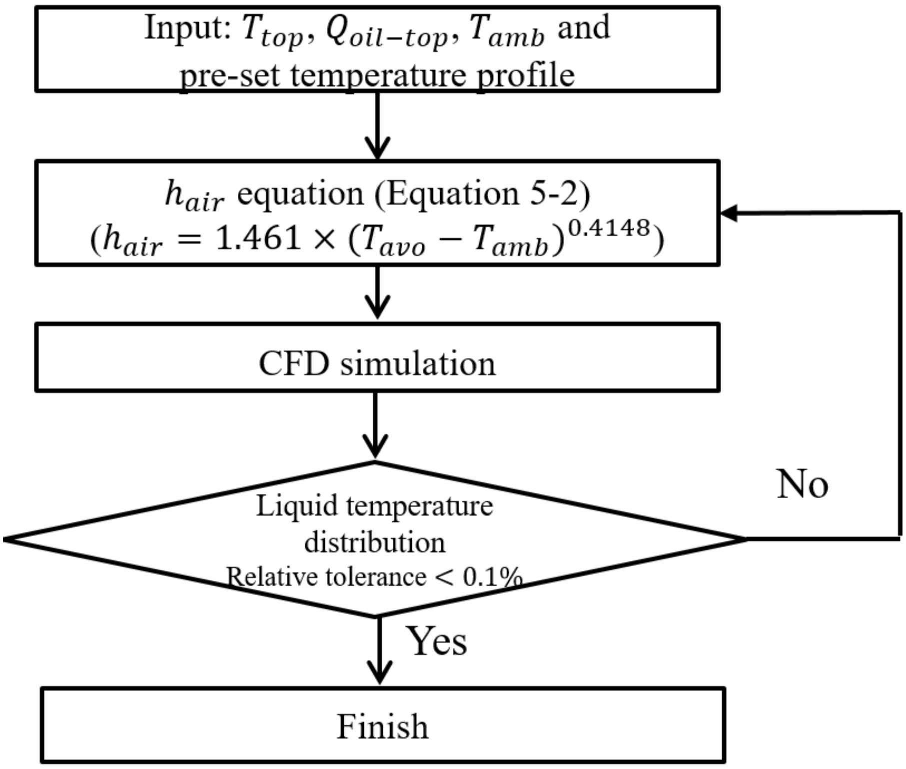

Figure 5-5 Iterations of reduced radiator CFD model adopted with h_{air} equation

Although the detailed air domain is not included in the reduced radiator CFD model, the insulating and radiator wall domains are both simulated. The liquid temperature distribution, the surface temperature distribution and the heat dissipation demonstrated in Section 4.2.1 are all solved by the reduced radiator CFD model.

In this section, the reduced radiator CFD simulations adopted with the h_{air} equation (Equation 5-2) are validated by the full radiator CFD simulations and a set of experiments (under different loading conditions with thermal head as 0.5 m and the coolant as the mineral oil). Moreover, the application of h_{air} equation (Equation 5-2) have been compared with the other empirical h_{air} in the literature.

5.2.1 Simulation Results and Verifications

In Chapter 4, the full radiator CFD simulations were verified by 7 sets of experiments, which was conducted under different loading conditions with 0.5 m thermal head and the coolant as a mineral oil. In this section, the reduced radiator CFD model are used to simulate the same scenarios, with the same model input as the ones in the full radiator CFD models (as given in Table 4-5). Table 5-5 summarizes the results of the reduced radiator CFD simulations, the full radiator CFD simulations and the experimental measurements in terms of the bottom liquid temperature (T_{bot}) and total heat dissipation (P).

Table 5-5 Comparison of the results of reduced radiator CFD simulations, full radiator CFD simulations and experimental measurements

Case No.	Reduced radiator CFD simulation results		Full radiator CFD simulation results		Experimental measurements	
	P (W)	T_{bot} (°C)	P (W)	T_{bot} (°C)	P (W)	T_{bot} (°C)
1	181	25.2	185	25.0	190	24.3
2	367	29.5	378	29.4	392	28.7
3	577	38.9	580	38.8	600	38.1
4	808	38.9	820	38.6	800	38.7
5	1058	44.3	1066	43.7	1022	44.5
6	1231	47.7	1248	47.4	1212	47.8
7	1475	55.7	1485	55.4	1437	56.3

As observed in Table 5-5, the differences of the bottom liquid temperature (T_{bot}) between the reduced radiator CFD model and the full radiator CFD model are within 0.3 K, and the mismatches of the total heat dissipation are less than 2.2%. The differences between two CFD models are likely due to uncertainties from curve fitted h_{air} Equation 5-2 (average difference as 0.19 W/(m^2·K) and maximum difference as 0.30 W/(m^2·K)). Moreover, the simulation results of the reduced CFD model adopted with h_{air} Equation 5-2 are also comparable to all seven sets of experiments with the maximum deviation of 1 K in bottom liquid temperature (T_{bot}) and 6.4% in total heat dissipation (P).

As previously mentioned, the liquid temperature distribution is of great interest, and the accuracy of its distribution along the vertical direction is important in analysing the thermosiphon pressure, and thus, the liquid velocity. Therefore, the minimum, medium and maximum power loss conditions in Table 5-5 (case 1, 4 and 7) are taken as the examples, to compare the reduced and full radiator CFD simulation results in details, as shown in Figure 5-6, Figure 5-7 and Figure 5-8.

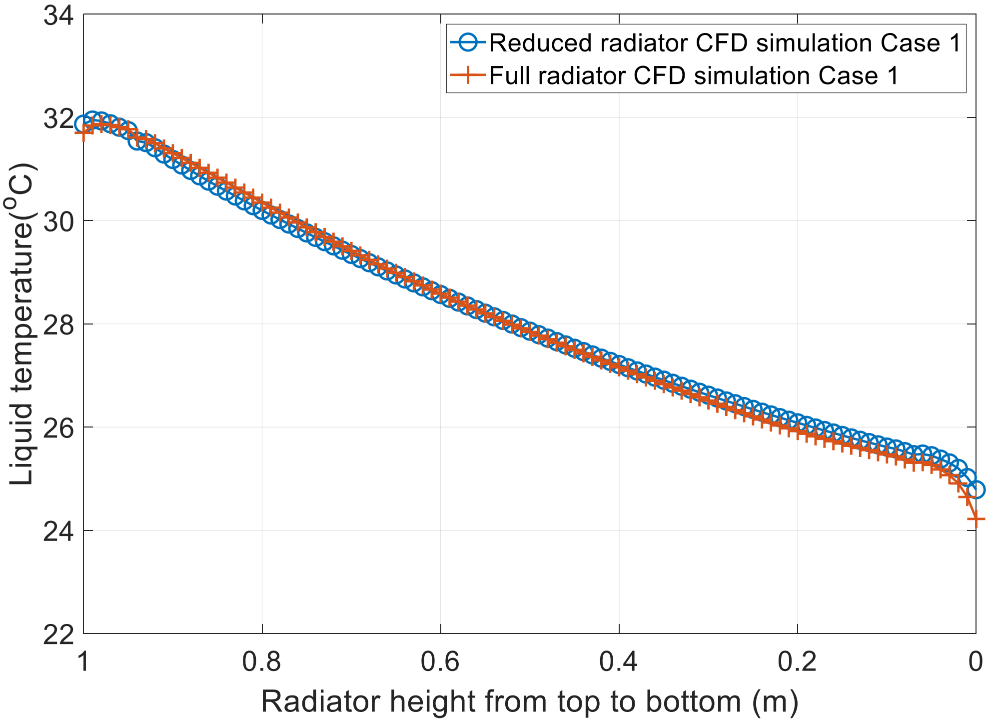

Figure 5-6 Liquid temperature comparison between reduced and full radiator CFD models of Case 1

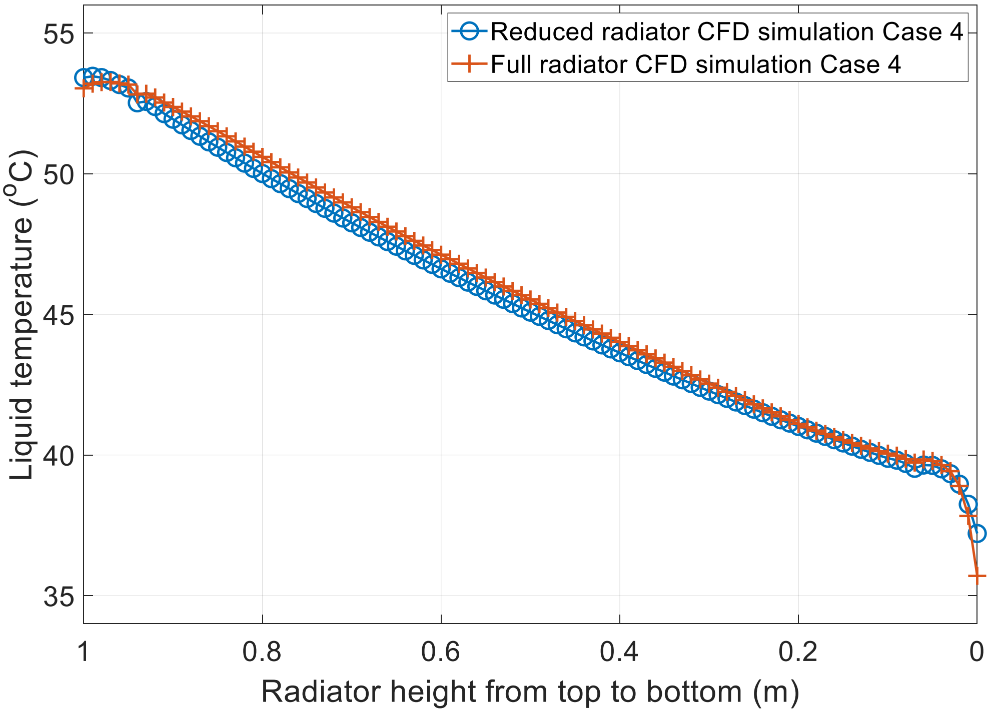

Figure 5-7 Liquid temperature comparison between reduced and full radiator CFD models of Case 4

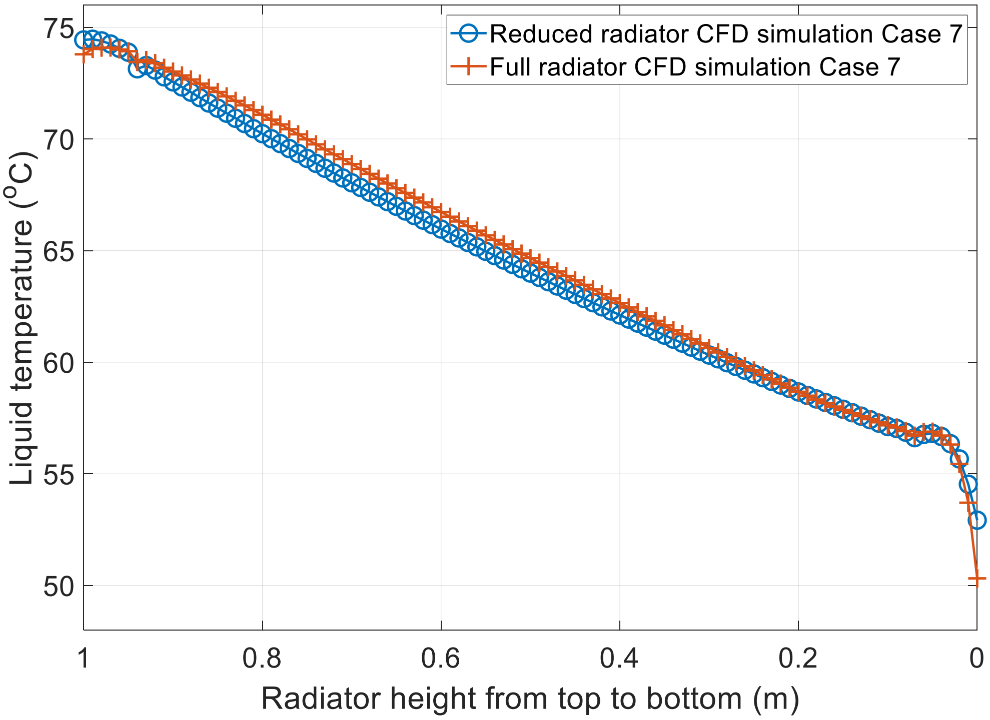

Figure 5-8 Liquid temperature comparison between reduced and full radiator CFD models of Case 8

As seen in all three figures above, the largest temperature different between the reduced and full radiator CFD simulations occurs at the radiator bottom panel surfaces, where the localised h_{air} is much larger than the h_{air} from Equation 5-2 (as shown as the 'bottom panel surface' in Table 5-2). It should be noted that the liquid temperature at the radiator bottom panel surfaces is not the bottom liquid temperature, which is extracted at the radiator outlet as highlighted in Figure 4-1 (a). Comparing the rest of the vertical heights (except for the bottom panel surfaces) from Case 1 to Case 7, the differences of the liquid temperature between the reduced radiator CFD model and the full radiator model are less than 0.3 K.

By model comparisons and experimental validations, the boundary conditions and h_{air} equation used in the reduced radiator CFD model have been fully justified. It is worth mentioning that the processing time of one simulation scenario using the reduced model is approximate 2 hours, whereas that of the full model exceeds 50 hours. Therefore, the proposed methodology can greatly reduce the computational demand whilst keeping the accuracy of results. This would be even more important when integrating the radiator model to the CCL model.

5.2.2 Comparison of h_{air} Equations in Literature

In the literature [80, 83, 94, 100-102], empirical h_{air} equations have been used in the transformer radiator CFD modelling and analytical calculations, and some generic h_{air} equations can also be found in [93, 95, 103-105]. All the empirical equations are given in Table 5-6, it should be noted that most equations are in dimensionless format, and one in [103] directly defines the relationship between the air heat transfer coefficient (h_{air}) and the average surface temperature of the heated wall in an air natural cooling mode.

Table 5-6 Empirical h_{air} equations from literature

Reference [100]	$N_u = \frac{h_{air}L}{k_{air}} = 1.22 \times (0.6108 \times Ra_L)^{0.2364}$	Equation 5-3
Reference [80, 83, 93, 101]	$N_u = \frac{h_{air}L}{k_{air}} = [0.825 + \frac{0.387 \cdot {Ra_L}^{1/6}}{(1 + (0.492/\mathrm{Pr})^{9/16})^{8/27}}]^2$	Equation 5-4
Reference [83]	$N_u = \frac{h_{air}s}{k_{air}} = \frac{1}{24} Ra_s \cdot \frac{s}{L}[1 - \exp(-\frac{35}{Ra_S \cdot s/L}]^{\frac{3}{4}}$	Equation 5-5
Reference [102]	$N_u = \frac{h_{air}s}{k_{air}} = (\frac{576}{\left(\frac{R_a s}{L}\right)^2} + \frac{2.873}{\left(\frac{R_a s}{L}\right)^{0.5}})^{-0.5}$	Equation 5-6
Reference [95]	$Nu = \frac{h_{air}L}{k_{air}} = 0.59(Ra_L)^{1/4}$	Equation 5-7
Reference [103]	$h_{air} = 1.42(\frac{T_w - T_{amb}}{L})^{1/4}$	Equation 5-8
Reference [104]	$Nu = \frac{h_{air}L}{k_{air}} = 0.021(Ra_L)^{0.4}$	Equation 5-9
Reference [105]	$Nu = \frac{h_{air}L}{k_{air}} = 0.\ 1(Ra_L)^{0.33}$	Equation 5-10

The h_{air} calculated from different empirical equations [80, 83, 93-95, 100-105] and Equation 5-3 derived in Section 5.1.3 are plotted in Figure 5-9, where the average liquid temperature (T_{avo}) is in the range of 25 to 80 °C and the ambient temperature (T_{amb}) is set as 20 °C.

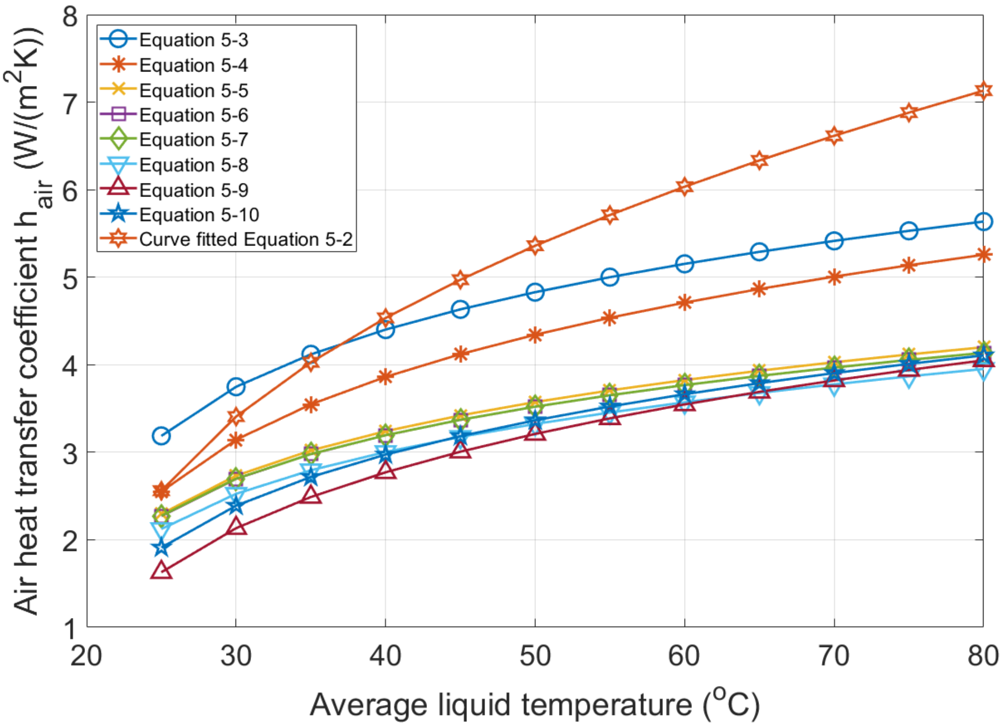

Figure 5-9 Comparison between h_{air} Equation 5-2 and empirical h_{air} equations in literature [80, 83, 93-95, 100-105]

As seen in Figure 5-9, the h_{air} Equation 5-2 derived in Section 5.1.3 is higher than the values estimated from the previous empirical equations in [80, 83, 93-95, 100-105]. It is because the previous empirical equations were derived by either pure analytical methods or experiments based on a flat vertical plate with a constant wall temperature or a uniform heat flux condition. For transformer radiators, the curvature on the radiator panel surfaces is designed to provide a better air convection than a flat plate, therefore it is expected to have a higher air heat transfer coefficient (h_{air}). The methodology of deriving an air heat transfer coefficient (h_{air}) equation based on the CFD modelling and transformer radiator geometry, illustrated in this section, can greatly reduce the uncertainty in the simulations or calculations.

To quantitatively study the effects of h_{air} equations, the simulation results of the reduced CFD model using h_{air} Equation 5-2 and previous empirical equations [80, 83, 93-95, 100-105] were compared. Two extreme conditions of heat dissipation in the experiments in Table 4-5, i.e., Case 1 (minimum heat dissipation) and Case 7 (maximum heat dissipation), are taken as examples. The key parameters, i.e., bottom liquid temperature (T_{bot}) and total heat dissipation (P), calculated by using different h_{air} equations are presented in Table 5-7.

When compared with experimental measurements, the simulations using previously published h_{air} equations overestimate the bottom liquid temperature (T_{bot}) by 0.9 K to 5.2 K, and underestimated the total heat dissipation (P) by 4.3% to 26.3%.

Table 5-7 Reduced radiator CFD simulation results using different h_{air} equations

	Case 1 in Table 4-5 (minimum heat dissipation)		Case 7 in Table 4-5 (Maximum heat dissipation)	
	P (W)	T_{bot} (°C)	P (W)	T_{bot} (°C)
Experiment data	190.0	24.3	1437.0	56.3
h_{air} Equation 5-2	181.0	25.2	1476.0	55.7
h_{air} Equation 5-3 [100]	181.8	25.2	1278.3	58.5
h_{air} Equation 5-4 [80, 83, 93, 101]	170.1	25.7	1220.5	59.3
h_{air} Equation 5-5 [83]	161.6	26.0	1096.0	61.0
h_{air} Equation 5-6 [102]	160.9	26.1	1087.4	61.1
h_{air} Equation 5-7 [95]	160.9	26.1	1087.7	61.1
h_{air} Equation 5-8 [103]	156.9	26.2	1060.0	61.5
h_{air} Equation 5-9 [104]	147.6	26.6	1059.2	61.5
h_{air} Equation 5-10 [105]	153.8	26.4	1074.7	61.3

Previously in [80, 88], the adoption of an h_{air} empirical equation showed a good agreement with the experiments under one loading only condition, such that the simulation results of the reduced model adopted with the Equation 5-3 is comparable to the experimental measurements in Case 1. However, none of the empirical equations in [80, 83, 93-95, 100-105] managed to provide the same reliable calculations of key parameters, under different conditions, as the h_{air} Equation 5-2 developed in Section 5.1.3.

Therefore, an air heat transfer coefficient (h_{air}) equation derived from CFD simulations and based on the transformer radiator geometry is recommended for the radiator thermal modelling, as well as the transformer CCL thermal modelling.

5.3 Influencing Factors on h_{air} Equation

An air heat transfer coefficient (h_{air}) equation has been previously derived from CFD simulations in Section 5.1.3, and the application of the h_{air} equation has been verified by a set of experimental using a mineral oil. It is worth mentioning that the influencing factors on the h_{air} equation are not only loading conditions represented by the top liquid temperature (T_{top}) and total liquid flow rate ($Q_{oil-top}$) as in Section 5.1.3., but also the fluid properties. Documented in the 'Heat Transfer' [95], the heat transfer coefficient is affected by the fluid material properties. There are two kinds of fluids in the radiator modelling, as the insulating liquid and the air.

The influences of the material properties of the insulating liquid are studied by considering different types of the insulating liquid, which is reported in Section 5.3.1. The effect of the air properties is investigated by varying the ambient temperature in Section 5.3.2.

5.3.1 Effect of Type of Insulating Liquid

In this section, the effect of insulating liquid properties on the h_{air} Equation 5-2 is analysed and quantitatively studied by the full radiator CFD simulations. As the same as the mineral oil, the full radiator CFD simulations of the scenarios in Table 5-4 are repeated concerning two different insulating liquids, i.e., a Gas-to-Liquid (Shell Diala S4 ZX-I) and a synthetic ester liquid (MIDEL 7131).

The h_{air} extracted from all radiator CFD simulations of all three insulating liquids are plotted in Figure 5-10 and curve fitted as Equation 5-11.

$$h_{air} = 1.499 \times (T_{avo} - T_{amb})^{0.4158} \qquad \text{Equation 5-11}$$

where h_{air} is the air heat transfer coefficient ($W/(m^2 \cdot K)$), T_{avo} is for average liquid temperature (°C), T_{amb} is for the ambient temperature (°C).

As seen in Figure 5-10, the h_{air} Equation 5-2 curve-fitted with only the mineral oil simulation results matches well with the h_{air} Equation 5-11 obtained by considering all three insulating liquids. The average and maximum h_{air} differences between Equation 5-2 and Equation 5-11 are 0.02 W/(m^2·K) and 0.03 W/(m^2·K), respectively; the average and maximum relative differences h_{air} differences between Equation 5-2 and Equation 5-11 are 0.5% and 0.6 %, respectively. Therefore, the h_{air} Equation 5-2 is applicable to model the thermal behaviour of different insulating liquid by being adopted in a reduced radiator CFD model.

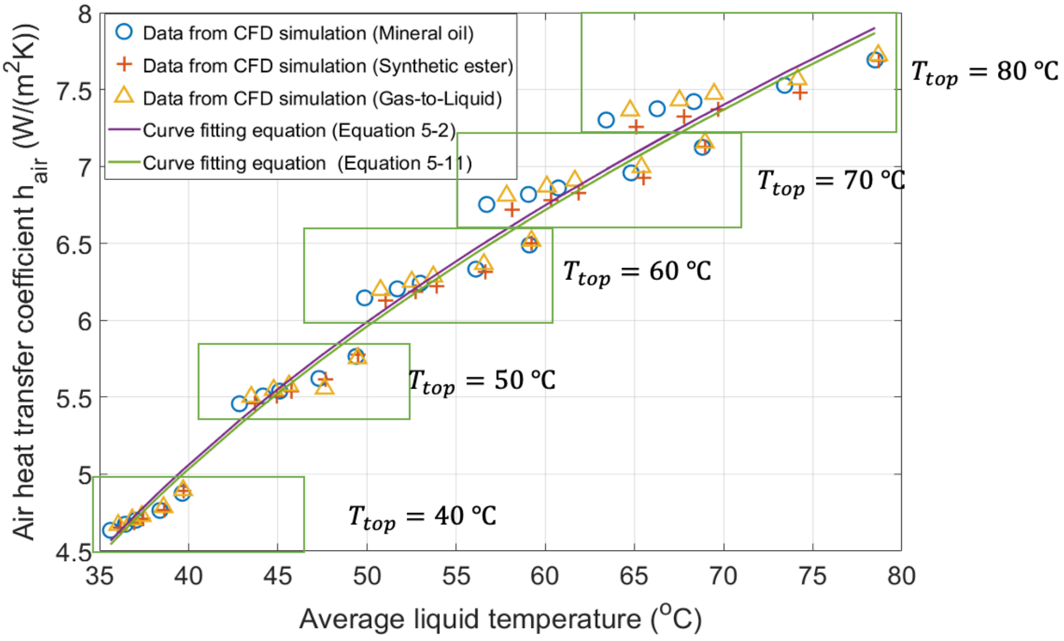

Figure 5-10 Comparison of h_{air} equation of different insulating liquids

The simulation results also indicate that the effect of different insulating liquids on the derived h_{air} equation is negligible. This is because the dominating cooling process of a transformer radiator in air natural (AN) cooling mode is the air convection. The liquid convection, which is affected by the insulating liquid properties, imposes less impact on the overall cooling.

The total liquid flow rate as the $5 \times 10^{-5}\ m^3/s$ is taken as an example, and the total heat dissipation and the average liquid temperatures of all three different insulating liquids are depicted in Figure 5-11 (a) and (b), respectively. The maximum difference of the average liquid temperature among all three liquids is 1.4 K, and the maximum relative different of the total power dissipation is 4.0%. Providing the same top liquid temperature and the total liquid flow rate, there is no significant differences among different insulating liquids.

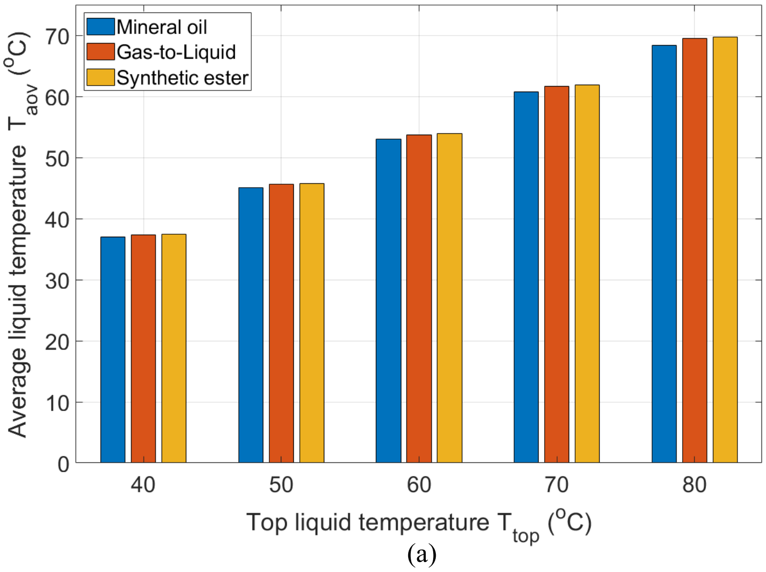

(a)

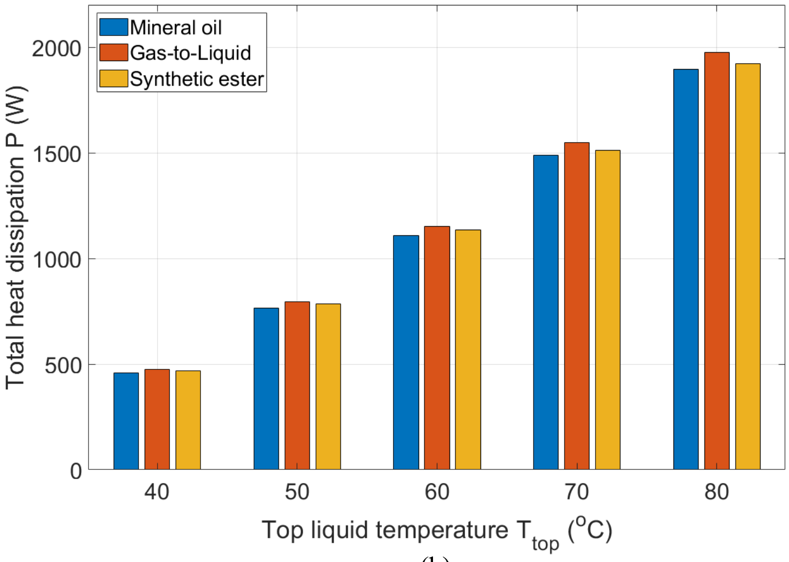

(b)

Figure 5-11 Comparisons of total heat dissipation filled with three different insulating liquids under the total liquid flow rate as $5 \times 10^{-5}\ m^3/s$

5.3.2 Effect of Ambient Temperature

The impact of ambient temperature on Equation 5-2 is analysed by using the verified full radiator CFD model. Apart from the full matrix in CFD parametric study shown in Table 5-4, another two sets of simulations with the mineral oil as the coolant were conducted at ambient temperatures of 0 °C and 40 °C, respectively. The inputs of CFD simulations are given in Table 5-8.

Table 5-8 Input of additional full radiator CFD simulations at different T_{amb}

T_{amb} (°C)	T_{top} (°C)	Q_{oil} (10^{-5} m^3/s)
0	20, 30, 40, 50, 60	5
40	60, 70, 80, 90, 100	5

To eliminate the changes in air properties, i.e. dynamic viscosity (μ), density (ρ) and specific heat capacity (C_p), due to varying the ambient temperatures (T_{amb}), Equation 5-2 is transformed into a dimensionless form using the Nusselt number (N_u) and the Rayleigh number (R_{aL}), as shown in Equation 5-12.

$$N_u = 0.0062 \times (R_{aL})^{0.48} \qquad \text{Equation 5-12}$$

where N_u is the Nusselt number, R_{aL} is the Rayleigh number calculated using the radiator panel length as the geometric characteristic.

The calculated h_{air} from dimensionless Equation 5-12 is compared with the values from CFD simulations in Figure 5-12. Evidently, the air heat transfer coefficient (h_{air}) obtained from the additional simulation matches well with the calculations from Equation 5-12. The average and maximum discrepancies of the air heat transfer coefficient (h_{air}) between Equation 5-12 and additional full CFD simulations are 0.08 $W/(m^2K)$ and 0.18 $W/(m^2K)$, respectively. Therefore, once the h_{air} equation is transformed into a dimensionless form, it can incorporate the effects of ambient temperatures, which would greatly improve the applicability of the equation in practise.

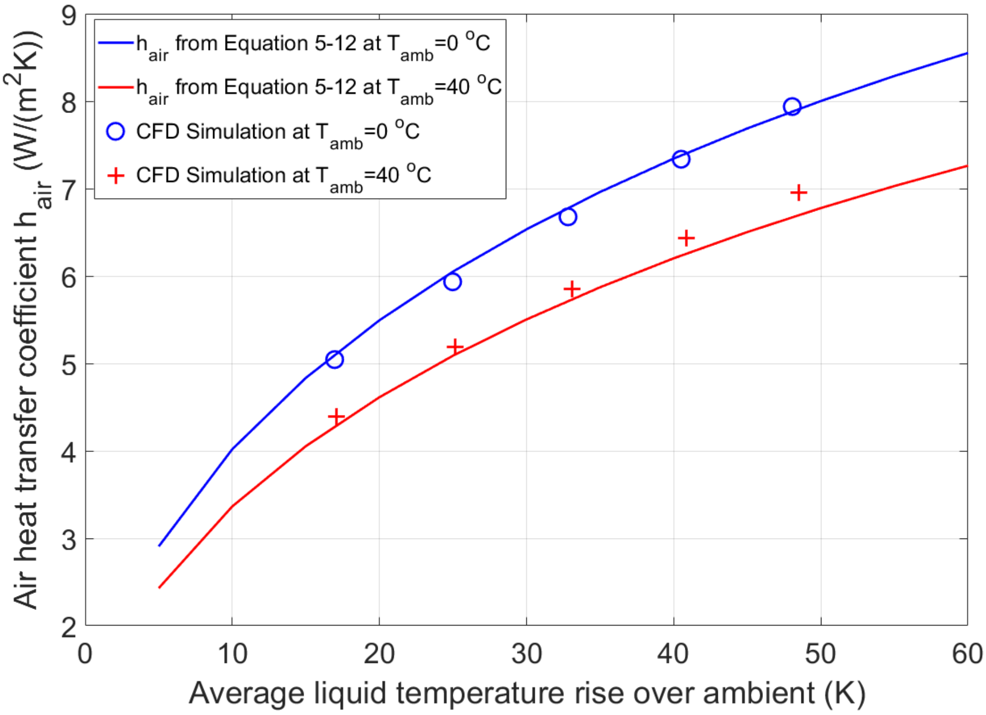

Figure 5-12 Ambient temperature effect on h_{air} equation

As can also be observed from Figure 5-12, the air heat transfer coefficient (h_{air}) decreases as the ambient temperature (T_{amb}) increases. This is mainly because the key material property, dynamic viscosity of air (μ_{air}), positively related to the ambient temperature. The higher dynamic viscosity increases the pressure loss of air when flowing from radiator bottom to top, and thus, it results in a lower air heat transfer coefficient (h_{air}).

However, a lower air heat transfer coefficient (h_{air}) does not necessarily mean that the radiator would dissipate less heat when the ambient temperature (T_{amb}) is high. The bottom liquid temperature rises above ambient temperature (ΔT_{bot}) calculations with different ambient temperatures are plotted in Figure 5-13 (a), where the bottom liquid temperature rises are not affected by the ambient temperatures. Hence, the total heat dissipations are the same according to liquid energy conservation equation (Equation 4-13). The convective heat dissipation (P_{conv}) and radiative heat dissipation (P_{radi}) are shown in Figure 5-13 (b), where the summation of convective and radiative heat dissipation is equal to the total heat dissipation. Although the convective heat dissipation decreases as the ambient temperature drops, the radiative heat dissipation increases when the ambient temperature increases.

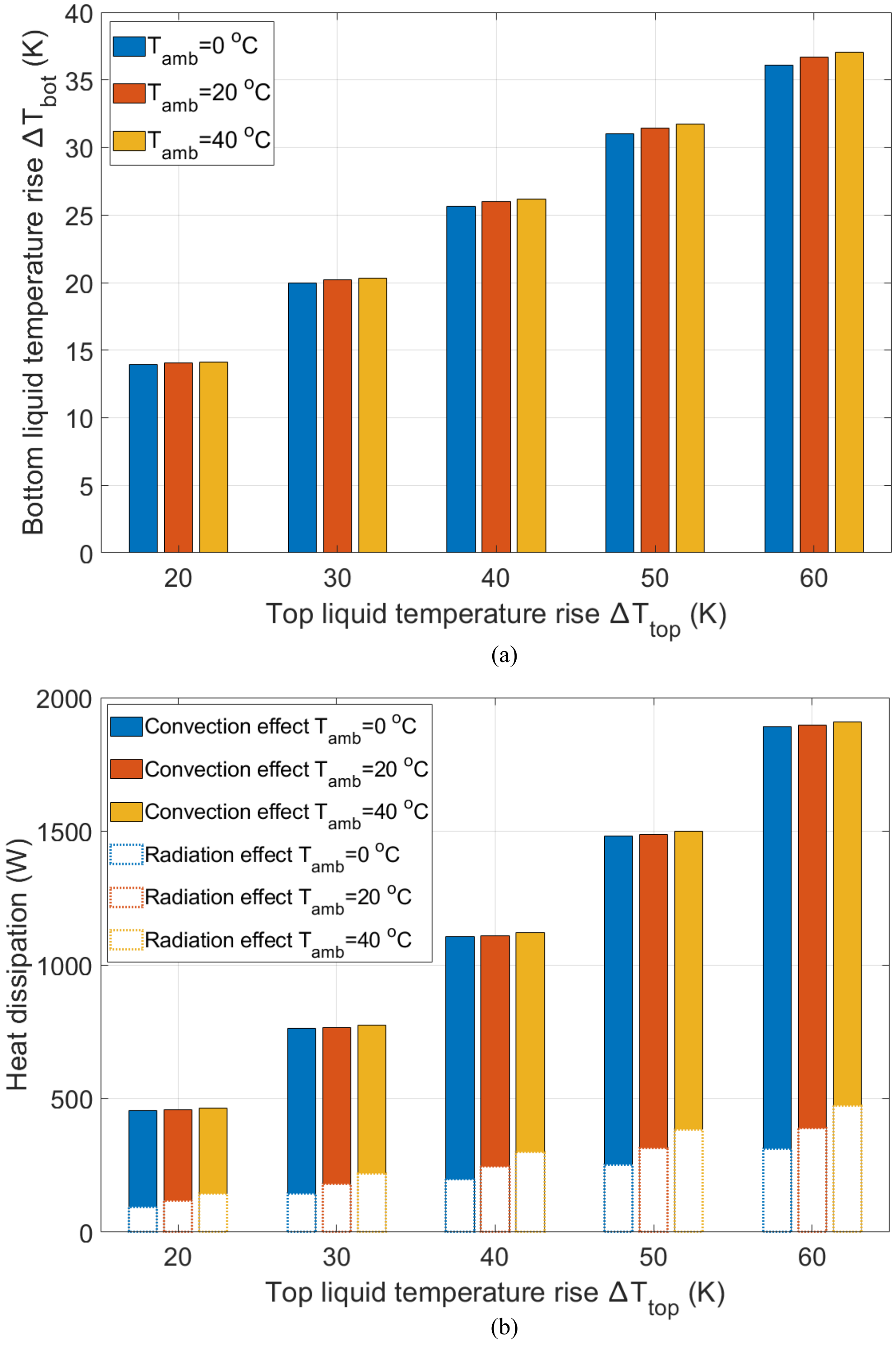

(a)

(b)

Figure 5-13 Simulation results in different ambient temperature (a) bottom liquid temperature rise (b) convective and radiative heat dissipation

This is mainly because of the radiation coefficient (h_{radi}), as expressed in Equation 5-13 and Equation 5-14. An increasing ambient temperature (T_{amb}) results in a higher average liquid temperature (T_{avo}), both of which contribute to a higher radiation heat transfer coefficient (h_{radi}) as expressed in Equation 5-14. Therefore, under a lower ambient temperature, a stronger radiation effect can compensate a weaker convective effect of a transformer radiator. Therefore, the changes of the total heat dissipation would be minor.

$$q_{rad} = A_{out}\sigma\varepsilon\left({T_{avo}}^4 - {T_{amb}}^4\right) = A_{out}h_{radi}(T_{avo} - T_{amb}) \quad \text{Equation 5-13}$$

$$h_{radi} = A_{out}\sigma\varepsilon({T_{avo}}^2 + {T_{amb}}^2)(T_{avo} + T_{amb}) \quad \text{Equation 5-14}$$

where q_{rad} is the heat dissipation by radiation (W/m^2), A_{out} is surface area of outwards facing surface (m^2), σ is for Stefan-Boltzmann constant, ε is for emissivity of transformer radiator, T_{avo} is the average liquid temperature (K), T_{amb} is the ambient temperature (K), h_{radi} is radiation heat transfer coefficient ($W/(m^2 \cdot K)$).

Moreover, to the 4-panel radiator, the ratio of the outwards facing surface area to the radiator surface area is 25%. The simulation results show that the radiative heat dissipation contributes a 16.5% to 31.0% of the total heat dissipation at the present study, which is around the ratio of the surface areas (25%). The conclusion confirms the discussion in Section 2.5.1, as ‘the ratio of the radiative heat dissipation to the total heat dissipation is approximately equal to the ratio of the outwards facing surface area to the radiator total surface area’. It is also worth mentioning that the radiative heat dissipation is not only affected by the radiator geometry, but also by the other factors, e.g., the top liquid temperature and the ambient temperature.

5.4 Summary

The reduced radiator CFD model has been successfully developed, which replaces the air domain simulation by using the air heat transfer coefficient. By analysing the insulating liquid and air flow distributions, it has been advised that a maximum six h_{air} can be considered to represent different kinds of surfaces of a radiator. Therefore, the applications of adopting six h_{air}, two h_{air} and one h_{air} were compared with the experimentally verified full radiator CFD model concerning the bottom liquid temperature, the total heat dissipation and the liquid temperature distribution along the vertical direction. It can be concluded that one h_{air} is sufficient to represent the convection of the complex air flow around the transformer radiator under one loading condition. To represent different loading conditions, an h_{air} equation is obtained by the parametric sweep of the top liquid temperature and total liquid flow rate at the radiator top using the full radiator CFD simulations.

The reduced radiator CFD simulations adopted with the h_{air} equation have been comprehensively verified by both a full radiator CFD model and experiments of different operating conditions. Compared with the full radiator CFD simulations, the differences in the calculations of bottom liquid temperature are within 0.3 K, and mismatch of the total heat dissipation is less than 2.2%. In the experiment verification, the maximum deviations of the bottom liquid temperature and the total heat dissipation introduced by the reduced radiator CFD simulation are 1 K and 6.4 %, respectively. It is also found that the reduced radiator CFD model significantly reduces the processing time compared with the full radiator CFD simulation, from the previous 50 hours to 2 hours at the present.

The CFD parametric study produces a more representative h_{air} equation compared to the existing empirical equations in the literature [80, 83, 93-95, 100-105]. The adoption of the optimised h_{air} equation in the reduced radiator CFD model is the main reason to have a better agreement with experimental results.

Through additional CFD simulations, the derived h_{air} equation is found to be applicable for alternative transformer liquids. Moreover, the ambient temperature effect on the h_{air} equation can be resolved by transforming the equation into a dimensionless form. Such conclusions will be further verified by conducting CCL CFD modelling and the corresponding experimental verification.

Chapter 6 CCL CFD Modelling using the Reduced Radiator Model

A reduced radiator model that adopts an air heat transfer coefficient equation as a replacement of the air flow simulation was developed and experimentally verified in the radiator only scenario in Chapter 5. The reduced radiator model not only reduces the computational demands of modelling, but also ensures the accuracy of the liquid temperature calculation within the radiator. In this chapter, a CCL CFD model integrated with the reduced radiator model will be established and experimentally verified by a set of temperature-rise tests.

Firstly, the development of a CCL CFD model by implementing the reduced radiator model is introduced in terms of the model geometry, the input, the boundary conditions and the mesh refinement strategy in Section 6.1. Next, the data processing is demonstrated by using a case of 800 W power injection (the rated loading condition based on the current density calculation of the winding given in Table 3-3), and the simulation results under different loading conditions are presented in Section 6.2. Section 6.3 focuses on the experimental verification of the CCL CFD simulation results in terms of top, bottom liquid temperatures and the liquid velocity at the winding inlet.

6.1 Development of CCL CFD Model

The CCL CFD model is focused on the calculation of liquid temperature and flow distributions within the CCL, and the results will be experimentally verified by the temperature-rise tests. Therefore, the model geometry should be constructed based on the experimental setup. Following that, the model configuration in terms of inputs, boundary conditions and the coupling process are explained.

6.1.1 Model Geometry

The configuration of the three-dimensional (3D) CCL CFD model with a 0.5 m thermal head is shown in Figure 6-1 (a), and the key dimensions are given by the front view of the model in Figure 6-1 (b). All the components involved in the liquid circulation are considered, i.e. the winding, the 4-panel 1-meter-high radiator, the transparent box and the connecting pipework. During a temperature-rise test, the winding assembly, the transparent box and the connecting pipework are all wrapped with a thermal insulation material, and hence the heat dissipated by these components is negligible. In this case, the temperature gradient across the enclosure or wall of such components can be neglected, and the enclosure and the wall are excluded in the CCL CFD model.

The dimensions of the winding model are $0.12 \times 0.09 \times 0.46\ m$ (x, y and z in Figure 6-1 (a)), and the dimensions of the transparent box are $0.06 \times 0.06 \times 0.10\ m$ (x, y and z in Figure 6-1 (a)). All the connecting pipes are of the same inner diameter, which is 0.0326m, as shown in Figure 6-1 (b).

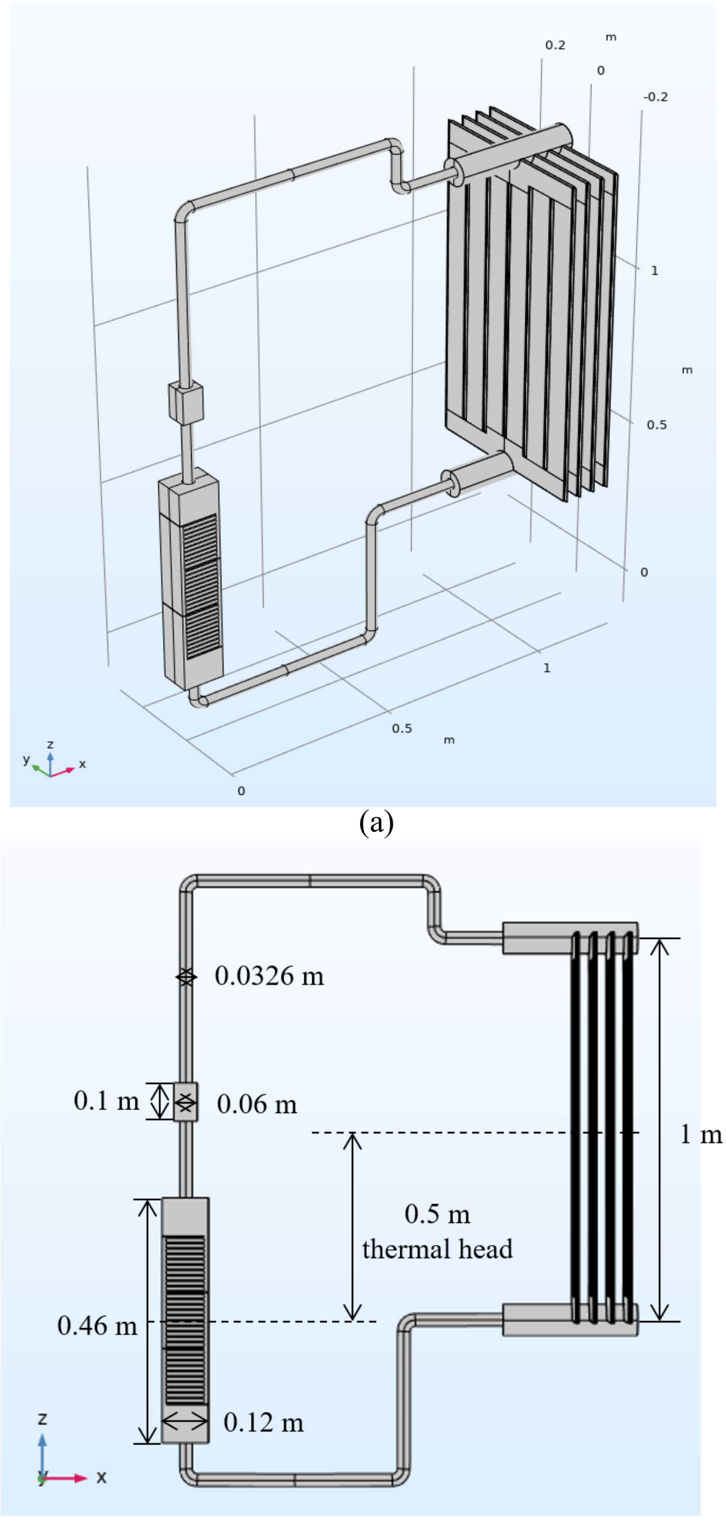

(a)

(b)

Figure 6-1 Configuration of CCL CFD model (a) 3-D drawing (b) front view

In addition, the geometry of the winding disc is modelled as a homogenous block (shown in Figure 6-1 (b), as opposed to the four aluminium bars in the experimental setup (shown in Figure 3-1 in Section 3.1). The simplification of the winding geometry was validated in

[55], in which the calculations of the liquid temperature and flow distributions were proven not affected. This geometric simplification brings the benefits of less computational requirements in terms of meshing and processing time.

The geometry on the radiator side of the CCL CFD model is built the same as the reduced radiator CFD model described in Chapter 5.

6.1.2 Model Setup

The main objective of the CCL CFD model is to simulate the liquid temperature and flow distributions. Therefore, all the heat transfer processes within the liquid should be considered. The insulating liquid is heated by the winding discs via the thermal conduction and convection, and then the heat is transported from the insulating liquid to the radiator domain by thermal conduction and convection. Finally, the heat is dissipated from the radiator to the environment by the thermal conduction, convection and radiation.

In the CCL CFD model, the thermal conduction and convection of the insulating liquid are modelled by conservations of mass, momentum and energy, i.e. Equation 4-5, Equation 4-6 and Equation 4-7 [92].

The thermal conduction at the radiator is governed by the Fourier's law of conduction, Equation 4-2 [95]; the thermal convection effect of the air is constituted by Newton's law of cooling (Equation 5-1 [95]) instead of the air flow CFD simulation; and the thermal radiation is simulated by the Stefan-Boltzmann law, Equation 4-8 [95]. The heat transfer processes and the governing equations on the radiator side of the CCL CFD model are the same as the reduced radiator CFD model.

The model inputs and their setting boundaries of the CCL CFD model are summarized in Table 6-1. The power injection is set by an equivalent heat flux density on the surfaces of each winding disc. In addition, the surfaces of the winding, the transparent box and the connecting pipework are all set as adiabatic, as they are wrapped with thermal insulation material. Due to a symmetric geometry of the CCL experimental setup, it is only necessary to model half of the setup in the CFD model, in which the xz plane at $y = 0.045\ m$ is set as the plane of symmetry. This can significantly reduce the simulation time. The heat dissipation on the radiator side in the CCL CFD simulation is composed of convective and radiative heat dissipation, which are modelled by setting the h_{air} equation and the radiator surface emissivity. And the ambient temperature is also input as a reference temperature in the the Equation 5-1 and Equation 4-8, for determining the convective and radiative heat dissipation, respectively.

Table 6-1 Model inputs and setting boundaries of CCL CFD model

Inputs of CCL CFD model	Setting boundary
Power injection P (W)	Surfaces of each winding disc
h_{air} equation $(W/(m^2 \cdot K))$, emissivity ε	Radiator surfaces
Ambient temperature T_{amb} (°C)	Reference value

It is also important to establish the coupling process between the liquid temperature profile and the air heat transfer coefficient equation (Equation 5-2). In Equation 5-2, the average liquid temperature (T_{avo}) is needed to calculate the air heat transfer coefficient (h_{air}), which in turn also influences the T_{avo}. Therefore, the iterative calculations are conducted between the T_{avo} and the h_{air}. Although the RTD sensors ($T_{bot-mid}$, $T_{bot-inlet}$, $T_{top-outlet}$ and $T_{top-mid}$) for the liquid temperate measurement are included in the CCL CFD model as shown in Figure 6-2, only the temperatures at the top and bottom connecting pipes, i.e. $T_{top-pipe}$ and $T_{bot-pipe}$, are involved in the iterative process of calculating T_{avo}. This is because the liquid temperatures obtained at the middle of the pipes are more stable and less influenced by the local liquid flow than those of the four RTD sensors at the buffer zones. A high stability helps the convergence of CFD simulation through iterations. The convergence criterion is that the relative tolerance of the temperature distribution between two iterations is less than 10^{-3}.

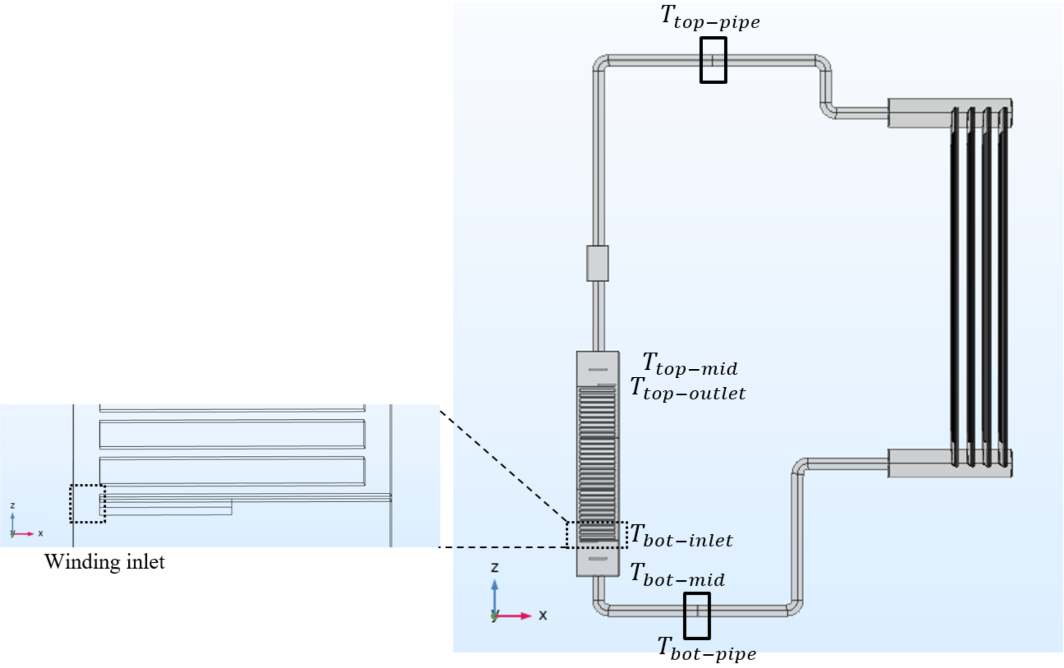

Figure 6-2 Liquid temperatures used for iterative calculations in CCL CFD simulations

All the material properties of the insulating liquid, including density (ρ), specific heat capacity (C_p), thermal conductivity (k) and dynamic viscosity (μ), are temperature dependent. The temperature-dependencies of different liquids used in the CCL CFD simulations are specified by the manufacturers as given in Equation 4-9, Equation 4-10 and Equation 4-11 [96-98].

6.1.3 Mesh Refinement

The CCL CFD model is simulated using the COMSOL Multiphysics (version 5.4), which solves the conservations of mass, momentum and energy with the finite element method. In the CCL CFD simulations, the meshes consist of layers of hexahedral elements for the flow boundary layer and tetrahedral elements for the rest of flow domains. An example of the winding section is zoomed in Figure 6-3.

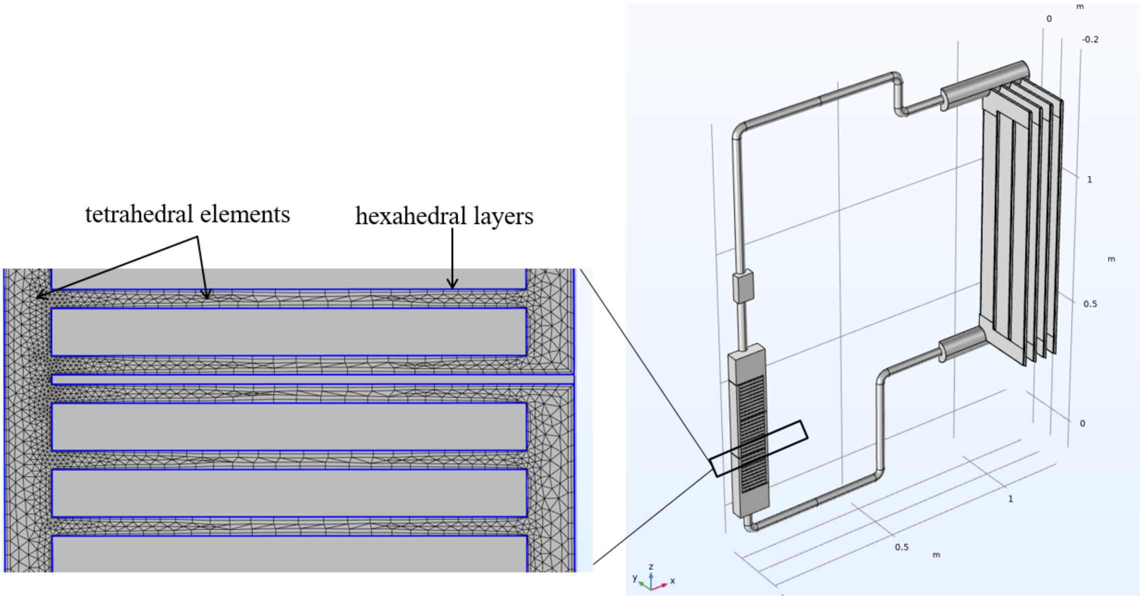

Figure 6-3 Mesh pattern of a CCL CFD model

A benchmark CFD case corresponding to a power injection of 800 W, an ambient temperature of 20 ℃, a thermal head of 0.5 m, and with a mineral oil, is chosen for the mesh refinement study. In the mesh refinement study, the tracking parameters of each mesh size (alternatively the total number of domain elements (N_{de})), are the top and bottom liquid temperatures (T_{top} and T_{bot}) and the liquid velocity at winding inlet (v_{oil}). The results of mesh refinement study are shown in Table 6-2. According to the trend of the tracking parameters varying with the number of domain elements, 'Mesh 4' in Table 6-2 is chosen as the optimal solution. With further increasing the mesh elements from 'Mesh 4', the changes of the liquid temperatures and liquid velocity are within 0.1 K and 0.3%, respectively. Therefore, the pattern of 'Mesh 4' in Table 6-2 is adopted for all CCL CFD model simulations in Chapter 6 and 7.

Table 6-2 Mesh refinement results of a CCL CFD model

Mesh	Mesh 1	Mesh 2	Mesh 3	Mesh 4	Mesh 5
N_{de}	561523	969453	1,833,196	4,951,152	8,579,210
T_{top} (℃)	55.6	55.2	55.1	54.8	54.7
T_{bot} (℃)	37.5	37.9	38.0	38.0	38.0
v_{oil} (m/s)	0.0338	0.0333	0.0336	0.0340	0.0341

6.2 Simulation Results

In this section, simulation results of the CCL CFD modelling under different loading conditions (power injection from 190 W to 1437 W) with a 0.5m thermal head and the mineral oil as a coolant are reported. The exact power injection inputs and the ambient temperatures are referred to the experimental measurements, which are given in Table 4-5. It is noted that under each loading condition, the ambient temperature is slightly different in the experiments. Therefore, the air heat transfer coefficient equation for each loading condition is derived from the dimensionless Equation 5-12 (in Section 5.3.2) and is expressed by Equation 6-1. The air heat transfer coefficient equations under each loading condition are also given in Table 6-3.

$$h_{air} = \frac{0.0062 \times (R_{aL})^{0.48} \times k_{air}}{L} \qquad \text{Equation 6-1}$$

where h_{air} is the air heat transfer coefficient ($W/(m^2 \cdot K)$), R_{aL} is the Rayleigh number using the panel length as the geometric characteristic, k_{air} is the air thermal conductivity ($W/(m \cdot K)$), and L is the panel length as 1 m.

Table 6-3 Inputs of CCL CFD simulations in thermal head as 0.5 m and with a mineral oil

Model input from measurements		Air heat transfer coefficient equation from dimensionless Equation 5-12
Power injection P (W)	Ambient temperature T_{amb} (°C)	Air heat transfer coefficient equation h_{air} ($W/(m^2K)$)
190	20.2	$h_{air} = 1.267 \times (T_{avo} - T_{amb})^{0.4202}$
392	20.0	$h_{air} = 1.27 \times (T_{avo} - T_{amb})^{0.4197}$
600	24.8	$h_{air} = 1.211 \times (T_{avo} - T_{amb})^{0.4281}$
800	20.4	$h_{air} = 1.264 \times (T_{avo} - T_{amb})^{0.4207}$
1022	20.9	$h_{air} = 1.256 \times (T_{avo} - T_{amb})^{0.4219}$
1212	21.2	$h_{air} = 1.251 \times (T_{avo} - T_{amb})^{0.4226}$

1437	25.3	$h_{air} = 1.190 \times (T_{avo} - T_{amb})^{0.433}$

In the CCL CFD simulations, not only the global parameters, i.e., top and bottom liquid temperatures and the liquid velocity, but also the liquid temperature distributions are of great interest. Therefore, how the key parameters and the temperature distribution are extracted is firstly demonstrated by using the 800 W power loss condition as an example. It is worth mentioning that the liquid temperature distribution from the CCL CFD model is obtained by an in-house developed MATALB program. Next, all the simulation results of the global parameters are presented. Moreover, a sensitivity study of the air heat transfer coefficient is also carried out by conducting additional CCL CFD simulations.

6.2.1 Data Processing

The temperature and flow distributions of the insulating liquid, as well as the radiator temperature, are modelled in the CCL CFD model. The radiator and liquid temperature profile under the example condition is shown in Figure 6-4, where the highest liquid temperature is 69.2 ℃ and the lowest radiator surface temperature is 33.7 ℃. As observed in Figure 6-4, liquid temperature is increasing from the winding bottom to the top, and then decreasing from the radiator top to bottom. As the boundaries of the connecting pipework and the transparent box are modelled as adiabatic, the liquid temperature does not change when flowing through those components.

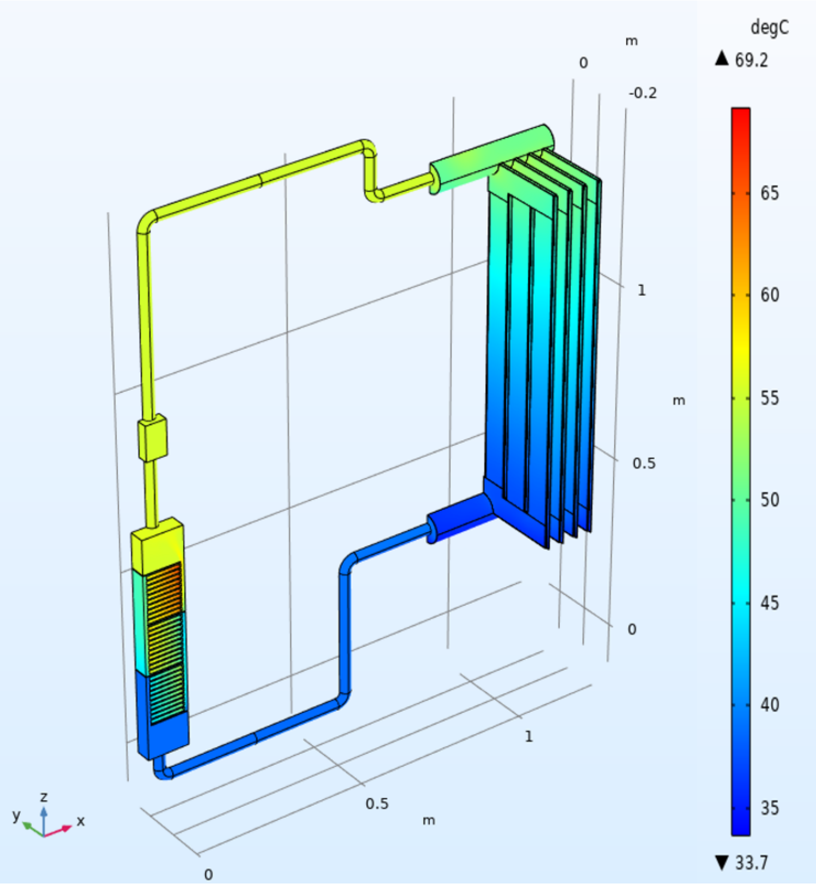

Figure 6-4 Temperature profile of CCL CFD simulation under the example condition

In the CCL CFD simulations, the top and bottom liquid temperatures and the liquid velocity at the winding inlet are the key parameters, because they are essential for a winding only CFD model to further estimate the hot-spot temperature and its location.

As previously introduced, all 4 RTD sensors ($T_{bot-mid}$, $T_{bot-inlet}$, $T_{top-outlet}$ and $T_{top-mid}$ in Figure 6-2) for liquid temperature measurements are included in the CCL CFD model, whereas the iteration between the average liquid temperature and air heat transfer coefficient is coupled by using the liquid temperatures at the middle of top and bottom connecting pipes. The liquid temperatures extracted at different locations are herein compared under the example condition.

The temperature of each RTD sensor is calculated by a volumetric average temperature directly from the CFD software (COMSOL Multiphysics version 5.4). The liquid temperatures of the cross-sections at the middle of the top and bottom connecting pipes ($T_{top-pipe}$ and $T_{bot-pipe}$ in Figure 6-2) are extracted by the in-house developed MATLAB program. On each cross-section, the temperatures are captured at every 0.1 mm in both y

and z directions, and then 440 temperatures in total are averaged to represent the $T_{top-pipe}$ / $T_{bot-pipe}$.

The results of the liquid temperatures from the CCL CFD simulation under the example condition are given in Table 6-4. As illustrated from the table, $T_{bot-mid}$ and $T_{bot-inlet}$ are identical to $T_{bot-pipe}$, whereas a slight difference, 0.25 K, has been observed between $T_{top-outlet}$ and $T_{top-mid}$ due to the localised flow distribution. Moreover, insignificant differences, which are less than 0.25 K, is found among all three top liquid temperatures, i.e. $T_{top-pipe}$, $T_{top-outlet}$, and $T_{top-mid}$. To further investigate the liquid temperatures under different conditions, which will be presented in Chapter 7, the liquid temperatures at the middle of the top/bottom pipes ($T_{top-pipe}$ and $T_{bot-pipe}$) are used to represent the top/bottom liquid temperatures (T_{top} and T_{bot}).

Table 6-4 liquid temperatures from the CCL CFD simulation under the example condition

Power input	Liquid temperatures extracted in buffer zone				Liquid temperatures extracted at the middle of connecting pipework	
P (W)	$T_{bot-mid}$ (°C)	$T_{bot-inlet}$ (°C)	$T_{top-outlet}$ (°C)	$T_{top-mid}$ (°C)	$T_{bot-pipe}$ (°C)	$T_{top-pipe}$ (°C)
800	38.61	38.61	55.26	55.51	38.61	55.29

The liquid velocity (v_{oil}) is extracted from the CCL CFD simulation at the winding inlet as shown in Figure 6-2 (dimensions as $9 \times 10\ mm$ in x and y directions) every 0.5 mm both in x and y directions, and then the velocities at all 360 points are averaged. In the example condition, the liquid velocity (v_{oil}) extracted at the inlet of the bottom pass is 0.0342 m/s. The liquid velocity is also calculated from Equation 3-3 (energy conservation equation) by using the top and bottom liquid temperatures in Table 6-4, as 0.0337 m/s in the example condition. Evidently, there is a negligible difference between two liquid velocities, whose absolute and relative differences are 0.0005 m/s and 1.5% respectively. To investigate the liquid velocity under different conditions in Chapter 7, the liquid velocity (v_{oil}) extracted at the winding inlet is used.

Apart from the top and bottom liquid temperatures (T_{top} and T_{bot}) and the liquid velocity (v_{oil}), the liquid temperature distribution is also vital due to the following reasons:

- Liquid temperature profile within the winding can determine whether a 3D or a 2D winding only CFD model should be built to study the hot-spot temperature and its location, which will be discussed later in this section;
- Liquid temperature distribution of the CCL helps estimate the thermosiphon pressure, which can be used to analyse the liquid velocity [38, 72].

The liquid temperatures within the winding are extracted from the CCL CFD simulation at two sliced xz-planes, one is on the surface ($y = 0\ m$) and the other is at the middle of the winding ($y = 0.045\ m$). The liquid temperature at the xz-plane at $y = 0.045\ m$ is taken as an example and shown in Figure 6-5 (a). The liquid temperature colour contour at the first three horizontal cooling ducts of the 2nd winding pass are shown in Figure 6-5 (b).

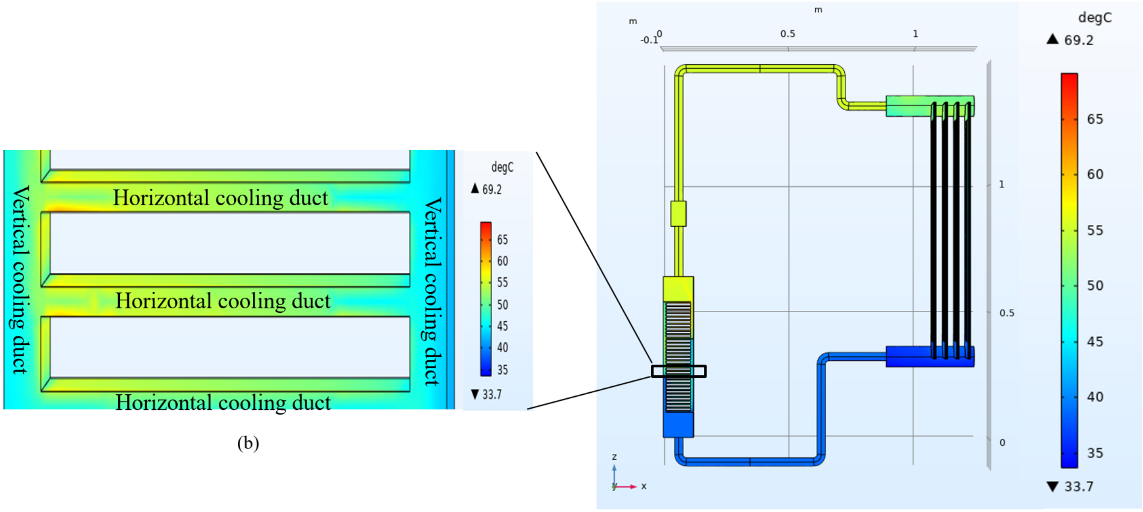

(b)

(a)

Figure 6-5 Liquid temperature extraction (a) liquid temperature distribution in the CCL (b) zoomed in liquid temperature at the horizontal and vertical cooling ducts

The liquid temperature at the two sliced xz-planes is extracted as the surface average temperature in each horizontal cooling duct. For each horizontal cooling duct at the two xz-planes ($y = 0\ m$ and $y = 0.045\ m$), liquid temperatures are captured every 5 mm and 0.5 mm in the x and z directions, respectively. The liquid temperature of each horizontal cooling duct is then calculated as the average of all 160 temperatures within the same cooling duct. Figure 6-6 shows the liquid temperatures of each horizontal cooling duct from the winding bottom to the top at the two xz-planes.

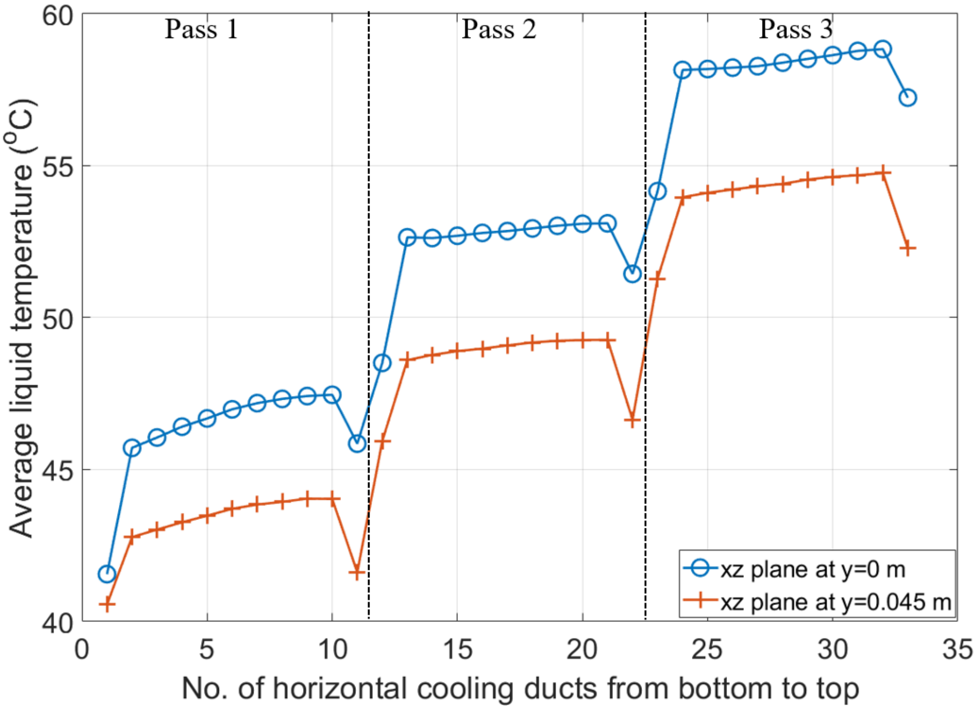

Figure 6-6 Liquid temperature distribution at each horizontal cooling duct at two sliced cross-section

As seen in Figure 6-6, the liquid temperatures at two cross-sections have the similar distributions from pass 1 to pass 3. However, there is an obvious temperature increase in the y direction, and the temperature differences between the two cross-sectional planes are from 1.0 to 5.0 K. Therefore, the liquid temperature within the winding under the example condition is in a 3D distribution. Consequently, the winding only CFD model for studying the hot-spot temperature has to be built in 3D.

As discussed in the IEC standard [24] and literature [38, 72], the liquid temperature along the winding height can be assumed as a linear distribution. Specifically in [38, 72], the liquid temperature distribution in the radiator was also assumed to be linear. Based on these assumptions, an analytical equation was proposed to estimate the liquid velocity for the natural cooled transformer.

In the CCL CFD simulation under the example condition, the 3D liquid temperature distribution along the winding vertical direction is extracted. Different to the liquid temperature extraction on the xz-planes shown in Figure 6-6, the 3D liquid temperatures within the winding are captured at every 5 mm, 3 mm and 0.5 mm in x, y and z directions in each horizontal cooling duct. At the same height (z direction), the liquid temperatures at 300 positions are averaged, the distribution of which is shown in Figure 6-7 (a). The liquid temperature within the radiator is also extracted at every which 0.5 mm, 5 mm and 10 mm in x, y and z directions, how the liquid temperatures are extracted is presented in details in Section 4.2.1. And its distribution along vertical direction (z direction) is shown in Figure 6-7 (b).

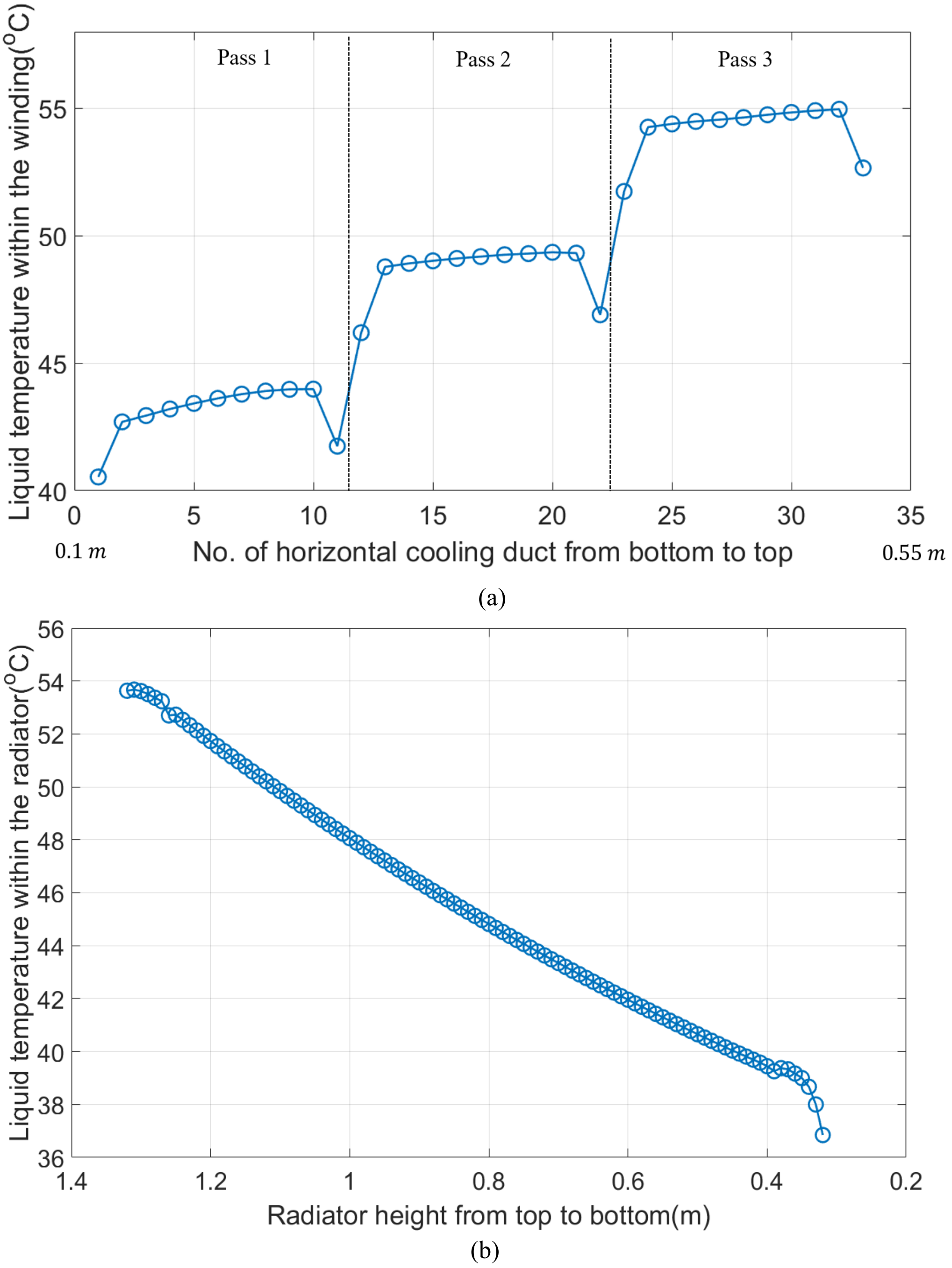

(a)

(b)

Figure 6-7 Liquid temperature distribution from the CCL CFD simulation under the example condition (a) within winding (b) within radiator

As seen in Figure 6-7 (a), under the example condition, the liquid temperature within the winding cannot be analysed as a linear distribution. A clear temperature gradient is observed between the adjacent passes, which is due to the zig-zag flow fashion within the winding. As for the liquid temperature in the radiator in the example condition, the liquid temperature distribution along the vertical direction is approximately linear. The understandings of the liquid temperature in the winding and the radiator under various conditions can help identifying the limitations in the analytical method developed in [38, 72].

6.2.2 Global Parameters under Different Loading Conditions

The global parameters, i.e., bottom, top liquid temperatures and liquid velocity at the winding inlet (v_{oil}), of the CCL CFD simulations under different loading conditions are summarised in Table 6-5. The power injections were changing from 190 W to 1437 W, corresponding to the loading condition from 0.5 p.u. to 1.3 p.u.. The ambient temperature is varied from 20.0 °C to 25.3 °C.

Table 6-5 Results of CCL CFD simulations under 0.5 m thermal head and with a mineral oil

Input conditions		CCL CFD simulations		
Power injection P (W)	Ambient temperature T_{amb} (°C)	Top liquid temperature T_{top} (°C)	Bottom liquid temperature T_{bot} (°C)	Liquid velocity at winding inlet v_{oil} (m/s)
190	20.2	34.5	24.8	0.0143
392	20.0	42.4	29.4	0.0218
600	24.8	53.5	39.2	0.0300
800	20.4	55.3	38.6	0.0342
1022	20.9	61.4	42.7	0.0391
1212	21.2	67.2	47.3	0.0437
1437	25.3	76.3	55.7	0.0494

As seen in Table 6-5, in different loading conditions, the top liquid temperatures are between 34.5 °C and 76.3 °C, whilst the bottom liquid temperature is ranging from 24.8 °C to 55.7 °C. The liquid temperature rise is varied from 9.7 K to 20.6 K, which is close to the liquid natural cooled power transformer. The liquid velocity at the winding inlet is from 0.0143 m/s to 0.0494 m/s. It also should be noted that such a range of the liquid velocity is too low to be measured accurately by the commercial flow meters.

6.2.3 Sensitivity Study

In the curve-fitting process of the air heat transfer coefficient equation introduced in Section 5.1.3, the maximum difference of the air heat transfer coefficient between the data and the curve-fitted equation (Equation 5-2) is 0.3 $W/(m^2 \cdot K)$. To study the influences of the deviations (less than 0.3 $W/(m^2 \cdot K)$) of the air heat transfer coefficient on the CCL CFD modelling, a sensitivity study is conducted under the minimum and maximum power injections, which are 190 W and 1437 W, respectively. In each of these two cases, the power injection and the ambient temperature are kept the same, whilst a ±0.3 $W/(m^2 \cdot K)$ is added in the air heat transfer coefficient equation. The 0.3 $W/(m^2 \cdot K)$ contributes to a 9.3% change of the h_{air} under 190 W power injection, whilst it makes a 5.1% variation of the h_{air} under 1437 W power injection. Table 6-6 presents the model inputs and simulation results. As observed from the simulation results, the changes in the liquid temperatures and liquid velocity caused by the ±0.3 $W/(m^2 \cdot K)$ variations of air heat transfer coefficient are less than 1 K and 0.7%, respectively. This confirms that the reduced radiator CFD model using the h_{air} equation is satisfactory in the CCL CFD model.

Table 6-6 CCL CFD simulation results of the sensitivity study of air heat transfer coefficient

Model input			Simulation results		
P (W)	T_{amb} (°C)	h_{air} $(W/(m^2K))$	T_{top} (°C)	T_{bot} (°C)	v_{oil} (m/s)
190	20.2	$h_{air} = 1.267 \times (T_{avo} - T_{amb})^{0.4202} - 0.3$	34.9	25.1	0.0143
190	20.2	$h_{air} = 1.267 \times (T_{avo} - T_{amb})^{0.4202}$	34.5	24.8	0.0143
190	20.2	$h_{air} = 1.267 \times (T_{avo} - T_{amb})^{0.4202} + 0.3$	34.3	24.5	0.0142
1437	25.3	$h_{air} = 1.190 \times (T_{avo} - T_{amb})^{0.433} - 0.3$	77.2	56.7	0.0496
1437	25.3	$h_{air} = 1.190 \times (T_{avo} - T_{amb})^{0.433}$	76.3	55.7	0.0494

1437	25.3	$h_{air} = 1.190 \times (T_{avo} - T_{amb})^{0.433} + 0.3$	75.5	54.8	0.0492

6.3 Experimental Verification

This section reports the experimental verification of the developed CCL CFD simulations. A set of temperature-rise tests with a 0.5 m thermal head design and filled with a mineral oil were carried out under 7 loading conditions. The same conditions were used in the CCL CFD simulations shown in Section 6.2.

Table 6-7 compares the top and bottom liquid temperatures (T_{top} and T_{bot}) between the experiments and the CCL CFD simulations. The top/bottom liquid temperature from measurements is the average value of readings of two sensors in the last one hour. Therefore, the top/ bottom liquid temperature is the average value of 120 readings. The values in Table 6-7 shows the average value, and the maximum and minimum value of all 120 readings are given in the square bracket.

As seen in Table 6-7, the temperature differences between the experiments and CCL CFD simulations are from 0.2 K to 2.2 K. These discrepancies are resulted from following two reasons:

- Uncertainties from the air heat transfer coefficient (within 1 K, given in Section 6.2.3);
- Uncertainties of the sensors and the locations of sensors for liquid temperature measurements (given as the temperature variation in Table 6-7).

Table 6-7 Liquid temperature comparison between CCL CFD simulation and experimental measurements

Experimental measurements				CCL CFD simulation results	
$P\ (W)$	T_{amb} (℃)	T_{top} (℃)	T_{bot} (℃)	T_{top} (℃)	T_{bot} (℃)
190	20.2	32.8 [31.9-33.5]	24.3 [23.4-24.8]	34.5	24.8
392	20.0	40.2 [39.1-41.2]	28.7 [27.6-29.5]	42.4	29.4
600	24.8	51.8 [51.0-52.5]	38.1 [37.9-38.4]	53.5	39.2
800	20.4	55.0 [54.2-55.2]	38.5 [37.9-38.8]	55.3	38.6

1022	20.9	62.0 [61.4-62.5]	44.5 [44.0-45.0]	61.4	42.7
1212	21.2	66.6 [65.8-68.1]	47.8 [47.5-48.5]	67.2	47.3
1437	25.3	76.2 [75.4-77.4]	56.3 [55.9-56.8]	76.3	55.7

The liquid velocities from the temperature-rise tests and the CCL CFD simulations are compared in Table 6-8. As seen in Table 6-8, the absolute differences of the liquid velocity between CCL CFD simulations and the experimental measurements are less than 0.0022 m/s, and the relative differences are within 12.3%.

As previously introduced in Section 3.3.3, the liquid velocity in the experiment is calculated by the energy conservation equation, as Equation 3-3. In Equation 3-3, the liquid velocity is in an inverse relationship with the liquid temperature rise (ΔT_{oil}). By using the maximum and minimum liquid temperatures (T_{top} and T_{bot}) in Table 6-7, the ranges of the calculated liquid velocity can be determined using Equation 3-3. It should be noted that the minimum liquid velocity is corresponding to the maximum liquid temperature rise, which is derived by the maximum top liquid temperature and minimum bottom liquid temperature. As for the maximum liquid velocity, the minimum top liquid temperature and maximum bottom liquid temperature are used.

The ranges of the liquid velocities under different experimental conditions are given in the square bracket in Table 6-8. As observed from the table, the liquid velocities from the CCL CFD simulations are all in the ranges of the liquid velocities from the experiments.

Table 6-8 Liquid velocity comparison between CCL CFD simulation and experimental measurements

Experimental measurements		Liquid velocity calculated from the measurements using Equation 3-3	CCL CFD simulations
P (W)	T_{amb} (℃)	v_{oil} (m/s)	v_{oil} (m/s)
190	20.2	0.0163 [0.0137-0.0196]	0.0143
392	20.0	0.0240 [0.0208-0.0296]	0.0218
600	24.8	0.0311 [0.0292-0.0339]	0.0300
800	20.4	0.0348 [0.0328-0.0369]	0.0342

1022	20.9	0.0410 [0.0388-0.0438]	0.0391
1212	21.2	0.0450 [0.0410-0.0490]	0.0437
1437	25.3	0.0498 [0.0461-0.0533]	0.0494

6.4 Summary

In this Chapter, a CCL CFD model is developed based on the reduced radiator CFD model to calculate the liquid flow and temperature distributions within the CCL. An in-house MATLAB program is developed to extract the liquid temperature distribution of the winding and the radiator within the CCL. It is worth emphasizing that the liquid temperature distribution within the winding can help identify whether a further winding only CFD model can be modelled as 2D or 3D. The liquid temperature profiles of the winding and the radiator benefit the analysis of the thermosiphon pressure, which is essential to calculate the liquid velocity.

The CCL CFD model has been successfully verified by a set of experiments under different loading conditions with a thermal head of 0.5 m and a mineral oil. The maximum difference of top and bottom liquid temperatures between simulations and experiments is 2.2 K, and the mismatch of the liquid velocity is less than 12.3%. These discrepancies between the CCL CFD simulations and the experimental measurements are mainly caused by (1) uncertainties of the sensors and the sensor locations of the liquid temperature measurement in the experiment (2) a variation of h_{air} value as $\pm 0.3\ W/(m^2 \cdot K)$ from the h_{air} equation. It should also be noted liquid velocities from the CCL CFD simulations are all in the ranges of the calculated liquid velocities from the experiments, where these ranges are determined from the variation of the liquid temperature measurements.

Chapter 7 Liquid Temperatures and Velocity in CCL Models under Various Conditions

In Chapter 6, the methodology of a CCL CFD modelling was developed, which was experimentally verified under the conditions of 0.5 m thermal head, a mineral oil filling and different loading levels. To further investigate the applicability of the CCL CFD model and understand the liquid thermal behaviours, CFD simulations are carried out under a wide range of conditions, including 14 loading levels, 3 thermal heads, 5 ambient temperatures and 3 insulating liquids. Correspondingly, the experiments in this Chapter were conducted under 7 loading levels, 3 thermal heads and 3 insulating liquids.

The effect of loading conditions on liquid temperatures and velocity are reported in Section 7.1, followed by the effect of thermal head in Section 7.2. Next, a set of CFD simulations are conducted in Section 7.3 to study the impact of the ambient temperature on the liquid temperatures and the velocity. In Section 7.4, the thermal performances of three insulating liquids are compared in terms of the liquid temperatures and velocity under the KNAN cooling mode. It should be emphasized that the trends of the liquid temperatures and the velocities are focused, and hence, the influencing parameter in each section is the only variable in the CCL CFD simulations (except in Section 7.3, the ambient temperature in all the others simulations are set as 20 ℃). In the experiments, the power injections have a maximum 5% fluctuation, and the ambient temperatures in all 61 sets of experiments are varied from 18.1 ℃ to 25.3 ℃.

7.1 Effect of Loading Conditions

The loading conditions are represented by the total power loss within the winding, and which is the focus in this section. The CCL CFD simulations are conducted to study the effect of the loading conditions, which are parametrically swept from 100 W to 1400 W with an interval of 100 W (14 cases in total). To study the impacts of the loading conditions only, the ambient temperature in all 14 CCL CFD simulations is fixed as 20 ℃ to avoid the influences of the ambient temperature. Hence, the air heat transfer coefficient equation used for the CCL CFD simulations in this section is the same, which was given in Equation 5-2.

7 sets of experiments (with a 0.5 m thermal head and a mineral oil filling) are used in this section, in which the power losses are varied from 190 W to 1437 W, and the ambient temperature is in the range from 20.0 ℃ to 25.3 ℃. The experimental results in this section are the same as in Chapter 6. However, different to the focus on the model verification in Section 6.3, the experimental results in this section are used to analyse the trends of the liquid temperatures and velocities under different loading conditions.

As the ambient temperatures in the experiments are slightly higher than the ones used in the CFD simulations, the liquid temperature rises over the ambient temperature ($T - T_{amb}$) instead of the absolute temperatures are compared, including top liquid temperature rises ΔT_{top} in Figure 7-1 (a), bottom liquid temperature rises ΔT_{bot} in Figure 7-1 (b), and the liquid temperature rise $\Delta T_{oil} = T_{top} - T_{bot}$ in Figure 7-1 (c). It is observed that ΔT_{top} and ΔT_{bot} from the CCL CFD simulations are very close to those from the experimental measurements. ΔT_{oil} from the CFD simulations are slightly higher than those from the experimental results. ΔT_{oil} shows an exponential relationship with the total power loss. Summing up the results in Figure 7-1 (a), (b) and (c), the maximum differences of ΔT_{top}, ΔT_{bot} and ΔT_{oil} are 2.5 K, 1.8 K and 1.7 K.

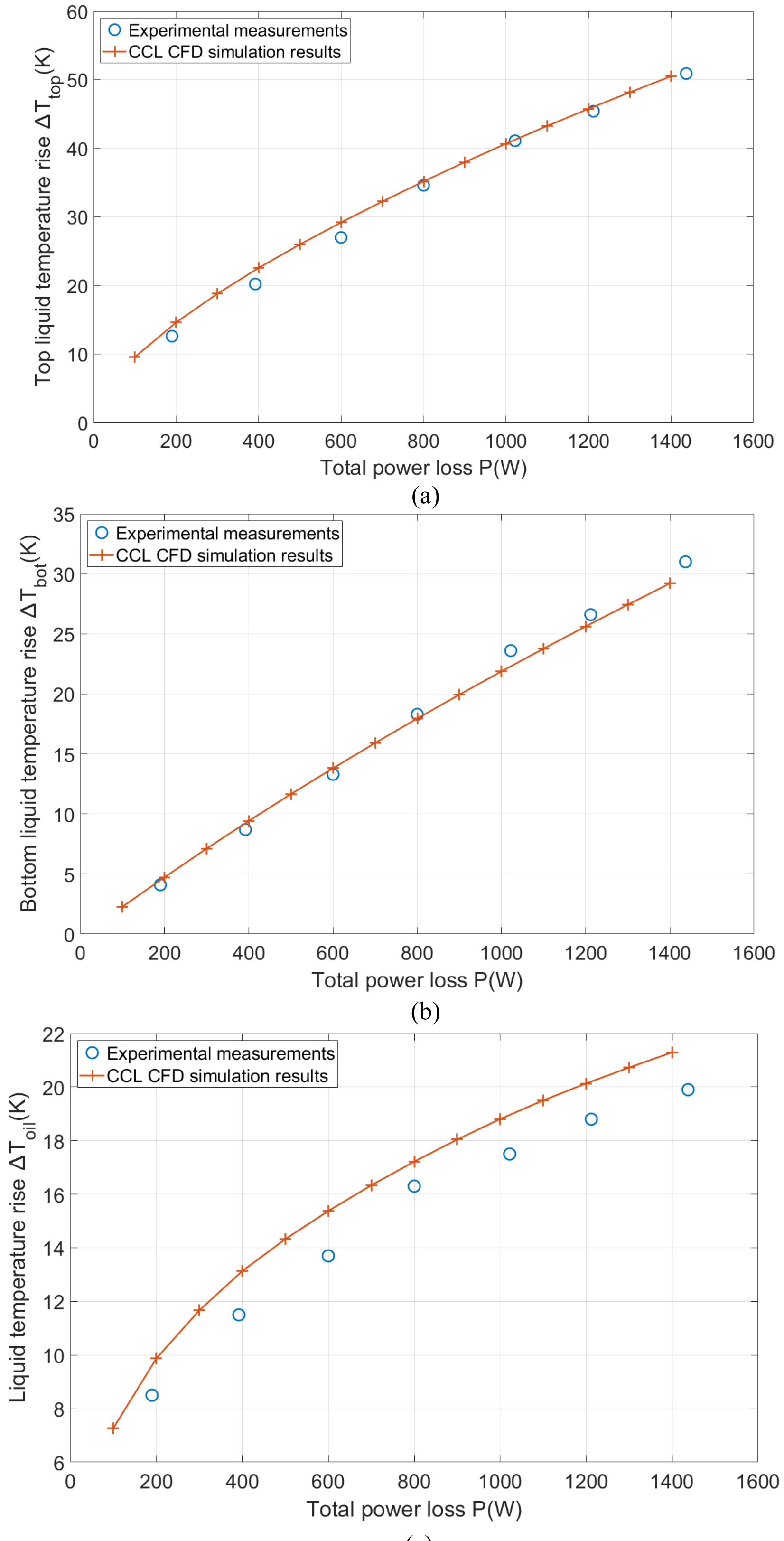

(a)

(b)

(c)

Figure 7-1 Comparison of liquid temperature rises between CFD simulations and experimental measurements, 0.5 m thermal head, mineral oil (a) top liquid temperature rise (b) bottom liquid temperature rise (c) liquid temperature rise

The comparison of the liquid velocity between the CCL CFD simulations and the experiments is shown in Figure 7-2. Figure 7-2 (a) presents a relationship between the liquid velocity (v_{oil}) and the total power loss, and Figure 7-2 (b) depicts the v_{oil} versus the square root of the total power loss ($\sqrt{P}$). The values of the v_{oil} in the CFD simulations and experiments are close; the maximum absolute difference between the simulations and the experiments is 0.0030 m/s.

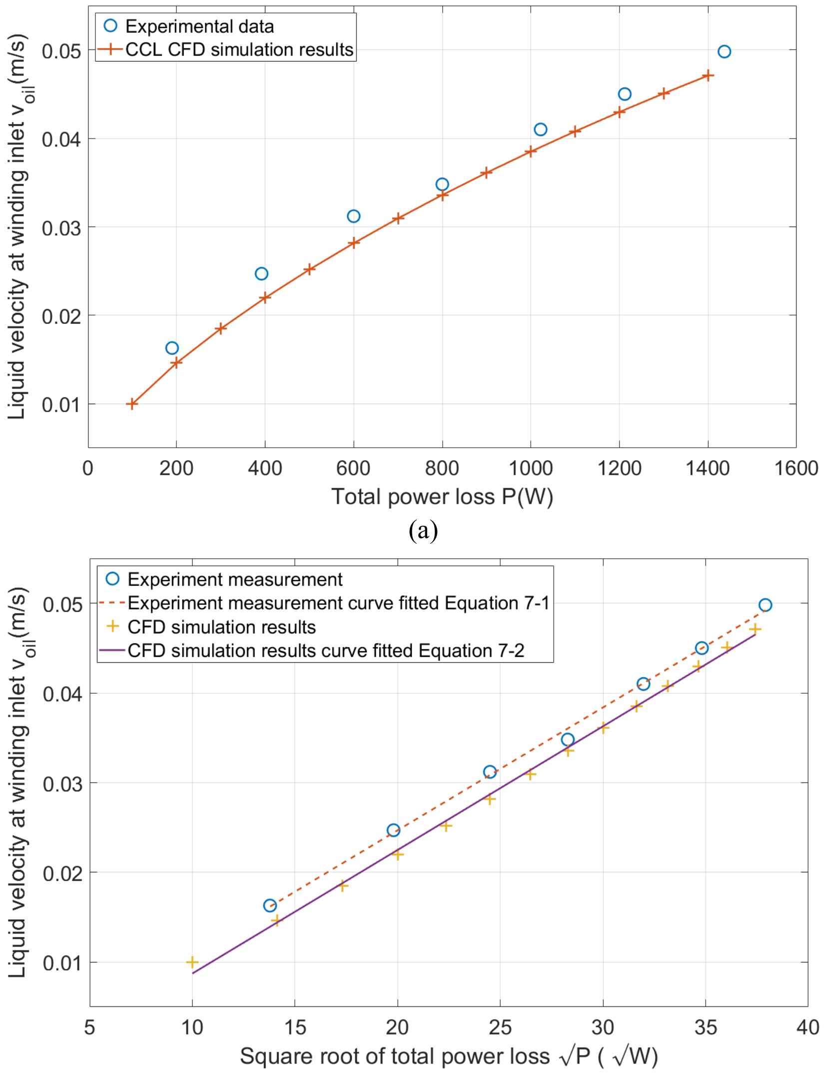

(a)

(b)

Figure 7-2 Liquid velocity between CFD simulations and experimental measurements in a 0.5 m thermal head with a mineral oil (a) velocity against power loss (b) velocity against square root of power loss

v_{oil} against $\sqrt{P}$ from experiments and CCL CFD simulations are both least-square curve-fitted, as expressed in Equation 7-1 and Equation 7-2, respectively. The coefficients of the determination (R^2) in the curve fitting processes of both equations are 0.99; and the maximum differences between the original data and curved fitted equation are 0.0010 m/s and 0.0006 m/s for Equation 7-1 and Equation 7-2, respectively. As indicated in Equation 2-15 [72], the liquid velocity was assumed to be approximately proportional to $\sqrt{P}$. And it is evidently observed that v_{oil} is in a linear relationship with $\sqrt{P}$ from both the experimental measurements and the CCL CFD simulations.

$$\mathrm{v}_{oil-Exp} = 0.0014\sqrt{P} - 0.0027 \qquad \text{Equation 7-1}$$

$$\mathrm{v}_{oil-CFD} = 0.0013\sqrt{P} - 0.0051 \qquad \text{Equation 7-2}$$

where $\mathrm{v}_{oil-Exp}$ is the liquid velocity from the experiments (m/s), $\mathrm{v}_{oil-CFD}$ is the liquid velocity from the CCL CFD simulations (m/s), $\sqrt{P}$ is the square root of the power loss ($\sqrt{W}$).

7.2 Effect of Thermal Heads

Thermal head, referred to as the height difference of the middle of the winding and the middle of the radiator, is one of the key geometric parameters to the ONAN/KNAN transformer thermal design. In this section, the influences of the thermal head on the liquid temperatures and liquid velocity are studied by both CCL CFD simulations and experiments. The effects of three thermal heads, i.e., 0.3 m, 0.5 m and 0.7 m, are investigated. For the CCL CFD simulations at each thermal head, there are 14 power injections simulated from 100 W to 1400 W, where the ambient temperature is 20 ℃ and the h_{air} equation are the same as given in Equation 5-2. In the experiments at each thermal head, there are 7 power injections from around 190 W to 1442 W, and the ambient temperature is in the range from 20.0 to 25.3 ℃. In total, the results of 42 CFD simulations and the measurements of 21 sets of the experiments (both with a mineral oil) and are presented in this section.

Liquid temperature rises, ΔT_{top} , ΔT_{bot} and ΔT_{oil} , from both the experimental measurements and the CCL CFD simulations are compared in Figure 7-3. At different thermal heads, the trends of ΔT_{top}, ΔT_{bot} and ΔT_{oil} versus total power loss are the same. ΔT_{oil} shows exponential relationship with the total power loss. It is also worth emphasizing that the CCL CFD simulations with different thermal heads are also comparable with the experimental measurements. The maximum differences of ΔT_{top}, ΔT_{bot} and ΔT_{oil} are 2.6 K, 0.8 K and 2.2 K.

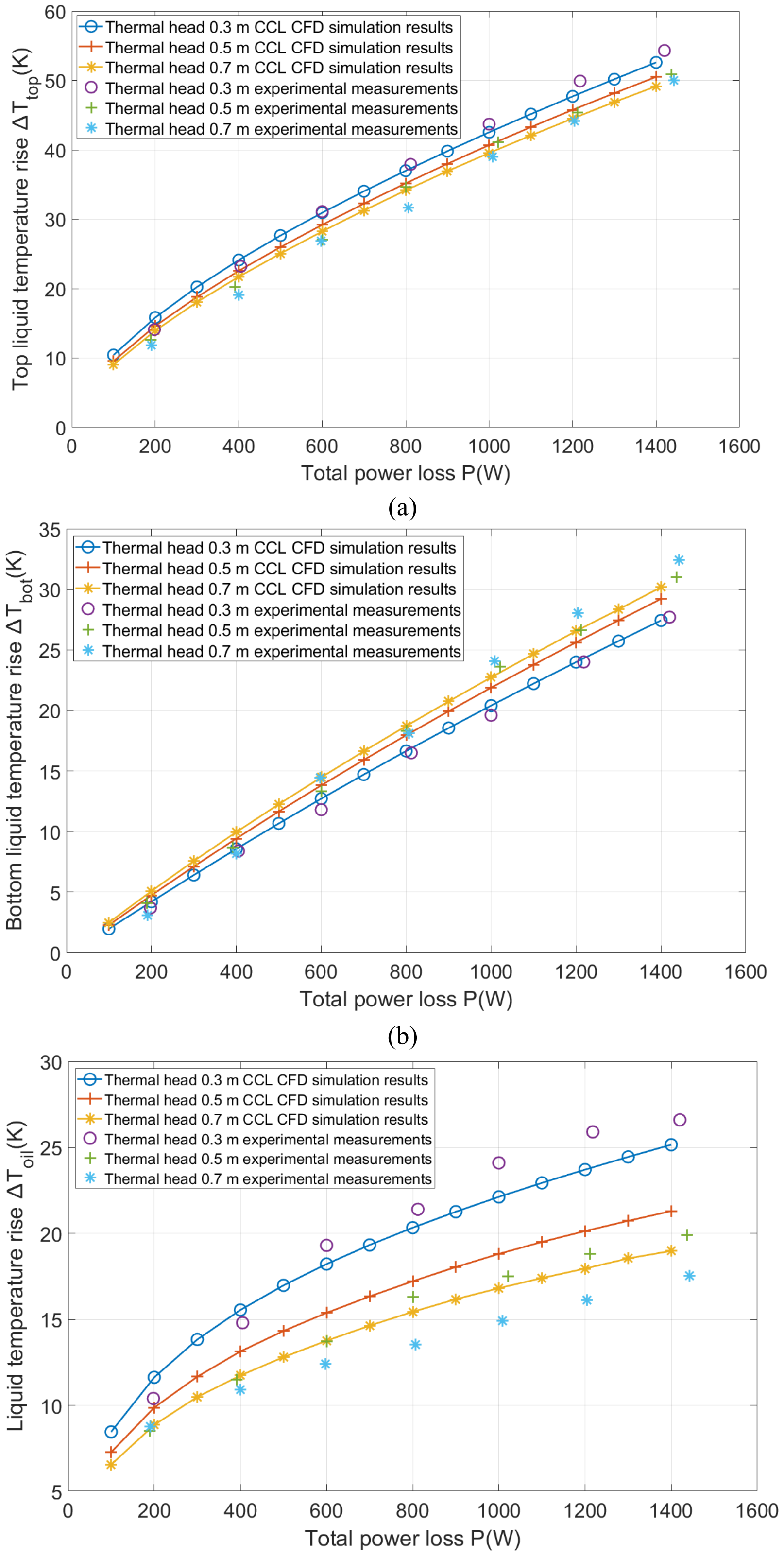

(a)

(b)

(c)

Figure 7-3 Comparison of liquid temperature rises between CFD simulations and experimental measurements under different thermal heads, mineral oil (a) top liquid temperature rise (b) bottom liquid temperature rise (c) liquid temperature rise

The liquid velocities with all three thermal heads from the experiments and the CCL CFD simulations are compared in Figure 7-4. The maximum absolute difference between the simulations and the experiments is 0.0047 m/s, and the maximum relative difference is 11.9%.

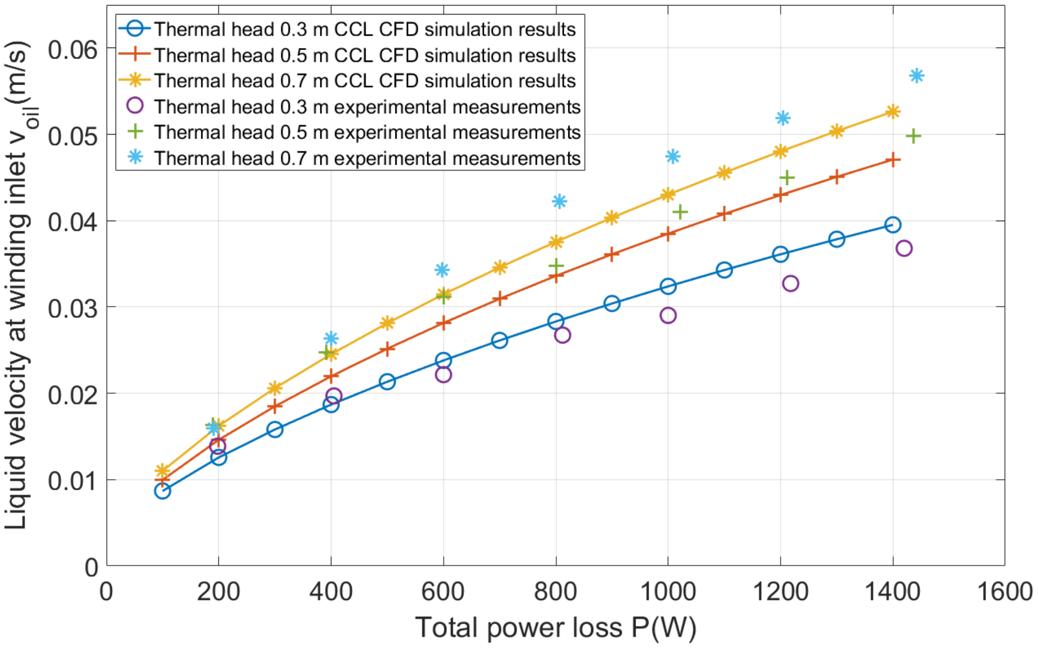

Figure 7-4 Comparison of liquid velocity between CFD simulations and experimental measurements at different thermal heads, mineral oil

It was found that a linear relationship between v_{oil} and $\sqrt{P}$ exists at the 0.5 m thermal head, as seen in Figure 7-2 (b) in Section 7.1. To verify such relationship at different thermal heads, the liquid velocities (v_{oil}) versus $\sqrt{P}$ at the 0.3 m and 0.7 m thermal heads are also least-square curve-fitted as expressed from Equation 7-3 to Equation 7-6. The maximum error in the least-square curve fitting process of all four equations (Equation 7-3 to Equation 7-6) is 0.0014 m/s.

$$\mathrm{v}_{oil-Exp-0.3m} = 0.0009\sqrt{P} + 0.0002 \qquad \text{Equation 7-3}$$

$$\mathrm{v}_{oil-CFD-0.3\,m} = 0.0011\sqrt{P} - 0.0007 \qquad \text{Equation 7-4}$$

$$\mathrm{v}_{oil-Exp-0.7m} = 0.0017\sqrt{P} - 0.0040 \qquad \text{Equation 7-5}$$

$$\mathrm{v}_{oil-CFD-0.7m} = 0.0015\sqrt{P} - 0.0060 \qquad \text{Equation 7-6}$$

where $\mathrm{v}_{oil-Exp}$ is the liquid velocity from the experiments (m/s), $\mathrm{v}_{oil-CFD}$ is the liquid velocity from the CCL CFD simulations (m/s), $\sqrt{P}$ is the square root of the power loss $(\sqrt{W})$, the subscriptions, i.e. 0.3 m and 0.7 m, represents thermal heads.

The curve-fitted Equation 7-3 to Equation 7-6, as well as the experiment and simulation results, are plotted in Figure 7-5 (a) and (b), for thermal head as 0.3 m and 0.7 m, respectively. It is clear that the linear relationship between v_{oil} and $\sqrt{P}$ explained in Section 7.1 is valid at different thermal heads from 0.3 m to 0.7 m.

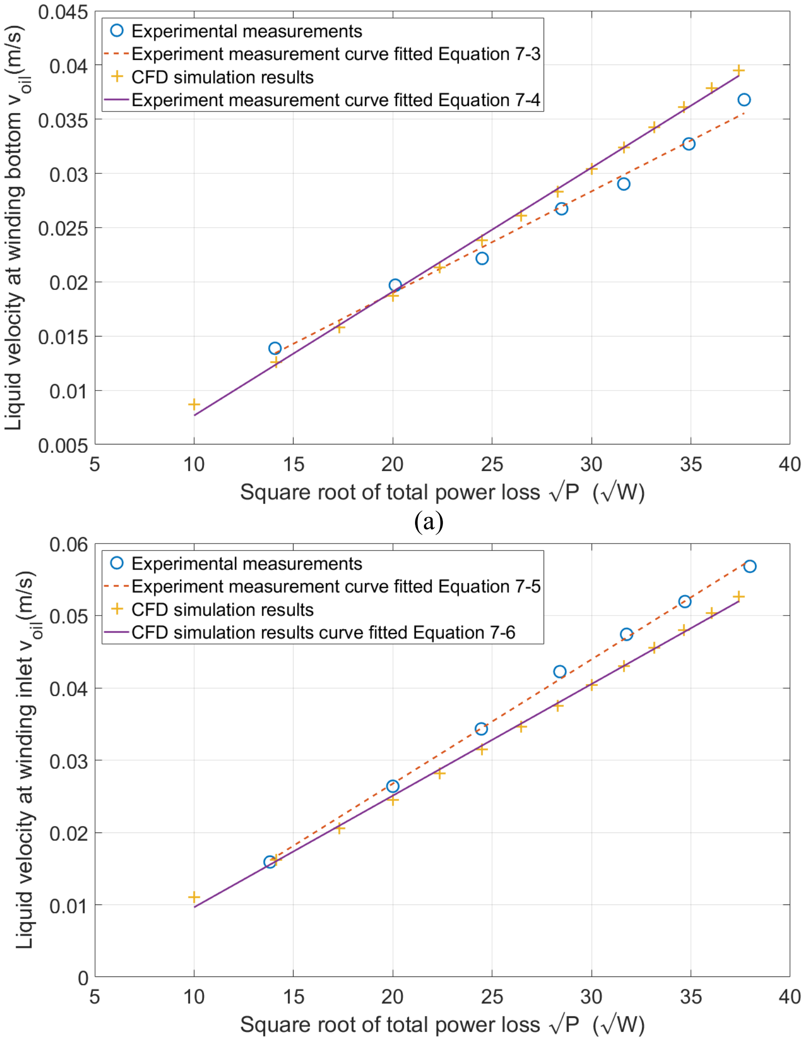

(a)

(b)

Figure 7-5 Comparisons of liquid velocity between CFD simulations and experimental measurements at different thermal heads, a mineral oil (a) thermal head as 0.3 m (b) thermal head as 0.7 m

It is also noted that the slopes and intercepts of the equations (either Equation 7-1, Equation 7-3 and Equation 7-5 from experimental measurements; or Equation 7-2, Equation 7-4 and Equation 7-6 from CCL CFD simulations) are influenced by the thermal heads. To understand the relationship between v_{oil} and the thermal head (h), the case of 800 W power loss is taken as an example, where the liquid velocities from experiments and CFD simulations are curve fitted with the square root of the thermal head ($\sqrt{h}$), as given in Equation 7-7 and Equation 7-8, respectively. The maximum absolute error of the curve fitting is $0.0006 m/s$. The curve fitted equation and the results from the experiments and the CCL CFD simulation are shown in Figure 7-6. As the same as given in Equation 2-15 in Section 2.4, the v_{oil} under the example condition (800 W power loss) increases linearly as the $\sqrt{h}$ rises.

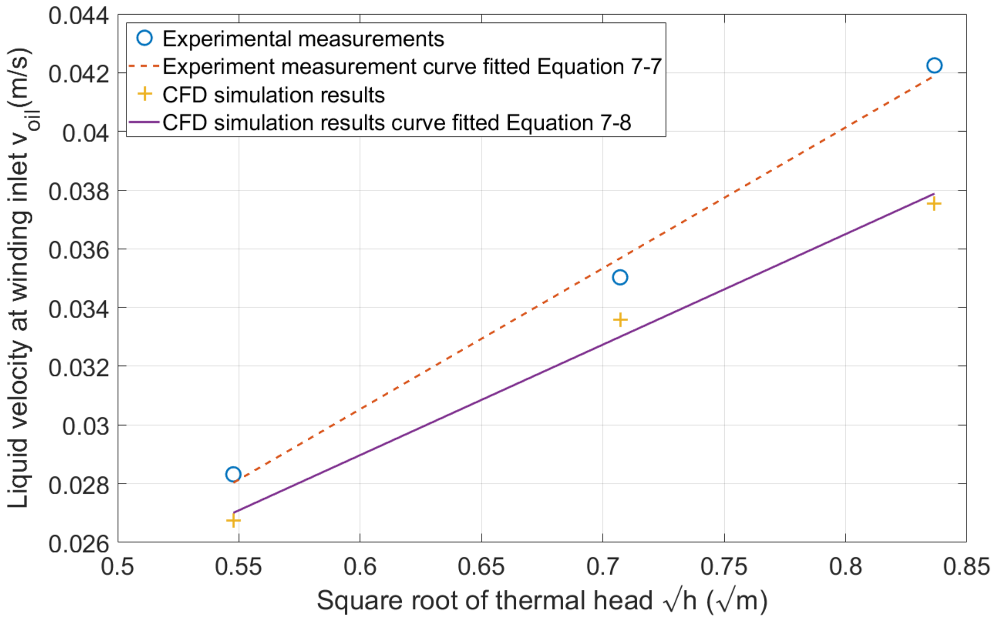

Figure 7-6 Liquid velocity between CFD simulations and experimental measurements under 800 W in different thermal heads with a mineral oil

$$v_{oil-Exp-800W} = 0.048\sqrt{h} + 0.002 \qquad \text{Equation 7-7}$$

$$v_{oil-CFD-800W} = 0.038\sqrt{h} + 0.006 \qquad \text{Equation 7-8}$$

To verify the relationship between v_{oil} and $\sqrt{h}$ in all the conditions, v_{oil} are least-square curve fitted with the square root of the product of total power loss and the thermal head ($\sqrt{Ph}$) from 21 sets of experiments and 42 sets of CFD simulations, as in Equation 7-9 and Equation 7-10, respectively. The maximum absolute error in the curve fitting processes of is 0.002 m/s. The curved fitted Equation 7-9 and Equation 7-10, as well as the simulation and experiment results, are plotted in Figure 7-7. It is clear that v_{oil} is proportional to $\sqrt{Ph}$.

And such a relationship is able to describe the results of 21 sets of the experiments and 42 CFD simulations in one go.

$$v_{oil-Exp} = 0.0018\sqrt{h} - 0.002 \qquad \text{Equation 7-9}$$

$$v_{oil-CFD} = 0.0019\sqrt{h} - 0.003 \qquad \text{Equation 7-10}$$

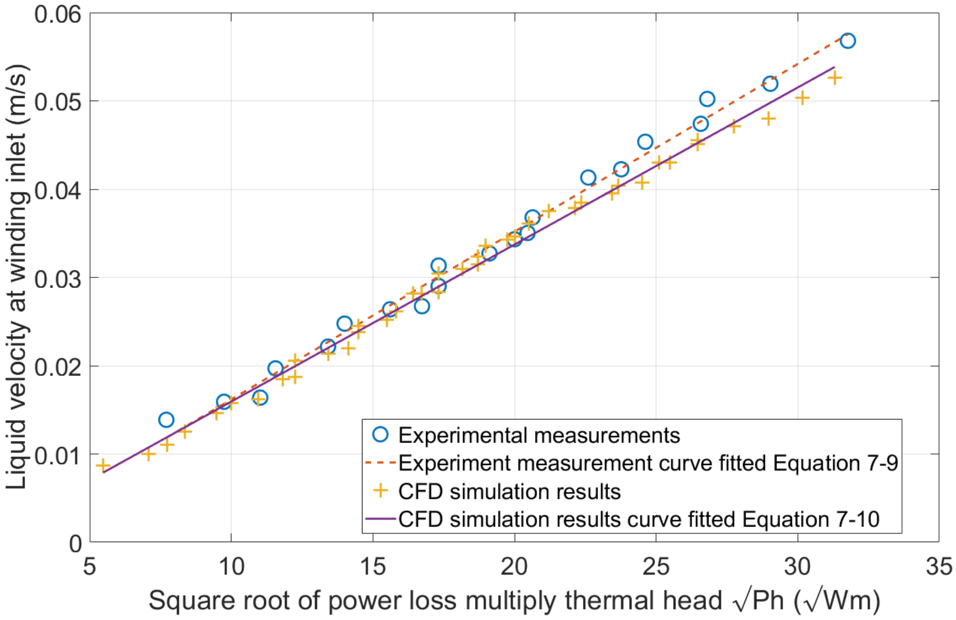

Figure 7-7 Liquid velocity versus the square root of power loss and thermal head ($\sqrt{Ph}$) in three different thermal heads

7.3 Effect of Ambient Temperature

As documented in IEC 60076-2 [24] for a liquid natural cooled transformer, when the ambient temperatures (T_{amb}) rises, the liquid velocity increases, and also the total power loss increases as the winding resistance increases. The increased liquid velocity and the total power loss would compensate each other, and hence, the temperature rises, including liquid temperatures and the winding temperatures, will be insignificantly affected. It should be noted that the total power loss increases around 7.8% for every 20 °C rise of ambient temperature.

To understand the effects of T_{amb} on T_{top}, T_{bot}, as well as v_{oil}, the CCL CFD simulations are conducted at T_{amb} from 0 °C to 40 °C with an interval of 10 °C. All the CCL CFD simulations are conducted with a 0.5 m thermal head and with the mineral oil as the coolant. In total, there have been 70 simulation cases presented in this section.

The input h_{air} equations for CCL CFD simulations at different T_{amb} are transformed from its dimensionless Equation 5-12, and are given in Table 7-1. As observed in Table 7-1, h_{air} Equation 7-13 for the T_{amb} at 20 ℃ is different to the h_{air} Equation 5-2 (derived in Section 5.1.3, and applied in Section 7.1 and 7.2).

Table 7-1 h_{air} equations of CCL CFD simulations at different ambient temperatures

Ambient temperature T_{amb} (℃)	Air heat transfer coefficient h_{air} $(W/(m^2K))$ equation	
0	$h_{air} = 1.63 \times (T_{avo} - T_{amb})^{0.40}$	Equation 7-11
10	$h_{air} = 1.50 \times (T_{avo} - T_{amb})^{0.42}$	Equation 7-12
20	$h_{air} = 1.40 \times (T_{avo} - T_{amb})^{0.43}$	Equation 7-13
30	$h_{air} = 1.30 \times (T_{avo} - T_{amb})^{0.43}$	Equation 7-14
40	$h_{air} = 1.21 \times (T_{avo} - T_{amb})^{0.44}$	Equation 7-15

ΔT_{top}, ΔT_{bot} and ΔT_{oil} from the CCL CFD simulations at different T_{amb} are shown in Figure 7-8. At the same total power loss, ΔT_{top} decreases by 3.5 K to 4.4 K because of an increasing T_{amb} from 0 to 40 ℃, whereas ΔT_{bot} is found to be increased by 1.6 K to 3.6 K under the same condition. Hence, ΔT_{oil} is decreasing with an increase of T_{amb}, which leads to an increase of v_{oil}. It is also observed that the changing rate of the ΔT_{top} at the same loading level is gradually decreasing, as the same as the changing rate of the ΔT_{bot}.

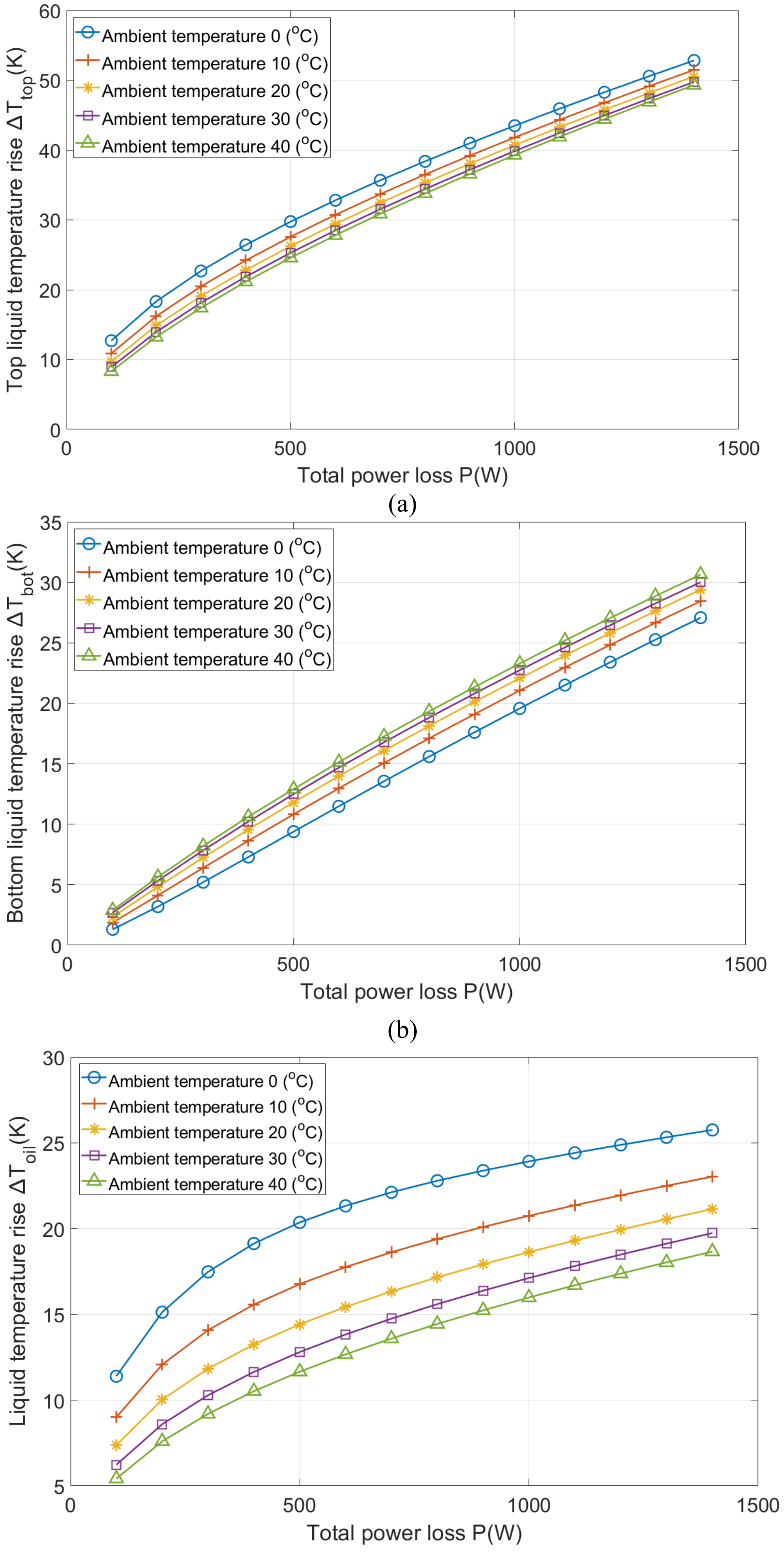

(a)

(b)

(c)

Figure 7-8 Liquid temperature rises from CFD simulations at different ambient temperatures (a) top liquid temperature rise (b) bottom liquid temperature rise (c) liquid temperature rise

Results of v_{oil} from the CCL CFD simulations at different T_{amb} are depicted in Figure 7-9. It is clear that v_{oil} increases with T_{amb} increasing. With the ambient temperature rises from 0 to 20 °C, v_{oil} increases by 16.3% to 33.6% at the same total power loss; with the ambient temperature changes from 20 to 40 °C, v_{oil} increases by 10.8% to 33.21%. The increasing rate of the liquid velocity is much larger than the increasing rate of the winding resistance, as a 7.8% increase for every 20 °C ambient temperature rise.

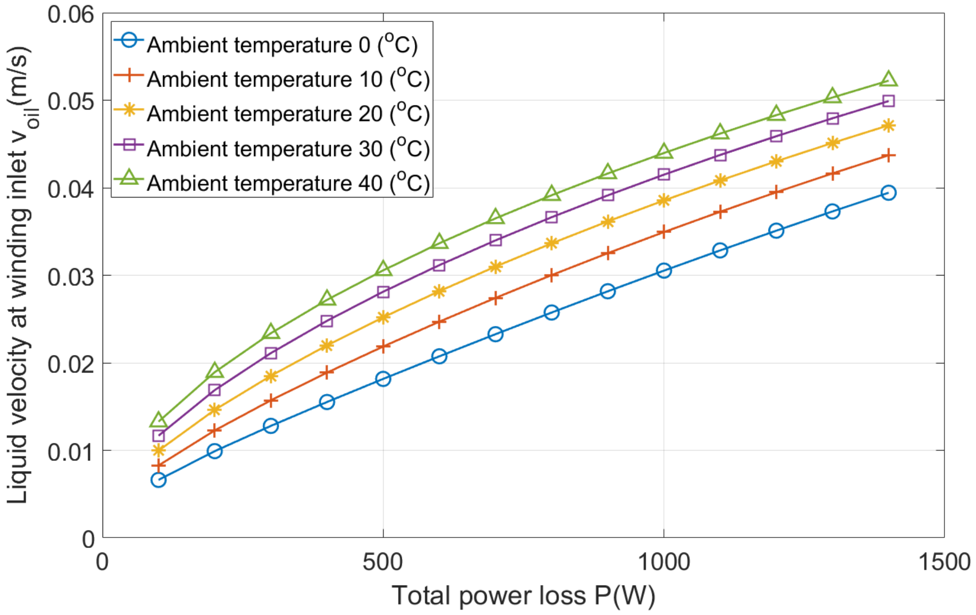

Figure 7-9 Liquid velocity from CFD simulations at different ambient temperatures, 0.5 m thermal head, mineral oil.

To further verify the previous finding of the relationship between v_{oil} and $\sqrt{P}$, v_{oil} versus $\sqrt{P}$ at different T_{amb} are curved fitted, as expressed from Equation 7-16 to Equation 7-20. The curved fitted equations are plotted in Figure 7-10, and it can be clearly seen that v_{oil} is proportional to $\sqrt{P}$, under all ambient temperatures investigated.

$$\mathrm{v}_{oil-0\,°\mathrm{C}} = 0.0012\sqrt{P} - 0.008 \qquad \text{Equation 7-16}$$

$$\mathrm{v}_{oil-10\,°\mathrm{C}} = 0.0013\sqrt{P} - 0.007 \qquad \text{Equation 7-17}$$

$$\mathrm{v}_{oil-20\,°\mathrm{C}} = 0.0014\sqrt{P} - 0.005 \qquad \text{Equation 7-18}$$

$$\mathrm{v}_{oil-30\,°\mathrm{C}} = 0.0014\sqrt{P} - 0.003 \qquad \text{Equation 7-19}$$

$$\mathrm{v}_{oil-40\,°\mathrm{C}} = 0.0014\sqrt{P} - 0.002 \qquad \text{Equation 7-20}$$

where v_{oil} is the liquid velocity from the experiments (m/s), the subscriptions represent the simulation results at different ambient temperatures, $\sqrt{P}$ is the square root of the power loss ($\sqrt{W}$).

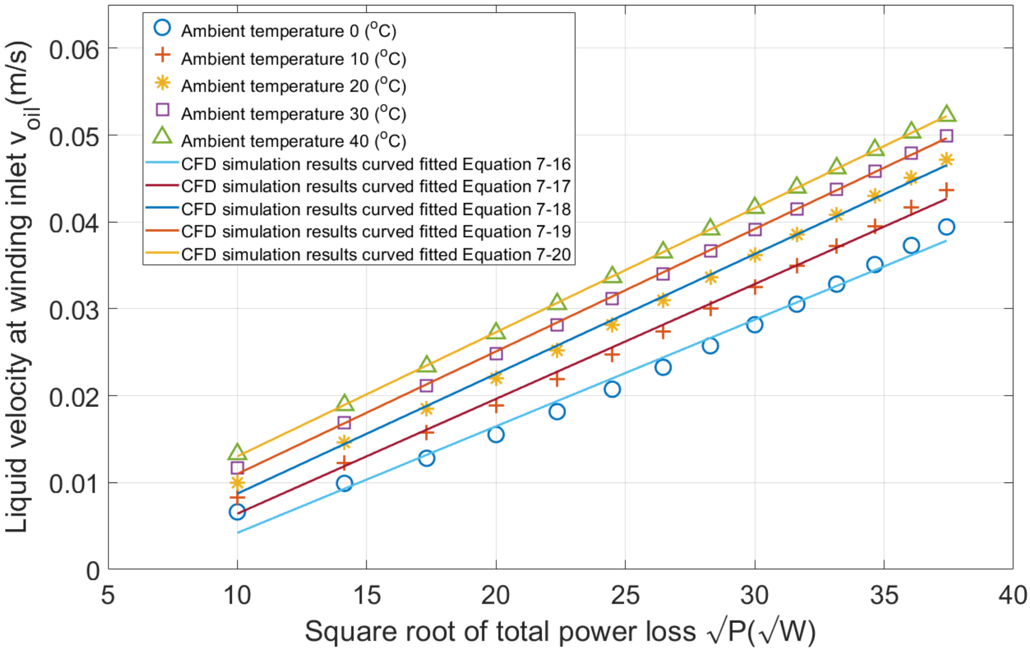

Figure 7-10 Liquid velocity from CFD simulations in different ambient temperatures with a mineral oil

As seen in both Figure 7-9 and Figure 7-10, v_{oil} increases with T_{amb}. This is because the dynamic viscosity of the insulating liquid decreases with the increase of liquid temperature. A lower dynamic viscosity (μ) leads to a lower hydraulic pressure drop, and hence, a higher liquid velocity. As seen from Equation 7-16 to Equation 7-20, the slopes of all five equations are close, however, the intercepts are different.

As indicated in Equation 2-15, v_{oil} is not only correlated with the $\sqrt{P}$ and $\sqrt{h}$, but also with the square root of the ratio of dynamic viscosity ($\sqrt{\frac{1}{\mu}}$). The 800 W power loss condition is taken as an example, and v_{oil} versus the square root of the dynamic viscosity ($\sqrt{\frac{1}{\mu}}$) is least-square curve fitted, as given in Equation 7-21. The maximum error in the curve fitted process is $0.0007 m/s$.

$$\mathrm{v}_{oil-800\,W} = 0.0018\sqrt{\frac{1}{\mu}} - 0.011 \qquad \text{Equation 7-21}$$

where v_{oil} is the liquid velocity from the experiments (m/s), μ is the dynamic viscosity $(kg/(m \cdot s))$.

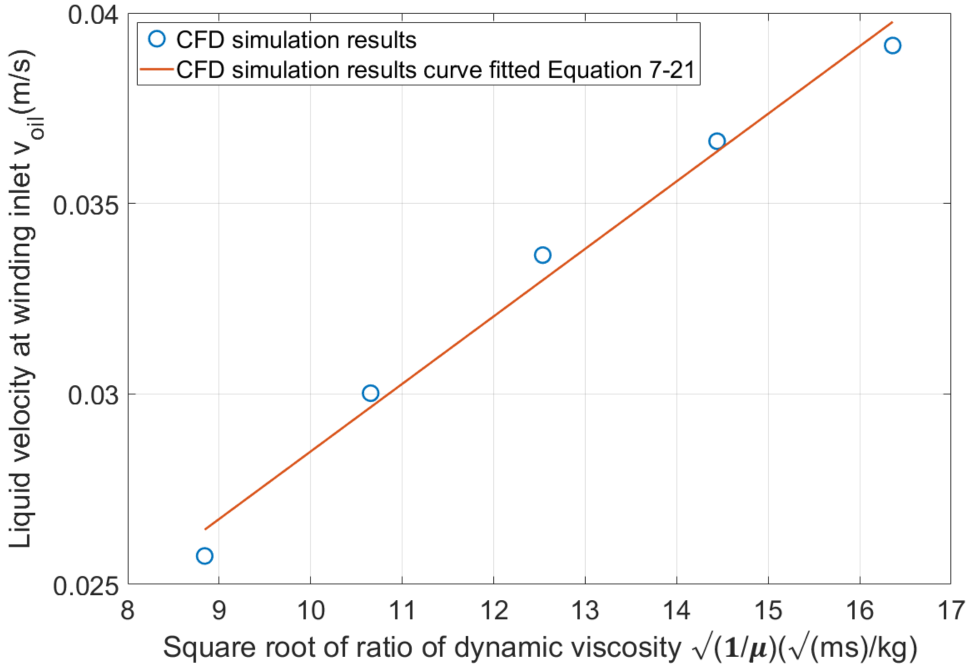

Figure 7-11 Liquid velocity from CFD simulations under 800 W power loss in different ambient temperature with a mineral oil

The curved fitted equations and the CCL CFD simulation results are shown in Figure 7-11. It shows that v_{oil} at different ambient temperatures follows a linear relationship versus $\sqrt{\frac{1}{\mu}}$ under the 800 W power injection condition. Next, v_{oil} is curved fitted with the $\sqrt{P\frac{1}{\mu}}$ by using all 70 cases, as in Equation 7-22.

$$\mathrm{v}_{oil} = 7.2 \times 10^{-5} \times \sqrt{P\frac{1}{\mu}} + 0.0064 \qquad \text{Equation 7-22}$$

where v_{oil} is the liquid velocity from the experiments (m/s), μ is the dynamic viscosity $(kg/(m \cdot s))$, P is the total power loss (W).

The curve fitted Equation 7-22 is shown in Figure 7-12, however, v_{oil} from the CCL CFD simulations does not show a good linear relationship with $\sqrt{P\frac{1}{\mu}}$. The maximum absolute error between the CCL CFD simulation results and the calculations from Equation 7-22 is 0.0053 m/s, and the maximum relative difference is as large as 55.6%. This is because the total power loss (P) also has an influence on $\sqrt{\frac{1}{\mu}}$. If v_{oil} was curve fitted with the $\sqrt{P\frac{1}{\mu}}$, the effects of the power loss (P) are double counted. Further work is required to understand the relationship between v_{oil} the total power loss and the ambient temperature where a new format instead of $\sqrt{P\frac{1}{\mu}}$ may be needed.

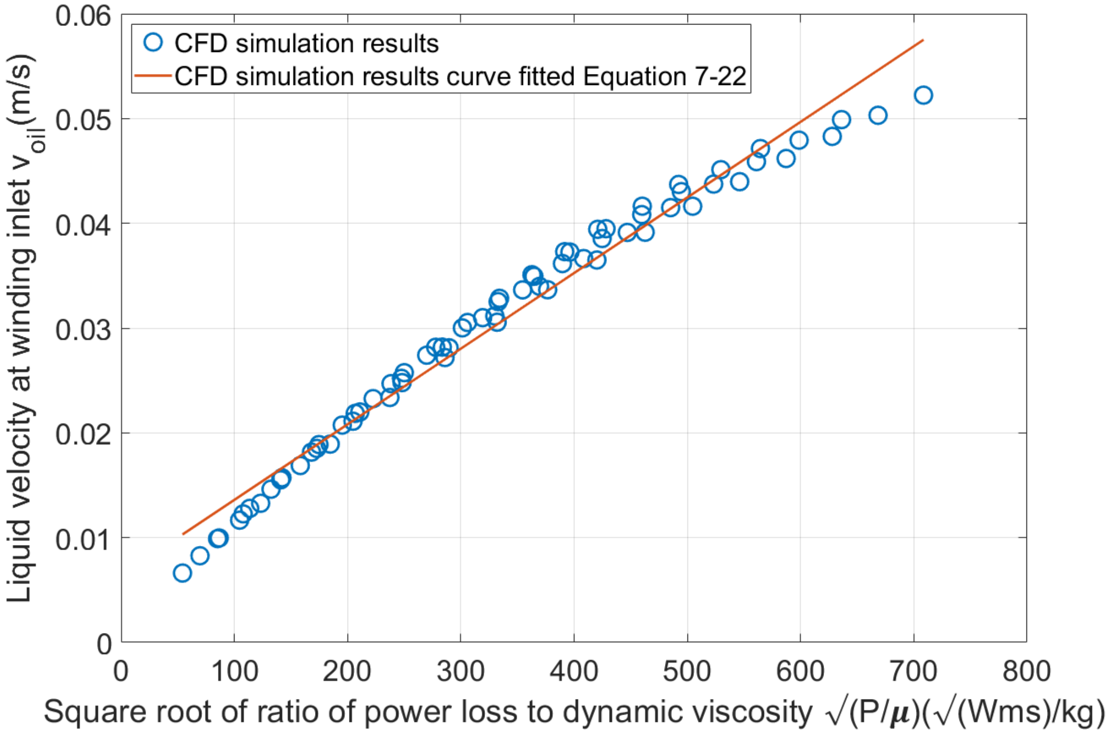

Figure 7-12 Liquid velocity versus $\sqrt{P\frac{1}{\mu}}$ from CFD simulations at different ambient temperatures

7.4 Effect of Type of Liquid

The CCL CFD model has been successfully verified by the experiments under different power losses and at different thermal heads. The liquid velocity at the winding inlet is found out to be proportional to the square root of the product of total power loss and the thermal head. In this section, the CCL CFD simulation is further verified by the experiments filled with alternative insulating liquids. Moreover, the cooling performances of different insulating liquids in terms of liquid flow rate are compared under various conditions.

7.4.1 Results of Gas-to-Liquid

To verify the CCL CFD simulation of the Gas-to-Liquid (Shell Diala S4 ZX-I), 20 sets of experiments (without the case with power loss of 1400 W and thermal head of 0.3 m) are used in this section, in which the power losses are varied from 200 W to 1400 W, and the ambient temperature is in the range from 18.1 ℃ to 25.0 ℃.

The CCL CFD model is used to conduct a parametric sweep of the power loss from 100 W to 1400 W (14 cases) and with three thermal heads, i.e. 0.3 m, 0.5 m and 0.7 m. There are in total 42 simulation scenarios, and the ambient temperature of all those cases is set as 20 ℃, and the h_{air} equation input in the CCL CFD simulations in this section is same as Equation 5-2.

As the ambient temperatures in the experiments are slightly different to the one in the CFD simulations, temperature rises ΔT_{top}, ΔT_{bot} and ΔT_{oil} are reported in Figure 7-13. As seen in Figure 7-13, the CCL CFD simulations with the Gas-to-Liquid are also comparable with the experimental measurements. The maximum differences of ΔT_{top}, ΔT_{bot} and ΔT_{oil} are 2.7 K, 2.5 K and 3.7 K.

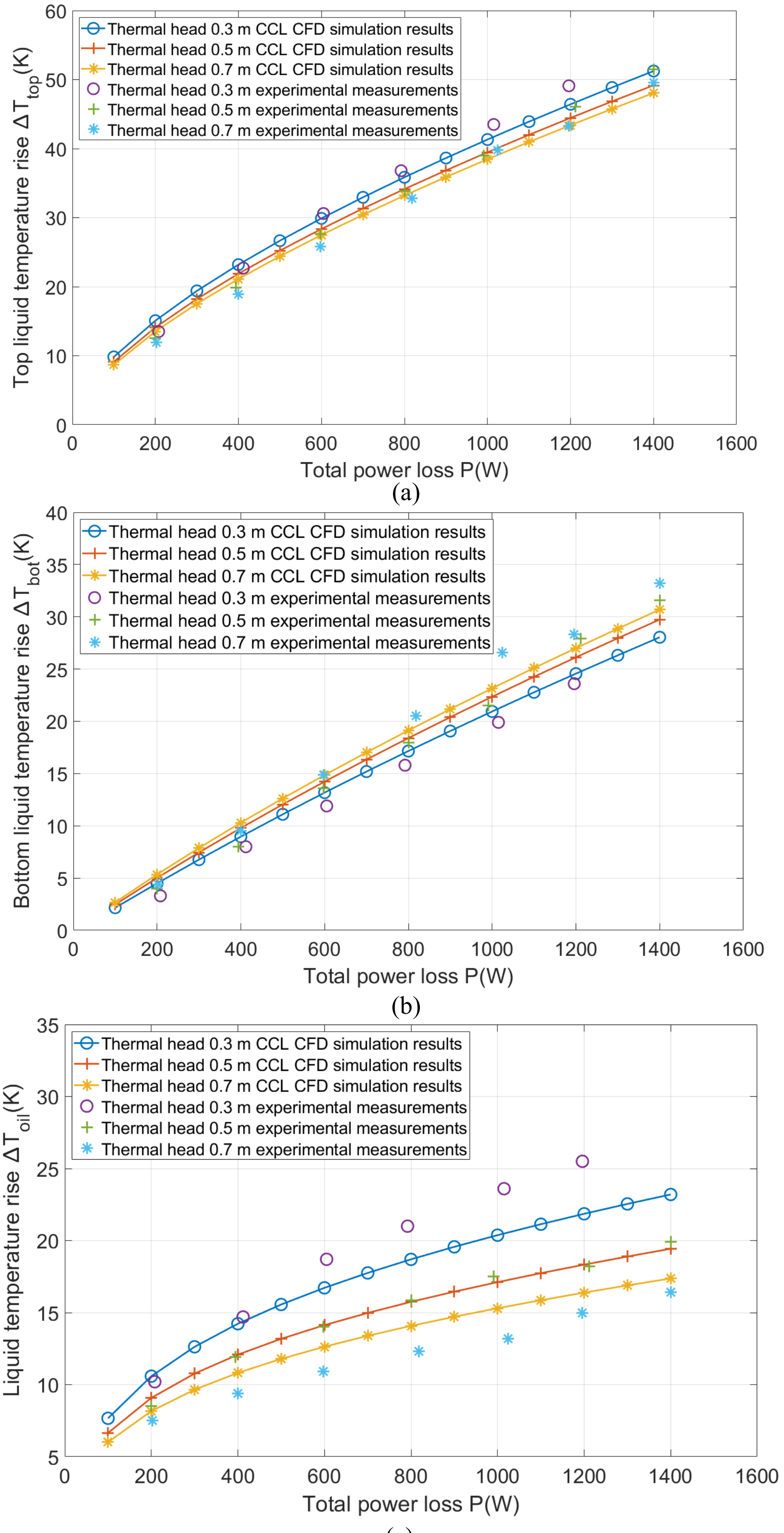

(a)

(b)

(c)

Figure 7-13 Comparison of liquid temperature rises between CFD simulations and experimental measurements, 0.5 m thermal head, Gas-to-Liquid (a) top liquid temperature rise (b) bottom liquid temperature rise (c) liquid temperature rise

The results of v_{oil} from the CCL CFD simulations are presented in Figure 7-14 (a). The increasing trends of v_{oil} from the CFD simulations and experiments are the same, and the average and maximum absolute differences between the simulations and the experiments are 0.0017 m/s and 0.0058 m/s, respectively.

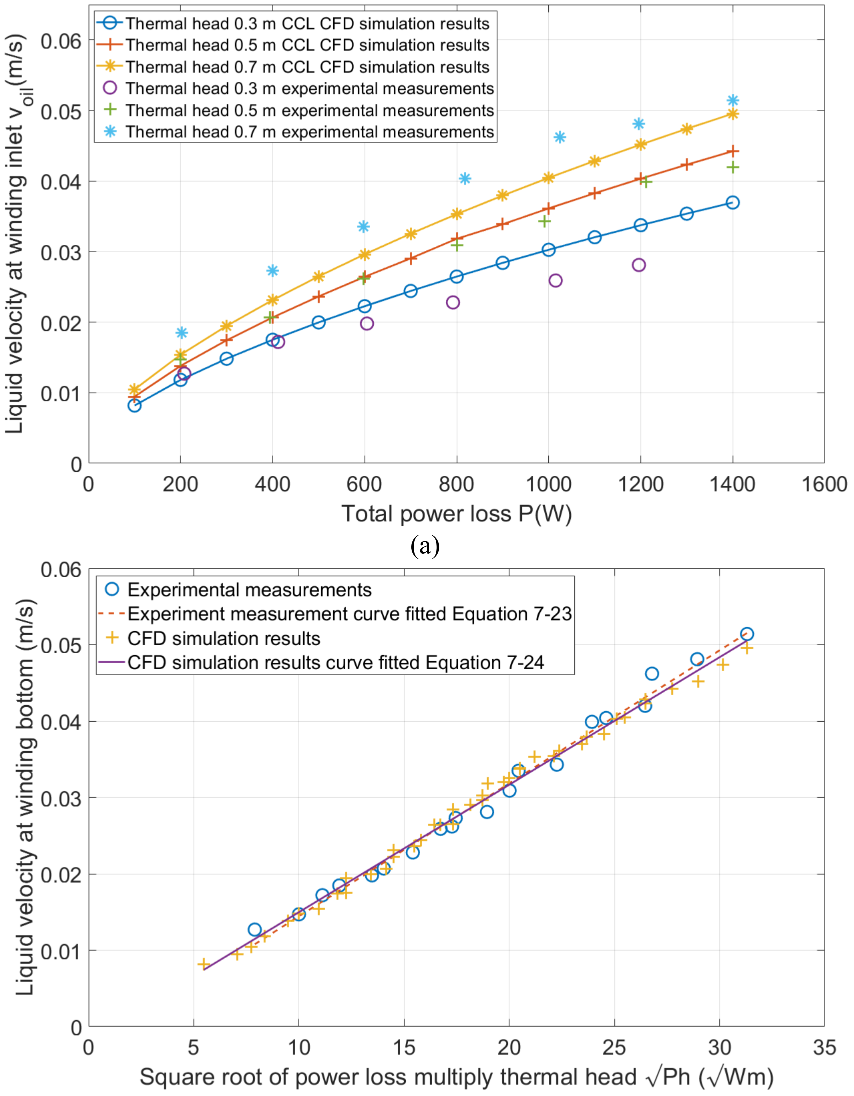

(a)

(b)

Figure 7-14 Liquid velocity between CFD simulations and experimental measurements in a 0.5 m thermal head with a Gas-to-Liquid (a) velocity against power loss (b) velocity against square root of power loss and thermal head

Figure 7-14 (b) depicts the relationship of v_{oil} versus the square root of the product of total power loss and the thermal head ($\sqrt{Ph}$). v_{oil} versus $\sqrt{Ph}$ from experiments and CCL CFD simulations is least-square curve fitted, as expressed in Equation 7-23 and Equation 7-24, respectively. The maximum differences between the original data and curved fitted equation are 0.0026 m/s and 0.0018 m/s for Equation 7-1 and Equation 7-2, respectively. Evidently, v_{oil} of the Gas-to-Liquid is also proportional to the $\sqrt{Ph}$, the same conclusion with the mineral oil.

$$\mathrm{v}_{GTL-Exp} = 0.0017\sqrt{Ph} - 0.0017 \quad \text{Equation 7-23}$$

$$\mathrm{v}_{GTL-CFD} = 0.0017\sqrt{Ph} - 0.0030 \quad \text{Equation 7-24}$$

where $\mathrm{v}_{oil-Exp}$ is the liquid velocity from the experiments (m/s), $\mathrm{v}_{oil-CFD}$ is the liquid velocity from the CCL CFD simulations (m/s), $\sqrt{P}$ is the square root of the power loss ($\sqrt{W}$).

7.4.2 Results of Synthetic Ester

To verify the validity of the CCL CFD model for another alternative insulating liquid, i.e. a synthetic ester, MIDEL 7131, 20 sets of experiments (without the case with power loss of 1400 W and thermal head of 0.3 m) are used in this section, in which the power losses are varied from 195 W to 1424 W, and the ambient temperature is in the range from 21.5 °C to 25.2 °C.

The parametric studies are carried out by using the CCL CFD model, the power loss is varied from 100 W to 1400 W (14 cases) and with three thermal heads, i.e. 0.3 m, 0.5 m and 0.7 m. There are in total 42 simulation scenarios, and the ambient temperature of all the cases is set as 20 °C, and the h_{air} equation is referred to Equation 5-2.

Temperature rise results of ΔT_{top}, ΔT_{bot} and ΔT_{oil} from both the experiments and the CFD simulations are given in Figure 7-15. The same as the mineral oil and the Gas-to-Liquid, ΔT_{oil} is approximately in an exponential relationship with the total power loss. The maximum differences of ΔT_{top}, ΔT_{bot} and ΔT_{oil} are 2.8 K, 2.7 K and 3.2 K.

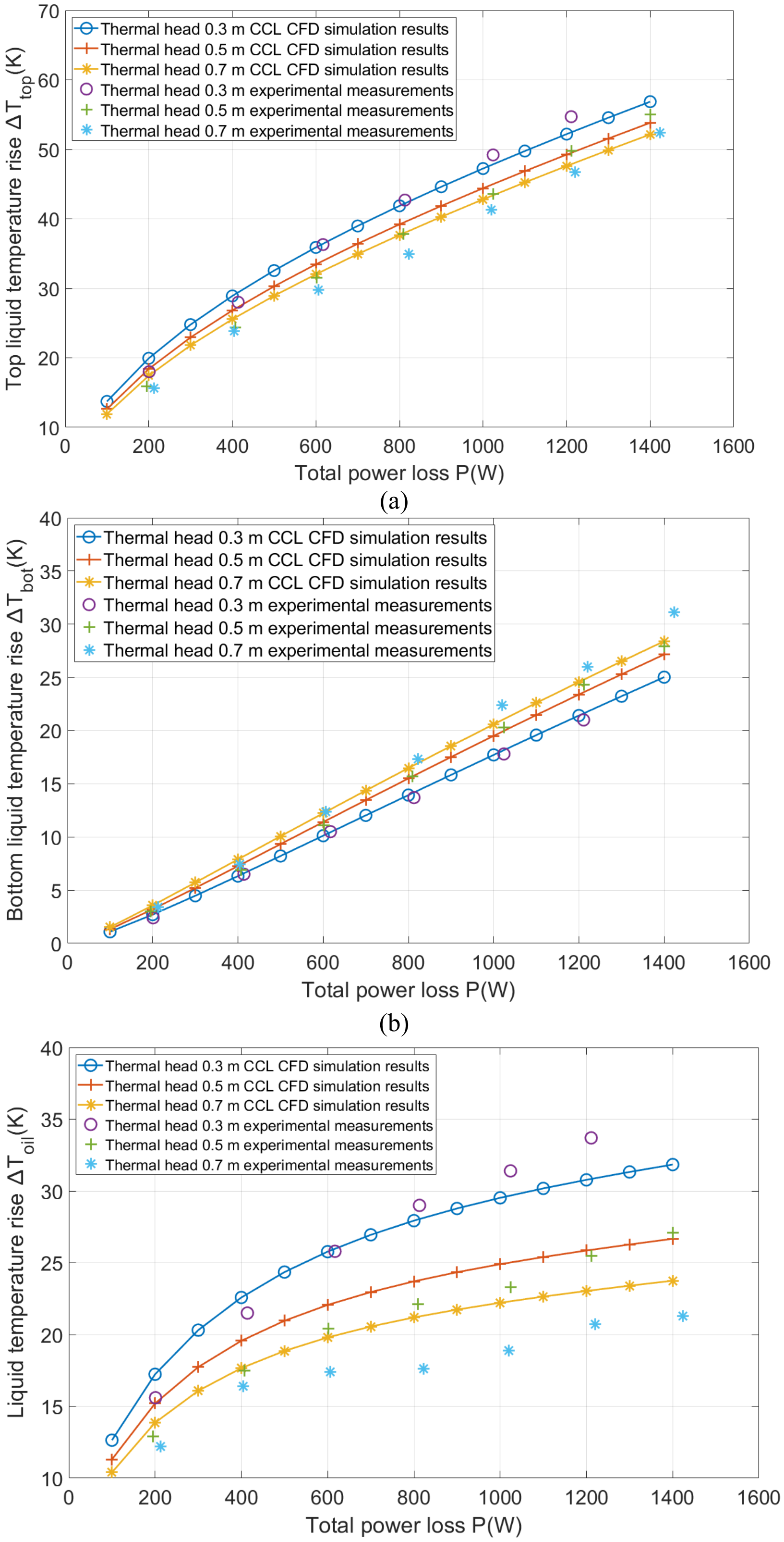

(a)

(b)

(c)

Figure 7-15 Comparison of liquid temperature rises between CFD simulations and experimental measurements, 0.5 m thermal head, synthetic ester (a) top liquid temperature rise (b) bottom liquid temperature rise (c) liquid temperature rise

The comparison of the liquid velocity between the CCL CFD simulations and the experiments is shown in Figure 7-16 (a). The increasing trends of v_{oil} with total power loss from the CFD simulations and experiments are the same; the average and the maximum absolute difference between the simulations and the experiments are 0.0015 m/s and 0.0043 m/s, respectively.

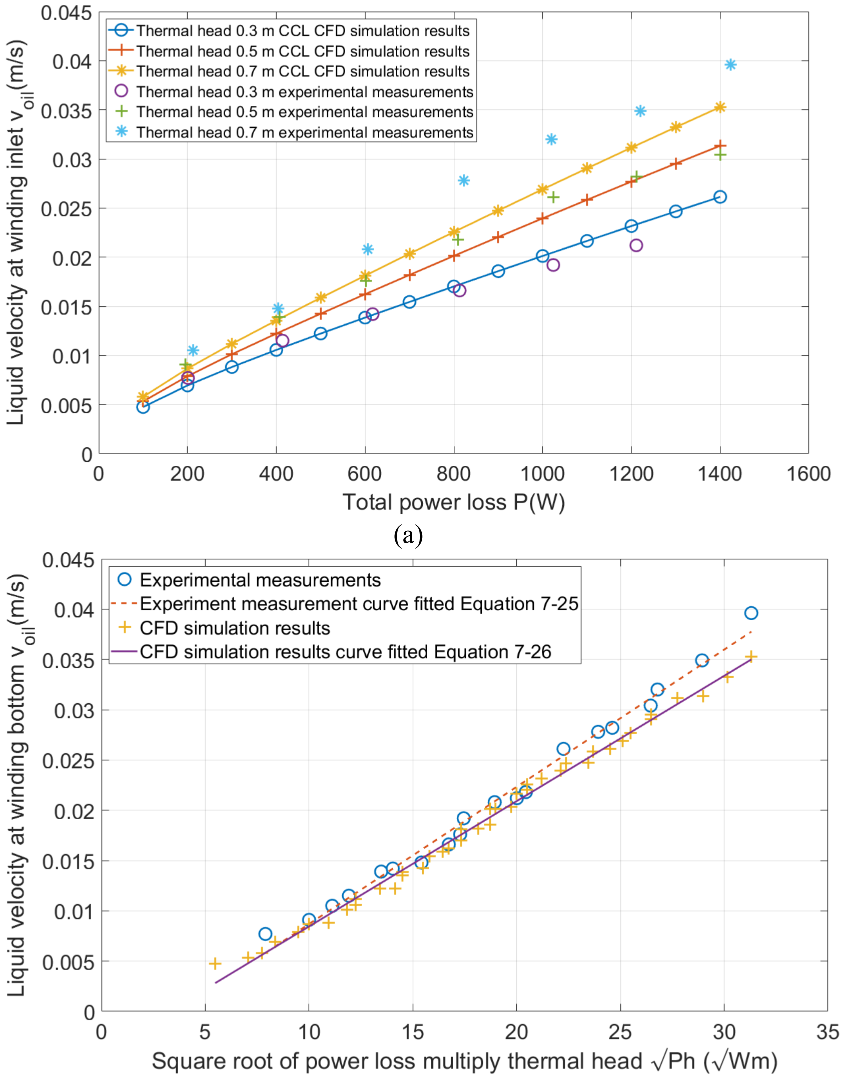

(a)

(b)

Figure 7-16 Liquid velocity between CFD simulations and experimental measurements, 0.5 m thermal head, synthetic ester (a) velocity against power loss (b) velocity against square root of power loss and thermal head

v_{oil} versus $\sqrt{Ph}$ of the synthetic ester is also least-square curve fitted, as expressed in Equation 7-25 (from experimental data) and Equation 7-26 (from the CFD simulation results). The maximum differences between the original data and curved fitted equation are 0.0018 m/s and 0.0019 m/s for Equation 7-25 and Equation 7-26, respectively. As shown in Section 7.2, Section 7.4.1 and Section 7.4.2, v_{oil} of different insulating liquids is proportional to $\sqrt{Ph}$ supported by both the experimental measurements and the CCL CFD simulations. The confirmed relationship may shed light to further work on developing dynamic thermal loading algorithms and also helps the transformer thermal design related with the thermal head.

$$\mathrm{v}_{SE-Exp} = 0.0014\sqrt{Ph} - 0.0049 \qquad \text{Equation 7-25}$$

$$\mathrm{v}_{SE-CFD} = 0.0012\sqrt{Ph} - 0.0040 \qquad \text{Equation 7-26}$$

where v_{SE-Exp} is the liquid velocity from the experiments (m/s), v_{SE-CFD} is the liquid velocity from the CCL CFD simulations (m/s), $\sqrt{P}$ is the square root of the power loss ($\sqrt{W}$), $\sqrt{h}$ is the square root of the power loss ($\sqrt{m}$).

7.4.3 Comparison of Different Insulating Liquids

To compare the thermal performances of different insulating liquids under the same thermal design, the results of simulations and experiments with the 0.5 m thermal head are taken as example. Temperature rises ΔT_{top}, ΔT_{bot} and ΔT_{oil} of all three insulating liquids at different total power losses are compared in Figure 7-17. The liquid temperature rises, ΔT_{top} and ΔT_{bot}, of the mineral oil are similar to those of the Gas-to-Liquid. However, the differences of the liquid temperature rises between the mineral oil and the synthetic ester are noticeably larger. ΔT_{top} of the synthetic ester is 3.1 K to 4.2 K higher than those of the mineral oil, whereas ΔT_{bot} of the synthetic ester is 1.0 K to 2.5 K lower than those of the mineral oil. As for the ΔT_{oil}, synthetic ester is 4.6 to 6.4 K higher than the mineral oil.

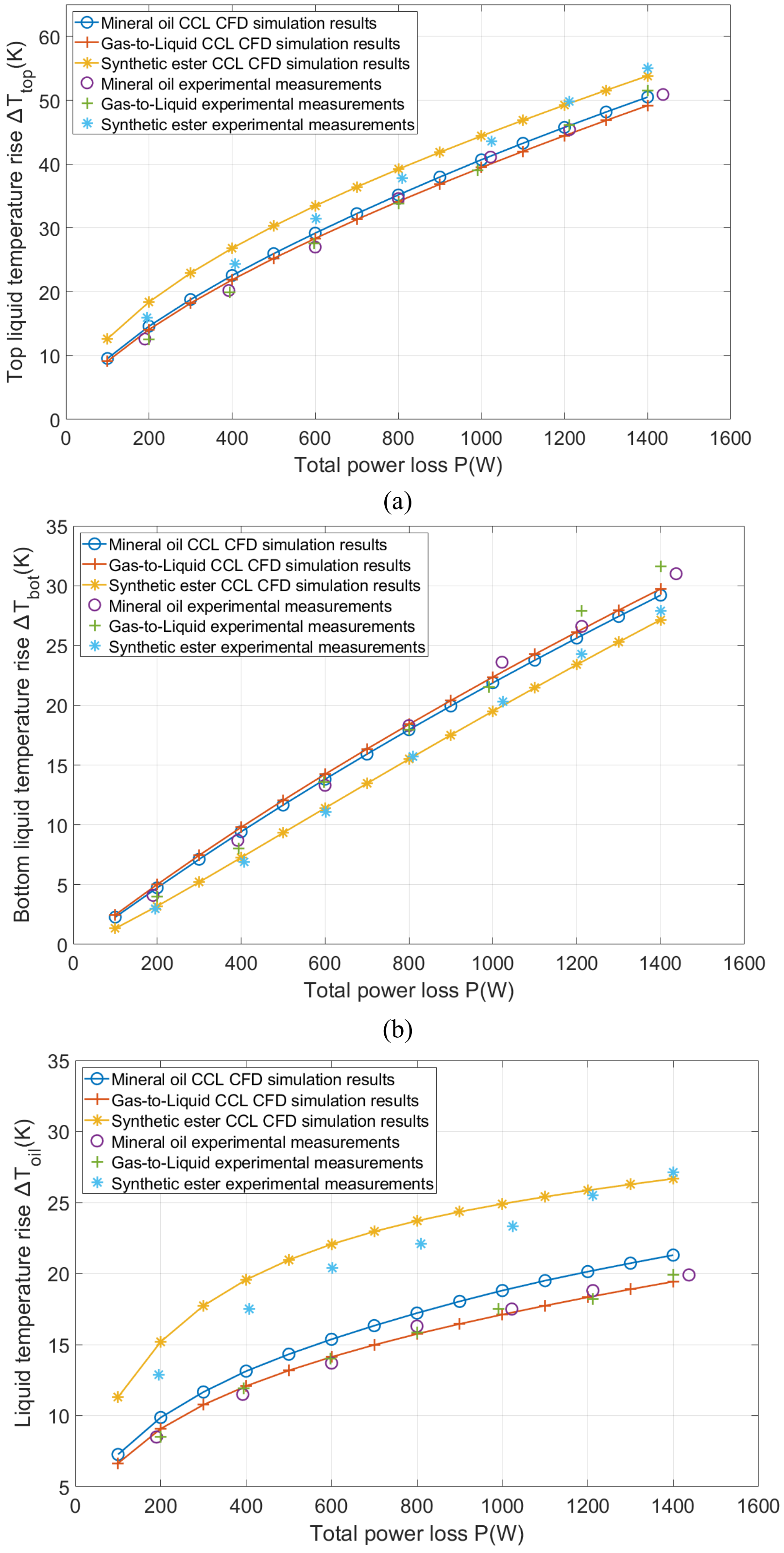

(a)

(b)

(c)

Figure 7-17 Comparison of liquid temperature rises among different insulating liquids, 0.5 m thermal head (a) top liquid temperature rise (b) bottom liquid temperature rise (c) liquid temperature rise

Because the CCL CFD simulations have been verified thoroughly under various conditions and the power injection and the ambient temperature have slight variations in the experiments, the CFD simulation results are summarised to compare the thermal performances among the three liquids. The top/bottom liquid temperatures of an alternative liquid, i.e. the Gas-to-Liquid and the synthetic ester liquid, are compared with those of the mineral oil in Table 7-2. Evidently, with respect to the liquid temperatures, the Gas-to-liquid behaves similarly to the mineral oil, though at different thermal heads. However, the top liquid temperature of the synthetic ester is around 2.9 K to 4.3 K higher than that of the mineral oil, whilst the bottom liquid temperature is around 0.9 K to 2.7 K lower.

Table 7-2 Comparison of the liquid temperatures among different insulating liquids

	Liquid temperature difference between the Gas-to-Liquid and the mineral oil (mineral oil as the benchmark case)		Liquid temperature difference between the synthetic ester liquid and the mineral oil (mineral oil as the benchmark case)	
Thermal head	Top liquid temperature difference	Bottom liquid temperature difference	Top liquid temperature difference	Bottom liquid temperature difference
0.3 m	$-1.3\ K < T < 0.6K$	$0.2\ K < T < 0.6K$	$3.3\ K < T < 4.3K$	$-2.3\ K < T < -0.9\ K$
0.5 m	$-0.5\ K < T < 1.2K$	$0.2\ K < T < 0.5K$	$3.0\ K < T < 4.2K$	$-2.5\ K < T < -0.9K$
0.7 m	$-0.4\ K < T < 1.1K$	$0.2\ K < T < 0.5K$	$2.9\ K < T < 3.9\ K$	$-2.3\ K < T < 1.0\ K$

Another point worth discussing is the top oil/liquid exponent in IEC 60076-2 thermal model [24], as discussed in Section 2.1.5. As discussed in Section 2.1.5, the exponents were derived from the extended transformer temperature-rise tests conducted at 0.7 p.u., 1 p.u. and 1.25 p.u.. For the extremely low or high loading conditions, the validities of the same exponent have not been verified. And the whether the liquid exponents would change or not when the same design of a transformer is filled with an alternative insulating liquid, has not been clarified. Moreover, there is neither no suggestions of the components for the bottom liquid temperature. Hence, in this section, the liquid components in different insulating liquids are derived from the verified CCL CFD simulations, as in Equation 7-27 and Equation 7-28 for top and bottom liquid temperatures, respectively.

$$\Delta T_{top} = \Delta T_{top-rate} \times (\frac{\text{loss}}{\text{rated loss}})^{x_{top}} \qquad \text{Equation 7-27}$$

$$\Delta T_{bot} = \Delta T_{bot-rate} \times (\frac{\text{loss}}{\text{rated loss}})^{x_{bot}}$$ Equation 7-28

where ΔT_{top} and ΔT_{bot} are the top and bottom liquid temperatures rise over ambient temperature (K), respectively; $\Delta T_{top-rate}$ and $\Delta T_{bot-rate}$ are the top and bottom liquid temperatures rise over ambient temperature (K) at the rated loading conditions, respectively, in this section, the 800 W case is taken as 1 p.u.; x_{top} and x_{bot} are the liquid exponents of the top and bottom liquid temperature, respectively.

The derived liquid components (x_{top} and x_{bot}) from different loading conditions, varied from 0.50 p.u. (200 W power loss) to 1.32 p.u. (1400 W power loss), are shown in Table 7-3. The maximum absolute error of the curve fitting of all the exponents in Table 7-3 is less than 0.3 K, which indicates that the top and bottom liquid components are valid from 0.5 p.u. to 1.32 p.u.. As also can be seen in the table, the top liquid component is varied from 0.54 to 0.66, which indicates the top liquid temperature is approximately in an exponential relationship with the total power loss. The bottom liquid component is in the range from 0.88 to 1.07, which fluctuates around the unit. Hence, the bottom liquid temperature tends to be in a linear relationship with the total power loss.

Table 7-3 Liquid temperature components from the CCL CFD simulations

	Mineral oil		Gas-to-Liquid		Synthetic ester liquid	
Thermal head	Top liquid component (x_{top})	Bottom liquid component (x_{bot})	Top liquid component (x_{top})	Bottom liquid component (x_{bot})	Top liquid component (x_{top})	Bottom liquid component (x_{bot})
0.3 m	0.62	0.92	0.63	0.90	0.54	1.07
0.5 m	0.64	0.89	0.65	0.88	0.55	1.03
0.7 m	0.65	0.88	0.66	0.86	0.58	1.00

Moreover, with a fixed geometry of the winding and the radiator, the increased thermal head leads to a decreased top liquid component, and an increased bottom liquid component. It also should be noted that change of liquid may lead to change of liquid exponent. Compared to the mineral oil, the top liquid component of the synthetic ester liquid has an average decrease of 12.6%, whilst the bottom liquid component has an average increase of

15.2%. Therefore, if a mineral oil filled and natural cooled transformer retro-filled with ester liquids, the liquid components need to be re-defined.

Liquid velocities v_{oil} of the three insulating liquids are at different total power losses are compared in Figure 7-18. The results show that v_{oil} of the Gas-to-Liquid is similar to that of the mineral oil and v_{oil} of the mineral oil is approximately two times of that of the synthetic ester.

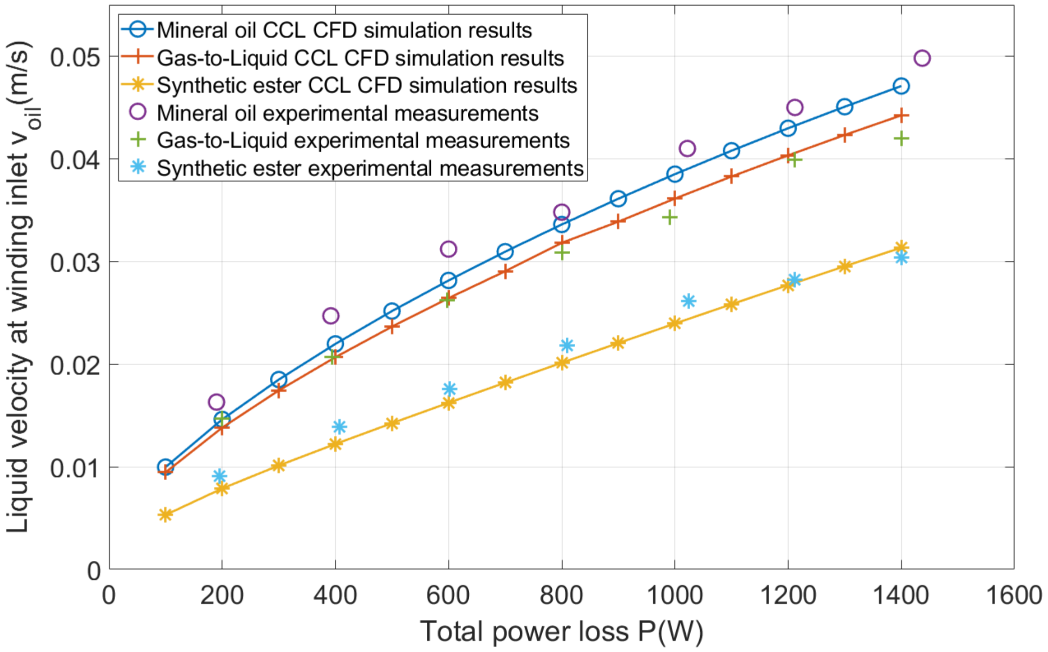

Figure 7-18 Comparison of liquid temperature rises among different insulating liquids, 0.5 m thermal head

To study the retro-filling scenario of the liquid natural cooled transformer, the liquid velocity ratio of an alternative liquid to the mineral oil is of great interest [72]. In this case, the liquid velocity ratio of the CFD simulations at three different thermal heads are compared in Figure 7-19.

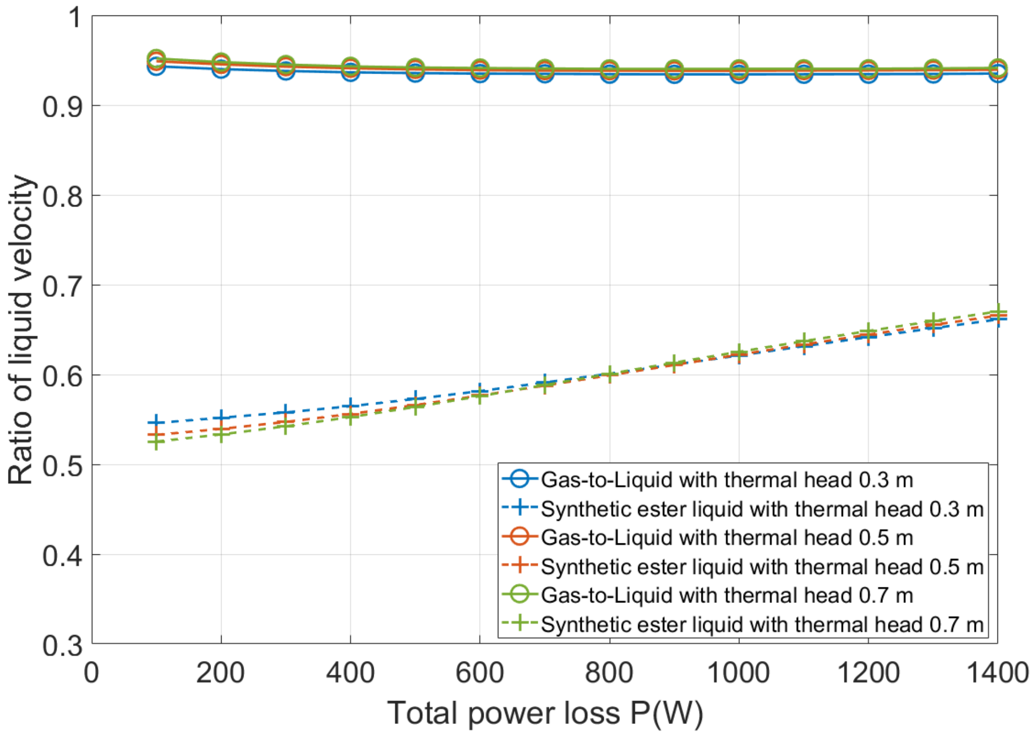

(a)

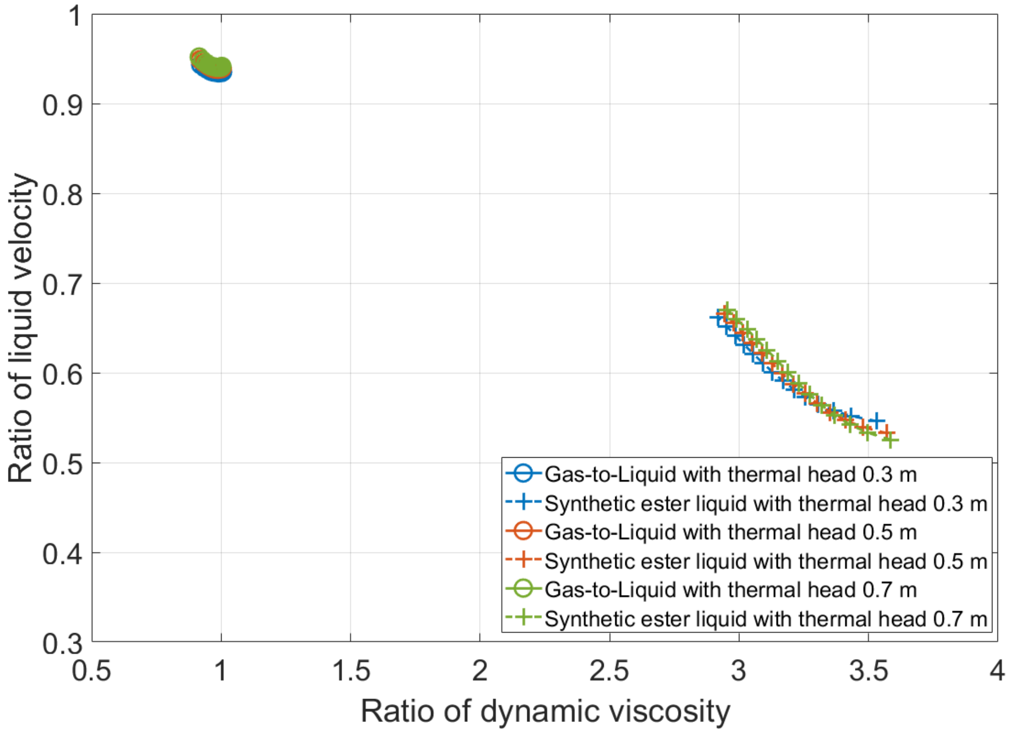

(b)

Figure 7-19 Ratio of liquid velocity of alternative liquid to the mineral oil from CFD simulations (a) versus power loss (b) versus ratio of the dynamic viscosity

As seen in Figure 7-19, the ratio of the liquid velocity for a fixed geometry of the winding and the radiator is not affected by the thermal head. With the total power loss (the loading condition) goes up, the ratio of the liquid velocity of the Gas-to-Liquid remains stable (95.2% to 94.1%), whilst the ratio of the synthetic ester liquid is rising from 52.5% to 67.0%. It is also found that the dynamic viscosity of the liquid is probably an important influencing factor to the liquid velocity ratios. As seen in Figure 7-19 (b), the larger the ratio of the dynamic viscosity is, the lower the ratio of the liquid velocity.

As previously documented in [72], an analytical equation (Equation 2-15) was proposed to estimate the ratio of the liquid velocity. The estimated ratio from Equation 2-15 is compared with the ratio from the CCL CFD simulations in Figure 7-20. As seen in Figure 7-20, the analytical equations of the Gas-to-Liquid provides the comparative ratios of the liquid velocity with the CCL CFD simulations. However, to the synthetic ester liquid, the results of the ratio of the liquid velocity from CFD simulations are obviously different from the analytical estimations based Equation 2-15. Analytical estimation underestimates the ratio of the liquid velocity of the synthetic ester liquid by 6.6% to 13.0%. The discrepancies are caused by the assumption:

- The liquid temperatures in the winding and the radiator are in a linear distribution manner;
- The geometric characteristic (C_g) of different insulating liquids is the same.

Therefore, to obtain a reliable liquid velocity for the liquid natural cooled transformer, the CCL CFD simulations are preferred.

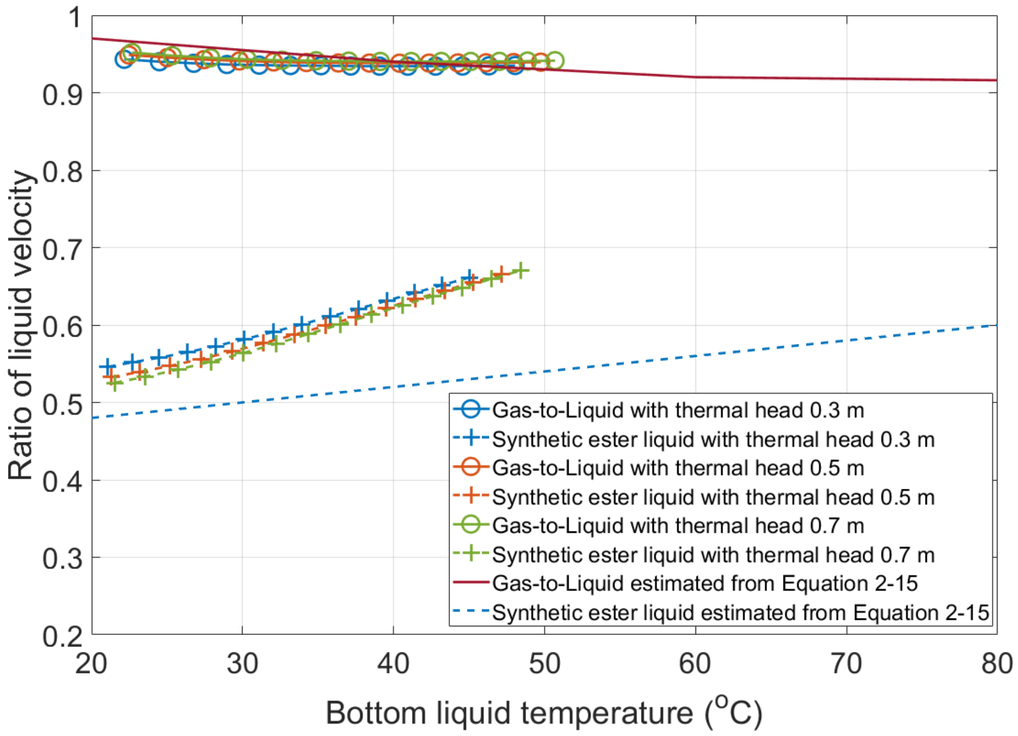

Figure 7-20 Comparion of ratio of liquid velocity between CCL CFD simulations and analytical estimations from [72]

7.5 Summary

The liquid temperatures and velocities under ON/KN cooling mode are comprehensively studied through both CFD simulations and experiments under different conditions, including the total power loss, the thermal head, the ambient temperature and the type of insulating liquid.

Under an increasing total power loss (proportional to the square of the loading levels), the top liquid temperature increases exponentially, and bottom liquid temperature increases linearly. The liquid velocity is found to be proportional to the square root of the total power loss. With a higher thermal head, the top liquid temperature increases, whereas the bottom liquid temperature decreases. The liquid velocity appears to increase when the thermal head rises, and it is proportional to the square root of the thermal head. There is a combined effect that the liquid velocity is proportional to the square root of the product of the total power loss and the thermal head, which is verified from both simulations and experiments and is valid for different insulating liquids. Moreover, with the same thermal geometry of the transformer windings and radiators, the liquid components as specified in [24] have very slight changes (for mineral oil: top liquid exponent changing from 0.62 to 0.65; bottom liquid exponent changing from 0.88 to 0.92).

When the ambient temperature goes up, the top liquid temperature rise over the ambient temperature decreases, and the bottom liquid temperature rise over the ambient temperature increases. The liquid velocity increases by 10.8% to 33.6% in every 20 ℃ increase of the ambient temperature, depending on the loading condition.

The thermal performances of three different insulating liquids are compared. In the liquid natural cooling mode, the liquid temperatures and velocities of the Gas-to-Liquid are similar to those of the mineral oil. The verified CCL CFD simulation results show that the changes of the liquid temperatures between the Gas-to-Liquid and the mineral oil are within 1.4K, and the changes of the liquid flow rate is within 6%. However, the cooling performance of the synthetic ester liquid is different from the mineral oil and the Gas-to-Liquid. Compared with the mineral oil, the top liquid temperature of the synthetic ester liquid is higher (from 2.9 K to 4.3 K) and the bottom liquid temperature is lower (from -3.5 K to -0.9 K). The liquid velocity of the synthetic ester liquid investigated in this thesis is 33.0% to 47.5% lower than the ones of the mineral oil. It is also found that the dominating material property to the liquid velocity is the dynamic viscosity. The closer the dynamic viscosity is, the closer the liquid velocity will be. The top and bottom liquid exponents specified in [24] are found to be changed if a transformer is filled with an alternative insulating liquid. Moreover, the ratios of the liquid velocity are compared between the analytical estimation in [72] and the CCL CFD simulations, where analytical estimation underestimates the velocity of the ester liquid.

Chapter 8 Conclusions and Future Work

In a liquid natural air natural (ONAN/KNAN) cooled power transformer, it is important to understand the interdependent relationship between the liquid temperature and liquid velocity to estimate the winding hot-spot temperature and its location under different conditions. In this PhD study, CFD simulations and experimental verifications of the liquid temperature and velocity in a complete-cooling-loop (CCL) setup are thoroughly investigated under various thermal design and operational conditions.

To construct such a CCL CFD model, firstly, an optimal transformer radiator CFD modelling strategy is found by using the air heat transfer coefficient equation to replace the detailed air flow simulations. Then, the reduced radiator model is implemented in the CCL CFD model, which solves the liquid temperatures and velocities simultaneously under different conditions. In parallel, an experimental CCL setup was established to fully verify the radiator and the CCL CFD simulations.

8.1 Research Conclusions

8.1.1 CCL Experimental Setup

A laboratory-scale CCL experimental setup is established to achieve a spontaneous insulating liquid flow, in which the only driven force of the liquid flow is the thermosiphon force. The design is representative to an ONAN/KNAN cooled transformer. It mainly consists of a modularised winding model, a 4-panel 1-meter-high radiator, the connecting pipework and a temperature measurement system. As it is a scaled down setup compared to a transformer, size matching between the winding model and the radiator is critical. This has been successfully achieved by the preliminary analysis so that the measured liquid temperatures and flow velocities in experiments are controlled within the typical ranges of these parameters for transformers in operation. The designed setup enables itself to vary the power loss (corresponding to the loading condition) and the thermal head, and it can also be filled with different insulating liquids to compare their thermal performance. In each temperature-rise test, the liquid, ambient and the radiator surface temperatures are measured.

8.1.2 Radiator Modelling and Verification

Full radiator CFD simulations

The liquid temperature distribution in the transformer radiator is important to determine the thermosiphon force of a liquid natural cooled transformer, and hence, the total liquid flow velocity. However, there is lack of research work on radiator modelling in terms of the liquid temperature and radiator surface temperature distributions, and in particular on experimentally verified modelling and simulations. Therefore, a full radiator CFD model including air domain is established first as the benchmark model.

The full radiator CFD model considers the thermal conduction, the insulating liquid and the air convections, the radiation on the outwards facing panel surfaces, and simulate both liquid and air flows inside and outside of the radiator. The simulations results are fully verified by a set of experiments in terms of the bottom liquid temperature, total heat dissipation and a surface temperature distribution under seven different loading conditions. The maximum absolute difference of the bottom liquid temperature between the full radiator CFD simulation and the experiments is within 0.9 K, the maximum relative difference of the total heat dissipation is within 4.3%, and the maximum absolute difference of the surface temperature is within 3.3 K. The accuracy of the full radiator CFD simulations is better than those published in the literature [80, 83, 84, 86, 87].

Reduced radiator CFD simulations

The full radiator CFD model considers all the heat transfer processes and the cooling media, which requires a high demand of computational efforts. Hence, it hinders its implementation into a CCL CFD model. Therefore, a reduced radiator CFD model is developed in this thesis, which replaces the air flow simulation (air convection) by using the air heat transfer coefficient. By comparing the full and reduced radiator CFD simulation under the same condition, the simulation results indicate that one h_{air} is sufficient to represent the convection of the complex air flow around the transformer radiator under one loading condition. An h_{air} equation is then derived to represent varying loading conditions by conducting the parametric sweep of the top liquid temperature and total liquid flow rate at the radiator top using the full radiator CFD simulations.

The reduced radiator CFD simulations adopted with the h_{air} equation have been comprehensively verified by both the full radiator CFD simulations and experiments of different operating conditions. Compared with the full radiator CFD simulations, the bottom liquid temperatures of the reduced radiator CFD simulations are within 0.3 K difference, and the total heat dissipation is within 2.2% difference. In the experimental verification, the maximum deviations of the bottom liquid temperature and the total heat dissipation introduced by the reduced radiator CFD simulations are 1.0 K and 6.4 %, respectively. It is also found that the reduced radiator CFD model significantly reduces the processing time to 2 hours compared with the full radiator CFD simulation of 50 hours for a typical simulation case. In addition, compared with the existing empirical equations in the literature [80, 83, 93-95, 100-105], the h_{air} equation derived in this thesis shows a better agreement with experimental results.

Effects of liquid type and ambient temperature on h_{air} Equation

The impacts of the liquid type and the ambient temperature on the derived h_{air} equation are investigated by additional CFD simulations. The h_{air} equation derived from the mineral oil is found to be applicable for alternative transformer liquids including a GTL oil and a synthetic ester liquid.

The effect of the ambient temperature on the h_{air} equation is more obvious. As the ambient temperature rises, the increased air dynamic viscosity leads to a decreased h_{air}. To consider the influences of the air material properties, the h_{air} equation has to be transformed into a dimensionless form, which successfully solves the impacts of the ambient temperature on the h_{air}.

8.1.3 CCL Modelling and Verification

CCL CFD simulations

The reduced radiator CFD model is incorporated into a CCL CFD model, which focuses on the evaluations of the interdependency of liquid temperatures and the liquid velocity under different loading conditions, with different thermal heads, in different ambient temperatures and of different insulating liquids. The effects of the above mentioned three influencing factors, i.e., the loading condition, the thermal head and the type of the insulating liquid, are also investigated by the experiments.

The CCL CFD simulations are first verified by a set of experiments where the ambient temperatures and the power losses as the inputs of the experiments and simulations are exactly matched. The maximum difference of top and bottom liquid temperatures between simulations and experiments is 2.2 K, and the mismatch of the liquid velocity is less than 12.3%. It should be noted that liquid velocities from the CCL CFD simulations are all in the uncertainty ranges of the calculated velocities based on the experiments, where the uncertainty ranges are determined from the variation of the liquid temperature measurements.

Liquid temperatures and velocities under different conditions

The liquid temperatures and velocities are comprehensively studied under different conditions, including the power loss, the thermal head and the ambient temperature by using a mineral oil.

With the increase of power loss injection (proportional to the square of the loading levels), the top liquid temperature increases exponentially, and bottom liquid temperature increases linearly. The liquid velocity is found to be proportional to the square root of the total power loss. With a higher thermal head, the top liquid temperature increases, whereas the bottom liquid temperature decreases. The liquid velocity increases when the thermal head rises, and the liquid velocity is proportional to the square root of the thermal head.

The relationship of the liquid velocity with the power loss or the thermal head is also valid at different ambient temperatures. When the ambient temperature increases, the top liquid temperature rise over the ambient temperature decreases, and the bottom liquid temperature rise over the ambient temperature increases. Depending on the loading condition, the liquid velocity increases from 10.8% to 33.6% in every 20 °C increase of the ambient temperature.

Comparison of different insulating liquids

The thermal performances of three different insulating liquids are compared. The relationship of the liquid velocity with the power loss or the thermal head is also valid for different insulating liquids. In the liquid natural cooling mode, the liquid temperatures and velocity of the Gas-to-Liquid are similar to those of the mineral oil. The verified CCL CFD simulation results show that the changes of the liquid temperatures between the Gas-to-Liquid and the mineral oil are within 1.4 K, and the changes of the liquid flow rate is within 6% under different conditions. However, the cooling performance of the synthetic ester liquid is noticeably different from the mineral oil and the Gas-to-Liquid. Compared with the mineral oil, the top liquid temperature of the synthetic ester liquid is higher, and the bottom liquid temperature is lower. The liquid velocities of the ester liquid investigated in this thesis is 33.0% to 47.5% lower than those of the mineral oil. It is also found that the dominating material property to the liquid velocity is the dynamic viscosity. The closer the viscosities between liquids, the closer the liquid velocities would be.

The liquid exponent, x, defined in the IEC standard 60076-2 [24] for this test setup is derived from the experimentally verified CCL CFD simulations. In addition to x (also defined as x_{top} in Section 7.4.2), x_{bot} (liquid exponent for calculation of the bottom liquid temperature) is also studied. The simulation results indicate that, with a fixed winding and radiator design and with the same insulating liquid, the top and bottom liquid components are similar even with different thermal heads. However, among different insulating liquids, the liquid exponents could vary. Compared with the ones of the mineral oil, the top liquid exponents of the synthetic ester liquid have an average 12.6% decrease, whilst the bottom liquid exponents have an average 15.2% increase.

Moreover, the analytical method proposed in the literature [72] is compared with the CCL CFD simulations on the liquid velocity calculation. Compared with the CCL CFD simulations, the analytical method may have an underestimation ranging from 6.6% to 13.0% of the total liquid flow velocity.

8.2 Future Work

The work reported in this thesis focused on understanding the thermal behaviour of the radiator and the complete-cooling-loop modelling for liquid natural air natural cooling mode in the steady-state condition. The future work can be conducted in both the steady-state condition and the dynamic condition.

Future work related to the winding in steady-state condition

The hot-spot temperature and its location at a transformer winding is of great interest for thermal design, operation and asset management. In the CCL CFD model, the winding disc is modelled as a homogenous block with uniform heat flux densities, to focus on the calculations of the liquid temperature and flow distributions. This geometric simplification brings the benefits of less computational requirements in terms of meshing and processing time.

The next step of the CFD simulations should adopt the paired bottom liquid temperature and liquid velocity at the winding inlet (from CCL CFD simulations in Chapter 6 and 7) into a winding only CFD model, focusing on the winding temperature distribution, as well as the hot-spot temperature and its location.

Different to the experiments in this thesis, a non-uniform loss profile which reflects the eddy current loss is suggested for the future work. Additionally, the Particle Image Velocimetry (PIV) based on a laser system should be used to measure the flow distributions of the insulating liquid within the winding. The application of the PIV system and the input of a non-uniform loss profile are both considered when designing the experimental setup (temperature sensors already embedded in the winding discs) reported in Chapter 3, however the restriction to laboratory access during the pandemic limited the present study. On top of the liquid temperature, the measured velocity and winding temperature profiles provide extra information to verify the CFD models. In addition, if the ambient temperature can be controlled, a wide range from a cold start to 40 ℃ ambient temperature should be experimentally studied.

The strategy can be used to model a transformer, and ultimately to be implemented into a thermal package of the transformer digital twin.

Future work related to radiator modelling in steady-state condition

The full radiator CFD model is established and verified. A dimensionless equation is found to empirically define the relationship between the Nusselt number and the Rayleigh number. However, its validity is only verified based on the geometry of the 4-panel 1-meter radiator. In this dimensionless equation, the length of the radiator panel (L) was chosen as the geometric characteristic.

However, in a power transformer, the radiator is longer in length and with more panels. Additional full radiator CFD simulations are needed to find out if the dimensionless equation can be universally applicable to different radiator sizes. To model multiple panels in different lengths, the geometric characterises defined as the pitch distance (s), associated with a correction factor defined as the ratio of the pitch distance to the panel length (s/L), may be more suitable.

In addition, the radiative heat dissipation, as well as the radiative coefficient, is influenced by the ratio of the outwards facing surface area to the all surface area of the radiator (A_{out}/A). Moreover, the radiative and convective heat dissipations are affected by the average liquid and ambient temperatures. Therefore, additional full radiator CFD simulations in different dimensions should also be conducted in different ambient temperatures to further validate if the ratio of the radiative heat dissipation to the convective heat dissipation is influenced by the ambient temperature

Future work related to dynamic condition

As introduced in Chapter 1, the future network loading levels would increase in general and become more dynamic due to the net-zero target. Hence, a Cigre Working Group (A2.60) is investigating the dynamic thermal behaviour of liquid-immersed power transformer. To the best knowledge of the author, only [106, 107] built the CFD models to study the dynamic thermal behaviour of the transformer.

In the present experimental setup developed in Chapter 3, the liquid and winding temperatures can be captured in every minute. Hence, the effects of the dynamic loading profile on the winding and liquid temperatures can be studied. Moreover, the hot-spot temperature and its location can be obtained from a cold start to different transient loading scenarios.

As for the simulation-based work, the CCL CFD model developed in Chapter 6 has been experimentally verified and further work needs to be conducted to determine whether it can be used to model the dynamic thermal behaviour.

Reference

[1] K. Anderson and A. Bows, "Beyond 'dangerous' climate change: emission scenarios for a new world," *Philosophical Transactions of the Royal Society A: Mathematical, Physical and Engineering Sciences,* vol. 369, no. 1934, pp. 20-44, 2011.

[2] Y. N. Harari, *Homo Deus: A Brief History of Tomorrow*. London: Vintage, 2016.

[3] M. New, D. Liverman, H. Schroder, and K. Anderson, "Four degrees and beyond: the potential for a global temperature increase of four degrees and its implications," *Philosophical Transactions of the Royal Society A: Mathematical, Physical and Engineering Sciences,* vol. 369, no. 1934, pp. 6-19, 2011.

[4] Commitee on Climate Change, "The Negetiations Explained," *26th United Nations Climate Change conference,* Glasgow, 2021. [online]. Available: https://ukcop26.org/wp-content/uploads/2021/11/COP26-Negotiations Explained.pdf

[5] *Paris Agreement,* United Nations 54113, 2015.

[6] "New Glasgow Climate Pact offers some 'breakthroughs' but also 'deep disappointment," 2021. [online]. Available: https://www.france24.com/en/europe/20211114-new-glasgow-climate-pact-offers-some-breakthroughs-but-also-deep-disappointment

[7] IChemE. (2019, July/August 2019) UK sets target for net zero emissions by 2050. *The Chemical Engineer*. 16.

[8] Commitee on Climate Change, "Reducing UK emissions: 2019 Progress Report to Parliament," London, UK, 2019.

[9] D. Calverley, R. Wood, S. Mander, K. Anderson, S. Glynn, and F. Nicholls, "Towards a 2 C future: emission reduction scenarios for Wales," *Report commissioned by the Climate Change Commission of the Welsh Assembly Government,* 2009.

[10] P. Richardson, M. Moran, J. Taylor, A. Maitra, and A. Keane, "Impact of electric vehicle charging on residential distribution networks: An Irish demonstration initiative," 2013.

[11] Commitee on Climate Change, "Reducing UK emissions: 2018 Progress Report to Parliament," London, UK, 2018.

[12] Smith, R. "Electricity Ten Year Statement 201." *National Grid , United Kingdom.* 2021. [Online]. Available: https://www.nationalgrideso.com/document/223046/download

[13] D. Feng, Z.D. Wang, and P. Jarman, "Getting the most out of historic reliability data," in *Proceedings of Prognostics and System Health Management Conference (PHM-2012 Beijing)*, pp. 1-6, 2012.

[14] Duarte, E., D. Falla, J. Gavin, M. Lawrence, T. McGrail, D. Miller, P. Prout, and B. Rogan, "A practical approach to condition and risk based power transformer asset replacement," in *Proceedings of International Symposium on Electrical Insulation*, pp. 1-4, 2010.

[15] S. J. Tee, "AGEING ASSESSMENT OF TRANSFORMER INSULATION THROUGH OIL TEST DATABASE ANALYSIS," The University of Manchester, 2016.

[16] Cigré, "Cigré Brochure 96 "Thermal Aspects of Transformers", *Working Group A12.09,* 1995.

[17] Cigré, "Cigré Brochure 393 "Thermal Performance of Transformers", *Working Group A2.24,* 2009.

[18] Cigré, "Cigré Brochure 659 "Transformer Thermal Modelling," *Working Group A2.38,* 2016.

[19] M. Heathcote, *J & P transformer book*. Newnes, 2011.

[20] *Power Transformers. Loading Guide for Mineral-oil-immersed Power Transformers*, BS IEC 60076-7:2018, 2018.

[21] J. Hill, Z.D. Wang, Q. Liu, C. Krause, and G. Wilson, "Analysing the power transformer temperature limitation for avoidance of bubble formation," *High Voltage,* vol. 4, no. 3, pp. 210-216, 2019.

[22] J. P. Hill, Z.D. Wang, Q. Liu, S. Matharage, A. Hilker, and D. Walker, "Improvements to the Construction of Bubble Inception Formulae for Use With Transformer Insulation," *IEEE Access,* vol. 7, pp. 171673-171683, 2019.

[23] IEEE, "IEEE Guide for Loading Mineral-Oil-Immersed Transformers and Step-Voltage Regulators," *IEEE standard C57.91*, 2011.

[24] *Power Transformers. Temperature rise for liquid-immersed transformers*, BS IEC 60076-2:2011, 2011.

[25] McNutt, William J., "Insulation thermal life considerations for transformer loading guides," vol. 7, no. 1, pp. 392-401, 1992.

[26] M. Daghrah, "EXPERIMENTAL STUDY OF TRANSFORMER LIQUID FLOW AND TEMPERATURE DISTRIBUTIONS," The University of Manchester, 2017.

[27] Transformer and Reactor Fittings. Cooling Equipment - Removable Radiators for Oil-Immersed Transformers, BS EN 50216-6:2002, 2002.

[28] P. Picher, F. Torriano, M. Chaaban, S. Gravel, C. Rajotte, and B. Girard, "Optimization of transformer overload using advanced thermal modelling," in *Proceedings of CIGRE Conference, Paris, France*, pp. A2-305, 2010.

[29] X. M. Lopez-Fernandez, P. Penabad-Duran, and J. Turowski, "Three-dimensional methodology for the overheating hazard assessment on transformer covers," *IEEE Transactions on Industry Applications,* vol. 48, no. 5, pp. 1549-1555, 2012.

[30] P. Jarman, "The importance of thermal design to transformer lifetime," *Transformers Magazine,* vol. 7, no. 2, pp. 60-67, 2020.

[31] M. P. Saravolac, "The use of optic fibres for temperature monitoring in power transformers." *IEE Colloquium on Condition Monitoring and Remanent Life Assessment in Power Transformers*. IET, 1994.

[32] D. Susa, M. Lehtonen, and H. Nordman, "Dynamic thermal modeling of distribution transformers," *IEEE Transactions on Power Delivery,* vol. 20, no. 3, pp. 1919-1929, 2005.

[33] M. Daghrah, Z.D. Wang, Q. Liu, and J.-N. Bérubé, "Effects of installation position of fibre optics temperature sensors (FOTS) on transformer hot-spot temperature

measurements," in *2nd annual Conference on Condition based Online Monitoring of Electric Assets (COMET)*, 2015.

[34] G. Swift, T. S. Molinski, and W. Lehn, "A fundamental approach to transformer thermal modeling. I. Theory and equivalent circuit," *IEEE Transactions on Power Delivery,* vol. 16, no. 2, pp. 171-175, 2001.

[35] G. Swift, T. S. Molinski, R. Bray, and R. Menzies, "A fundamental approach to transformer thermal modeling. II. Field verification," *IEEE Transactions on Power Delivery,* vol. 16, no. 2, pp. 176-180, 2001.

[36] D. Susa, M. Lehtonen, and H. Nordman, "Dynamic thermal modelling of power transformers," *IEEE transactions on Power Delivery,* vol. 20, no. 1, pp. 197-204, 2005.

[37] A. J. Oliver, "Estimation of transformer winding temperatures and coolant flows using a general network method," In *IEE Proceedings C (Generation, Transmission and Distribution) ,* vol. 127, no. 6, pp. 395-405, 1980, doi: 10.1049/ip-c:19800061.

[38] Z.D. R. Radakovic and M. S. Sorgic, "Basics of detailed thermal-hydraulic model for thermal design of oil power transformers," *IEEE Transactions on Power Delivery,* vol. 25, no. 2, pp. 790-802, 2010.

[39] E. Rahimpour, M. Barati, and M. Schäfer, "An investigation of parameters affecting the temperature rise in windings with zigzag cooling flow path," *Applied thermal engineering,* vol. 27, no. 11, pp. 1923-1930, 2007.

[40] J. Zhang and X. Li, "Oil cooling for disk-type transformer windings-part 1: theory and model development," *IEEE Transactions on Power Delivery,* vol. 21, no. 3, pp. 1318-1325, 2006.

[41] J. Zhang and X. Li, "Oil cooling for disk-type transformer windings-Part II: Parametric studies of design parameters," *IEEE Transactions on Power Delivery,* vol. 21, no. 3, pp. 1326-1332, 2006.

[42] J. Zhang and X. Li, "Coolant flow distribution and pressure loss in ONAN transformer windings $ Part I: Theory and model development," *IEEE Transactions on Power Delivery,* vol. 19, no. 1, pp. 186-193, 2004.

[43] J. Zhang and X. Li, "Coolant flow distribution and pressure loss in ONAN transformer windings. Part II: Optimization of design parameters," *IEEE Transactions on Power Delivery,* vol. 19, no. 1, pp. 194-199, 2004.

[44] W. Van der Veken, S. B. Paramane, R. Mertens, V. Chandak, and J. Coddé, "Increased efficiency of thermal calculations via the development of a full thermohydraulic radiator model," *IEEE Transactions on Power Delivery,* vol. 31, no. 4, pp. 1473-1481, 2015.

[45] J. Declercq and W. Van der Veken, "Accurate hot spot modeling in a power transformer leading to improved design and performance," *IEEE transmission and distribution conference*, vol. 2, pp. 920-924, 1999.

[46] H. Wong, *Handbook of essential formulae and data on heat transfer for engineers*. Longman London, 1977.

[47] W. M. Rohsenow, J. P. Hartnett, and E. N. Ganic, "Handbook of heat transfer applications," *New York, McGraw-Hill Book,* 1985.

[48] W. Wu, Z.D. Wang, A. Revell, H. Iacovides, and P. Jarman, "Computational fluid dynamics calibration for network modelling of transformer cooling oil flows-part I

heat transfer in oil ducts," *IET Electric Power Applications,* vol. 6, no. 1, pp. 19-27, 2012.

[49] W. Wu, Z.D. Wang, A. Revell, and P. Jarman, "Computational fluid dynamics calibration for network modelling of transformer cooling oil flows-part II: pressure loss at junction nodes," *IET Electric Power Applications,* vol. 6, no. 1, pp. 28-34, 2012.

[50] X. Zhang, Z.D. D. Wang, Q. Liu, P. Jarman, A. Gyore, and P. Dyer, "Investigation of Convective Heat Transfer Efficiency in the Horizontal Cooling Duct of a Disc Type Transformer Winding," *in 19th International Symposium on High Voltage Engineering (ISH), Pilsen, Czech Republic,* 2015.

[51] J. Coddé, W. Van der Veken, and M. Baelmans, "Assessment of a hydraulic network model for zig–zag cooled power transformer windings," *Applied thermal engineering,* vol. 80, pp. 220-228, 2015.

[52] X. Zhang and Z.D. Wang, "Assessment of Hydraulic Network Models in Predicting Reverse Flows in OD Cooled Disc Type Transformer Windings," *IEEE Access,* vol. 7, pp. 139249 - 139257, 2019.

[53] F. Torriano, H. Campelo, P. Labbé, M. Quíntela, and P. Picher, "Experimental and numerical thermofluid study of a disc-type transformer winding scale model," in *2016 XXII International Conference on Electrical Machines (ICEM)*, pp. 2833-2839, 2016.

[54] A. Skillen, A. Revell, H. Iacovides, and W. Wu, "Numerical prediction of local hot-spot phenomena in transformer windings," *Applied Thermal Engineering,* vol. 36, pp. 96-105, 2012.

[55] F. Torriano, M. Chaaban, and P. Picher, "Numerical study of parameters affecting the temperature distribution in a disc-type transformer winding," *Applied thermal engineering,* vol. 30, no. 14, pp. 2034-2044, 2010.

[56] E. Kranenborg, C. Olsson, B. Samuelsson, L. Lundin, and R. Missing, "Numerical study on mixed convection and thermal streaking in power transformer windings," *in 5th European Thermal-Sciences Conference*, 2008.

[57] M. Daghrah, X. Zhang, Z.D. Wang, Q. Liu, P. Jarman, and D. Walker, "Flow and temperature distributions in a disc type winding-part I: Forced and directed cooling modes," *Applied Thermal Engineering,* vol. 165, p. 114653, 2020.

[58] X. Zhang, Z.D. Wang, and Q. Liu, "Prediction of Pressure Drop and Flow Distribution in Disc Type Transformer Windings in an OD Cooling Mode," *IEEE Transactions on Power Delivery,* vol. 32, no. 4, pp. 1655-1664, 2017.

[59] X. Zhang, M. Daghrah, Z.D. D. Wang, Q. Liu, P. Jarman, and M. Negro, "Experimental Verification of Dimensional Analysis Results on Flow Distribution and Pressure Drop for Disc Type Windings in OD Cooling Modes," *IEEE Transactions on Power Delivery,* vol. 33, no. 4, pp. 1647-1656, 2018.

[60] X. Zhang, Z.D. D. Wang, and Q. Liu, "Interpretation of Hot Spot Factor for Transformers in OD Cooling Modes," *IEEE Transactions on Power Delivery,* vol. 33, no. 3, pp. 1071-1080, 2017.

[61] M. Nakadate, K. Toda, K. Sato, D. Biswas, C. Nakagawa, and T. Yanari, "Gas cooling performance in disc winding of large-capacity gas-insulated transformer," *IEEE Transactions on Power Delivery,* vol. 2, pp. 903-908, 1996.

[62] P. Allen, O. Szpiro, and E. Campero, "Thermal analysis of power transformer windings," *ELECTRIC MACHINES AND ELECTROMECHANICS,* vol. 6, no. 1, pp. 1-11, 1981.

[63] X. Zhang, Z.D.D. Wang, Q. Liu, P. Jarman, A. Gyore, and P. Dyer, "Numerical investigation of influences of coolant types on flow distribution and pressure drop in disc type transformer windings," in *International Conference on Condition Monitoring and Diagnosis (CMD)*, pp. 52-55, 2016.

[64] S. Tenbohlen, N. Schmidt, C. Breuer, S. Khandan, and R. Lebreton, "Investigation of Thermal Behavior of an Oil-Directed Cooled Transformer Winding," *IEEE Transactions on Power Delivery,* vol. 33, no. 3, pp. 1091-1098, 2018.

[65] X. Zhang, M. Daghrah, Z.D. Wang, and Q. Liu, "Flow and temperature distributions in a disc type winding-Part II: Natural cooling modes," *Applied Thermal Engineering,* vol. 165, p. 114616, 2020.

[66] S. Tenbohlen, N. Schmidt, S. Khandan, C. Breuer, and R. Lebreton, "Investigation of Thermal Behavior of an Oil Directed Cooled Transformer Winding," *IEEE Transactions on Power Delivery,* vol. 33, no. 3, pp. 1091-1098, 2017.

[67] F. Torriano, P. Picher, and M. Chaaban, "Numerical investigation of 3D flow and thermal effects in a disc-type transformer winding," *Applied thermal engineering,* vol. 40, pp. 121-131, 2012.

[68] M. Daghrah, Z.D. Wang, Q. Liu, A. Hilker, and A. Gyore, "Experimental Study of the Influence of Different Liquids on the Transformer Cooling Performance," *IEEE Transactions on Power Delivery,* vol. 34, no. 2, pp. 588-595, 2019.

[69] A. Santisteban, A. Piquero, F. Ortiz, F. Delgado, and A. Ortiz, "Thermal modelling of a power transformer disc type winding immersed in mineral and ester-based oils using network models and CFD," *IEEE Access,* vol. 7, pp. 174651-174661, 2019.

[70] A. Santisteban Díaz, F. Delgado San Román, A. Ortiz Fernández, I. Fernández Diego, and C. J. Renedo Estébanez, "Numerical study of the cooling capacity of several alternative liquids in zig-zag cooling system of a power transformer," 2016.

[71] A. Santisteban, F. Delgado, A. Ortiz, I. Fernández, C. Renedo, and F. Ortiz, "Numerical analysis of the hot-spot temperature of a power transformer with alternative dielectric liquids," *IEEE Transactions on Dielectrics and Electrical Insulation,* vol. 24, no. 5, pp. 3226-3235, 2017.

[72] X. Zhang, Z.D. Wang, Q. Liu, A. Gyore, and K. Rapp, "Investigation of the Total Flow Rates in Oil Natural Transformer Retrofilling Scenarios," in *20th International Conference on Dielectric Liquids (ICDL)*, pp. 1-4, Rome, Italy, 2019.

[73] R. Lecuna, F. Delgado, A. Ortiz, P. B. Castro, I. Fernandez, and C. J. Renedo, "Thermal-fluid characterization of alternative liquids of power transformers: A numerical approach," *IEEE Transactions on Dielectrics and Electrical Insulation,* vol. 22, no. 5, pp. 2522-2529, 2015.

[74] R. Girgis, M. Bernesjö, and G. K. Frimpong, "Detailed performance of a 50 MVA transformer filled with a natural ester oil versus mineral oil," *Paper A2–107, CIGRE Conferecen,* 2010.

[75] K. Dongjin, K. Kyosun, W. Jungwook, and K. Yungsig, "Hot spot temperature for 154 kV transformer filled with mineral oil and natural ester fluid," *IEEE*

Transactions on Dielectrics and Electrical Insulation, vol. 19, no. 3, pp. 1013-1020, 2012.

[76] M. Yamaguchi, T. Kumasaka, Y. Inui, and S. Ono, "The Flow Rate in a Self-Cooled Transformer," *IEEE Transactions on Power Apparatus and Systems,* vol. 100, no. 3, pp. 956-963, 1981.

[77] R. W. Fox, A. T. McDonald, and P. J. Pritchard, *Fluid Mechanics*, Eighth ed. New York: John Wiley & Sons , 2012.

[78] F. Torriano, H. Campelo, M. Quintela, P. Labbé, and P. Picher, "Numerical and experimental thermofluid investigation of different disc-type power transformer winding arrangements," *International Journal of Heat and Fluid Flow,* vol. 69, pp. 62-72, 2018.

[79] M. Stebel *et al.*, "Thermal analysis of 8.5 MVA disk-type power transformer cooled by biodegradable ester oil working in ONAN mode by using advanced EMAG–CFD–CFD coupling," *International Journal of Electrical Power & Energy Systems,* vol. 136, pp. 107737, 2022.

[80] G. R. Rodriguez, L. Garelli, M. Storti, D. Granata, M. Amadei, and M. Rossetti, "Numerical and experimental thermo-fluid dynamic analysis of a power transformer working in ONAN mode," *Applied Thermal Engineering,* vol. 112, pp. 1271-1280, 2017.

[81] R. B. Fdhila *et al.*, "Thermal modeling of power transformer radiators using a porous medium based CFD approach," in *International Conference on Computational Methods for Thermal Problems,* pp. 5-7, Dalian, China, 2011,.

[82] C. Olsson, "Buoyancy driven flow in counter flow heat exchangers," in *Journal of Physics: Conference Series*, vol. 395, no. 1, pp. 012058, 2012.

[83] M.-g. Kim, S. M. Cho, and J.-K. Kim, "Prediction and evaluation of the cooling performance of radiators used in oil-filled power transformer applications with non-direct and direct-oil-forced flow," *Experimental Thermal and Fluid Science,* vol. 44, pp. 392-397, 2013.

[84] S. B. Paramane, K. Joshi, W. Van der Veken, and A. Sharma, "CFD study on thermal performance of radiators in a power transformer: effect of blowing direction and offset of fans," *IEEE Transactions on Power Delivery,* vol. 29, no. 6, pp. 2596-2604, 2014.

[85] V. Chandak, S. Paramane, W. d Veken, and J. Coddé, "Numerical investigation to study effect of radiation on thermal performance of radiator for onan cooling configuration of transformer," in *IOP Conference Series: Materials Science and Engineering*, vol. 88, no. 1, pp. 012033, 2015.

[86] S. B. Paramane, W. Van der Veken, and A. Sharma, "A coupled internal–external flow and conjugate heat transfer simulations and experiments on radiators of a transformer," *Applied Thermal Engineering,* vol. 103, pp. 961-970, 2016.

[87] Y. J. Kim and M. Y. Ha, "A study on the performance of different radiator cooling systems in large-scale electric power transformer," *Journal of Mechanical Science and Technology,* vol. 31, no. 7, pp. 3317-3328, 2017.

[88] L. Garelli, G. R. Rodriguez, M. Storti, D. Granata, M. Amadei, and M. Rossetti, "Reduced model for the thermo-fluid dynamic analysis of a power transformer

radiator working in ONAF mode," *Applied Thermal Engineering,* vol. 124, pp. 855-864, 2017.

[89] S. Anishek, R. Sony, J. J. Kumar, and P. M. Kamath, "Performance analysis and optimisation of an oil natural air natural power transformer radiator," *Procedia Technology,* vol. 24, pp. 428-435, 2016.

[90] W. Wu, Z.D. Wang, and A. Revell, "Natural convection cooling ducts in transformer network modelling," in *International Symposium on High Voltage Engineering*, 2009.

[91] J. Zhang, X. Li, and M. Vance, "Experiments and modeling of heat transfer in oil transformer winding with zigzag cooling ducts," *Applied thermal engineering,* vol. 28, no. 1, pp. 36-48, 2008.

[92] T. L. Bergman, F. P. Incropera, D. P. DeWitt, and A. S. Lavine, *Fundamentals of heat and mass transfer*. John Wiley & Sons, 2011.

[93] S. W. Churchill and H. H. Chu, "Correlating equations for laminar and turbulent free convection from a vertical plate," *International Journal of Heat and Mass Transfer,* vol. 18, no. 11, pp. 1323-1329, 1975.

[94] S. Zhao, X. Zhang, Q. Liu, M. Wilkinson, M. Negro, and M. Daghrah, "Effect of Thermal Conduction on Transformer Radiator CFD Modelling," in *8th International Conference on Condition Monitoring and Diagnosis (CMD)*, pp. 242-245, 2020.

[95] J. Holman, "Heat transfer," tenth edition, The McGraw-Hill Companies. USA, 2010.

[96] N. AB. 2021. [online]. Available: https://www.nynas.com/en/product-areas-solutions/transformer-oils/oils/nytro-gemini-x/

[97] Shell. 2021. [online]. Available: http://www.shell.com/business-customers/lubricants-for-business/shell-diala-electrical-oils.html

[98] M. I. Material. "MIDEL 7131 Prodct Brochure" 2021. [online]. Available: https://www.midel.com/app/uploads/2018/05/MIDEL-7131-Product-Brochure.pdf

[99] COMSOL, "CFD Module User’s Guide," 2019. [online]. Available: https://doc.comsol.com/5.5/doc/com.comsol.help.cfd/CFDModuleUsersGuide.pdf

[100] J. Gastelurrutia, J. C. Ramos, G. S. Larraona, A. Rivas, J. Izagirre, and L. Del Río, "Numerical modelling of natural convection of oil inside distribution transformers," *Applied thermal engineering,* vol. 31, no. 4, pp. 493-505, 2011.

[101] A. A. Taheri, A. Abdali, and A. Rabiee, "A novel model for thermal behavior prediction of oil-immersed distribution transformers with consideration of solar radiation," *IEEE Transactions on Power Delivery,* vol. 34, no. 4, pp. 1634-1646, 2019.

[102] L. Raeisian, H. Niazmand, E. Ebrahimnia-Bajestan, and P. Werle, "Thermal management of a distribution transformer: an optimization study of the cooling system using CFD and response surface methodology," *International Journal of Electrical Power & Energy Systems,* vol. 104, pp. 443-455, 2019.

[103] E. Eckert and T. W. Jackson, "Analysis of turbulent free-convection boundary layer on flat plate," *National Aeronautics and Space Administration,* Washington DC, 1950.

[104] C. Y. Warner and V. S. Arpaci, "An experimental investigation of turbulent natural convection in air at low pressure along a vertical heated flat plate," *International Journal of Heat and Mass Transfer,* vol. 11, no. 3, pp. 397-406, 1968.

[105] F. Bayley, "An analysis of turbulent free-convection heat-transfer," *Proceedings of the Institution of Mechanical Engineers,* vol. 169, no. 1, pp. 361-370, 1955.

[106] S. Khandan and S. Tenbohlen, "Transient Thermal Condition of Natural Oil-cooled Disc-type Winding," in *20th International Conference on Dielectric Liquids (ICDL)*, pp. 1-4, 2019.

[107] L. Wang, L. Zhou, H. Tang, D. Wang, and Y. Cui, "Numerical and experimental validation of variation of power transformers' thermal time constants with load factor," *Applied Thermal Engineering,* vol. 126, pp. 939-948, 2017.

Appendix -1: Simplification of Oil Channel Shape of Radiator

To the stamped plate transformer radiator, the oil channel shape looks much closer like an elliptical shape rather than a rectangular shape, as shown in Fig. 0-1. However, there are more mesh constraints of the CFD model built on elliptical oil channel than the model using rectangular oil channel. By the modelling experience, more constraints result in a long processing time and a hard convergence.

Therefore, the reduced radiator CFD model is adopted to study the differences between two radiator geometries, i.e. one is built with elliptical oil channels and the other is built by rectangular oil channels. The cross-sectional view of the middle of an oil channel from two model geometries is shown in Fig. 0-1.

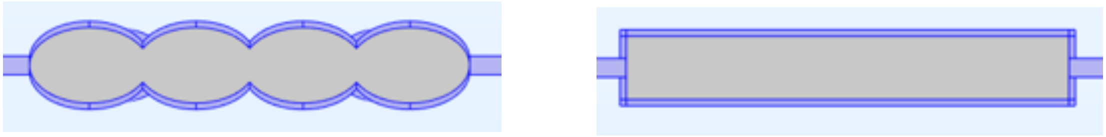

(a) Elliptical oil channel

(b) Rectangular oil channel

Fig. 0-1 Different shapes of oil channel in radiator CFD model (grey part for the oil domain, purple part for the radiator steel wall)

The key geometric characteristics to the thermal behaviour of the transformer radiator, i.e., surface area and liquid volume per panel, is given in TABLE 0-1. It is worth mentioning that the geometry of either the elliptical oil channel or rectangular oil channel is based on the measurement of the 4-panel 1-meter-high transformer radiator introduced in Section 3.1.2.

TABLE 0-1 Geometric characteristics of 4-panel radiator and its CFD models

Geometric characteristics (per panel)	Manufacture datasheet	‘Elliptical oil-channel’ CFD radiator model	‘Rectangular roil-channel’ radiator CFD model
Surface area (m^2)	1.12	1.13	1.13
Liquid volume (l)	3.44	3.44	3.45

The input conditions of the reduced CFD simulations are summarized in TABLE 0-2. A larger difference is expected at a higher top oil temperature between two geometries, and hence, the top liquid temperature is fixed at $80\ ℃$ when ambient temperature is set as $20\ ℃$. Two different air heat transfer coefficients are investigated; and five liquid flow rates are simulated to represent such radiator operated at different conditions.

TABLE 0-2 Input conditions for the reduced radiator CFD model

Material properties	Insulating liquids	Mineral oil (Gemini X)
Model Input	Top liquid temperature (T_{top})	80 ℃
	Air heat transfer coefficient (h_{air})	$6 \text{ and } 8\ W/(m^2K)$
	Oil flow velocity (Q_{oil})	$10-50\times10^{-5}\ m^3/s$
	Ambient temperature (T_{amb})	$20\ ℃$

The CFD simulation results are compared in term of the bottom oil temperature (T_{bot}) and total heat dissipation of the radiator (P). As seen in TABLE 0-3, the maximum difference of T_{bot} between the CFD simulations of two different geometries is less than 0.2 K, and the mismatch of the P under all scenarios is within 3.3%.

As for the processing time, each case of radiator CFD model with 'Elliptical oil channel' takes more than 8 hours, whereas each case of radiator CFD model with 'Rectangular oil channel' maximally takes 3 hours. Therefore, the radiator CFD model built by the rectangular oil channel is chosen in this PhD project.

TABLE 0-3 Radiator CFD model simulation eesults of 'Elliptical oil-channel' radiator model and 'Rectangular oil-channel' radiator model

Reduced radiator CFD Model Simulation Results								
Model input	h_{air}=6 ($W/(m^2\cdot K)$)				h_{air}=8 ($W/(m^2\cdot K)$)			
Q_{oil} ($10^{-5}\ m^3/s$)	Elliptical oil-channel		Rectangular oil-channel		Elliptical oil-channel		Rectangular oil-channel	
	T_{bot} (°C)	$P\ (W)$	T_{bot} (°C)	$P\ (W)$	T_{bot} (°C)	$P\ (W)$	T_{bot} (°C)	$P\ (W)$
10	70.7	1402.4	70.5	1444.3	68.2	1783.3	67.8	1839.1

20	75.3	1457.6	75.2	1501.9	73.9	1873.6	73.9	1933.1
30	76.8	1479.5	76.8	1525.2	75.9	1909.3	75.8	1970.9
40	77.6	1493.3	77.6	1539.9	76.9	1931.5	76.8	1994.8
50	78.1	1503.5	78.0	1550.7	77.5	1948.1	77.5	2012.6

Publication List

Journal Paper

[P1] S. Zhao, Q. Liu, M. Wilkinson, G. Wilson and Z. Wang, "A Reduced Radiator Model for Simplification of ONAN Transformer CFD Simulation," in *IEEE Transactions on Power Delivery*, doi: 10.1109/TPWRD.2022.3142889.

[P2] S. Zhao, X. Zhang, Q. Liu, and Z. Wang, " Investigating Liquid Temperatures and Total Flow Rates in Liquid Natural Cooled Transformers," in IEEE Transactions on Power Delivery. (to be submitted)

Conference Paper

[P3] S. Zhao, X. Zhang, Q. Liu, M. Wilkinson, M. Negro, and M. Daghrah, "Effect of Thermal Conduction on Transformer Radiator CFD Modelling," in 2020 8th International Conference on Condition Monitoring and Diagnosis (CMD), 2020: IEEE, pp. 242-245.

[P4] S. Zhao, X. Zhang, Q. Liu, M. Wilkinson, M. Negro, and M. Daghrah, " Development of an Experimental Setup to Study Temperature Distribution of Liquid Natural Cooled Power Transformers," in 2021 22nd International Symposium on High Voltage Engineering (ISH), 2021.

[P5] S. Zhao, Q. Liu, Z.D. Wang, M. Wilkinson, M. Daghrah G. Wilson and E. Van Schaik, " Investigation of Air Convection Heat Transfer Coefficient of a Natural Cooled Transformer Radiator," in 2022 International Conference on High Voltage Engineering and Application (ICHVE), 2022. (to be submitted)